Schweizerische Eidgenossenschaft
Confédération suisse
Confederazione Svizzera
Confederaziun svizra

Eidgenössisches Departement für Umwelt, Verkehr, Energie und Kommunikation UVEK
Département fédéral de l'environnement, des transport, de l'énergie et de la communication DETEC
Dipartimento federale dell'ambiente, dei trasporti, dell'energia e delle communication DATEC

Bundesamt für Strassen
Office fédéral des routes
Ufficio federale delle Strade

Carbonation – passivation behavior and corrosion kinetic under the combined effect of wet-dry cycles in presence of chlorides

Karbonatisierung – Passivierungsverhalten und Korrosionskinetik bei zyklischen Feuchtebedingungen unter der Anwesenheit von Chloriden

Carbonatation – passivation et corrosion vitesse sous l`action de cyclique humide et sécheresse et en présence de chlorures

TFB AG
Stefanie v. Greve-Dierfeld

Paul-Scherer-Institut PSI
Daniel Grolimund
Pavel Trtik

Reseach project BGT_20_03A_01 at the request of the Federal Roads Office FEDRO

March 2026 **1818**

Schweizerische Eidgenossenschaft
Confédération suisse
Confederazione Svizzera
Confederaziun svizra

Eidgenössisches Departement für Umwelt, Verkehr, Energie und Kommunikation UVEK
Département fédéral de l'environnement, des transport, de l'énergie et de la communication DETEC
Dipartimento federale dell'ambiente, dei trasporti, dell'energia e delle communication DATEC

Bundesamt für Strassen
Office fédéral des routes
Ufficio federale delle Strade

Carbonation – passivation behavior and corrosion kinetic under the combined effect of wet-dry cycles in presence of chlorides

Karbonatisierung – Passivierungsverhalten und Korrosionskinetik bei zyklischen Feuchtebedingungen unter der Anwesenheit von Chloriden

Carbonatation – passivation et corrosion vitesse sous l`action de cyclique humide et sécheresses et en présences de chlorures

TFB AG
Stefanie v. Greve-Dierfeld

Paul-Scherer-Institut PSI
Daniel Grolimund
Pavel Trtik

Reseach project BGT_20_03A_01 at the request of the Federal Roads Office FEDRO

March 2026 **1818**

Imprint

Research center and project team

Project management
Stefanie v. Greve-Dierfeld

Members
Daniel Grolimund
Pavel Trtik

Accompanying Commission

President
Ueli Angst

Members
Barbara Lothenbach
Kristian Schellenberg
Martin Käser
Fabrizio Moro

Applicant

Federal Roads Office FEDRO

Source

This document is available for free download at http://www.mobilityplatform.ch

Table of contents

Summary

Motivation and objective

Both carbonation and chloride ingress in concrete alter the chemical composition and proportions of the hydrate phases and the pore solution chemistry and modify the pore structure and the moisture content of the concrete. These changes can influence the rate of the other transport process (chloride ingress or carbonation). In addition, they affect the initiation of corrosion as well as corrosion propagation.

However, summarized evaluations and systematic investigations addressing how these combined effects influence the respective deterioration mechanisms, corrosion initiation, and corrosion propagation under Swiss (CH) climate conditions are currently not available. Performance-based as well as prescriptive requirements to ensure durability in national and European standardization have been developed considering individual deterioration mechanisms only, although structures exposed to spray mist or water spray from de-icing salts (XD1/XD3) are always simultaneously exposed to atmospheric CO_2 (XC4).

For example, SN EN 206 in combination with SIA 262 assumes, for exposure class XD1&XC4, that carbonation is the governing deterioration mechanism and therefore only the carbonation resistance must be verified. There are currently no studies demonstrating whether carbonation is always the governing deterioration mechanism. Likewise, it remains unclear under which conditions simultaneous exposure becomes decisive in XD1&XC4 environments and what consequences this has for durability.

In SIA 269/2, when estimating the corrosion risk, it is stated that the critical chloride content (C_{crit} ≥ 0.4% by mass of binder) may be lower for carbonated or partially carbonated concrete. However, information on the quantitative reduction of C_{crit} or the pH level or the critical distance between the reinforcement and the carbonation front at which the critical chloride content changes is lacking.

With the aim of removing obstacles to the use of more sustainable concrete and concrete structures, Exposure Resistance Classes (ERC) will be introduced in EN 1992-1-1, at least for exposure classes XC, XD and XS classes. Depending on the exposure class, the required concrete cover is specified as a function of the material resistance (XRC, XRDS with C=Carbonation, D=Deicing salts and S=Sea salts), see Fig. 1 (top) for XRC classes and (bottom) XRD classes. Inevitably, if material resistance requires the same cover for chloride and carbonation, simultaneous effects can occur, with consequences for durability that have not yet been clarified.

Table 6.3 (CH) — Minimum concrete cover $c_{min,dur}$ for carbon reinforcing steel - carbonation

ERC	Exposure class (carbonation)							
	XC1		XC2		XC3		XC4	
	Design service life (years)							
	50	100	50	100	50	100	50	100
XRC 1	10	10	10	10	10	10	10	15
XRC 2	10	10	10	15	10	15	10	20
XRC 3	10	10	10	15	10	20	15	25
XRC 4	10	10	15	20	15	25	20	30
XRC 5	10	10	15	20	20	30	25	35
XRC 6	10	10	20	25	25	35	30	40
XRC 7	10	10	20	25	30	40	35	45
XRC 8	10	10	25	30	35	45	40	50
XRC 9	10	10	25	30	40	50	45	55

Table 6.4 (CH) — Minimum concrete cover cmin,dur for carbon reinforcing steel — Chlorides

ERC	Exposure class (Chlorides)			
	XD1=XD2a(CH)		XD3 = XD2b(CH)	
	Design service life (Year)			
	50	100	50	100
XRDS 1	10	20	20	30
XRDS 2	15	25	25	35
XRDS 3	15	25	30	40
XRDS 4	20	30	30	40
XRDS 5	20	30	35	45
XRDS 6	25	35	35	45
XRDS 7	25	35	40	50
XRDS 8	25	35	40	50
XRDS 9	25	35	45	55
XRDS 10	25	35	45	55
XRDS 12	30	40	50	-
XRDS 14	30	40	55	-
XRDS 16	30	40	-	-
XRDS 18	30	40	-	-
XRDS 24	35	45	-	-
XRDS 30	40	50	-	-
XRDS 40	45	55	-	-

Fig. 1 *Concrete cover in dependency of XRC (top) and XRD (bottom) classes (for the foot notes, the national Annex is referred to)*

This leads to the following research questions:

- What is the influence of simultaneous action on each deterioration process?
- Which process is the governing deterioration mechanism?
- Do current standards adequately address the risks associated with combined exposure?

Methodology

The test setup shown in Fig. 2 (top) was chosen to investigate the effects of combined exposure on the carbonation process. The following exposure sequences were investigated:

- Accelerated carbonation (R0-CO_2)
- Accelerated carbonation followed by water spraying (Wf-CO_2)
- Accelerated carbonation followed by exposure to chloride solution (Wf-Cl-CO_2)

The experimental set-up shown in Fig. 2 (bottom) was chosen to investigate the combined effect on chloride transport. The following exposure sequences were applied:

- Application of chloride solution (R0-Cl)
- Air storage followed by exposure to a chloride solution (Wf-Cl)
- Accelerated carbonation followed by exposure to a chloride solution (Wf-Cl-CO_2)

The transfer to standard conditions was carried out using parallel standard tests, and the transfer to XD1&XC4 conditions was carried out using combined aging tests and microstructural investigations.

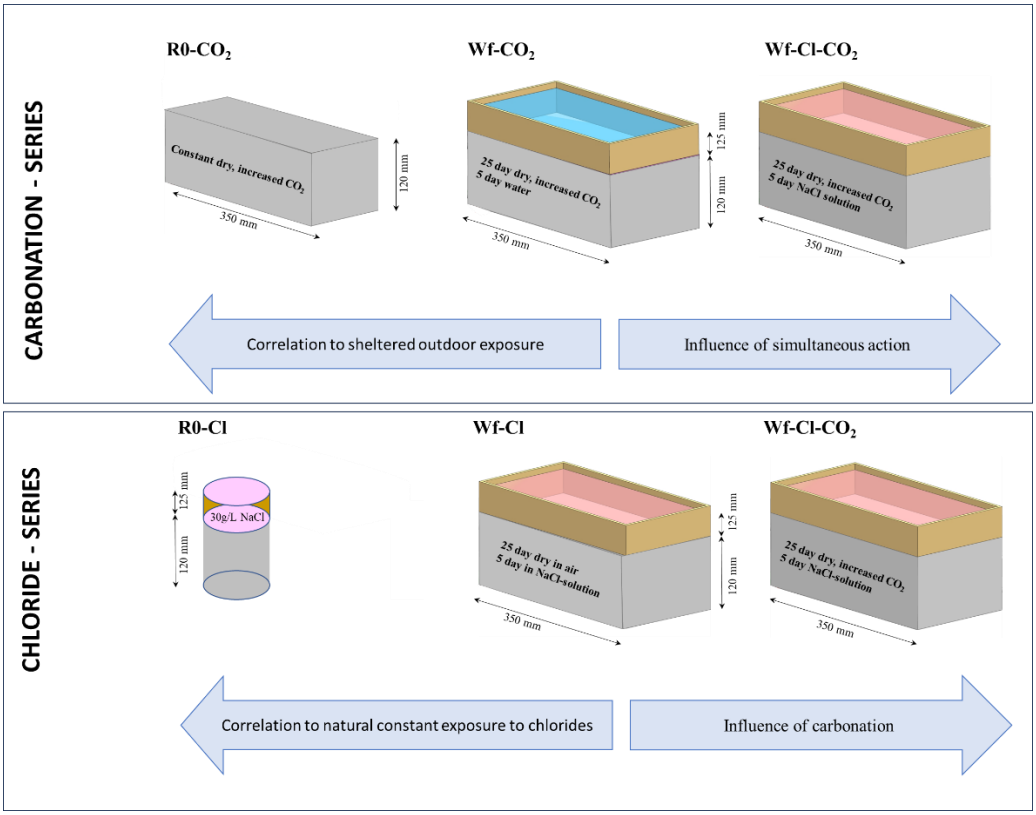

Fig. 2 *Experimental setup for investigating the influence of combined exposure on carbonation (top) and chloride ingress (bottom).*

To determine the influence of the combined effect on corrosion behaviour and the critical chloride content, the onset of corrosion and the corrosion rates were determined on separately prepared samples subjected to Wf-Cl, Wf-Cl-CO_2, and Wf-CO_2 exposure conditions.

Influence of chlorides on carbonation

Figure 3 (top) illustrates the influence of carbonation on the phase composition. During carbonation, calcium-bearing hydrate phases are generally converted into calcium carbonate ($CaCO_3$) (Fig. 3, top left), which often results in a reduction of total porosity but at the same time in a coarsening of the pore structure. Consequently, the pore solution pH decreases. If chlorides are present in the concrete, part of the chlorides is chemically bound (Fig. 3, top right), mainly through the conversion of AFm phases into Friedel's salt. During subsequent carbonation, Friedel's salt is destabilized and converted into $CaCO_3$, leading to the release of previously bound chlorides. In this case, the porosity is not significantly affected beyond the changes caused by carbonation alone.

The influence of chlorides on the moisture distribution in carbonated concrete is shown in Fig. 3 (middle). The coarser pore structure formed during carbonation leads to pronounced moisture fluctuations extending to greater depths when combined with irrigation (Fig. 3, middle left). This is indicated by the highlighted blue area, representing zones of high moisture content at electrical resistivities of ρ = 0 - 500 Ωm and dry concrete at ρ > 5000 Ωm. In contrast, the presence of chlorides results in less pronounced moisture fluctuations at shallower depths and in a generally higher degree of saturation (Fig. 3, middle right).

The influence of chlorides on the carbonation rate is shown in Fig. 3 (bottom). As gaseous CO_2 transport occurs only through the air-filled pore space, irrigation is known to slow down carbonation (Fig. 3, bottom left). However, the increased saturation in the presence of chlorides leads to a further reduction of the carbonation rate under combined exposure conditions (Fig. 3, bottom right).

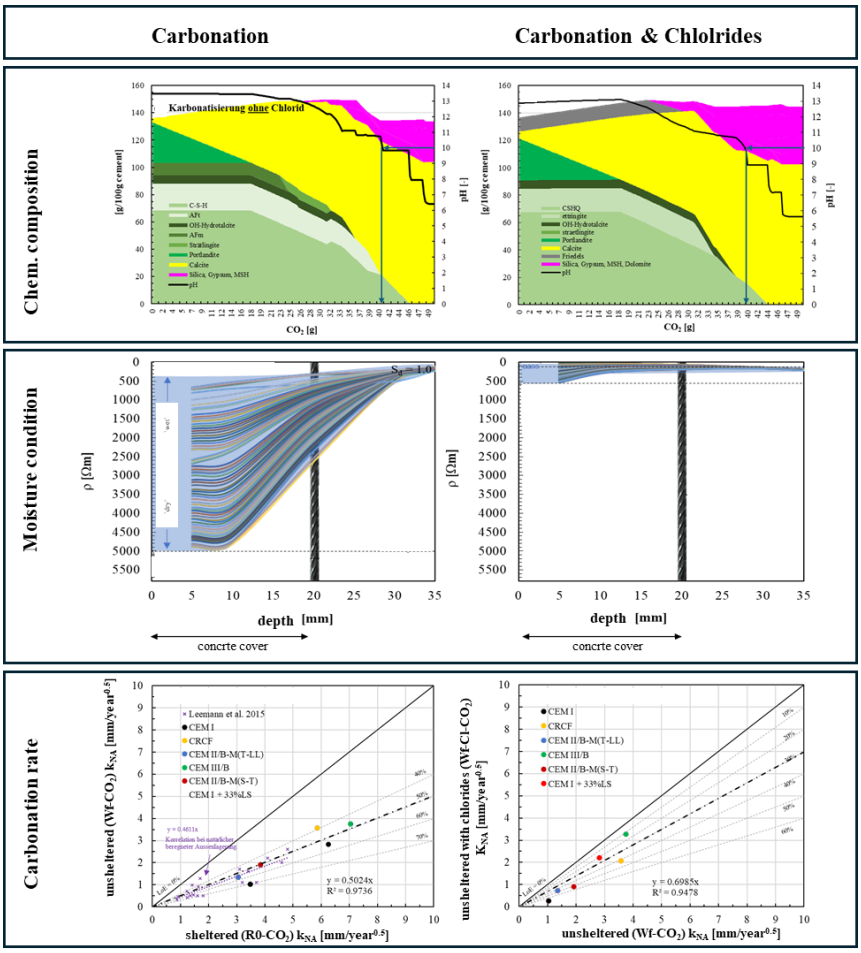

Fig. 3 *Carbonation in (left) chloride free conditions (right) in conditions with simultaneous chloride ingress, (top) differences in chemical composition (middle) differences in moisture gradients and (bottom) differences in on carbonation rate.*

Influence of carbonation on chloride transport

Figure 4 (top) shows the influence of carbonation on the total chloride content. Without simultaneous carbonation, chlorides penetrate less deeply but accumulate in higher local concentrations, as indicated by the dark red area in Fig. 4 (top left). With simultaneous carbonation, chlorides penetrate significantly deeper but are distributed over a larger area, resulting in lower local chloride contents. This is illustrated by the lighter red tones in Fig. 4 (top right). This behavior can be attributed to the reduced chloride-binding capacity of carbonated concrete and the coarser pore structure.

The chloride ingress observed by µXRF analysis in Fig. 4 (top) is reflected in the chloride profiles shown in Fig. 4 (middle). In carbonated concrete, the chloride maximum occurs at greater depths and at lower peak chloride contents (Fig. 4, middle right) compared to non-carbonated concrete (Fig. 4, middle left). Nevertheless, a distinct chloride maximum develops even under alternating wetting conditions, in contrast to concrete permanently exposed to a chloride solution, where the maximum chloride content is ideally expected at the surface.

Compared to permanent exposure to a chloride solution, chloride ingress is significantly faster under alternating wetting and drying conditions, as capillary absorption is much faster than diffusive transport (Fig. 4, bottom left). The release of previously bound chlorides and the coarser pore structure in carbonated concrete lead to a further, although only slightly increased, rate of chloride penetration (Fig. 4, bottom right).

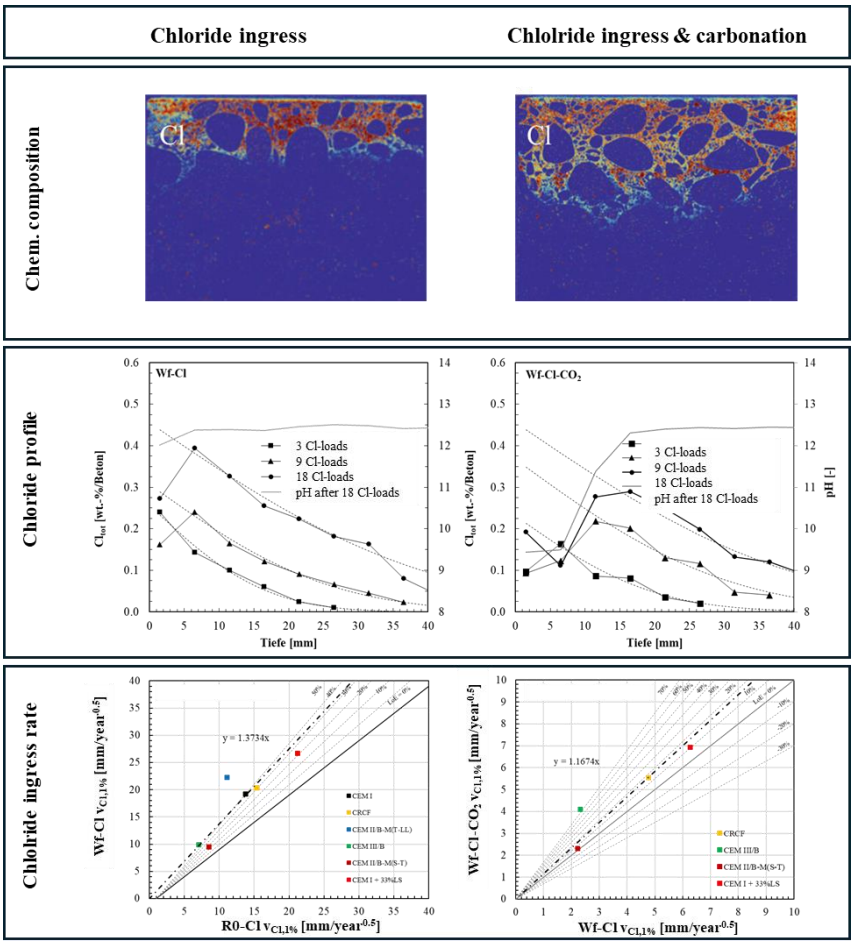

Fig. 4 *Chloride transport without (left) and with (right) carbonation (top) chloride content using µXRF, (middle) profiles of the total chloride content compared to the pH value and (bottom) chloride penetration rate.*

Predicting the occurrence of combined effects

Systematic investigations showed that chloride transport in carbonated concrete is similar or up to 1.2 times faster, while carbonation in chloride-contaminated concrete is about 30% slower.

By relating these findings to real Swiss (CH) exposure conditions, it was possible to identify combinations of carbonation coefficient and chloride resistance, as defined in SIA 262/1 Annex I or B, that lead to an increased risk of combined action. As moisture conditions and the frequency of chloride exposure vary under real XD1 conditions, this relationship is represented as a bandwidth in Fig. 5 (a).

Furthermore, the question arises whether the risk of combined effects can be assessed without explicit knowledge of carbonation coefficients or chloride resistances. For this purpose, relationships between carbonation rate and w/CaO, as well as between chloride penetration rate and w/SiO_2, were confirmed. The ratio of chloride penetration rate to carbonation rate can therefore be expressed as a function of the SiO_2/CaO ratio (Fig. 5 (b)). If the ratio SiO_2/CaO results in $k_{NA}/v_{Cl} > 1$, carbonation is the governing process under the given exposure conditions. If $k_{NA}/v_{Cl} < 1$, chloride ingress is faster. A ratio close to unity indicates a high probability of simultaneous action.

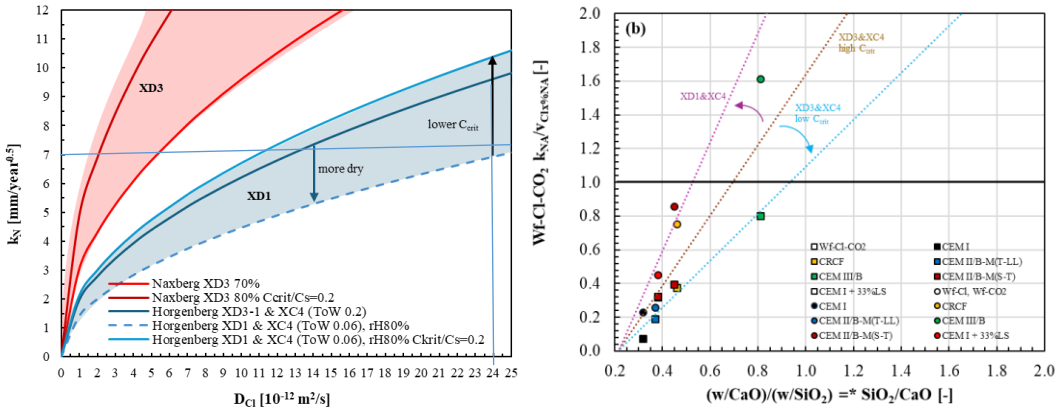

Fig. 5 *(a) Combination of k_N and D_{Cl} and (b) CaO/SiO_2 ratios indicating a high probability of simultaneous action.*

Consequences of simultaneous effects on corrosion initiation

The critical chloride content (C_{crit}), expressed as total chloride content and determined using phenolphthalein, decreased to approximately 0.2–0.4 wt.% of binder at a carbonation front distance of about 6 mm from the reinforcement (Fig. 6 (a)). At this depth, the pH gradient corresponds to values of approximately 10.5–11.5. Under alternating moisture conditions, C_{crit} decreased to 0.3–0.4 wt.% of binder, while solution tests at full saturation yielded values around 0.2 wt.% of binder. This reduction was independent of the C_{crit} of the non-carbonated concrete.

This reduction is attributed to the lower chloride-binding capacity at reduced pH values, leading to a C_{crit} of approximately 0.3 wt.% of binder in concrete tests at a pH of around 11 (Fig. 6 (b)). In solution tests, chloride binding was generally lower due to the higher pore solution volume and a reduced physical binding of chlorides to C(-A)-S-H, resulting in a further decrease of C_{crit} to approximately 0.2 wt.% of binder.

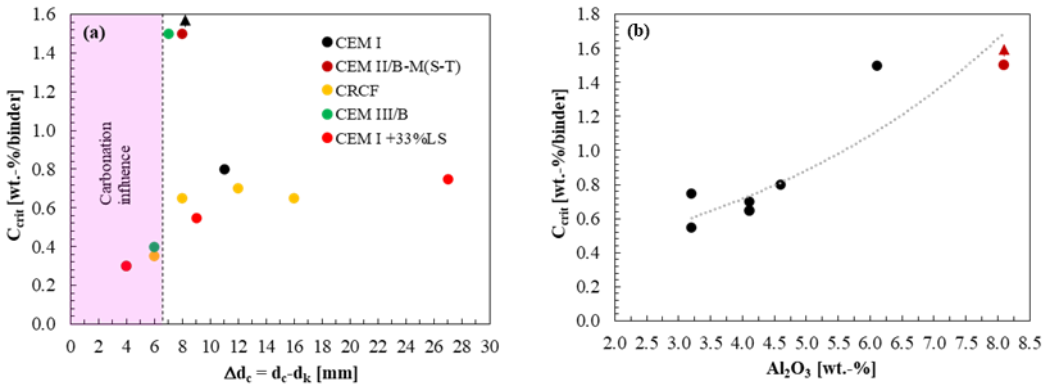

Fig. 6 *C_{crit} as a function of the distance of the carbonation front from the reinforcement (a) and C_{crit} as a function of Al_2O_3 for non-carbonated concrete (b).*

In summary, the combined effect on the critical corrosion-inducing chloride content is as follows:

- With carbonation, the C_{crit} can drop to 0.2-0.4.
- The drop in the C_{crit} to the level of 0.2-0.4 is independent of the critical chloride content in the non-carbonated concrete.
- At corrosion initiation, the distance between the carbonation depth and the reinforcement is approx. 6 mm.
- The corresponding pH value at this depth was approx. 10.5-11.5.
- In these investigations, the C_{crit} correlated very well with the Al_2O_3 content, although the SiO_2 content and w/b value should also play an integral role.

Corrosion rate with combined action

To estimate the effect of combined action on corrosion, Fig. 7(a) presents the macro-corrosion rates under wet conditions for all reinforcing bars in which corrosion initiation was observed, including individual data points. The dashed horizontal line indicates the mean corrosion rate for carbonation-induced corrosion, chloride-induced corrosion, and corrosion under combined chloride and carbonation exposure. Fig. 7(b) shows the corresponding micro-corrosion rates.

Although the corrosion period was relatively short, the following conclusions can be drawn: Under combined exposure, the corrosion rate is approximately twice as high as that observed for chloride-induced corrosion. Carbonation-induced corrosion exhibits the lowest corrosion rates. The same ranking applies to the micro-corrosion rates. For carbonation-induced corrosion, the ratio between micro- and macro-corrosion is approximately 1:1. In contrast, for corrosion in the presence of chlorides, macro-corrosion dominates, with a ratio of micro- to macro-corrosion of approximately 0.5.

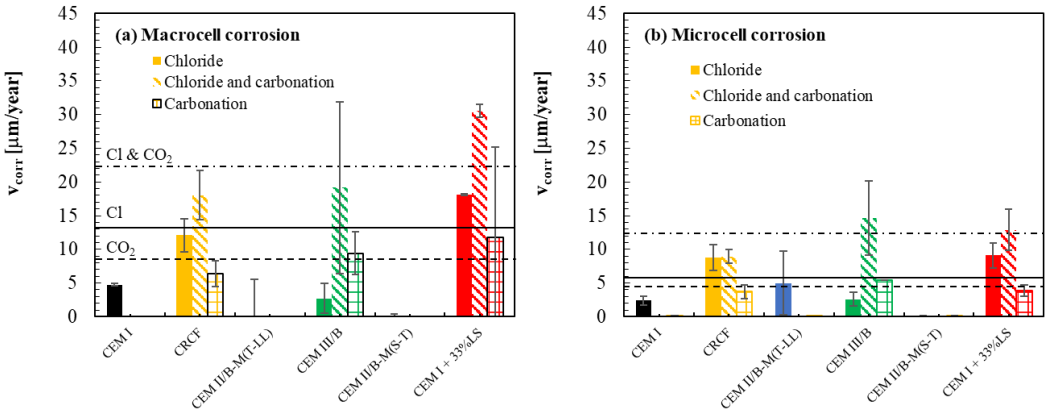

Fig. 7 *Macro-corrosion rates (a) and micro-corrosion rates (b) for chloride-induced corrosion, chloride-induced corrosion in carbonated concrete, and carbonation-induced corrosion.*

Risk of combined action in standards

Using the correlation between the carbonation coefficient expressed as KW and the chloride diffusion coefficient expressed as CW (as defined in SN EN 206 and SIA 262/1), as well as the material parameter SiO_2/CaO, it is possible to identify concrete compositions that are susceptible to combined action under XD3&XC4 and XD1&XC4 exposure conditions. Fig. 8 illustrates these relationships. Areas with dominant chloride ingress are shown in dark grey, areas with dominant carbonation in light grey, and intermediate zones indicate simultaneous progression. The performance ranges of tested NPK-A to NPK-F concretes are added.

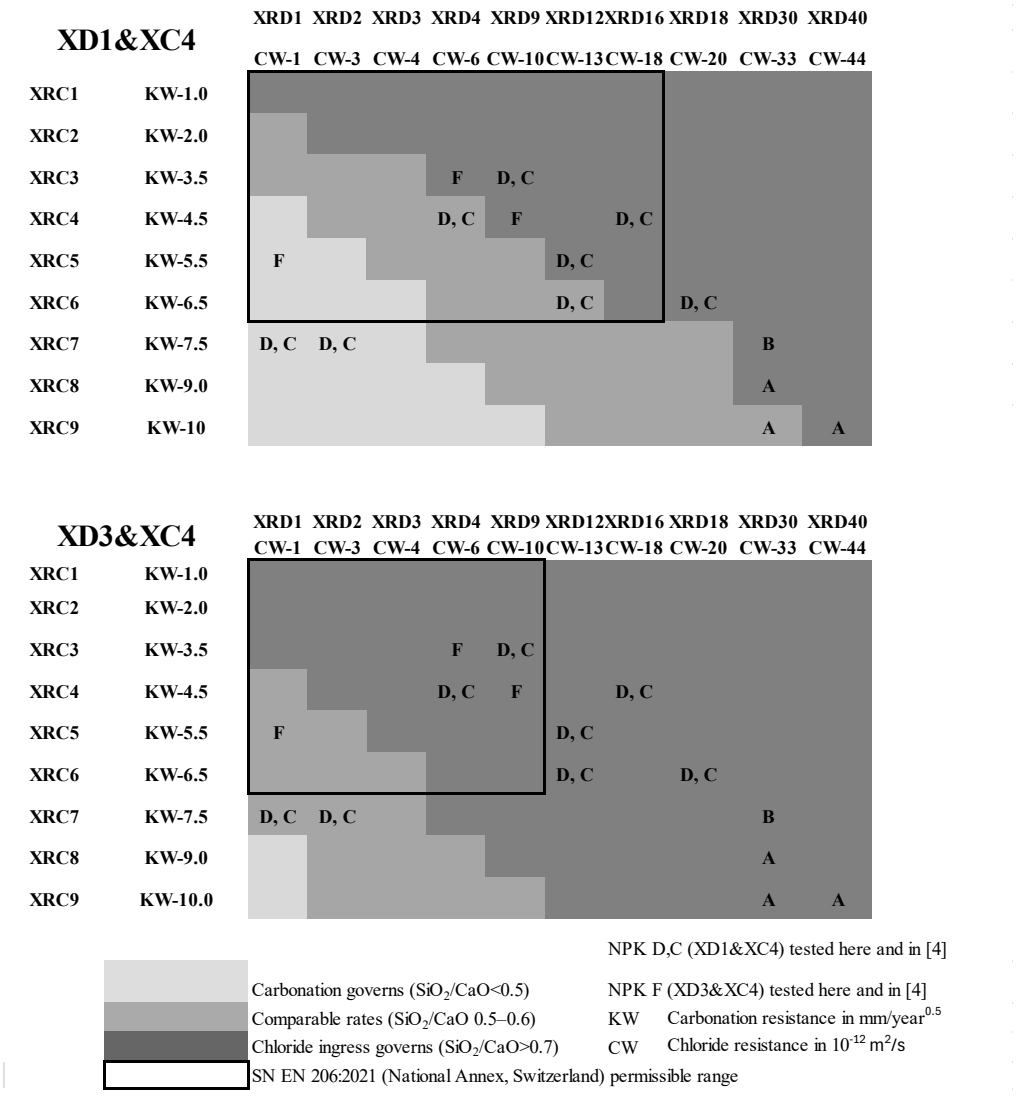

Fig. 8 *Estimation of class combinations leading to combined action for (top) XD1&XC4 and (bottom) XD3&XC4 exposure classes.*

(a) Assessment of the risk for combined action in SN EN 206 (black square range Fig. 8)

For **XD1**&XC4 exposure, SN EN 206 specifies a carbonation resistance requirement of KW-6.5, while no explicit limit is defined for chloride resistance. Based on the investigated NPK-D concretes, a corresponding chloride diffusion coefficient of approximately CW-18 can be derived. The required concrete cover is identical for XC4 and XD1.

Under XD1&XC4 exposure, chloride ingress is faster if the required material performance is exactly met, despite identical cover requirements. The reason for this is the slowing of carbonation progress in chloride contaminated concrete.

Critical conditions for combined actions occur for concretes with carbonation resistance close to the limit value KW-6.5 and moderate chloride resistance (CW between 6–10). In this case, corrosion is induced earlier than expected from chloride ingress solely and the corrosion progress is accelerated.

For **XD3**&XC4 exposure, SN EN 206 requires KW-6.5 and CW-10. In this case, the required concrete cover is higher for XD3 than for XC4 solely.

Where the limiting values for KW and CW are exactly met, chloride ingress determines the corrosion initiation. But at lower chloride resistance, combined effects are possible. Because the concrete cover is higher than required for carbonation solely, combined action seems not critical for corrosion initiation before the end of design service life.

(b) Assessment according to EN 1992-1-1:2023

The Exposure Resistance Class (ERC) concept introduced in EN 1992-1-1:2023 allows a balance between material resistance and concrete cover. Higher resistance can compensate for reduced cover and vice versa. This approach facilitates the use of more sustainable concrete mixes that may not comply with the fixed KW limits of SN EN 206. A single concrete composition may also be applied to several exposure classes if the cover is adjusted accordingly.

Because cover and resistance are defined separately for each exposure class, combinations of XRC and XRDS classes requiring identical cover were identified. These combinations may lead to combined action. To avoid corrosion risk due to combined action, the middle grey combinations in fig. 8 should be avoided.

Summary and need for further research

The main findings and remaining research needs are summarized below:

- in chloride-contaminated concrete, saturation increases and leads to slower carbonation progress
- In carbonated concrete, bound chlorides dissolve and can slightly accelerate the penetration of chlorides.
- The risk of combined action can be estimated from carbonation and chloride resistances according to SIA 262/1 or from the SiO_2/CaO ratio. To avoid combined actions, the critical combinations in Fig. 8 shall be avoided.
- The critical chloride content increases with Al_2O_3 and SiO_2 content of the binder. Upon carbonation, the critical chloride content is reduced to approx. 0.2-0.4 independent from binder composition.
- The corrosion rate is higher for chloride-loaded and carbonated concrete than for chloride-loaded or carbonated concrete.
- If the limiting values in SN EN 206 are exactly met, the risk for combined action is low.
- For the combination of XRD and XRC classes, to avoid the risk of combined action Fig. 8 can be considered.

Zusammenfassung

Motivation und Stand der Normung

Sowohl die Karbonatisierung als auch das Eindringen von Chloriden verändern die chemische Zusammensetzung der Hydratphasen, die Porenlösung, die Porenstruktur sowie den Feuchtegehalt des Betons. Diese Veränderungen beeinflussen die Transportprozesse und wirken sich auf die Korrosionsinitiierung und -ausbreitung aus.

Derzeit liegen keine zusammenfassenden Bewertungen zu kombinierten Karbonatisierungs- und Chlorideinflüssen unter Schweizer Klimabedingungen vor. Bestehende Dauerhaftigkeitsanforderungen berücksichtigen in der Regel nur einzelne Schädigungsmechanismen, obwohl Bauwerke unter XD-Exposition stets auch CO_2 (XC4) ausgesetzt sind.

SN EN 206 und SIA 262 gehen für XD1&XC4 davon aus, dass die Karbonatisierung maßgebend ist. Belastbare Nachweise hierfür fehlen jedoch. Ebenso weist SIA 269/2 darauf hin, dass der kritische Chloridgehalt in karbonatisiertem Beton reduziert sein kann, ohne dass quantitative Angaben vorliegen.

Mit dem ERC-Konzept in EN 1992-1-1 wird der Betonüberdeckung ein Materialwiderstand zugeordnet. Diese Widerstandsgrössen sind beispielsweise XRC bei Karbonatisierung und XRD bei Chlorideinwirkung. XRC ist vergleichbar mit dem Karbonatisierungswiderstand KW und XRDS ist vergleichbar mit dem Chloridwiderstand CW. Abb. 1 zeigt wie in Abhängigkeit der Expositionsklasse neu die Bewehrungsüberdeckung in Abhängigkeit des Materialwiderstands (XRC, XRDS) zugeordnet ist.

Zwangsläufig ist bei optimal auf die Überdeckung abgestimmtem Chlorid- und Karbonatisierungswiderstand des Betons mit kombiniertem Angriff zu rechnen.

Table 6.3 (CH) — Minimale Betondeckung $c_{min,dur}$ für Kohlenstoffstahl — Karbonatisierung

ERC	Exposure class (carbonation)							
	XC1		XC2		XC3		XC4	
	planmässige Nutzungsdauer (Jahre)							
	50	100	50	100	50	100	50	100
XRC 1	10	10	10	10	10	10	10	15
XRC 2	10	10	10	15	10	15	10	20
XRC 3	10	10	10	15	10	20	15	25
XRC 4	10	10	15	20	15	25	20	30
XRC 5	10	10	15	20	20	30	25	35
XRC 6	10	10	20	25	25	35	30	40
XRC 7	10	10	20	25	30	40	35	45
XRC 8	10	10	25	30	35	45	40	50
XRC 9	10	10	25	30	40	50	45	55

Tabelle 6.4 (CH) — Minimale Betondeckung cmin,dur für unlegierten Betonstahl — Chlorid

ERC	Expositionsklasse (Chlorid)			
	XD1=XD2a(CH)		XD3 = XD2b(CH)	
	Geplante Nutzungsdauer (Jahre)			
	50	100	50	100
XRDS 1	10	20	20	30
XRDS 2	15	25	25	35
XRDS 3	15	25	30	40
XRDS 4	20	30	30	40
XRDS 5	20	30	35	45
XRDS 6	25	35	35	45
XRDS 8	25	35	40	50
XRDS 9	25	35	45	55
XRDS 10	25	35	45	55
XRDS 12	30	40	50	-
XRDS 14	30	40	55	-
XRDS 16	30	40	-	-
XRDS 18	30	40	-	-
XRDS 30	40	50	-	-
XRDS 40	45	55	-	-

***Abb. 1** Betonüberdeckung in Abhängigkeit der XRC- (oben) und XRD-Klassen (unten)*

Damit stellen sich folgende Fragen:

- Welchen Einfluss hat die simultane Einwirkung auf den jeweils anderen Schädigungsprozess?
- Welchen Einfluss hat die simultane Einwirkung auf den korrosionsfortschritt?
- Wann besteht das Risiko für kombinierte Einwirkung in heutigen Normen?

Methodik und Vorgehensweise

Zur Untersuchung der Auswirkungen einer kombinierten Einwirkung auf den Karbonatisierungsprozess wurde der in Abb. 2 (oben) dargestellte Versuchsaufbau verwendet. Folgende Expositionsabfolgen wurden untersucht:

- Beschleunigte Karbonatisierung (R0-CO_2)
- Beschleunigte Karbonatisierung mit anschließender Wasserbeaufschlagung (Wf-CO_2)
- Beschleunigte Karbonatisierung mit anschließender Beaufschlagung mit Chloridlösung (Wf-Cl-CO_2)

Zur Untersuchung der kombinierten Einwirkung auf den Chloridtransport wurde der in Abb. 2 (unten) dargestellte Versuchsaufbau gewählt. Dabei wurden folgende Expositionsabfolgen angewendet:

- Beaufschlagung mit Chloridlösung (R0-Cl)
- Luftlagerung mit anschließender Beaufschlagung mit Chloridlösung (Wf-Cl)
- Beschleunigte Karbonatisierung mit anschließender Beaufschlagung mit Chloridlösung (Wf-Cl-CO_2)

Die Übertragung der Versuchsergebnisse auf Normbedingungen erfolgte mittels parallellaufender Normprüfungen. Die Übertragung auf XD1&XC4-Expositionsbedingungen wurde anhand von Auslagerungsversuchen sowie ergänzenden Bauwerksuntersuchungen durchgeführt.

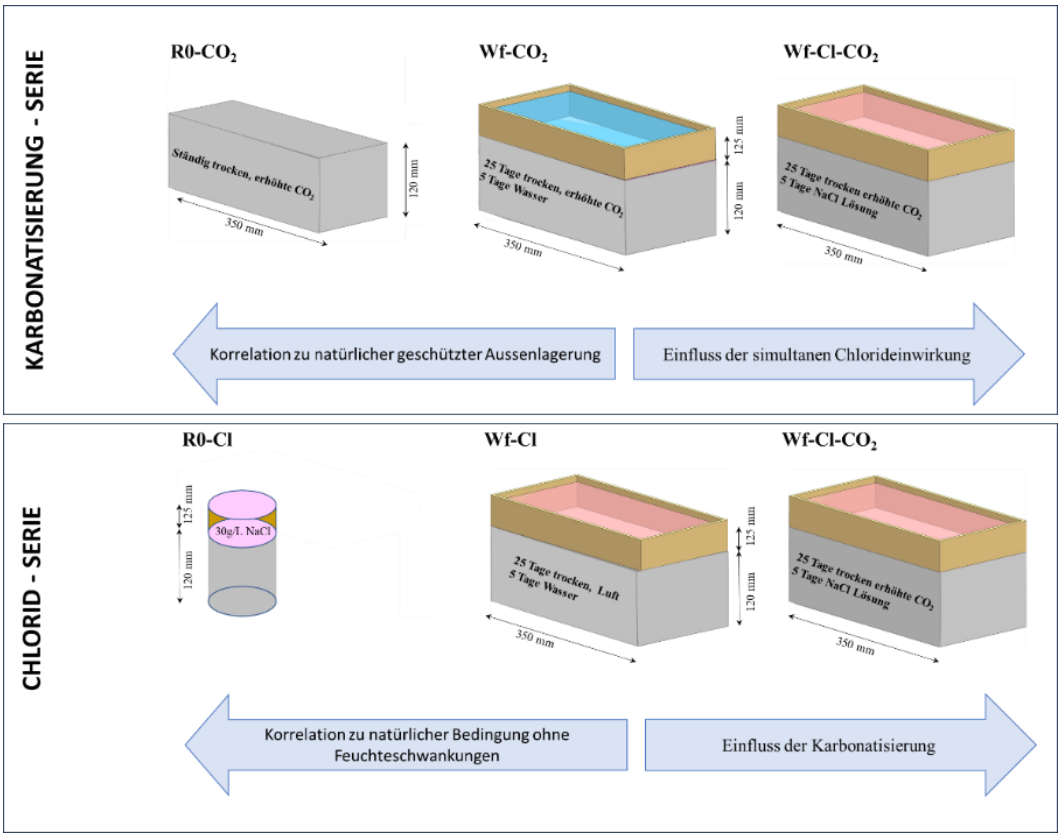

***Abb. 2** Versuchsaufbau zur Untersuchung des Einflusses der kombinierten Einwirkung auf die Karbonatisierung oben und Chlorid unten.*

Zur Bestimmung des Einflusses der kombinierten Einwirkung auf das Korrosionsverhalten und den kritischen Chloridgehalt wurden an gesondert hergestellten Proben (Wf-Cl, Wf-Cl-CO_2 und Wf-CO_2) sowohl der Korrosionsbeginn als auch die Korrosionsraten ermittelt.

Einfluss von Chloriden auf die Karbonatisierung

Der Einfluss der Karbonatisierung auf die Phasenzusammensetzung ist in Abb. 3 (oben) dargestellt. Im Zuge der Karbonatisierung werden die calciumgebundenen Phasen im Allgemeinen zu $CaCO_3$ umgewandelt (Abb. 3 oben links). Dies führt häufig zu einer Verringerung der Gesamtporosität, gleichzeitig jedoch zu einer gröberen Porenstruktur. Infolge dieser Umwandlungen sinkt der pH-Wert des Betons.

Sind Chloride im Beton vorhanden, wird ein Teil davon chemisch gebunden (Abb. 3 oben rechts). Dabei werden AFm-Phasen in Friedel'sches Salz umgewandelt. Während der Karbonatisierung wird das Friedel'sche Salz ebenfalls in $CaCO_3$ überführt, wodurch gebundene Chloride wieder freigesetzt werden. Die Porosität wird dadurch im Vergleich zur reinen Karbonatisierung kaum zusätzlich beeinflusst.

Der Einfluss von Chloriden auf den Feuchtehaushalt in karbonatisiertem Beton ist in Abb. 3 (Mitte) dargestellt. Die gröbere Porenstruktur infolge der Karbonatisierung führt bei Beregnung zu ausgeprägten Feuchteschwankungen bis in grössere Tiefen (Abb. 3 Mitte links). Dies ist durch den blau hinterlegten Bereich mit hoher Feuchte bei ρ = 0-500 Ωm und trockenem Beton bei ρ > 5000 Ωm dargestellt.

Das Vorhandensein von Chloriden führt hingegen zu weniger ausgeprägten Feuchteschwankungen die zudem nur geringere Tiefen beeinflussen und zu einer insgesamt höheren Sättigung des Betons (Abb. 3 Mitte rechts).

Der Einfluss auf die Karbonatisierungsgeschwindigkeit ist in Abb. 3 (unten) dargestellt. Da der Gastransport ausschliesslich über den Luftraum erfolgt, verlangsamt eine erhöhte Feuchte infolge der Beregnung die Karbonatisierung bekanntermassen (Abb. 3 unten links). Die höhere Sättigung bei Anwesenheit von Chloriden bewirkt, dass sich die Karbonatisierung bei kombinierter Einwirkung von Beregnung und Chloriden nochmals zusätzlich verlangsamt (Abb. 3 unten rechts).

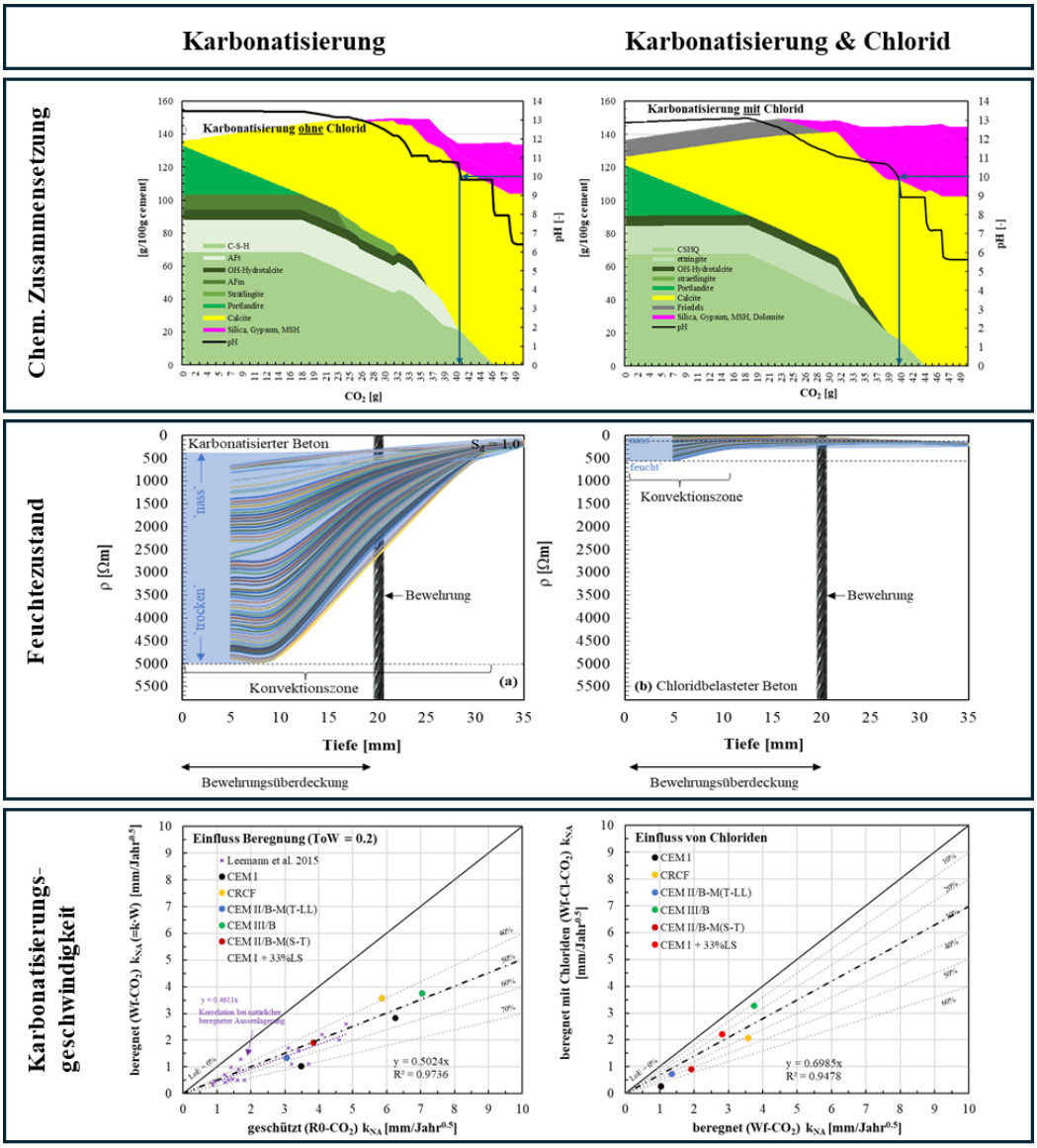

Abb. 3 *Einfluss von (links) Beregnung und (rechts) Chloriden auf die Karbonatisierung, (oben) Unterschiede in der chemischen Zusammensetzung (Mitte) Einfluss auf Feuchtegradienten und (unten) Einfluss auf die Karbonatisierungsgeschwindigkeit.*

Einfluss der Karbonatisierung auf den Chloridtransport

Der Einfluss der Karbonatisierung auf den Gesamtchloridgehalt ist exemplarisch in Abb. 4 (oben) dargestellt. Ohne zeitgleich stattfindende Karbonatisierung dringen Chloride zwar weniger tief ein, dafür jedoch in grösserer Menge, was durch den dunkelroten Bereich in Abb. 4 (oben links) deutlich wird.

Bei gleichzeitig ablaufender Karbonatisierung dringen Chloride deutlich tiefer ein, verteilen sich jedoch auf einen grösseren Bereich, sodass lokal geringere Chloridgehalte vorliegen. Dies wird durch die schwächeren Rottöne in Abb. 4 (oben rechts) verdeutlicht. Ursächlich hierfür sind sowohl die geringere Chloridbindungskapazität des karbonatisierten Betons als auch die gröbere Porenstruktur.

Der anhand der μXRF-Analysen dargestellte Chlorideintrag in Abb. 4 (oben) spiegelt sich in den Chloridprofilen in Abb. 4 (Mitte) wider.

Bei Karbonatisierung liegt das Chloridmaximum in grösserer Tiefe, jedoch mit geringeren maximalen Chloridgehalten (Abb. 4 Mitte rechts) als ohne Karbonatisierung (Abb. 4 Mitte

links). Dennoch tritt auch unter reinen Wechselfeuchtbedingungen ein Chloridmaximum im Beton auf. Dies unterscheidet sich von Beton, der dauerhaft einer Chloridlösung ausgesetzt ist, bei dem der maximale Chloridgehalt im Idealfall an der Oberfläche zu erwarten ist.

Im Vergleich zu dauerhaft einer Chloridlösung ausgesetztem Beton dringen Chloride bei wechselnder Befeuchtung deutlich schneller ein, da die kapillare Aufnahme um ein Vielfaches schneller erfolgt als der diffusive Transport (Abb. 4 unten links). Die Freisetzung zuvor gebundener Chloride sowie die gröbere Porenstruktur führen im karbonatisierten Beton zu einer zusätzlichen, insgesamt jedoch geringfügigen Beschleunigung des Chlorideintrags (Abb. 4 unten rechts).

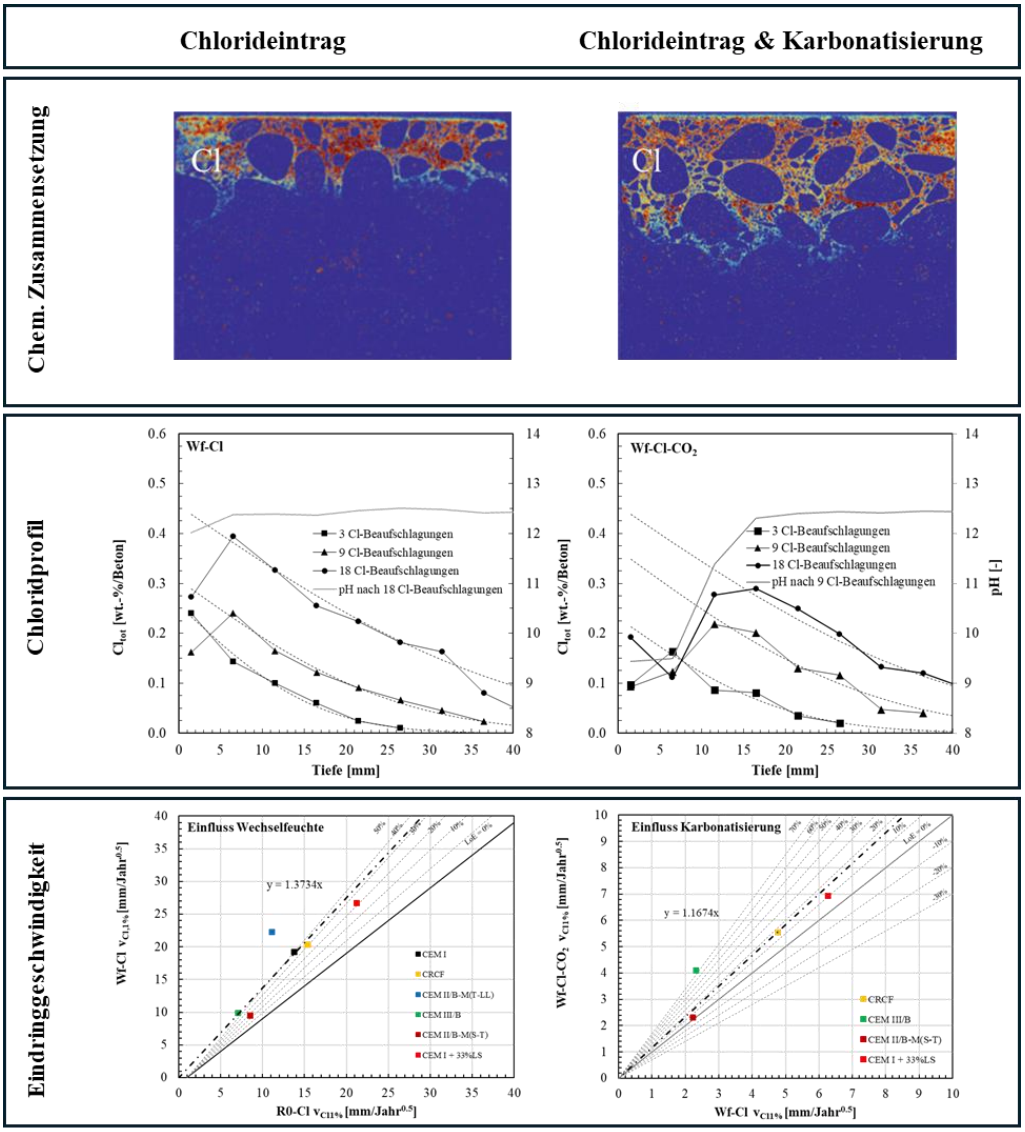

Abb. 4 *Chloridtransport ohne (links) und mit (rechts) Karbonatisierung (oben) Chloridgehalt mittels μXRF, (Mitte) Profile des Gesamtchloridgehalts im Vergleich zum pH-Wert und (unten) Chlorideindringrate.*

Vorhersage des Auftretens kombinierter Einwirkung

Aus den systematischen Untersuchungen konnte festgestellt werden, dass der Chloridtransport in karbonatisiertem Beton gleich schnell bzw. bis zu 1,2-fach schneller stattfindet und dass die Karbonatisierung in chloridbelastetem Beton rund 0,7-fach langsamer voranschreitet.

Auf Basis dieser Ergebnisse sowie deren Korrelation mit realen Bauwerksbedingungen in der Schweiz konnte in dieser Arbeit abgeleitet werden, welche Kombinationen aus Karbonatisierungskoeffizient und Chloridwiderstand nach SIA 262/1 Anhang I bzw. B zu einem erhöhten Risiko einer kombinierten Einwirkung führen.

Da unter realen XD1-Bedingungen unter anderem die Feuchtezustände und die Frequenz der Chloridbelastung schwanken, wird die Korrelation zwischen Chloridwiderstand und Karbonatisierungskoeffizient in Abb. 5 (a) als Bandbreite dargestellt.

Ferner stellt sich die Frage, ob das Risiko einer kombinierten Einwirkung auch ohne direkte Kenntnis der Karbonatisierungskoeffizienten bzw. Chloridwiderstände abgeschätzt werden kann. Zu diesem Zweck wurde in dieser Arbeit der Zusammenhang zwischen der Karbonatisierungsgeschwindigkeit und dem Verhältnis w/CaO sowie zwischen der Chlorideindringgeschwindigkeit und dem Verhältnis w/SiO_2 bestätigt.

Das Verhältnis von Chlorideindring- zu Karbonatisierungsgeschwindigkeit kann damit durch das Verhältnis von SiO_2 zu CaO beschrieben werden (Abb. 5 (b)). Führt ein Verhältnis von SiO_2/CaO zu einem Verhältnis von $k_{NA}/v_{Cl} > 1$, ist unter den angegebenen Expositionsbedingungen der Karbonatisierungsprozess der dominierende, schnellere Prozess. Bei einem Verhältnis von $k_{NA}/v_{Cl} < 1$ dringen Chloride schneller ein. Bei einem Verhältnis von etwa 1 ist das Risiko für eine simultane Einwirkung besonders hoch.

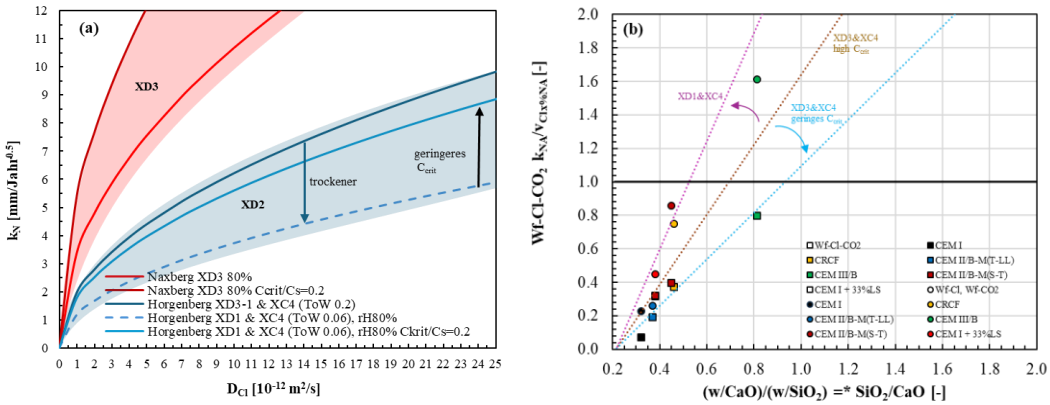

Abb. 5 *(a) Kombination von k_{NA} und D_{Cl}, die je nach Referenzbedingung mit hoher Wahrscheinlichkeit zu simultanen Einwirkungsprozessen führen, und (b) CaO/SiO_2-Verhältnis, das mit hoher Wahrscheinlichkeit auf simultane Einwirkungsprozesse hinweist.*

Folgen simultaner Einwirkung auf die Korrosionsinitiierung

Der kritische Chloridgehalt, angegeben als Gesamtchloridgehalt, nahm ab einem Abstand der Karbonatisierungsfront von der Bewehrung von rund 6 mm auf etwa 0,2–0,4 Gew.-% bezogen auf den Zement ab (vgl. Abb. 6 (a)). Der pH-Gradient in dieser Tiefe entspricht einem pH-Wert von etwa 10,5–11,5.

Im nicht karbonatisierten Beton (Abb. 6 (b)) hing der kritische Chloridgehalt stark vom Al2O3 Gehalt ab und nahm mit diesem zu.

Die Abnahme auf ein einheitliches Niveau von 0,2–0,4 Gew.-%/Zement, unabhängig vom kritischen Chloridgehalt des spezifischen Betons vor der Karbonatisierung bestätigt die Abnahme bzw. das Aufheben der Chloridbindefähigkeit des Zementsteins.

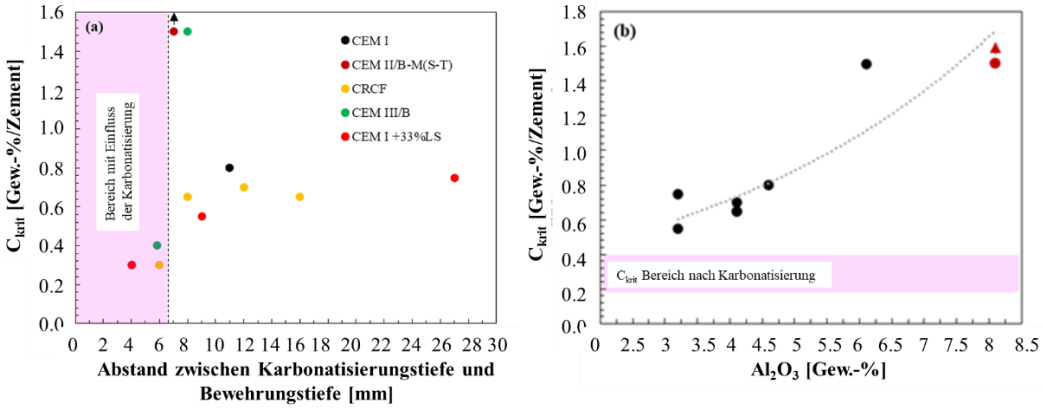

Abb. 6 *C_{krit} in Abhängigkeit des Abstands der Karbonatisierungsfront von der Bewehrung (a) und C_{krit} in Abhängigkeit des Al_2O_3 bei nicht karbonatisiertem Beton (b).*

Zusammenfassend hat die kombinierte u.a. folgende Auswirkung auf den kritischen korrosionsauslösenden Chloridgehalt:

- Bei Karbonatisierung kann der C_{krit} auf 0.2-0.4 absinken.
- Der Abfall des C_{krit} auf das Niveau von 0.2-0.4 ist unabhängig vom kritischen Chloridgehalt im nicht karbonatisierten Beton.
- Bei Korrosionsinitiierung liegt der Abstand zwischen Karbonatisierungstiefe und Bewehrung ca. 6 mm.
- Der korrespondierende pH-Wert lag in dieser Tiefe bei ca. 10.5-11.5.
- In diesen Untersuchungen korrelierte der C_{krit} sehr gut mit dem Al_2O_3 Gehalt, obwohl der SiO_2 Gehalt und w/b-wert ebenfalls eine integrale Rolle spielen sollte.

Korrosionsgeschwindigkeit bei kombinierter Einwirkung

Zur Abschätzung der Auswirkungen der kombinierten Einwirkung auf die Korrosion sind in Abb. 7 (a) die Makrokorrosionsraten unter nassen Bedingungen aller Bewehrungsstäbe, bei denen eine Korrosionsinitiierung festgestellt wurde, inklusive Streubalken dargestellt. Die gestrichelte horizontale Linie kennzeichnet die mittlere Korrosionsrate bei karbonatisierungsinduzierter (CO_2) Korrosion, chloridinduzierter (Cl) Korrosion sowie bei kombinierter Einwirkung von Chloriden und Karbonatisierung ($Cl\&CO_2$).

In Abb. 7 (b) sind die zugehörigen Mikrokorrosionsraten dargestellt.

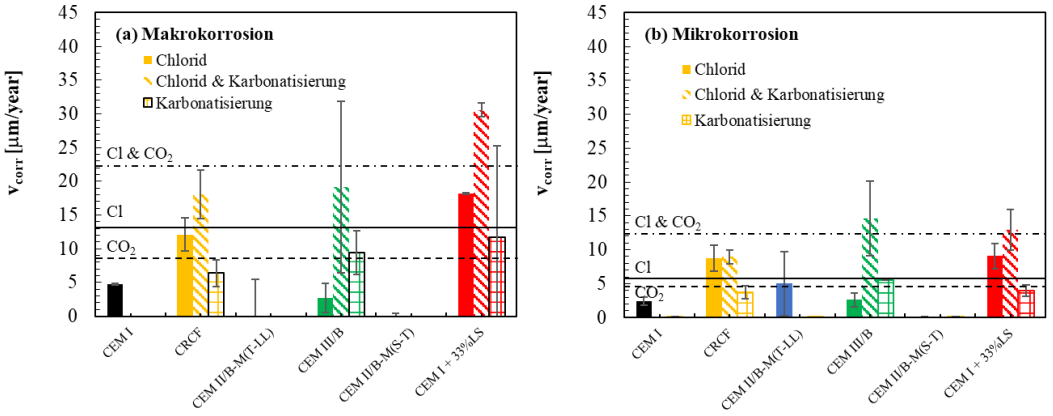

Abb. 7 *Makrokorrosionsraten (a) und Mikrokorrosionsraten (b) für nur chloridinduzierte Korrosion, chloridinduzierte Korrosion in karbonatisiertem Beton und karbonatisierungsinduzierte Korrosion.*

Obwohl die Korrosionsraten – insbesondere bei Anwesenheit von Chloriden – aufgrund des kurzen Beobachtungszeitraums noch vergleichsweise gering sind, lassen sich folgende Tendenzen feststellen:

- Bei kombinierter Einwirkung ist die Korrosionsrate nahezu doppelt so hoch wie bei ausschliesslich chloridinduzierter Korrosion.
- Die Korrosionsrate bei karbonatisierungsinduzierter Korrosion liegt erwartungsgemäss auf dem niedrigsten Niveau.
- Das gleiche Ranking zeigt sich auch bei den Mikrokorrosionsraten.
- Das Verhältnis zwischen Mikro- und Makrokorrosion beträgt bei karbonatisierungsinduzierter Korrosion nahezu 1:1.
- Bei Korrosion in Anwesenheit von Chloriden ist der Anteil der Makrokorrosion deutlich höher, mit einem Verhältnis von Mikro- zu Makrokorrosion von etwa 0,5:1.

Risiko kombinierter Einwirkung in Normen

Unter Verwendung der Korrelation zwischen dem Karbonatisierungskoeffizienten KW und dem Chloriddiffusionskoeffizienten CW (gemäss SN EN 206 und SIA 262/1) können Betonrezepturen identifiziert werden, die unter den Expositionsbedingungen XD3&XC4 sowie XD1&XC4 anfällig für kombinierte Einwirkungen sind. Anstelle der Materialwiderstände KW und CW kann auch anhand der Materialzusammensetzung SiO_2/CaO das Risiko für kombinierte Einwirkung abgeschätzt werden.

Abb. 8 veranschaulicht das Risiko für kombinierte Einwirkung anhand der Materialwiderstände KW und CW nach SN EN 206 bzw. den zugehörigen ERC Klassen nach prSN EN 1992-1-1:2026.

Bereiche mit dominierendem Chlorideintrag sind dunkelgrau dargestellt, Bereiche mit dominierender Karbonatisierung hellgrau. Die Zwischenzonen kennzeichnen eine simultane Progression beider Prozesse. Zusätzlich sind die Leistungsbereiche der geprüften Betone NPK-A bis NPK-F dargestellt.

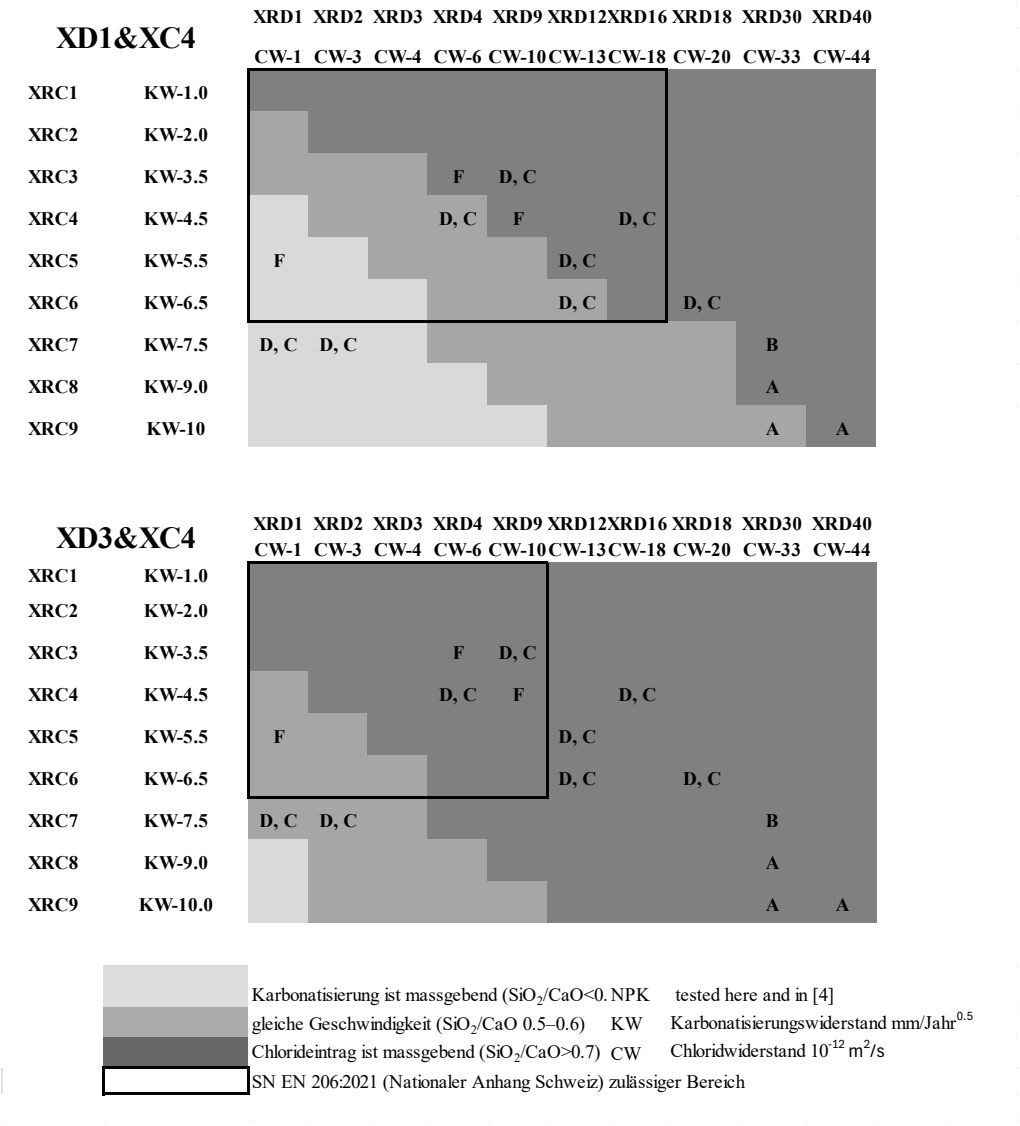

Fig. 9 *Abschätzung von Klassenkombinationen mit Risiko kombinierter Einwirkung für (oben) XD1&XC4 und (unten) XD3&XC4.*

(a) Bewertung des Risikos kombinierter Einwirkung nach SN EN 206 (schwarzer Bereich in Abb. 8)

Für die Expositionskombination XD1&XC4 fordert die SN EN 206 eine Karbonatisierungsbeständigkeit von KW-6,5, während kein expliziter Grenzwert für die Chloridbeständigkeit vorgegeben ist. Auf Basis der untersuchten NPK-D-Betone kann ein entsprechender Chloridwiderstand von etwa CW-18 abgeleitet werden. Die geforderte Betondeckung ist für XC4 und XD1 identisch.

Unter XD1&XC4-Bedingungen verläuft der Chlorideintrag schneller, wenn die geforderten Materialkennwerte gerade eingehalten werden, trotz identischer Betondeckung. Ursache dafür, dass nicht beide Prozesse gleich schnell verlaufen ist, dass die Karbonatisierung in chloridbelastetem Beton langsamer abläuft.

Kritische Bedingungen für kombinierte Einwirkungen treten bei Betonen mit einer Karbonatisierungsbeständigkeit nahe dem Grenzwert KW-6,5 und einer moderaten Chloridbeständigkeit (CW zwischen 6 und 10) auf. In diesem Fall wird Korrosion früher ausgelöst, als allein aufgrund des Chlorideintrags zu erwarten wäre, und der Korrosionsfortschritt wird beschleunigt.

Für XD3&XC4 fordert die SN EN 206 KW-6,5 und CW-10. In diesem Fall ist die erforderliche Betondeckung für XD3 höher als für XC4 allein.

Werden die Grenzwerte für KW und CW exakt eingehalten, bestimmt der Chlorideintrag die Korrosionsinitiierung. Bei geringerer Chloridbeständigkeit sind jedoch kombinierte Effekte möglich. Da die Betondeckung aber höher ist als für reine Karbonatisierung erforderlich, erscheint eine kritische kombinierte Einwirkung vor Ablauf der Nutzungsdauer in der Regel unwahrscheinlich.

(b) Bewertung nach EN 1992-1-1:2023

Das in EN 1992-1-1:2023 eingeführte Konzept der Exposure Resistance Classes (ERC) erlaubt einen Ausgleich zwischen Materialbeständigkeit und Betondeckung. Eine höhere Materialbeständigkeit kann eine reduzierte Betondeckung kompensieren und umgekehrt.

Dieser Ansatz erleichtert den Einsatz nachhaltiger Betonmischungen, die die festen KW-Grenzwerte der SN EN 206 nicht erfüllen. Eine einzelne Betonrezeptur kann zudem für mehrere Expositionsklassen verwendet werden, sofern die Betondeckung entsprechend angepasst wird.

Da Betondeckung und Materialbeständigkeit für jede Expositionsklasse separat festgelegt werden, wurden Kombinationen von XRC- und XRDS-Klassen mit identischer Betondeckung identifiziert. Diese Kombinationen können zu kombinierter Einwirkung führen.

Zur Vermeidung eines erhöhten Korrosionsrisikos sollten bei der Wahl der ERC Klassen Kombinationen die mittelgrauen Bereiche in Abb. 8 vermieden werden.

Zusammenfassung und weiterer Forschungsbedarf

Die wichtigsten Ergebnisse und der verbleibende Forschungsbedarf lassen sich wie folgt zusammenfassen:

- In chloridbelastetem Beton erhöht sich die Sättigung, was zu einer Verlangsamung der Karbonatisierung führt.
- In karbonatisiertem Beton lösen sich gebundene Chloride und können den Chlorideintrag leicht beschleunigen.
- Das Risiko kombinierter Einwirkung kann anhand der Karbonatisierungs- und Chloridbeständigkeit nach SIA 262/1 oder über das SiO_2/CaO-Verhältnis abgeschätzt werden. Kritische Kombinationen gemäss Abb. 8 sollten vermieden werden.
- Der kritische Chloridgehalt steigt mit zunehmendem Al_2O_3- und SiO_2-Gehalt des Bindemittels. Nach Karbonatisierung sinkt er unabhängig von der Bindemittelzusammensetzung auf etwa 0,2–0,4 Gew.-%.
- Die Korrosionsrate ist bei gleichzeitig chloridbelastetem und karbonatisiertem Beton höher als bei rein chlorid- oder karbonatisierungsbelastetem Beton.
- Werden die Grenzwerte der SN EN 206 exakt eingehalten, ist das Risiko kombinierter Einwirkung gering.
- Für Kombinationen von XRD- und XRC-Klassen kann Abb. 8 zur Risikobewertung herangezogen werden.

Résumé

Motivation et état de la normalisation

La carbonatation ainsi que la pénétration des chlorures modifient la composition chimique des phases hydratées, la solution interstitielle, la structure des pores ainsi que la teneur en humidité du béton. Ces modifications influencent les processus de transport et ont un impact sur l'initiation et la propagation de la corrosion.

À l'heure actuelle, il n'existe pas d'évaluations synthétiques concernant les effets combinés de la carbonatation et des chlorures dans les conditions climatiques suisses. Les exigences existantes en matière de durabilité ne prennent généralement en compte que des mécanismes de dégradation isolés, bien que les ouvrages exposés à la classe XD soient également soumis en permanence au CO_2 (XC4).

Les normes SN EN 206 et SIA 262 considèrent, pour les classes XD1 & XC4, que la carbonatation est le mécanisme déterminant. Toutefois, il n'existe pas de preuves solides à ce sujet. De même, la norme SIA 269/2 indique que la teneur critique en chlorures peut être réduite dans le béton carbonaté, sans fournir de données quantitatives.

Avec le concept ERC introduit dans l'EN 1992-1-1, un niveau de résistance du matériau est attribué à l'enrobage du béton. Ces grandeurs de résistance sont, par exemple, XRC pour la carbonatation et XRD pour l'action des chlorures. XRC est comparable à la résistance à la carbonatation KW, et XRDS est comparable à la résistance aux chlorures CW. La figure 1 montre comment, en fonction de la classe d'exposition, l'enrobage des armatures est désormais défini en fonction de la résistance du matériau (XRC, XRDS).

Il en résulte inévitablement que, même lorsque la résistance du béton à la pénétration des chlorures et à la carbonatation est optimisée par rapport à l'enrobage, il faut s'attendre à une attaque combinée.

Table 6.3 (CH) - Enveloppe minimale du béton cmin,dur pour l'acier d'armature au carbone - Carbonatation

ERC	Classe d'exposition (Carbonatation)							
	XC1		XC2		XC3		XC4	
	Durée de vie nominale (années)							
	50	100	50	100	50	100	50	100
XRC 1	10	10	10	10	10	10	10	15
XRC 2	10	10	10	15	10	15	10	20
XRC 3	10	10	10	15	10	20	15	25
XRC 4	10	10	15	20	15	25	20	30
XRC 5	10	10	15	20	20	30	25	35
XRC 6	10	10	20	25	25	35	30	40
XRC 7	10	10	20	25	30	40	35	45
XRC 8	10	10	25	30	35	45	40	50
XRC 9	10	10	25	30	40	50	45	55

Table 6.4 (CH) — Enveloppe minimale du béton cmin,dur pour l'acier d'armature au carbone - Chlorures

ERC	Classe d'exposition (Chlorures)			
	XD1=XD2a(CH)		XD3 = XD2b(CH)	
	Durée de vie nominale (années)			
	50	100	50	100
XRDS 1	10	20	20	30
XRDS 2	15	25	25	35
XRDS 3	15	25	30	40
XRDS 4	20	30	30	40
XRDS 5	20	30	35	45
XRDS 6	25	35	35	45
XRDS 7	25	35	40	50
XRDS 8	25	35	40	50
XRDS 9	25	35	45	55
XRDS 10	25	35	45	55
XRDS 12	30	40	50	-
XRDS 14	30	40	55	-
XRDS 16	30	40	-	-
XRDS 18	30	40	-	-
XRDS 24	35	45	-	-
XRDS 30	40	50	-	-
XRDS 40	45	55	-	-

***Fig. 1** Enrobage du béton en fonction des classes XRC (en haut) et XRD (en bas).*

Les questions suivantes se posent dès lors :

- Quelle est l'influence de l'action simultanée sur chacun des processus de dégradation
- Quelle est l'influence de l'action simultanée sur la progression de la corrosion
- Dans quelles conditions les normes actuelles présentent-elles un risque d'action combinée

Méthodologie et procédure

Pour l'étude des effets d'une action combinée sur le processus de carbonatation, le dispositif expérimental présenté à la figure 2 (en haut) a été utilisé. Les séquences d'exposition suivantes ont été examinées :

- Carbonatation accélérée (R0-CO_2)
- Carbonatation accélérée suivie d'une exposition à l'eau (Wf-CO_2)
- Carbonatation accélérée suivie d'une exposition à une solution chlorurée (Wf-Cl-CO_2)

Pour l'étude de l'influence combinée sur le transport des chlorures, le dispositif expérimental présenté à la figure 2 (en bas) a été retenu. Les séquences d'exposition suivantes ont été appliquées :

- Exposition à une solution chlorurée (R0-Cl)
- Stockage à l'air suivi d'une exposition à une solution chlorurée (Wf-Cl)
- Carbonatation accélérée suivie d'une exposition à une solution chlorurée (Wf-Cl-CO_2)

La transposition des résultats expérimentaux aux conditions normatives a été réalisée au moyen d'essais normalisés menés en parallèle. L'extrapolation aux conditions d'exposition XD1 & XC4 a été effectuée sur la base d'essais de mise en œuvre en conditions réelles ainsi que d'investigations complémentaires sur des ouvrages existants.

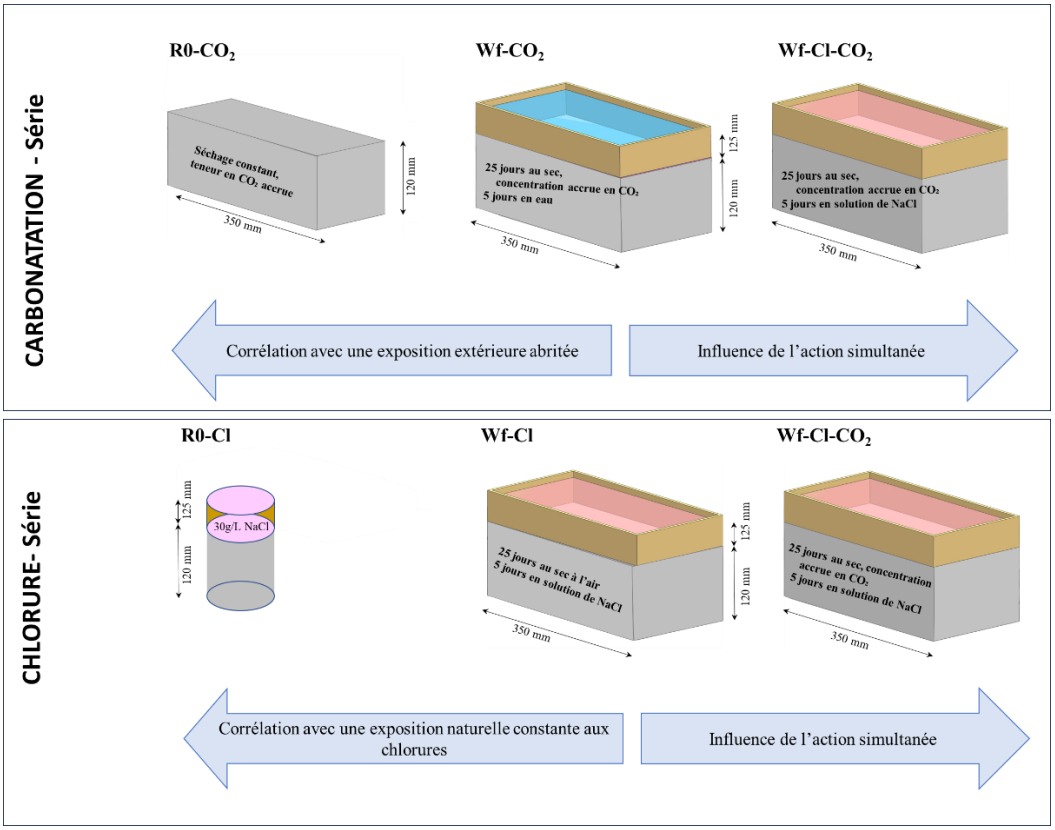

***Fig. 2** Dispositif expérimental pour l'étude de l'influence de l'action combinée sur la carbonatation (en haut) et sur la pénétration des chlorures (en bas).*

Afin de déterminer l'influence de l'action combinée sur le comportement à la corrosion et sur la teneur critique en chlorures, des éprouvettes spécialement fabriquées (Wf-Cl, Wf-Cl-CO_2 et Wf-CO_2) ont été utilisées pour mesurer à la fois le début de la corrosion et les vitesses de corrosion.

Influence des chlorures sur la carbonatation

L'influence de la carbonatation sur la composition des phases est présentée à la Fig. 3 (en haut). Au cours de la carbonatation, les phases liées au calcium sont généralement transformées en $CaCO_3$ (Fig. 3, en haut à gauche). Cela entraîne souvent une diminution de la porosité totale, tout en provoquant simultanément un grossissement de la structure poreuse. À la suite de ces transformations, le pH du béton diminue.

Lorsque des chlorures sont présents dans le béton, une partie d'entre eux est chimiquement liée (Fig. 3, en haut à droite). Dans ce processus, les phases AFm sont transformées en sel de Friedel. Lors de la carbonatation, le sel de Friedel est également converti en $CaCO_3$, ce qui entraîne la libération des chlorures initialement liés. Par conséquent, la porosité n'est que très peu affectée par rapport à une carbonatation pure.

L'influence des chlorures sur le régime hydrique du béton carbonaté est illustrée à la Fig. 3 (au centre). La structure poreuse plus grossière résultant de la carbonatation conduit, en cas d'arrosage, à des variations d'humidité marquées jusqu'à des profondeurs importantes (Fig. 3, au centre à gauche). Ceci est représenté par la zone en bleu indiquant une humidité élevée pour ρ = 0–500 Ωm et un béton sec pour ρ > 5000 Ωm.

En revanche, la présence de chlorures entraîne des variations d'humidité moins prononcées, affectant uniquement des profondeurs plus faibles, et conduit à un degré de saturation globalement plus élevé du béton (Fig. 3, au centre à droite).

L'influence sur la vitesse de carbonatation est présentée à la Fig. 3 (en bas). Étant donné que le transport des gaz s'effectue exclusivement par les pores remplis d'air, une humidité accrue due à l'arrosage ralentit de manière bien connue la carbonatation (Fig. 3, en bas à

gauche). La saturation plus élevée en présence de chlorures entraîne, en cas d'action combinée de l'arrosage et des chlorures, un ralentissement supplémentaire du processus de carbonatation (Fig. 3, en bas à droite).

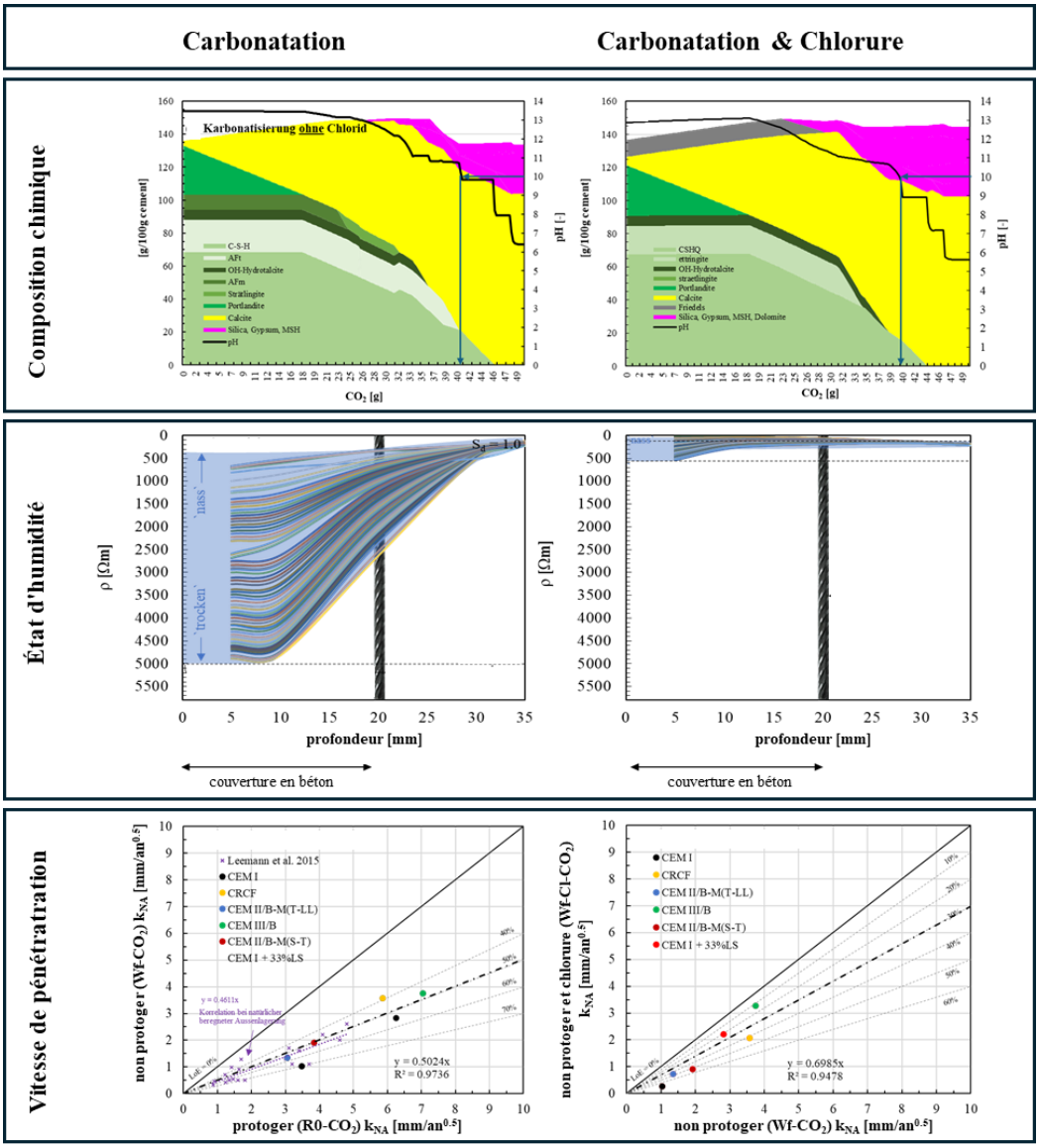

Fig. 3 *Influence de l'arrosage (à gauche) et des chlorures (à droite) sur la carbonatation, (en haut) différences dans la composition chimique, (au centre) influence sur les gradients d'humidité et (en bas) influence sur la vitesse de carbonatation.*

Influence de la carbonatation sur le transport des chlorures

L'influence de la carbonatation sur la teneur totale en chlorures est illustrée de manière exemplaire à la Fig. 4 (en haut). En l'absence de carbonatation simultanée, les chlorures pénètrent certes moins profondément, mais en plus grande quantité, ce qui est clairement visible par la zone rouge foncé de la Fig. 4 (en haut à gauche).

En présence d'une carbonatation simultanée, les chlorures pénètrent nettement plus profondément, mais se répartissent sur une zone plus étendue, ce qui conduit localement à des teneurs en chlorures plus faibles. Ceci est mis en évidence par les teintes rouges plus claires dans la Fig. 4 (en haut à droite). Ces effets sont dus à la fois à la capacité réduite de fixation des chlorures dans le béton carbonaté et à la structure poreuse plus grossière.

L'apport en chlorures représenté par les analyses µXRF à la Fig. 4 (en haut) se reflète dans les profils de chlorures présentés à la Fig. 4 (au centre).

En cas de carbonatation, le maximum de chlorures se situe à une plus grande profondeur, mais avec des teneurs maximales plus faibles (Fig. 4, au centre à droite) que sans carbonatation (Fig. 4, au centre à gauche). Néanmoins, même dans des conditions d'humidité alternée, un maximum de chlorures apparaît dans le béton. Cela se distingue du comportement d'un béton exposé en permanence à une solution chlorurée, pour lequel la teneur maximale en chlorures est idéalement attendue à la surface.

Comparativement à un béton exposé en permanence à une solution chlorurée, les chlorures pénètrent nettement plus rapidement sous des conditions d'humidité alternée, car l'absorption capillaire est plusieurs fois plus rapide que le transport diffusif (Fig. 4, en bas à gauche). La libération des chlorures précédemment liés ainsi que la structure poreuse plus grossière entraînent, dans le béton carbonaté, une accélération supplémentaire, globalement toutefois limitée, de la pénétration des chlorures (Fig. 4, en bas à droite).

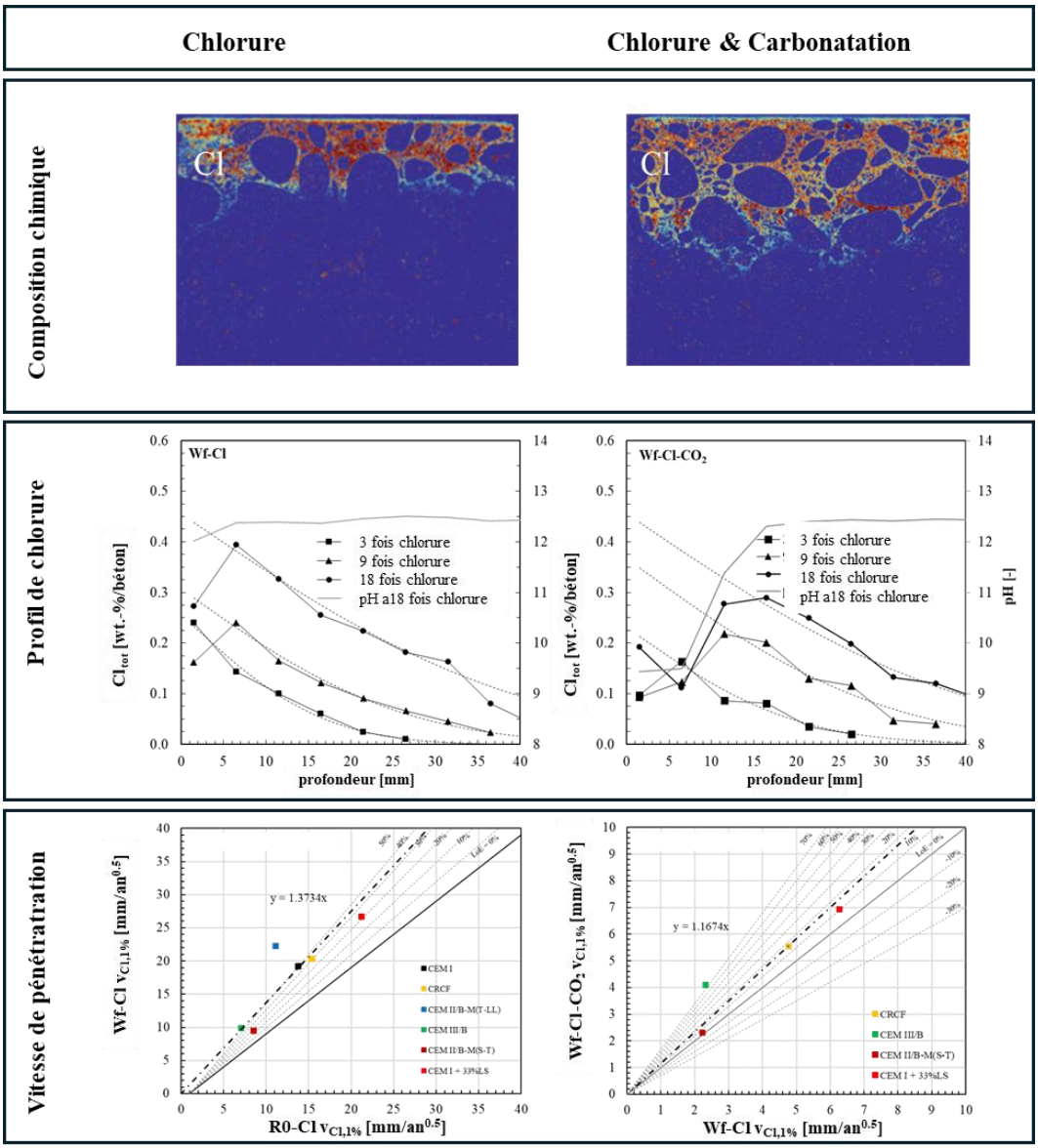

Fig. 4 *Transport des chlorures sans (à gauche) et avec (à droite) carbonatation : (en haut) teneur en chlorures mesurée par µXRF, (au centre) profils de la teneur totale en chlorures en comparaison avec le pH, et (en bas) vitesse de pénétration des chlorures.*

Prévision de l'apparition d'une action combinée

À partir des investigations systématiques, il a été constaté que le transport des chlorures dans le béton carbonaté se déroule à une vitesse comparable, voire jusqu'à 1,2 fois plus rapide, et que la carbonatation dans les bétons exposés aux chlorures progresse environ 0,7 fois plus lentement.

Sur la base de ces résultats ainsi que de leur corrélation avec les conditions réelles des ouvrages en Suisse, il a été possible, dans le cadre de ce travail, de déterminer quelles combinaisons du coefficient de carbonatation et de la résistance aux chlorures selon la SIA 262/1, annexes I et B, conduisent à un risque accru d'action combinée.

Étant donné que, dans des conditions réelles XD1, notamment les états d'humidité et la fréquence des sollicitations par les chlorures varient, la corrélation entre la résistance aux chlorures et le coefficient de carbonatation est représentée sous forme de plage de variation à la Fig. 5 (a).

Par ailleurs, se pose la question de savoir si le risque d'une action combinée peut être estimé sans connaissance directe des coefficients de carbonatation ou des résistances aux chlorures. À cet effet, le présent travail a confirmé la relation entre la vitesse de carbonatation et le rapport w/CaO, ainsi qu'entre la vitesse de pénétration des chlorures et le rapport w/SiO_2.

Le rapport entre la vitesse de pénétration des chlorures et la vitesse de carbonatation peut ainsi être décrit par le rapport SiO_2/CaO (Fig. 5 (b)). Lorsque le rapport SiO_2/CaO conduit à un rapport k_{NA}/v_{Cl} > 1, le processus de carbonatation constitue, dans les conditions d'exposition considérées, le processus dominant et le plus rapide. Pour un rapport k_{NA}/v_{Cl} < 1, la pénétration des chlorures est plus rapide. Pour un rapport proche de 1, le risque d'action simultanée est particulièrement élevé.

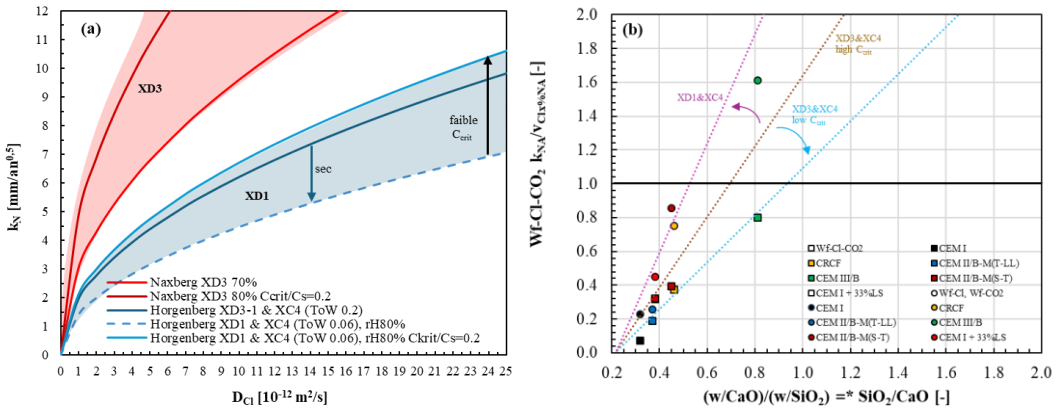

Fig. 5 *(a) combinaison de k_N et D_{Cl} qui, selon la condition de référence, a une forte probabilité de conduire à des processus d'action simultanée et (b) CaO/SiO_2 qui peut conduire à des processus d'action simultanée avec une forte probabilité.*

Conséquences d'une action simultanée sur l'initiation de la corrosion

La teneur critique en chlorures, exprimée en teneur totale en chlorures, diminue à partir d'une distance d'environ 6 mm entre le front de carbonatation et les armatures pour atteindre environ 0,2 à 0,4 % en masse rapporté au ciment (cf. Fig. 6 (a)). Le gradient de pH à cette profondeur correspond à une valeur d'environ 10,5 à 11,5.

Dans le béton non carbonaté (Fig. 6 (b)), la teneur critique en chlorures dépend fortement de la teneur en Al_2O_3 et augmente avec celle-ci.

La diminution vers un niveau uniforme de 0,2 à 0,4 % en masse rapporté au ciment, indépendamment de la teneur critique spécifique du béton avant carbonatation, confirme la réduction, voire la suppression, de la capacité de fixation des chlorures de la pâte de ciment.

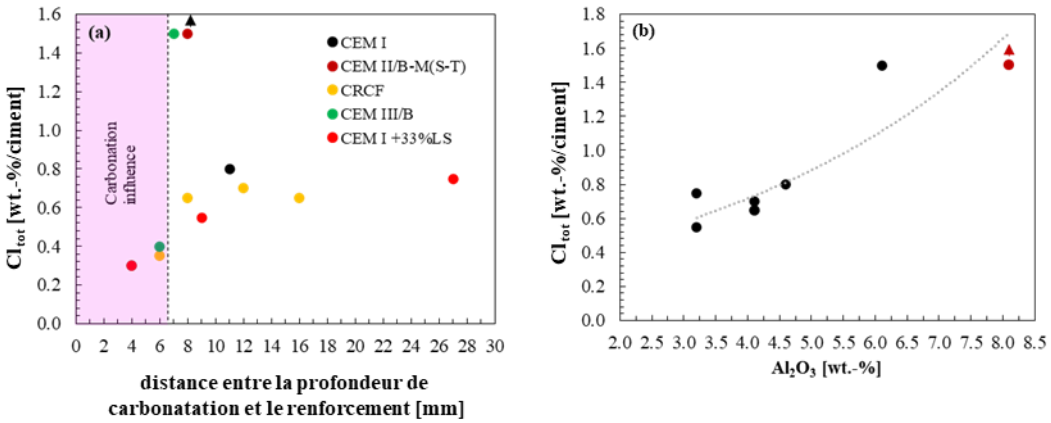

Fig. 6 *C_{crit} en fonction de la distance entre le front de carbonatation et l'armature (a) et C_{crit} en fonction de l'Al_2O_3 pour un béton non carbonaté (b).*

En résumé, l'action combinée a notamment les effets suivants sur la teneur critique en chlorures déclenchant la corrosion :

- En présence de carbonatation, C_{crit} peut diminuer jusqu'à 0,2–0,4 %.
- La diminution de C_{crit} à ce niveau est indépendante de la teneur critique en chlorures dans le béton non carbonaté.
- Lors de l'initiation de la corrosion, la distance entre la profondeur de carbonatation et les armatures est d'environ 6 mm.
- La valeur de pH correspondante à cette profondeur est d'environ 10,5–11,5.
- Dans ces investigations, C_{crit} a montré une très bonne corrélation avec la teneur en Al_2O_3, bien que la teneur en SiO_2 et le rapport w/b jouent également un rôle intégral.

Vitesse de corrosion en cas d'action combinée

Afin d'estimer les effets de l'action combinée sur la corrosion, les vitesses de macrocorrosion mesurées en conditions humides pour toutes les barres d'armature présentant une initiation de corrosion sont représentées à la Fig. 7 (a), y compris les barres d'erreur. La ligne horizontale en pointillés indique la vitesse moyenne de corrosion pour la corrosion induite par la carbonatation (CO_2), la corrosion induite par les chlorures (Cl) ainsi que la corrosion résultant de l'action combinée des chlorures et de la carbonatation (Cl & CO_2).

Les vitesses correspondantes de microcorrosion sont présentées à la Fig. 7 (b).

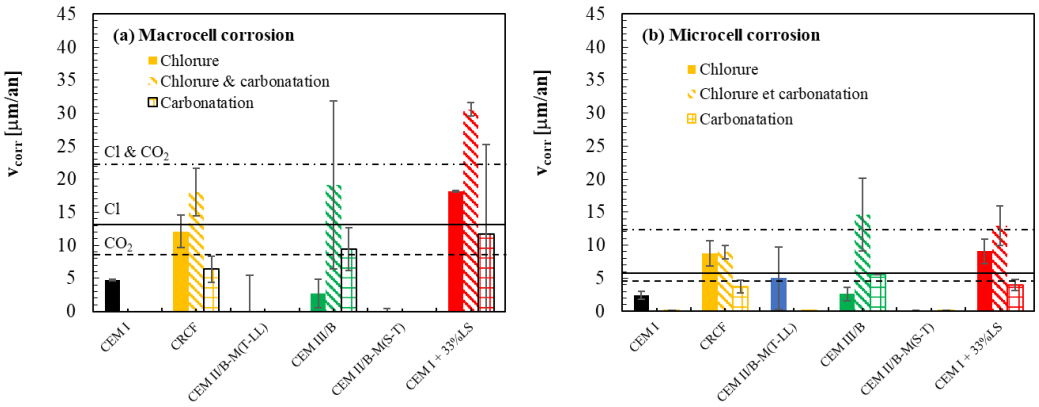

***Fig. 7** Vitesses de macrocorrosion (a) et de microcorrosion (b) pour la corrosion induite uniquement par les chlorures, la corrosion induite par les chlorures dans un béton carbonaté, et la corrosion induite par la carbonatation.*

Bien que les vitesses de corrosion — en particulier en présence de chlorures — soient encore relativement faibles en raison de la courte durée d'observation, les tendances suivantes peuvent être identifiées :

- En cas d'action combinée, la vitesse de corrosion est presque deux fois plus élevée que dans le cas d'une corrosion induite uniquement par les chlorures.
- La vitesse de corrosion liée à la carbonatation se situe, comme prévu, au niveau le plus faible.
- Le même classement est également observé pour les vitesses de microcorrosion.
- Le rapport entre micro- et macrocorrosion est proche de 1:1 dans le cas de la corrosion induite par la carbonatation.
- En présence de chlorures, la part de macrocorrosion est nettement plus élevée, avec un rapport micro/macrocorrosion d'environ 0,5:1.

Risque d'action combinée dans les normes

En utilisant la corrélation entre le coefficient de carbonatation KW et le coefficient de diffusion des chlorures CW (selon la SN EN 206 et la SIA 262/1), il est possible d'identifier des formulations de béton susceptibles de présenter une action combinée sous les conditions d'exposition XD3 & XC4 ainsi que XD1 & XC4. En alternative aux résistances des matériaux KW et CW, le risque d'action combinée peut également être estimé à partir de la composition du matériau, notamment du rapport SiO_2/CaO.

La Fig. 8 illustre le risque d'action combinée à partir des résistances des matériaux KW et CW selon la SN EN 206, respectivement des classes ERC correspondantes selon la prSN EN 1992-1-1:2026.

Les zones dominées par la pénétration des chlorures sont représentées en gris foncé, celles dominées par la carbonatation en gris clair. Les zones intermédiaires indiquent une progression simultanée des deux processus. En complément, les domaines de performance des bétons étudiés NPK-A à NPK-F sont également présentés.

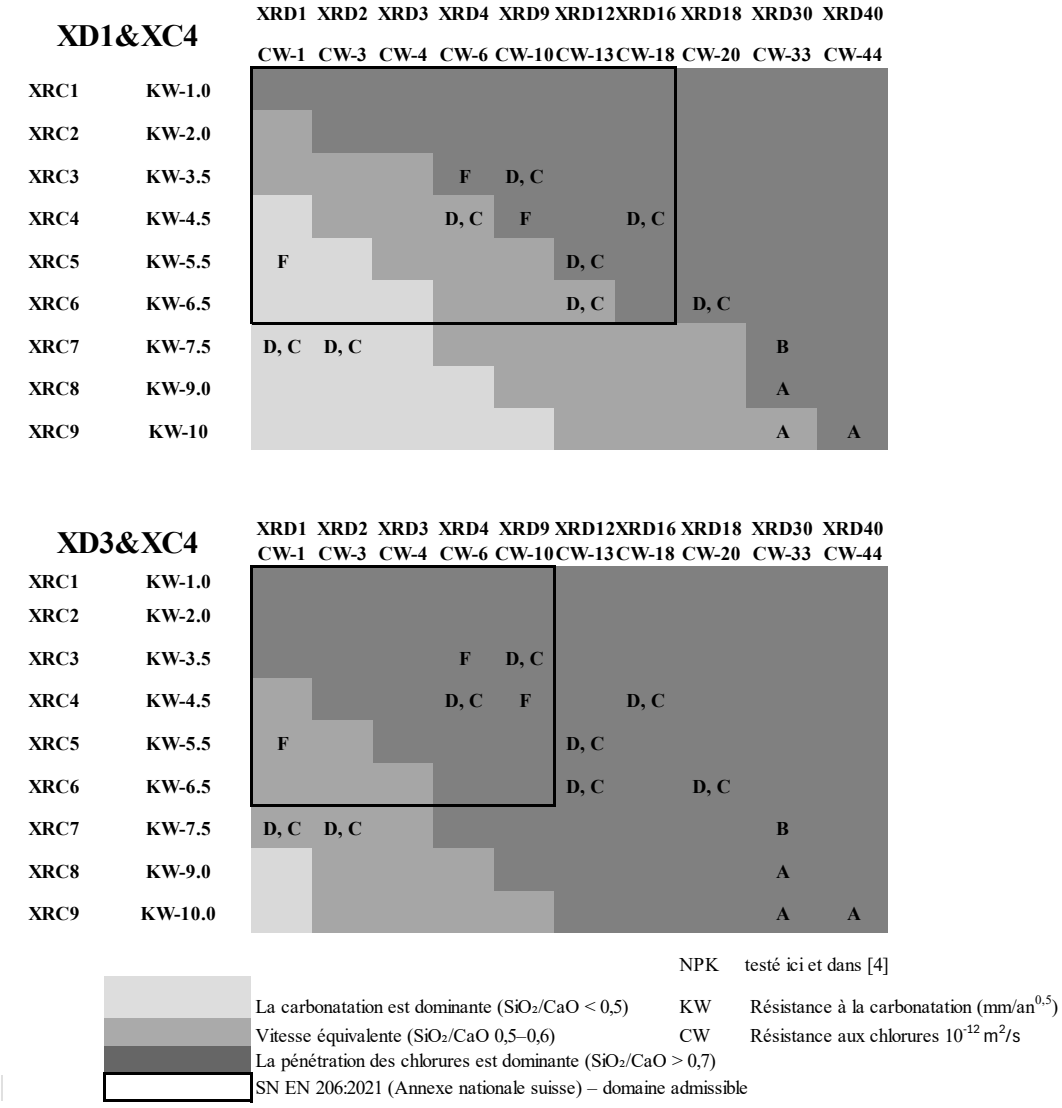

Fig. 8 *Estimation des combinaisons de classes présentant un risque d'action combinée pour (en haut) XD1 & XC4 et (en bas) XD3 & XC4.*

(a) Évaluation du risque d'action combinée selon la SN EN 206 (zone noire dans la Fig. 8)

Pour la combinaison d'exposition XD1 & XC4, la SN EN 206 exige une résistance à la carbonatation de KW-6,5, tandis qu'aucune valeur limite explicite n'est définie pour la résistance aux chlorures. Sur la base des bétons NPK-D étudiés, une résistance aux chlorures correspondante d'environ CW-18 peut être déduite. L'enrobage requis est identique pour XC4 et XD1.

Dans les conditions XD1 & XC4, la pénétration des chlorures progresse plus rapidement lorsque les paramètres matériaux exigés sont juste respectés, malgré un enrobage identique. Cela s'explique par le fait que la carbonatation est ralentie dans les bétons exposés aux chlorures, ce qui conduit à une évolution non simultanée des deux processus.

Des conditions critiques d'action combinée apparaissent pour des bétons présentant une résistance à la carbonatation proche de la valeur limite KW-6,5 et une résistance modérée aux chlorures (CW compris entre 6 et 10). Dans ce cas, la corrosion est initiée plus précocement que ce qui serait attendu sur la seule base de la pénétration des chlorures, et sa progression est accélérée.

Pour XD3 & XC4, la SN EN 206 exige KW-6,5 et CW-10. Dans ce cas, l'enrobage requis pour XD3 est supérieur à celui exigé pour XC4 seul.

Lorsque les valeurs limites de KW et CW sont strictement respectées, la pénétration des chlorures détermine l'initiation de la corrosion. En revanche, en cas de résistance réduite aux chlorures, des effets combinés peuvent apparaître. Toutefois, l'enrobage étant plus élevé que celui requis pour une carbonatation pure, une action combinée critique avant la fin de la durée d'utilisation est généralement peu probable.

(b) Évaluation selon l'EN 1992-1-1:2023

Le concept des Exposure Resistance Classes (ERC), introduit dans l'EN 1992-1-1:2023, permet une compensation entre la résistance du matériau et l'enrobage du béton. Une résistance accrue du matériau peut compenser un enrobage réduit, et inversement.

Cette approche facilite l'utilisation de formulations de béton durables ne satisfaisant pas aux valeurs limites strictes de KW définies dans la SN EN 206. Une même formulation peut également être utilisée pour plusieurs classes d'exposition, à condition que l'enrobage soit adapté en conséquence.

Étant donné que l'enrobage et la résistance du matériau sont définis séparément pour chaque classe d'exposition, des combinaisons de classes XRC et XRDS présentant un enrobage identique ont été identifiées. Ces combinaisons peuvent conduire à une action combinée.

Afin d'éviter un risque accru de corrosion, il est recommandé, lors du choix des classes ERC, d'éviter les combinaisons correspondant aux zones gris moyen de la Fig. 8.

<u>Résumé et besoins de recherche supplémentaires</u>

- Les principaux résultats ainsi que les besoins de recherche restants peuvent être résumés comme suit :
- Dans les bétons exposés aux chlorures, le degré de saturation augmente, ce qui entraîne un ralentissement de la carbonatation.
- Dans le béton carbonaté, les chlorures liés se libèrent et peuvent légèrement accélérer la pénétration des chlorures.
- Le risque d'action combinée peut être estimé à l'aide de la résistance à la carbonatation et aux chlorures selon la SIA 262/1 ou à partir du rapport SiO_2/CaO. Les combinaisons critiques conformément à la figure 8 doivent être évitées.

- La teneur critique en chlorures augmente avec la teneur en Al_2O_3 et en SiO_2 du liant. Après carbonatation, elle diminue indépendamment de la composition du liant pour atteindre environ 0,2 à 0,4 % en masse.
- La vitesse de corrosion est plus élevée dans les bétons simultanément exposés aux chlorures et à la carbonatation que dans les bétons soumis uniquement aux chlorures ou uniquement à la carbonatation.
- Lorsque les valeurs limites de la SN EN 206 sont strictement respectées, le risque d'action combinée est faible.
- Pour les combinaisons de classes XRD et XRC, la figure 8 peut être utilisée pour l'évaluation du risque.

1 Introduction and literature review

1.1 Performance-based durability in BD EC2

With the aim to ease the application of more eco efficient concrete, CEN TC 250 SC2 WG 1 implemented a performance-based durability concept in chapter 6.4 of the new Eurocode prEN 1992-1-1:2023 [1]. Herein Exposure Resistance Classes ERC classify concretes with respect to the resistance against corrosion induced by carbonation (class-XRC) or by chlorides (class XRDS). For each carbonation resistance (XRC) and chloride resistance (XRDS) the minimum concrete cover is proposed in dependency of exposure class and service life. Due to for example the differences in climate condition and building practice, the concrete cover is a national determined parameter (NDP). Therefore, in the following, the proposed concrete covers following the Swiss approach in CEN TC 250 SC2 TG10 (WG110) [2] are given.

The XRC classes are shown in Fig. 8. A limited number of classes reflecting the proposal for ERC table in NA EN 1992-1-1 from [4] is shown in black. The number of each class indicates the limit for the carbonation rate for example for the carbonation resistance class XRC6, the concrete shall exhibit a maximum carbonation rate of 6 mm/year$^{0.5}$. For the intended concrete resistance (e.g. XRC6), the present exposure class (e.g. XC4) and the intended design service life (e.g. 50 years) the concrete cover is 30 mm. The concrete is than described for example as follows: C30/37; XRC6, (XRDS2); Cl 0.1; C3; D_{max} 32; XC4, XD3, XF2; $c_{min,dur}$ = 30mm and c_{nom} = 40 mm.

Table 6.3 (CH) — Minimum concrete cover $c_{min,dur}$ for carbon reinforcing steel - carbonation

ERC	Exposure class (carbonation)							
	XC1		XC2		XC3		XC4	
	Design service life (years)							
	50	100	50	100	50	100	50	100
XRC 1	no durability requirements		10	10	10	10	10	15
XRC 2			10	15	10	15	10	20
XRC 3			10	15	10	20	15	25
XRC 4			15	20	15	25	20	30
XRC 5			15	20	20	30	25	35
XRC 6			20	25	25	35	30	40
XRC 7			20	25	30	40	35	45
XRC 8			25	30	35	45	40	50
XRC 9			25	30	40	45	45	55
XRC 10			30	35	40	50	45	55
XRC 11			30	35	45	55	50	60
XRC 12			35	40	45	55	50	60

NOTE 1 XRC classes for resistance against corrosion induced by carbonation are derived from the carbonation depth [mm] (characteristic value 90 % fractile) assumed to be obtained after 50 years under reference conditions (400 ppm CO_2 in a constant 65 %-RH environment and at 20 °C). The designation value of XRC has the dimension of a carbonation rate [mm/√(years)].
NOTE 2 The recommended minimum concrete cover values cmin,dur assume execution and curing according to minimum CC3.
NOTE 3 The minimum covers can be increased by an additional safety element Δcdur,γ considering special requirements (e.g. more extreme environmental conditions).

Fig.8 *Exposure resistance class corresponding concrete cover in dependency of Exposure Class and Design service life for Carbonation induced corrosion [2], herein XC1 resembles X0(CH) because the corrosion progress in this exposure class is considered insignificant.*

The XRC classes have been derived from interpolation of data from real structures (Symbols), from model prediction in CH climate conditions and extrapolation of exposure tests in Visp and Wildegg in [2] as shown in Fig. 9. The black lines indicate the proposed minimum concrete cover for each XRC-class. The dotted black line indicates a reduction of the proposed concrete cover in [2].

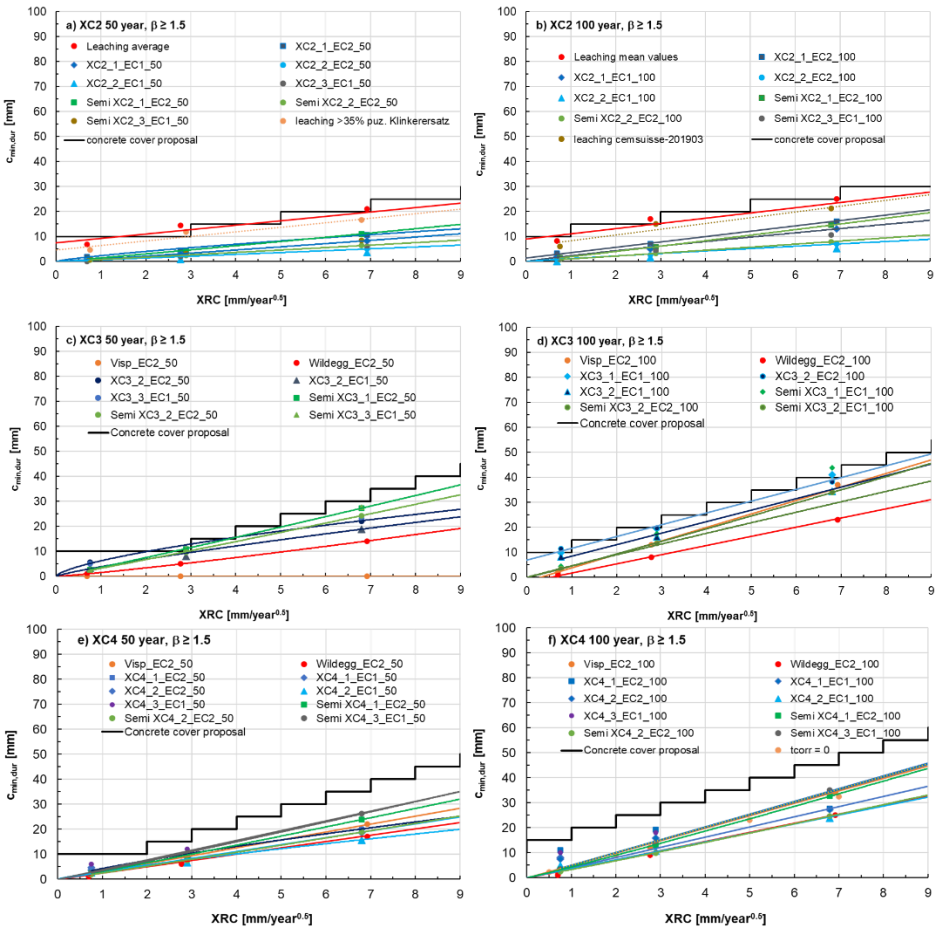

Fig.9 *Parameter study performed in [2] to derive the concrete cover for XRC classes in (a) XC2 50 year, (b) XC2 100 year, (c) XC3 50 year, (d) XC3 100 year, (e) XC4 50 year and (f) XC4 100 year service life.*

The XRDS classes are shown in Fig. 10. The number of each class indicates the limit for the chloride resistance represented by the chloride diffusion coefficient expected after 50 years under reference conditions. For example, for the chloride resistance class XRDS18, the concrete shall exhibit a maximum chloride diffusion coefficient of 18 10^{-13} m^2/s. The concrete exposed to XD1, XC4 is than described for example as follows: C30/37; XRC7, XRDS18, Cl 0.1; C3; D_{max} 32; XC4, XD1, XF2; $c_{min,dur}$ = 30 mm.

Table 6.4 (CH) — Minimum concrete cover cmin,dur for carbon reinforcing steel — Chlorides

ERC	Exposure class (Chlorides)			
	XD1=XD2a(CH)		XD3 = XD2b(CH)	
	Design service life (Year)			
	50	100	50	100
XRDS 1	10	20	20	30
XRDS 2	15	25	25	35
XRDS 3	15	25	30	40
XRDS 4	20	30	30	40
XRDS 5	20	30	35	45
XRDS 6	25	35	35	45
XRDS 7	25	35	40	50
XRDS 8	25	35	40	50
XRDS 9	25	35	45	55
XRDS 10	25	35	45	55
XRDS 12	30	40	50	-
XRDS 14	30	40	55	-
XRDS 16	30	40	-	-
XRDS 18	30	40	-	-
XRDS 24	35	45	-	-
XRDS 30	40	50	-	-
XRDS 40	45	55	-	-

Fig.10 *Exposure resistance class corresponding concrete cover in dependency of Exposure Class and Design service life for Chloride induced corrosion [2].*

The XRDS classes have been derived from interpolation of data from real structures (Symbols) and from model prediction in CH climate conditions [2] as shown in Fig. 11. The black lines indicate the proposed minimum concrete cover for each XRC-class. The dotted black line indicates a possible reduction of the proposed concrete cover in [2].

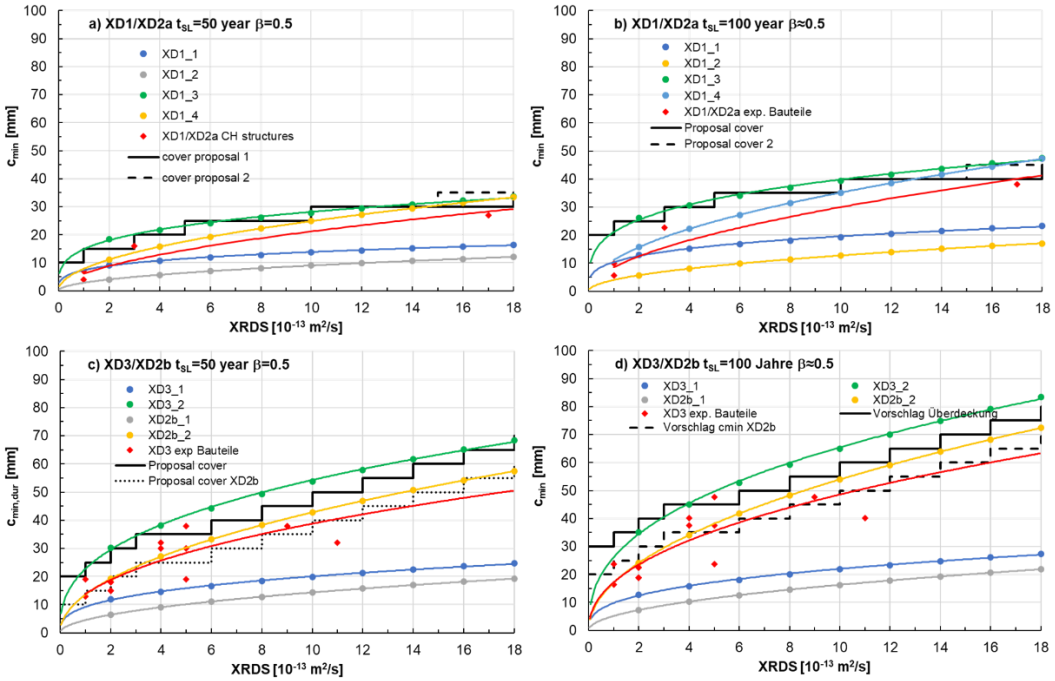

Fig.11 *Parameter study performed in [2] to derive the concrete cover for XRDS classes in (a) XD1 50 year, (b) XD1 100 year, (c) XD3 50 year and (d) XD3 100-year service life.*

The beneficial effect of the concept with respect to the use of eco efficient concrete can be seen in Fig. 12. In Fig. 12 to the XRC classes the corresponding carbonation resistance KW according to SIA 262/1 Annex I has been added. The numbers are derived from exposure tests according to SN EN 12390-10 [3] (sheltered) performed in [4-6]. To the KW the corresponding current NPK Classes are added for information. Furthermore, the reduction or increase in GWP derived from literature review and analyses in [4] are added. As can be seen, a concrete with a lower carbonation resistance, for example XRC9 (which corresponds to a NPK-A) can currently, according to SN EN 206 be used in the exposure class XC2 solely. Currently NPK-A cannot be used for XC3 exposed structural elements even with increased concrete cover, although this concrete shows a reduced GWP compared to NPK-C. In the future, with the ERC concept in EC2 [1], this concrete can be applied but with an increased concrete cover. Despite the higher concrete cover, the GWP is reduced. Another benefit is that the concrete producer can apply his portfolio to a larger area of application. In turn a higher carbonation resistance in XRC3 for example, representing prefabricated higher performance concrete, can benefit from a lower concrete cover. In this figure, the concrete cover is given as c_{nom}.

Reduction (-) or increase (+) in GWP		w/CaO	Sorte	KW	ERC
lower	upper				
81	46	0.65	-	1.0	XRC 1
64	37	0.75	F	2.0	XRC 2
48	28	0.90	F,C	3.5	XRC 3
32	19	1.00	C, F	4.5	**XRC 4**
16	9	1.15	C, F	5.5	XRC 5
0	0	1.25	C, B	6.5	**XRC 6**
-16	-10	1.35	B, C	7.5	XRC 7
-33	-19	1.50	A, B	9.0	XRC 8
-49	-29	1.60	A	10.0	**XRC 9**

Fig. 12 *XRC-Classes and correlation with the carbonation resistance KW, hints for concrete NPK (Sorten), w/CaO and GWP from [4].*

w/SiO_2	$w/(SiO_2+Al_2O_3)$	Sorte	CW	ERC
1.5	1.30	F	1	**XRDS 1**
1.6	1.35	F	2	**XRDS 2**
1.8	1.45	**F**	**4**	**XRDS 4**
2.1	1.55	F, D	6	**XRDS 6**
2.3	1.70	F, D	9	**XRDS 8**
2.4	1.80	**F, D**	**10**	**XRDS 9**
2.6	1.90	D	13	**XRDS 12**
2.7	2.00	D	15	**XRDS 14**
2.8	2.10	D	18	**XRDS 16**
2.9	2.30	**D***	**20**	**XRDS 18**
3.1	2.50	B	26	**XRDS 24**
3.5	2.90	**B, A**	**33**	**XRDS 30**
4.3	3.50	**A**	**44**	**XRDS 40**

* CEM II/B-LL included [4]

Fig. 13 *XRDS-Classes and correlation with the chloride resistance CW, hints for concrete NPK (Sorten), w/SiO_2 and $w/(SiO_2+Al_2O_3)$ from [4].*

1.2 Performance-based durability design in SN EN 206 & SIA262

The performance-based approach according to SN EN 206 [7] is currently based on so called concrete `Sorten`. Under the umbrella of one `Sorte` several exposure classes are listed, in which this specific `Sorte` can be applied. A specific `Sorte` must fulfil the requirements for example for the carbonation resistance KW, the chloride resistance CW and/or some other performance requirements and requirements for the concrete composition. Fig. 14 repeats the respective table of concrete `Sorten` where the corresponding exposure classes and requirements for these concretes are summarized.

Tabelle NA.6 Anforderungen an die Zusammensetzung und Prüfung der üblichen Betonsorten mit einem Grösstkorn der Gesteinskörnung von 8 mm bis 63 mm

Bezeichnung Anforderungen	**Sorte 0 (Null)**	**Sorte A**	**Sorte B**	**Sorte C**	**Sorte D (T1)**	**Sorte E (T2)**	**Sorte F (T3)**	**Sorte G (T4)**
Expositionsklasse (Kombination der aufgeführten Klassen)	X0(CH)	XC2(CH)	XC3(CH)	XC4(CH), XF1(CH)	XC4(CH), XD1(CH), XF2(CH)	XC4(CH), XD1(CH), XF4(CH)	XC4(CH), XD3(CH), XF2(CH)	XC4(CH), XD3(CH), XF4(CH)
Maximaler *w*/*z*-Wert bzw. w/z_{eq}-Wert	–	0,65	0,60	0,50	0,50	0,50	0,45	0,45
Mindestzementgehalt z_{min}, in kg/m³ [1),2)]	–	280	280	300	300	300	320	320
Dauerhaftigkeits-prüfungen [3)]	Keine	Keine	WL [4)], KW	KW	KW, FT	KW, FT	CW, FT	CW, FT
Andere Anforderungen	SN EN 12620+A1:2008 enthält Anforderungen an die Gesteinskörnungen							
Frei gegebene Zement-arten (Tabelle NA.1)	Bei der Kombination von Expositionsklassen gilt für die Wahl des Zementes jeweils die strengste Anforderung							

[1)] Der Mindestzementgehalt gilt für Betone ohne Zusatzstoffe und mit einem Grösstkorn D_{max} 32 mm. Wird ein anderes Grösstkorn D_{max} verwendet, ist der Zementgehalt entsprechend Tabelle NA.7 anzupassen.
[2)] Bei der Zementart CEM II/B-LL sind die Fussnoten der Tabelle NA.1 zu beachten.
[3)] Prüfungen gemäss Norm SIA 262/1:2019, Anhang A, B, C und I, für die Wasserleitfähigkeit (WL), Chloridwiderstand (CW), Frost-Tausalz-Widerstand (FT) und Karbonatisierungswiderstand (KW). Bei den Prüfungen gelten die Grenzwerte und Kriterien gemäss Ziffer NA.8.2.3.4 (Tabelle NA.14).
[4)] Die Bestimmung der Wasserleitfähigkeit ist durchzuführen, falls der Nachweis gemäss Ziffer NA.8.2.3.5 zu erbringen ist.

Fig. 14 *Requirement for the concrete composition and performance testing in SN EN 206:2021 [7].*

The required concrete cover for specific exposure classes is given in SIA 262 [8] in Table 18, see Fig. 15. Because SIA 262 specifies the nominal concrete cover c_{nom} and not c_{min}, SIA 262 also specifies the tolerance, which is mostly (i.e. cast against framework) for c_{nom} ≥ 20 mm +20 mm for c_{nom} ≥ 30 mm ± 10 mm and between 20 mm < c_{nom} < 30 mm it is – 5 mm and + 10 mm.

Tabelle 18: Planmässige Bewehrungsüberdeckung

(c) Bewehrungsüberdeckung c_{nom} [mm] [1)]	Expositionsklasse gemäss Tabelle 1							
	2) Bewehrungskorrosion in karbonatisiertem Beton				3) Bewehrungskorrosion induziert durch Chloride			
	XC1	XC2	XC3	XC4	XD1	XD2a	XD2b	XD3
Betonstahl	20	35		40	40		55	
Spannstahl bzw. Spannglied	30	45		50	50		65	
[1)] Die tabellierten Werte der Bewehrungsüberdeckung dürfen bei der Ausführung maximal um die Abweichungen gemäss Ziffer A.3.5 unter- oder überschritten werden.								

Fig. 15 *Nominal concrete cover in dependency of exposure class and type of reinforcement according to SIA 262 [8].*

Performance requirements for the concrete in dependency of exposure classes are shown in Fig. 16.

	Wasser-leitfähigkeit	Karbonatisierungswiderstand		Chlorid-widerstand
Prüfung gemäss SIA 262/1:2019	Anhang A	Anhang I		Anhang B
Prüfung ist durchzuführen bei den Expositions-klassen (CH)	XC3 [1)]	XC3	XC4, XD1, XD2a, XF1	XD2b, XD3
Prüfung ist durchzuführen bei den Betonsorten gemäss Tabelle NA.5	Sorte B [1)]	Sorte B	Sorte C, D und E	Sorte F und G
Grenzwert für Mittelwert	$q_w \leq 10$ g/m²h	$K_N \leq 6{,}5$ mm/Jahr$^{1/2}$ [2),3)]	$K_N \leq 5{,}0$ mm/Jahr$^{1/2}$ [2),4)]	$D_{Cl} \leq 10 \cdot 10^{-12}$ m²/s

6.5 (prNASNEN206:2024)

Fig. 16 *Performance requirements according to SN EN 206:2021 [7] with additions from the revision of prNA SN EN 206:2025 [9].*

Because in the next generation the performance limit for carbonation KW is 6.5 mm/year$^{0.5}$. Consequently, the cement types are limited for NPK-C allows a higher clinker reduction than NPK-B or in turn in NPK-B a fewer number of cement types can be used when the maximum w/c ratio is applied.

1.3 Prediction of corrosion in SIA 269/1, SIA MB 2069

prSIA 269/2 [3] predicts the corrosion initiation under moist conditions, like expected in XD3 as follows:

Chloridegehalt < 0,4 Massen-%/Zement: geringes Korrosionsrisiko
Chloridgehalt 0,4 bis 1,0 Massen-%/Zement: erhöhtes Korrosionsrisiko
Chloridgehalt > 1,0 Massen-%/Zement: hohes Korrosionsrisiko

(Chloride content < 0.4 wt.-%/cement: low risk for corrosion,
Chloride content 0.4 to 1.0 wt.-%/cement: medium risk for corrosion
Chloride content > 1.0 wt.-%/cement: high risk for corrosion)

The limits are provided for CEM I cements. It is noted that the critical chloride content may be different for differing cements.

Furthermore, prSIA 269/2 points out that the condition state prediction strongly depends on the evolution of moisture condition inside the structural element, but without further details.

It should be noted; that the SIA MB 2069 [10] offers a valuable test method to determine the concrete specific critical chloride content, even in partially carbonated concrete.

1.4 Dominating actions in standards

The project aims to assess which deterioration process dominates in real structures and to identify where and when the risk of simultaneous action occurs.

1.4.1 SIA 262 & SN EN 206:

According to project specifications, depending on the exposure class, either a specific concrete type is prescribed, regardless of whether the concrete is produced according to Annex ND (free composition) or under deemed-to-satisfy rules (NPK concrete). In this context, the concrete (Type C) must fulfil the requirements for carbonation resistance (XC4), although it is simultaneously exposed to chlorides (XD1).

This raises the question of whether, for certain binder types, the risk of chloride-induced corrosion exceeds the risk of carbonation-induced corrosion. Furthermore, it must be examined whether, for specific binders or mix designs, a risk of simultaneous action exists under XD1 & XC4 conditions and what consequences may result.

Consequently, it must be clarified whether the limiting value KW for XC4 & XD1 is sufficient to prevent chloride-induced corrosion.

ERC-concept in prEN1992-1-1:

After the implementation of EN 1992-1-1 in 2028, concrete will be specified by a combination of exposure classes, concrete cover, strength class, and design service life.

For example, concrete for a retaining wall exposed to airborne salt, with a design service life $t_{SL} \leq 100$ years and a nominal cover $c_{nom} = 50$ mm, could be specified as:

XC4 / XD1 / XF2, Cl 0.2, C3, C25/30, $f_{c,k,cube}$(28 days) ≤ 44 MPa, XRDS ≤ 7, XRC ≤ 8, FT medium.

The concrete producer must then develop a mix design that fulfils all these requirements.

This raises the question of whether a correlation exists between carbonation resistance and chloride resistance. Furthermore, it must be examined whether combinations of XC4 & XD1 or XC4 & XD3 can lead to simultaneous action at similar required concrete cover, and which additional measures may be necessary but are not yet addressed in the ERC concept.

1.4.2 SIA 269/2, SIA MB2069:

SIA 269/2 provides limiting values for critical chloride contents for CEM I concretes under moderate moisture conditions, excluding combined action of carbonation and chloride ingress. This raises the question of whether the performance of new materials with respect to critical chloride content can be assessed based on their composition.

Furthermore, it must be clarified whether a limiting value for the critical chloride content exists under combined action.

SIA 269/2 also requires the prediction of condition state development. However, information on the influence of combined action on further deterioration processes is currently lacking.

SIA MB 2069 provides a valuable test method for determining the critical chloride content, even in partially carbonated concrete. In addition, guidance is given on using measured critical chloride contents for service life prediction.

Nevertheless, the effects of further carbonation on chloride diffusion and on additional changes in C_{crit} are not yet sufficiently addressed. Consequently, the influence of simultaneous action on service life prediction remains unclear.

1.5 Comparable materials performance for SLD

1.5.1 Definition of service life t_{SL}:

In prEN 1992-1-1:2021, the design service life t_{SL} is defined as the sum of the corrosion initiation time t_{ini} and the corrosion propagation time t_{prop} (both in years), according to Eq. (1.5.1).

The corrosion propagation time is intended to end before cracking of the concrete cover occurs. It is derived from the long-term average corrosion rate v_{corr} (in µm/year) and the tolerable steel loss that does not yet lead to cover cracking, defined as a radial depth of 50 µm, according to Eq. (1.5.2).

For chloride-induced corrosion, the tolerable corrosion loss of 50 µm includes a pitting factor of 10.

Furthermore, in Eq. (1.5.2), i_{corr} denotes the corrosion current density in µA/cm², A_a is the corroding area in cm², I_{corr} is the corrosion current in A, ΔE is the potential difference in V, $R_{p,a}$ and $R_{p,c}$ are the anodic and cathodic polarization resistances in Ω, respectively R_E is the electrolytic resistance in Ω, and I_{self} is the microcell corrosion current in A [DAfStb 601 & 602].

$$t_{SL} = t_{ini} + t_{prop} \qquad \text{Eq.(1.5.1)}$$

$$t_{prop} = \frac{v_{corr}}{50} \; with \; v_{corr} \approx 11.6 \cdot i_{corr} \; ; i_{corr} = \frac{I_{corr}}{A_A} \; ; \; I_{corr} \approx \frac{\Delta E}{R_{P,A}+R_{P,C}+R_E} + I_{self} \qquad \text{Eq.(1.5.2)}$$

In prEN 1992-1-1:2021, two main approaches are used to determine the required concrete cover.

The first approach is based on durability design and determines the concrete cover for each ERC class using probabilistic or semi-probabilistic numerical and engineering models.

The resulting correlation between concrete cover and performance derived from modelling is then verified by comparison with the concrete cover and performance of concretes complying with the deemed-to-satisfy rules (second, verification approach).

1.5.2 Carbonation progress prediction:

The carbonation of concrete is mainly considered a diffusion-controlled process following Fick's first law and is commonly modelled using the square-root model.

Under unsheltered conditions, the outer, influential zone is affected by alternating wetting and drying periods. In contrast, below the surface zone, the moisture condition becomes constant once equilibrium is reached (see Fig. 17 (a) [11]). It can therefore be assumed that, after a certain drying period, carbonation is no longer significantly influenced by wetting and drying, and that the carbonation rate proceeds at a low but constant level.

In contrast, the model proposed by Bakker [12], shown in Fig. 17 (b), assumes that the concrete remains constantly wet and that carbonation occurs only during drying periods. Consequently, the carbonation rate continuously decreases and approaches very low values.

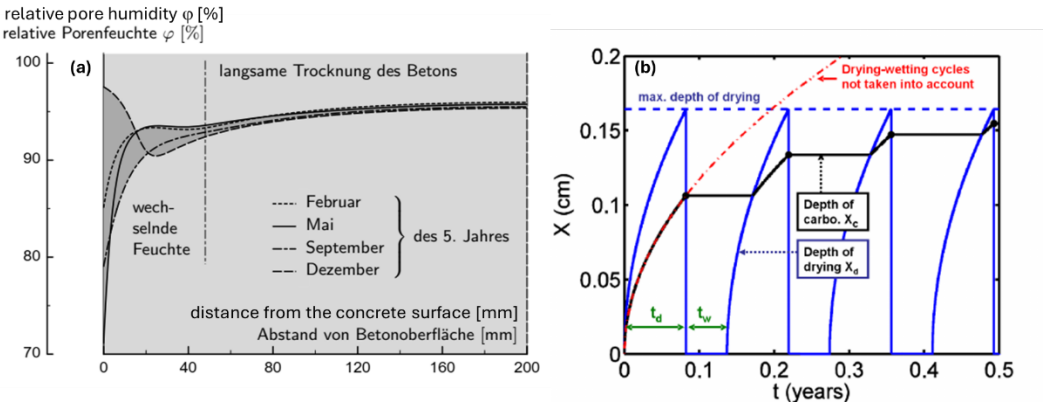

Fig. 17 *(a) Moisture distribution during wetting and drying cycles [11] and (b) Bakker model to model wet and dry conditions [12].*

Models used to predict the entire service life based on carbonation rates determined at early age under laboratory testing conditions are generally based on the Bakker model [12].

In these models, the carbonation rate decreases with time, resulting in a time exponent smaller than 0.5 [13,14], as expressed in Eq. (1.5.3) (Carbonation – Model 1).

$$x_c(t) = k \cdot t^n \cdot \sqrt{t} = k \cdot t^b \; with \; b = 0.5 \mp n \qquad \text{Eq.(1.5.3)}$$

Here, t corresponds to t_{ini} in years, k denotes the carbonation rate in mm/year$^{0.5}$, the dimensionless exponent n describes the decrease in carbonation rate over time, and the dimensionless time exponent b combines the square-root exponent with n.

For existing structures, however, where carbonation progress is extrapolated from mature structural elements, the carbonation rate is generally assumed to be constant but reduced to a lower level compared to laboratory conditions [15], as expressed in Eq. (1.5.4) (Carbonation – Model 2). Even if a slight decrease in the carbonation rate occurs during further carbonation progress, this model remains on the safe side.

$$x_c(t) = \{k \cdot W\} \cdot \sqrt{t} \qquad \text{Eq.(1.5.4)}$$

Here, t corresponds to t_{ini} in years, and k represents the carbonation rate reflecting the basic resistance of the selected concrete mix (e.g., water/cement ratio, cement type, and mineral additions) under reference conditions, as well as the influence of the basic environmental conditions (such as mean relative humidity and CO_2 concentration) on carbonation ingress. It also accounts for the influence of execution quality.

The factor W considers the varying meso-climatic conditions acting on the specific concrete member during the design service life, such as humidity and temperature.

Another modelling approach is presented in [16–18] and expressed in Eq. (1.5.5) (Carbonation – Model 3).

$$x_c(t) = A + k \cdot \sqrt{t} \qquad \text{Eq.(1.5.5)}$$

Here, t corresponds to t_{ini} in years, A denotes an empirical factor accounting for the initiation period of carbonation (in mm), and k represents the carbonation rate incorporating the combined effects of material properties, execution quality, and environmental conditions.

1.5.3 Chloride ingress prediction

In parts of [2], predictions of further chloride ingress are performed using Eqs. (1.5.6) to (1.5.8) (Chloride – Model 1). These equations are based on the error function solution of Fick's second law of diffusion [13,15].

Deviations from the ideal concentration profile near the surface are considered by the parameter Δx (in mm). The effect of chloride binding on the apparent diffusion coefficient $D_{app}(t)$ (in mm²/year) is considered by an ageing function with the dimensionless age exponent α.

Furthermore, x denotes the depth in mm, C_0 is the initial total chloride content, and $C_{s\Delta x}$ represents the apparent maximum total chloride concentration at depth Δx. Both C_0 and $C_{s\Delta x}$ are expressed in wt.-% of concrete or wt.-% of cement.

Rearranging Eq. (1.5.6) leads to Eqs. (1.5.7) and (1.5.8).

$$c(x,t) = c_0 + \left(c_{s,\Delta x} - c_0\right) \cdot erfc\left(\frac{x-\Delta x}{\sqrt{4 \cdot D_{app}(t0) \cdot \left(\frac{t0}{t}\right)^{\alpha} \cdot t}}\right) \quad \text{Eq.(1.5.6)}$$

$$x_{Cl}(t) = \Delta x + \left\{\sqrt{4 \cdot D_{app(t0)} \cdot t^{-\alpha}} \cdot inverfc\left(\frac{C_{Cl} - C_0}{C_{s,\Delta x} - C_0}\right)\right\} \cdot \sqrt{t_{ini}} \quad for\ t_0 = 1 \quad \text{Eq.(1.5.7)}$$

$$x_{Cl}(t) = \Delta x + v_{Cl}(t) \cdot \sqrt{t_{ini}} = \Delta x + v_{Cl} \cdot t_{ini}^{b} with\ b = 0.5 - \frac{\alpha}{2} \quad \text{Eq.(1.5.8)}$$

Here, x denotes the depth, c_0 is the initial chloride concentration, $C_{s\Delta x}$ represents the chloride concentration from the surface (Δx = 0) up to depth x (in mm), x_{Cl} is the depth corresponding to a given chloride concentration (in mm), and Δx accounts for deviations from the ideal profile, for example due to capillary water transport or wash-off effects.

D_{app} is the apparent diffusion coefficient under specific microclimatic conditions, concrete composition, pore structure, and chloride concentration levels, α is the age exponent, c_{Cl} is the chloride concentration for which the depth is calculated, v_{Cl} is the chloride ingress rate, comparable to the carbonation rate, and n describes the negative deviation from the square-root law.

Reference [19] analysed the applicability of the square-root model, Eq. (1.5.9) (Chloride – Model 2), for different types of chloride binding isotherms and for conditions involving simultaneous leaching and capillary absorption. The authors found that the square-root law is valid in hydrated concrete with chloride binding in equilibrium. Consequently, in line with [20], they concluded that early-age chloride profiles should be excluded.

Furthermore, for structural elements exposed to leaching, capillary absorption, or simultaneous carbonation, chloride contents within the influential depth should be disregarded.

$$x_{Cl,C\%}(t) = v_{Cl,C\%} \cdot \sqrt{t} \quad \text{Eq.(1.5.9)}$$

Fig. 18 shows (a) four idealised chloride profiles of the same concrete at different exposure times. The brown circles indicate the depths corresponding to a lower chloride content at each time point, while the red circles indicate the depths corresponding to a higher chloride content.

In Fig. 18 (b) the cycles are plotted over square root of time. The slope of the regression line represents the chloride ingress rate $v_{Cl,x\%}$ for the specific chloride content. Both regression lines cross the origin, because no deviation from ideal chloride profile was apparent in Fig. 18 (a).

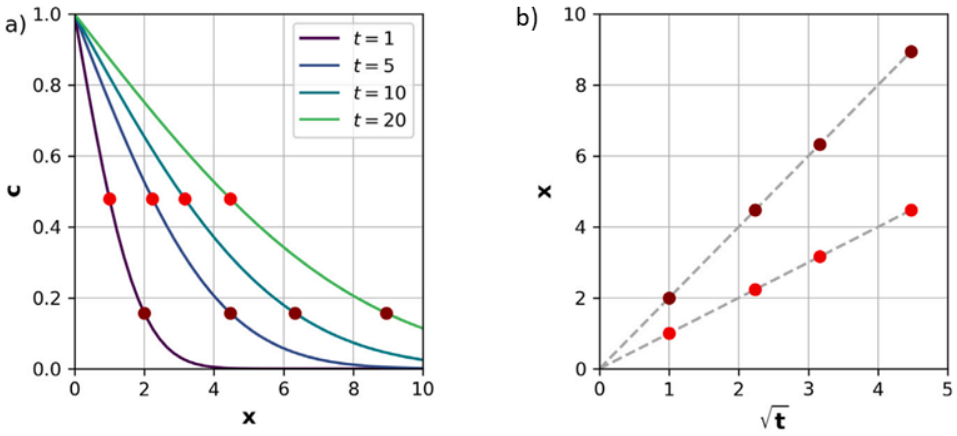

Fig. 18 *Using the time function for predicting chloride ingress (a) measured depth with a certain chloride concentration (b) plotted depth with a certain chloride concentration over square root of time for the assumption that the material does not age [19].*

References [20–22] describe chloride ingress using linear regression with respect to the square root of time, as expressed in Eq. (1.5.10) (Chloride – Model 3).

Due to initially pronounced effects of chloride binding and simultaneous processes such as capillary absorption, carbonation, and leaching on chloride ingress, the square-root model was found to be valid only after a concrete age of approximately 200 days.

This validation was based on chloride profiles obtained from site-cured structural elements exposed to submerged, tidal, and splash water conditions [20].

$$x_{Cl,C\%}(t) = B + v_{Cl,C\%} \cdot \sqrt{t} \qquad \text{Eq.(1.5.10)}$$

In Eq. (1.5.10), B represents the deviation from the ideal chloride profile in mm, and $v_{Cl,C\%}$ denotes the ingress rate (in mm/year$^{0.5}$) corresponding to a specific chloride concentration.

Under natural exposure conditions, simultaneous action and deviating ingress mechanisms (e.g. capillary absorption) lead to deviations from the ideal profile, as illustrated in Fig. 19 (a) to (c).

Figure 19 (a) shows chloride profiles determined at three different points in time, exhibiting deviations from the ideal profile in the surface regions. Figure 19 (b) presents the depth corresponding to a specified (critical) chloride content (C_{cr}). Figure 19 (c) shows the depth of C_{cr} plotted against the square root of time, together with the derivation of the chloride ingress rate ($v_{Cl,C\%} = a_{cr}$) and the intercept ($B = b_{cr}$) according to [20].

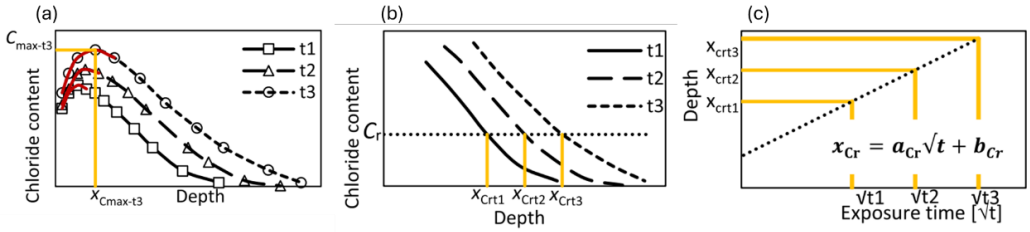

Fig. 19 *Determination of chloride ingress rate $v_{Cl,C\%}$ (=a_{Cr}) and constant B (=b_{Cr}) according to [20] with (a) chloride profiles with deviation from ideal profile, (b) depth with a certain (here critical) chloride content and (c) depth with critical chloride content over square root of time.*

1.6 Consequences of combined action

1.6.1 Consequences on chloride binding

In a porous system such as concrete in contact with a chloride-containing solution, the pore solution tends to reach equilibrium with the chloride concentration of the surrounding environment. In an ideal, fully saturated system, chlorides migrate through the concrete mainly by diffusion in order to reach this equilibrium.

Due to chloride binding in the cementitious matrix, only a fraction of the total chlorides can diffuse freely into the concrete. Only this free chloride fraction is able to locally destroy the passive layer surrounding the reinforcement and initiate chloride-induced corrosion. The mechanisms of chloride binding are well documented and can be classified as follows:

Chemical chloride binding occurs mainly through the formation of Friedel's and Kuzel's salts and is generally assumed to be relatively stable, although its development may take up to four months [23,24]. Since AFm phases favour the formation of Friedel's salt in the presence of NaCl [25,26], chemical binding is promoted by:

- increased C_3A content in Portland cement,
- higher contents of reactive Al_2O_3 in pozzolans [27–29],
- an optimum Ca/Al ratio between 3 and 7 in blended cements [30,31].

Partly reversible physical chloride binding occurs through adsorption on C-(A)-S-H surfaces. The physical binding capacity increases with:

- higher C/S ratios,
- higher Al/Si ratios,
- shorter mean silicate chain lengths,
- higher positive surface charge densities [24,25,29,30,32–40].

The proportion of chemically bound chlorides typically ranges between 20 % and 70 % [28,41,42], depending not only on material composition but also on experimental and environmental conditions.

In addition to chemical composition, elevated temperatures [43–47] and lower relative humidity [48,49] tend to increase chloride binding. Chloride compounds such as $CaCl_2$ and $MgCl_2$ also enhance binding [50–53]. In contrast, competing ions such as sulphates [54,55] and deviations of pH below or above an optimum value may reduce chloride binding [28]. The share of chemically bound chlorides is found between a wide range of 20% and 70% [28, 41, 42], not only due to the material but also experimental and environmental influences.

Since chloride binding is concentration-dependent, binding isotherms such as Langmuir, Freundlich, or linear models are commonly used to describe the relationship between free and bound chlorides. Under the relatively low chloride concentrations typically encountered in natural exposure conditions, linear isotherms are usually applied [25,43,56–60].

Chloride binding is further influenced by concrete composition, for example:

- Water-to-binder ratio (w/b):
  Increasing w/b is generally assumed to reduce chloride binding capacity, as dilution in a larger pore solution volume lowers the amount of bound chlorides. However, this effect is influenced by microclimatic conditions, degree of hydration, and experimental setup, leading to contradictory results [48,61–64].
- Reactive binder content:
  Higher contents are typically associated with increased chloride binding capacity.
- Limestone (LS):
  Limestone dilutes the reactive binder fraction and therefore reduces chloride binding, particularly the physically bound fraction [61].
- Blast furnace slag (BFS):

BFS is often assumed to enhance both chemical and physical binding due to increased contents of Friedel's salt and C-(A)-S-H [48,60,63,65,66]. However, some studies report lower binding compared to Portland cement because of higher sulphate and magnesium contents competing for incorporation and adsorption [28,61,67], especially at low NaCl concentrations (< 30 g/L).

- Fly ash (FA) and calcined clays:
  These materials generally increase the amount and proportion of chemically bound chlorides [28,60,63,67,68].
- Metakaolin (MK) and calcined clays:
  These tend to enhance both chemical and physical binding [68,69].
- Silica fume (SF):
  SF has been found to reduce chemical chloride binding due to dilution of C_3A [25,69–72].
- Recycled concrete fines (RCF):
  RCF generally exhibit slightly lower binding capacity with decreasing fines content. Conversely, increasing SiO_2 and Al_2O_3 contents tend to enhance binding [73].

Due to chloride binding, a slight reduction in total porosity and pore size has been reported [67,68,74–78].

When chloride-contaminated concrete undergoes carbonation, chemically bound chlorides are released. This process can be described by the carbonation reactions of Friedel's salt (Eq. 1.6.1) and Kuzel's salt (Eq. 1.6.2).

$$3CaO{\bullet}Al_2O_3{\bullet}CaCl_2{\bullet}10H_2O + 3CO_2 \rightarrow 3CaCO_3 + Al_2O_3 + Ca^{2+} + 2Cl^- + 10H_2O \quad \text{Eq. (1.6.1)}$$

$$3CaO{\bullet}Al_2O_3^-{\bullet}1/2CaSO_4{\bullet}1/2CaCl_2{\bullet}11H_2O + 3CO_2 \rightarrow 3CaCO_3 + Al_2O_3 + Ca^{2+} + Cl^- + 11H_2O \quad \text{Eq. (1.6.2)}$$

With progressive carbonation of C-(A-)S-H, physically bound chlorides are released. As carbonation is associated with a decrease in the pore solution pH, Fig. 20 illustrates the pH dependence of chloride binding according to [62].

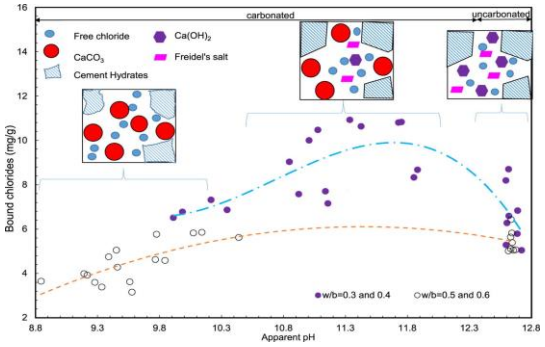

Fig. 20 *Strongly bound chlorides in dependency of pH for different w/c ratio [62].*

Due to calcium carbonate formation, total porosity may be slightly reduced, whereas extensive C-(A-)S-H carbonation has been reported to cause pore coarsening [79]. Moreover, increased free chloride contents have been shown to raise the water content and degree of saturation in partially saturated concrete [80].

Under saturated conditions, carbonation affects bound chlorides as follows:

- Their release increases the diffusion driving force and accelerates chloride ingress [81–82].
- The porosity reduction caused by chloride binding [67–68, 74–78] may be partially compensated by carbonation-induced porosity changes [79], although material-dependent effects may differ.

1.6.2 Consequences on chloride ingress and carbonation under cyclic conditions

When concrete is partially saturated, chloride diffusion is decelerated, as diffusion occurs only in water-filled pore spaces [67,83,84]. Under typical Swiss climate conditions (60–90 % relative humidity), corresponding to an equilibrium degree of saturation of approximately 15–50 %, the diffusion coefficient is expected to be about 0.1–0.3 times that under fully saturated conditions [49,85–92]. In addition to moisture conditions, temperature also affects chloride diffusion. At average temperatures of 10–12 °C, the diffusion coefficient is approximately 0.55–0.72 times that at 20 °C [13,93–95].

In contrast, CO_2 diffusion occurs primarily in air-filled pore spaces. Consequently, in partially saturated concrete at equilibrium (15–50 % saturation), CO_2 diffusion is 10–50 times faster than in saturated concrete [96]. However, the influence of temperature on CO_2 diffusion is less pronounced [79].

Influence of Cyclic Wetting and Drying:
Under cyclic wetting and drying conditions, solutions partially enter the concrete by capillary absorption [e.g. 48] and evaporate during drying phases [e.g. 86,87]. The affected region is commonly referred to as the convection zone [13] or influential depth [2].

Capillary transport of chlorides is approximately 20–26 times faster than diffusion [97,98]. Capillary absorption and evaporation, combined with wash-off and leaching processes, are considered responsible for the formation of a maximum total chloride concentration below the concrete surface [13,99,100]. Under cyclic exposure, this maximum concentration is generally found to be similar across different studies [13,82,100–104].

Carbonation progresses more slowly during wet periods and accelerates during dry periods. This behaviour is commonly modelled using a reduced time exponent ($0.2 \leq b \leq 0.4$) [5,13] or a constant reduction factor [13].

However, cyclic exposure conditions have also been reported to promote microcracking, which increases the influential depth, enhances capillary chloride ingress and diffusion, and accelerates CO_2 transport [105].

Under combined carbonation and chloride exposure, the following effects on transport processes have been reported:

- Carbonation
  Due to the increased moisture content in chloride-contaminated concrete, carbonation is generally decelerated. However, in concretes with substantially increased porosity (e.g. slag cements with enhanced chemical chloride binding), the reduction in carbonation rate is less pronounced and may even be slightly reversed [81,106].
- Chloride ingress
  Chloride ingress is significantly accelerated, with reported migration or diffusion coefficients 12–24 times higher than under non-carbonated conditions [81,107–113]. This increase is more pronounced in concretes with higher chloride binding capacity and higher w/c ratios [111,114] and has been attributed to changes in both pore solution chemistry and pore structure [112].
- Maximum chloride concentration
  The maximum chloride concentration is generally lower under cyclic exposure combined with carbonation [81,82,104,107,110,115,116]. This behaviour is attributed to wash-off effects caused by increased volumes of released chlorides [112] and to enhanced diffusion away from the concentration maximum, resulting in broader chloride profiles [81,103].
- Depth of maximum chloride concentration
  In concretes exposed to cyclic conditions without carbonation, the depth of maximum chloride concentration is usually similar when the convection zone exceeds the carbonation depth [81]. However, in carbonated concrete, it remains unclear whether this depth increases due to an enlarged convection zone caused by pore structure coarsening, or whether it follows the carbonation front when the convection zone is smaller.

1.6.3 Consequences on corrosion initiation

Chloride-induced corrosion initiation is characterized by the breakdown of the passive film through adsorption, penetration, film dissolution, or electrostriction mechanisms [117].

In standards, the onset of corrosion is usually described in terms of the total chloride content relative to the cement or concrete content. The critical chloride threshold level depends primarily on the properties of the steel–concrete interface, particularly the number of interfacial voids and the surface condition of the reinforcing steel, as well as on the moisture state (with the lowest threshold typically observed between 70 % and 90 % relative humidity), the degree of passive film ageing, and the concrete composition (notably the w/b ratio and binder type) [112–118].

Since only free chlorides contribute to corrosion initiation, the total chloride content required to trigger corrosion is strongly influenced by material-dependent chloride binding. Consequently, the free chloride content relative to the cement or binder content is often used in research studies. Because the pH, i.e. the OH^- concentration, plays a crucial role in the formation and stability of the passive layer, another frequently used threshold parameter is the $[Cl^-]/[OH^-]$ ratio. This ratio is particularly suitable for assessing the influence of combined carbonation and chloride ingress on corrosion initiation.

Tab. 1 *Chloride threshold levels for black steel reinforcement according to standards and guidelines and research and under the effect of simultaneous carbonation*

total Cl	**Unit**	**Condition**	**Standards**
0.2	wt.-%/binder	Initial content in concrete	SN EN 206
0.4	wt.-%/binder	Initial content in concrete	EN 1992-1-1
0.65	wt.-%/binder	Initial content in GGBFS concrete	Afnor
< 0.4	wt.-%/binder	Existing structures highly probable	SIA 269/2:2024
0.4 < c_{crit} < 1.0	wt.-%/binder	Existing structures probable	
< 1.0	wt.-%/binder	Existing structures possible	
0.5	wt.-%/binder	Existing structures	DAfStb Rili Sib
0.6	wt.-%/binder	General	*fib* MC SLD
0.4-0.6	wt.-%/binder	Existing structures in general	*fib* MC 2020
1-1.5	wt.-%/binder	Existing structures submerged	*fib* MC 2020
free Cl	**Unit**	**Condition, explanation**	**Reference**
0.07-1.16	wt.-%/cement	Literature review	[123-124]
0.59-1.29	wt.-%/binder		[125]
0.4 – 0.5	wt.-%/binder	As received reinforcement	[126]
≥ 1.25	wt.-%/binder	Cleaned reinforcement	
$[Cl^-]/[OH^-]$	**Unit**	**Condition, explanation**	***Reference***
0.01-45	-	All types	[124]
0.66-3	-	All types of concretes and conditions	[127-129]
≥ 3.0	-	MK or Slag blended cement	[130]
≥ 1.0	-	PC cement slurry	[130-131]
0.01-4.9	-	Synthetic pore solution test	[123]
0.05-20	-	Hardened cement pastes samples	[123]
≥ 1.0	-	PC cement slurry	[132]
0.05-2.0	-	Mortar samples using migration	[133-134]
≥ 1		OH- concentration of 1 Mol and pH 13	[131]
Partly carbonated concretes and mortars			
Type and limit	**Unit**	**Condition**	**Reference**
Cl_f ≤ 0.12 - 0.18	Wt.-%/cem.	CC-LL blends lab test	[135]
$[Cl^-]/[OH^-]$ < 0.9	-		
0.3 ≤ Cl_{tot} ≤ 0.7	Wt.-%/cem.	PC and PC+FA concrete exposure	[136]
$[Cl^-]/[OH^-]$ ≤ 0.5-0.6	-	PC cement slurry lab test	[137]

In the case of carbonation-induced corrosion in the absence of chlorides, corrosion initiation is governed primarily by the pore solution pH. At the onset of corrosion, pH values of approximately ≤ 9.2–11 have been reported [120,138–139]. This corresponds to a threshold limit of $[CO_3^{2-}]/[HCO_3^-] < 0.01–0.1$ [140].

Since phenolphthalein indicates carbonation at a pH of approximately 8.5, a distance of about 6 mm between the reinforcement and the measured carbonation depth is typically observed at corrosion initiation [138].

It can therefore be concluded that, under combined carbonation and chloride exposure, corrosion initiation occurs earlier due to the reduced critical chloride threshold (C_{crit}) and before the carbonation front reaches the reinforcement.

1.6.4 Consequences on corrosion progress

Chloride-induced corrosion is usually associated with localized macrocell corrosion, mainly driven by potential differences between anodic and cathodic regions of the reinforcement, although some degree of self-corrosion cannot be excluded [128,131,135,141-145]. According to [2], average corrosion rates for chloride-induced corrosion range from 3 to 50 µm/year for XD1, from 5 to 50 µm/year for XD2, and from 10 to 50 µm/year for XD3 exposure classes.

In contrast, carbonation-induced corrosion is generally characterized by uniform microcell corrosion, which is strongly influenced by the electrolytic resistivity, while macrocell activity cannot be entirely excluded [5,97,146–153]. Approximate corrosion rate ranges depending on exposure class are also provided in [2]: for XC2 (permanently high humidity), 5-10 µm/year; for XC3 (moderate humidity, sheltered from rain), 1-5 µm/year; and for XC4 (moderate to high humidity, not sheltered from rain), 4-12.5 µm/year.

When chloride-contaminated concrete undergoes carbonation, bound chlorides are released and hydroxyl ions are consumed. This process reduces the equilibrium potential and increases the microcell corrosion rate [Bui et al., 2023], increases the $[Cl^-]/[OH^-]$ ratio - leading to reduced polarization resistance and more negative corrosion potentials [130-131,154-155] - and decreases the ohmic resistance [126,156], thereby enhancing macrocell corrosion rates [157].

When chlorides are present in carbonation-induced corrosion, the resulting corrosion products are more soluble. This leads to increased ferrous ion concentrations at the steel-concrete interface and, consequently, to more negative equilibrium potentials, reduced anodic Tafel slopes, and more negative free corrosion potentials, resulting in higher microcell corrosion rates [157-158]. These effects are further intensified by increasing HCO_3^- concentrations [140,158-159]. Because both the open-circuit potential (OCP) and the electrolytic resistivity decrease in carbonated concrete in the presence of chlorides, macrocell corrosion currents are expected to increase [157,160].

Figure 21 illustrates the influence of simultaneous chloride and carbonation exposure (Cl + CO_2) on (left) concrete resistivity and (right) macrocell and microcell corrosion current densities, in comparison with single carbonation (CO_2) or single chloride (Cl) exposure [157].Chloride induced corrosion is usually referred to local macro cell corrosion mainly driven by the potential difference between anodic and cathodic acting reinforcement areas, whereas some self-corrosion cannot be excluded [128, 131, 135, 141-145]. In [2] average corrosion rates for chloride induced corrosion have been selected with $3 \leq \mu m \leq 50$ for XD1, with $5 \leq \mu m \leq 50$ for XD2 and with $10 \leq \mu m \leq 50$ for XD3.

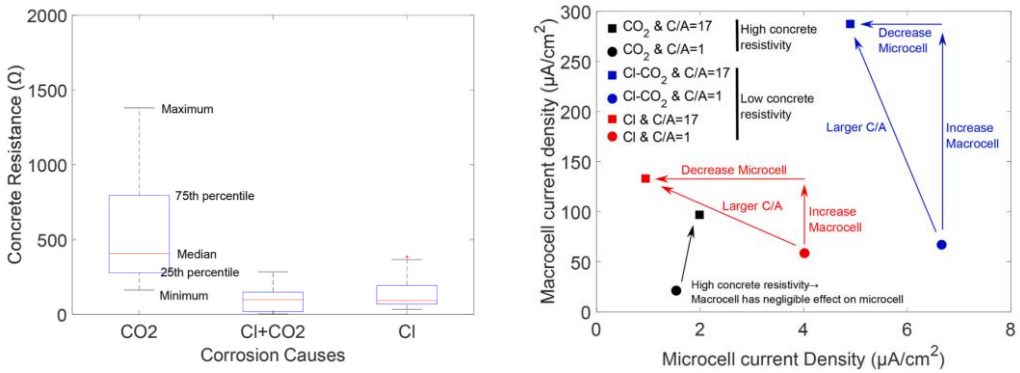

Fig. 21 *Effect of simultaneous carbonation and chloride exposure (Cl + CO_2) on (left) concrete electrical resistance and (right) microcell and macrocell corrosion current density, compared with individual carbonation (CO_2) and chloride-induced (Cl) corrosion processes [157].*

It can be concluded that progressive carbonation and increasing chloride contents in concrete lead to higher microcell and macrocell corrosion current densities.

2 Concrete investigation

2.1 Concrete mix design

2.1.1 Cement

Tab. 2 summarizes the cements used, their raw material densities, and oxide compositions, as determined by X-ray fluorescence (XRF). All cements are of Swiss origin.

***Tab. 2** Cement*

Oxides	CEM I 42.5N	CEM II/C-M(Q-LL) (CRCF)*	CEM II/B-M (T-LL) 42.5N	CEM III/B 32.5N LH/SR	CEM II/B-M(S-T) 42.5R HS	CEM II/B-LL 32.5R
SiO_2	19.8	26.76	18.15	30.5	24.93	14.5
Al_2O_3	4.6	5.89	4.12	8.1	6.12	3.2
Fe_2O_3	3.1	3.47	2.72	1.4	2.71	2.1
CaO	61.9	50.3	60.6	47.8	55.7	60.4
MgO	2.2	2.39	2.38	5.5	2.98	1.5
SO_3	3.3	3.69	2.64	3.9	3.4	2.4
K_2O	0.87	1.16	0.75	0.078	0.99	0.69
Na_2O	0.25	0.37	0.22	0.25	0.27	0.17
Cl_2	0.044	0.024	0.014	0.012	0.011	0.03
$CaCO_3$	5	12.3	15.4	1	1.9	38
Density [g/cm^3]	3.12	2.99	3.04	2.95	2.99	2.99

* CRCF (ZN/D) contains ordinary Portland cement, recycled concrete fines and oil shale

Tab. 3 shows the key oxides used in the correlations presented in this document, namely CaO, SiO_2, and the combined SiO_2 + Al_2O_3 content.

***Tab. 3** Decisive oxides*

Oxides	CEM I	CRCF	CEM II/B-M (T-LL)	CEM III/B	CEM II/B-M(S-T)	CEM II/B-LL
$CaO=CaO-CaO_{CaCO3}$	59.1	43.6	52.0	47.8/38.5*	54.6	39.1
$SiO_2=SiO_2-SiO_{2RCF}$	19.8	19**	18.15	30.5	24.93	14.5
$Al_2O_3 + SiO_2$	24.4	24.89	22.3	38.6	31.1	17.7

* Considering the degree of hydration of 80% [4] ** no curing effect is considered but for CEM II/C-M(F-T) (CRCF) the SiO_2 of recycled fines is deduced from SiO_2

The aggregates were obtained from the Holcim Schweiz AG gravel plant in Mülligen and are of alluvial origin. Prior to concrete mixing, the aggregates were kiln-dried. WG was added to the mixing water. Figure 22 illustrates the aggregate grading curve, while Tab. 4 summarizes the mass fraction, WG content, kiln-dry water content, and raw density of each fraction.

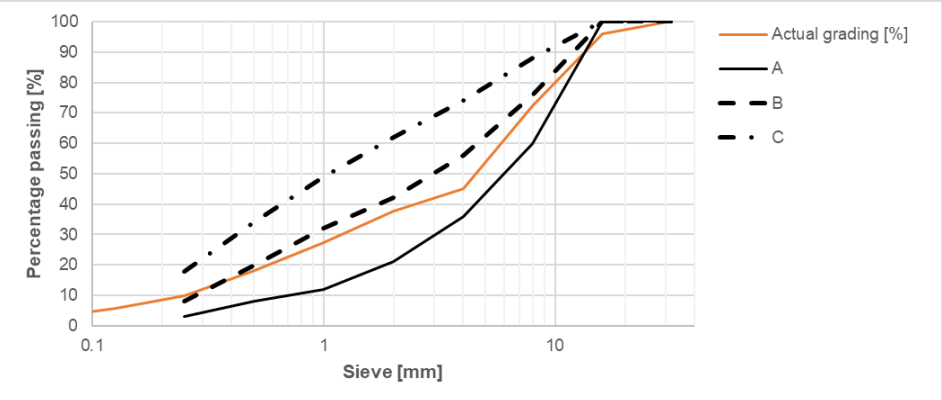

***Fig. 22** Aggregate grading curve.*

***Tab. 4** Aggregates*

Fraction	**0/2**	**0/4**	**4/8**	**8/16**
Type	Sand	Sand	Gravel	Gravel
Mass fraction [%]	20	25	30	25
W_G [wt.-%]	0.62	0.36	0.75	0.56
kiln dry water content [wt.-%]	1.41	7.06	3.1	1.28
Kiln dry raw density [kg/dm^3]	2.66	2.65	2.63	2.64

2.1.2 Reinforcement

The reinforced specimens contained hot-rolled ribbed carbon steel B500B (material number 1.0439) and ribbed stainless steel bars (material number 1.4404). Tab. 5 presents the chemical composition of the main alloying elements.

Prior to casting, the rebars were cleaned with ethanol. The 20 mm transition zone between the concrete specimen and the surrounding air was coated. The coating consisted of one layer of Portland cement paste applied to the steel surface, followed by two layers of epoxy coating.

The diameter of both the ribbed carbon steel and ribbed stainless steel rebars was 10 mm. Stainless steel was selected as the counter electrode (CE) to provide a similar electrochemical potential and to avoid polarization effects caused by the CE.

***Tab. 5** Reinforcement*

Material number	**Oxides**									
	Fe	**C**	**Si**	**Mn**	**P**	**S**	**V**	**Cr**	**Mo**	**Ni**
1.0439	97.81	0.22	0.53	1.44	0.025	0.022	0.038	-	-	-
1.4462	66.28	0.03	1.0	2.0	0.035	0.02	-	22	3.0	5.5

2.1.3 Concrete mix

The concrete composition is presented in Tab. 6. The plasticizer Sika Viscocrete 3082 (P) was added to achieve the target consistency class C3.

***Tab. 6** Concrete mix*

Mix	**02**	**03**	**04**	**05**	**06**	**07**
Binder type	CEM I	ZN/D	CEM II/B-M (T-LL)	CEM III/B	CEM II/B-M(S-T)	CEM II/B-LL
Binder content [kg/m^3]	300	300	300	300	300	300
Water content [kg/m^3]	150	150	150	150	150	150
w/c [-]	0.5	0.5	0.5	0.5	0.5	0.5
P [wt.%/cement]	0.6	0.6	0.6	0.4	0.8	0.5

Fig. 23 shows photographs of the mixing process, fresh concrete testing, and specimen preparation. Aggregates and cement were mixed for 3 minutes and allowed to rest for 1 minute. Subsequently, the mixing water was added, and the concrete was mixed for an additional 4 minutes.

After mixing, the fresh concrete temperature, air content, density, and flow table spread were measured. If necessary, additional plasticizer was added, followed by 2 minutes of further mixing.

The specimens were then compacted and kept in the formwork, sealed with plastic foil, under laboratory conditions for 24 hours. They were subsequently placed in a water bath at 20 °C for the designated curing period.

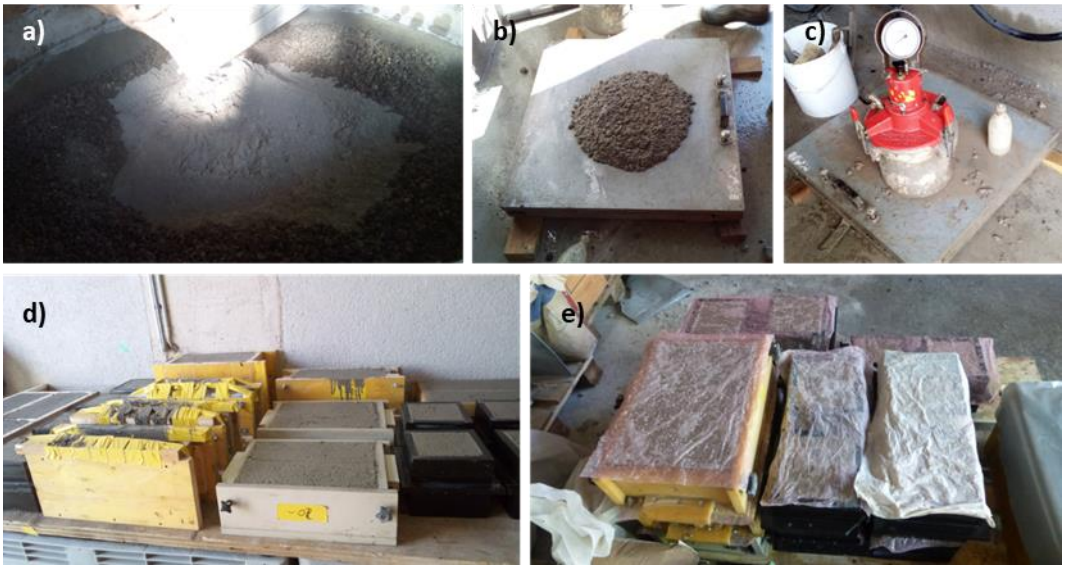

Fig. 23 *(a) Mixing of cement and aggregates, (b) flow table testing, (c) determination of air content, (d) specimen preparation, and (e) storage of specimens for 24 hours.*

2.2 Main samples

2.2.1 Exposure conditions

Two types of specimens were prepared to expose the concrete to different exposure regimes. One series was prepared without reinforcement and referred to as durability specimens (some equipped with multi-ring electrodes, MRE; see next chapter). The other series was prepared with reinforcement and referred to as corrosion specimens (see next chapter).

Specimens exposed to constant conditions according to standards, or to modified constant conditions, are referred to as reference specimens. For reference specimens under constant conditions, the specimen dimensions were selected in accordance with the standard sizes specified in SIA 262/1 Annex I and SN EN 12390-11.

Specimens exposed to cyclic wetting and drying conditions are referred to as Wf specimens.

Fig. 24 (a) and (b) show the reference specimens with dimensions according to SIA 262/1 Annex I and SN EN 12390-11, respectively. Fig. 24 (c), (d) and (e) present specimens for cyclic wetting and drying conditions with increased CO_2 concentration in the air during drying phases (Wf-CO_2), sodium chloride in the solution during wetting phases (Wf-Cl), and combined increased CO_2 concentration and sodium chloride exposure (Wf-Cl-CO_2), respectively.

The first exposure series was designed to investigate changes in carbonation progress as well as corrosion initiation and propagation when transitioning from laboratory standard conditions to cyclic conditions, both without and with chloride exposure:

(a) Carbonation series:
SIA 262/1-I / EN 12390-12 ← R0-CO_2 → Wf-CO_2 → Wf-Cl-CO_2

The second exposure series was designed to investigate changes in chloride ingress as well as corrosion initiation and propagation when transitioning from laboratory standard conditions to cyclic conditions, both without and with carbonation:

(b) Chloride series:
SIA 262/1-B / EN 12390-11 ← R0-Cl → Wf-Cl → Wf-Cl-CO_2

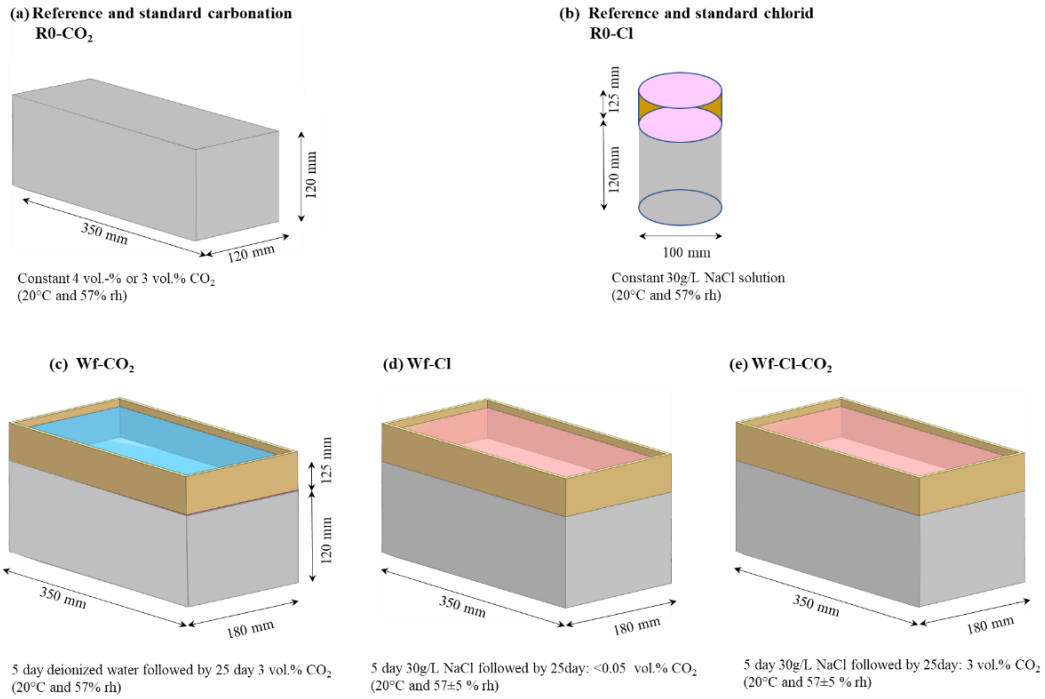

Fig. 24 *Durability samples for standard conditions (a) used for carbonation testing, (b) used for chloride diffusion testing.*

Reference and Wf specimens were prepared with identical heights to avoid differences in calcium depletion and chloride accumulation at the bottom of the specimens. Moreover, this height was selected to facilitate comparative modelling. The periodic application of solution to the Wf specimens resulted in a water level similar to that of the reference specimens. The comparable water level (125 mm) ensured a similar available chloride content per square centimetre of specimen surface and similar hydraulic pressure.

Additional cylindrical specimens with a diameter of 50 mm and a length of 50 mm were used for chloride migration testing in accordance with SIA 262/1 Annex B.

The chloride reference specimens and the Wf specimens were coated with epoxy on all faces except for the exposed top surface. The joints between the specimen surface and the frame (Wf specimens) or the tubes (chloride reference specimens) were sealed using joint sealant.

The sodium chloride solution was selected in accordance with relevant standards. Magnesium chloride ($MgCl_2$) and potassium chloride (KCl) are not commonly used as de-icing salts, while calcium chloride ($CaCl_2$) is applied only under very harsh conditions. According to information from the Canton of Graubünden (2021), the de-icing protocol consists of 70 % dry NaCl and 30 % water, or a solution containing 78 % water and 22 % NaCl. At extremely low temperatures, $CaCl_2$ is used at low contents (< 1 %) for economic reasons.

Typical application rates range from 10 to 15 g NaCl/m². During de-icing operations, chloride concentrations of 100–1000 mg/L are measured in wastewater, while 10–60 mg/L are found in groundwater [161]. According to [162], approximately 25 % of the applied NaCl is deposited within 10 m of the roadway. Consequently, a 30 g/L NaCl solution can be considered representative of the salt concentrations within this roadside zone.

Tab. 7 summarizes the different types of reference (constant) and cyclic exposure regimes. It includes the water curing times, preconditioning procedures, and detailed information on exposure conditions, durations, measurement campaigns, and measurement methods.

After curing, the specimens were kept in laboratory air for one week for preparation before the start of the exposure program. Subsequently, the wet phase was initiated, consisting of 5 days of either deionized water or NaCl solution applied to the top surface of the specimens.

During the wetting phase, the specimens were covered to prevent water evaporation and the associated changes in chloride concentration. This procedure also minimized excessive CO_2 consumption while maintaining the required relative humidity in the climate chamber surrounding the specimens.

***Tab. 7** Main samples, exposures and investigations*

Designation	Curing [day]	Exposure				Investigation	
		dry condition	Dry duration [day]	Wet condition	Wet duration [day]	Investigations & modelling	At time [day] / cycle [No.]
SIA 262/1-I Carbonation	3 d water, 25 d air curing (20°C, 57%rF)	T: 20°C CO2: 4 % vol.-% RH: 57%	63d	-	-	Carbonation depth	0d, 7d, 28d, 63d
SIA262/1-B Chloride migration	28d	-	-	force: 20 V, T: 20°C Anolyt: 30g/l NaCl in 0.2 M KOH, Katholyt: 0.2 Mol KOH	2-5d	Chloride ingress depth	2d – 5d
SN EN 12390-12 Carbonation	28 d water, 14 d air curing	T: 20°C CO_2:3 vol.-% RH: 57±5%	70d	-	-	Carbonation depth	0d, 7d, 28d, 70d
EN 12390-11 Chloride diffusion	28d water	-	-	T: 20°C Sole: 30g/L NaCl in deionized water	-	XRF Cl_{tot} ISE Cl_{WS}, pH	90d, 270d, 540d
R0-CO_2 Carbonation	91d water	T: 20°C CO_2^*:0.05±0.01% RH: 57±5%	540d	-	-	Carbonation depth GEMS	0d, 7d, 28d, 70d
R0-Cl Chloride ingress	91d water, 14 d air curing	-	-	T: 20°C Sole: 30g/L NaCl in deionized water	-	XRF Cl_{tot} ISE Cl_{WS}, pH GEMS	90d, 270d, 540d
Wf-Cl Chloride ingress	91d water, 14 d air curing	T: 20°C CO_2^*:0.05±0.01% RH: 57±5%	25d per cycle	T: 20°C Sole: 30g/L NaCl in deionized water	5 d per cycle	XRF Cl_{tot} ISE Cl_{WS}, pH μXRF GEMS	90d, 270d, 540d / 3, 9 and 18 cycles
Wf-CO_2 Carbonation	91d water, 14 d air curing	T: 20°C CO_2^*: 3 % RH: 57±3%	25d per cycle	T: 20°C Sole: deionized water	5 d per cycle	Carbonation depth μXRF, ISE pH GEMS	90d, 270d, 540d / 3, 9 and 18 cycles
Wf-Cl-CO_2 Chloride ingress & Carbonation	91d water, 14 d air curing	T: 20°C CO_2^*: 3 % RH: 57±3%	25d per cycle	T: 20°C Sole: 30g/L NaCl in deionized water	5 d per cycle	Carbonation depth XRF Cl_{tot} ISE Cl_{WS}, pH μXRF, GEMS	90d, 270d, 540d / 3, 9 and 18 cycles

2.2.2 Investigations

For destructive investigations, specimens were removed from their respective storage conditions after 3, 9, and 18 cycles (90, 270, and 540 days) and prepared for further analysis according to Fig. 25.

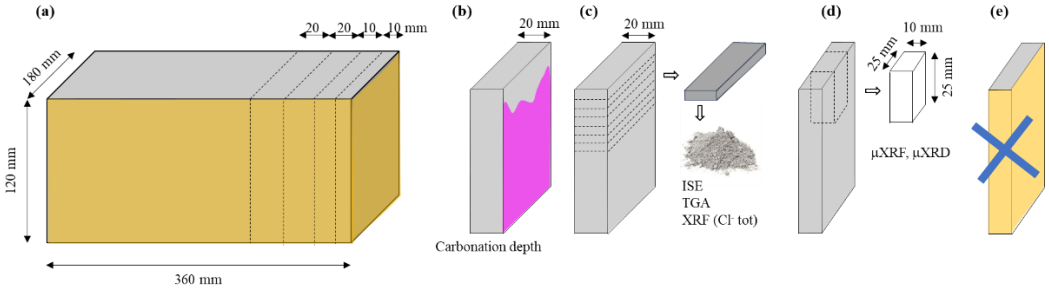

Fig. 25 *Preparation of Wf samples for analyses.*

During each measurement campaign, four slices were cut from each specimen (see Fig. 25 (a)). The remaining part of the specimen was coated with epoxy, the frame was reattached, and the specimen was returned to the climate chamber.

One slice was used to determine the carbonation depth by spraying with a pH indicator (Fig. 25 (b)). The second slice was further cut into 3 mm thick discs and ground in a ball mill. Half of the resulting concrete powder was used to determine the total chloride content by XRF analysis, while the other half was used to determine pH as well as free Cl^- and Ca^{2+} contents using ion-selective electrodes (ISE).

From the third slice, a specimen measuring 25 × 25 × 10 mm was cut, polished, and used for ion composition analysis by µXRF.

µXRF Analysis

µXRF (micro X-ray fluorescence) scanning was performed using an M4 Tornado IXRF system (Bruker), equipped with an Ag X-ray tube with a spot size of 20 µm and a silicon drift detector (SDD). The distance between measurement points was set to 25 µm, with a measurement time of 3 ms per point. The X-ray tube was operated at 50 kV and 600 µA under a vacuum of 20 mbar.

The scans provided a qualitative, spatially resolved description of the distribution of various elements from the exposed surface towards the interior, presented as elemental maps.

Carbonation Depth and Carbonation Rate

Carbonation specimens were sprayed with indicator solution, and the carbonation depth was measured. The carbonation rate was calculated using Eq. (2.2.1), where d_{km} represents the average carbonation depth in mm, k_s the carbonation rate, s the applied CO_2 concentration (4 vol.% or 3 vol.%), and t the exposure time in days.

$$x_{CO2} = k_s \cdot \sqrt{t} \qquad \text{Eq. (2.2.1)}$$

To compare measurements performed at different CO_2 concentrations, the carbonation rate determined at a specific CO_2 concentration was adjusted to a reference CO_2 concentration using Eq. (2.2.2).

$$k_{CO2,ref} = k_{CO2} \cdot \sqrt{\frac{CO_{2,ref}}{CO_2}} \qquad \text{Eq. (2.2.2)}$$

To determine the chloride content of the reference specimens (EN 12390-11 and R0), an inner core with a diameter of 80 mm was drilled (see Fig. 26). To assess the required depth for profile grinding, the specimen surface was sprayed with a 0.1 M $AgNO_3$ indicator solution in accordance with the protocol specified in SIA 262/1.

The core was subsequently cut into slices with a thickness of 3 mm and oven-dried at 105 °C. The slices were then ground to concrete powder with a particle size of approximately 100 µm. The total and free chloride contents were determined using the same procedure as for the Wf specimens.

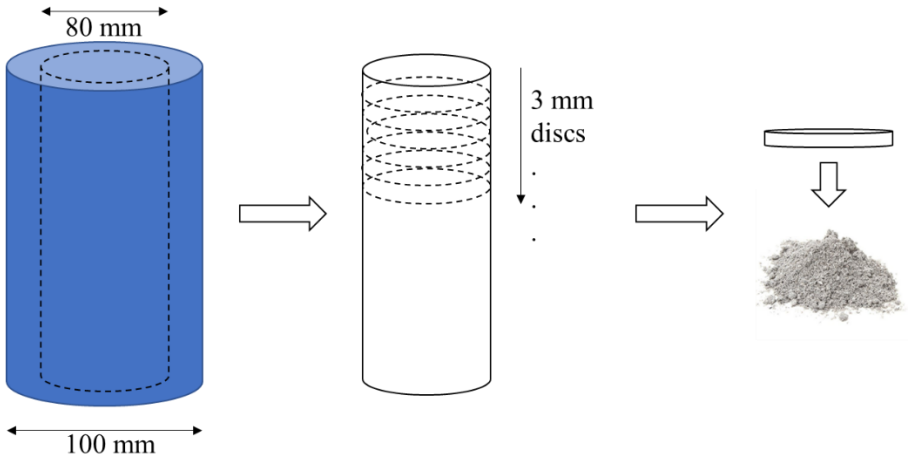

Fig. 26 *Preparation of reference Cl and R0-Cl specimens for chloride diffusion testing and further analysis.*

The chloride contents measured in the Wf and reference specimens were used to determine the chloride diffusion coefficient (D_{nss}), the surface chloride concentration (C_s), and the maximum chloride concentration ($C_{s\Delta x}$) using Eq. (2.2.3).

In this equation, C_x represents the chloride concentration at depth x (wt.-%), C_i is the initial chloride concentration, C_s is the calculated chloride concentration at the surface, and $C_{s\Delta x}$ is the chloride concentration at the depth of maximum chloride content (wt.-%). The function erf denotes the error function, x is the depth (m), D_{nss} is the chloride diffusion coefficient (m²/s), and t is the exposure time (s).

$$C_x = C_i + (C_s - C_i) \cdot \left(1 - erfc\left[\frac{x_{Cl}}{2 \cdot \sqrt{D_{nss} \cdot t}}\right]\right) \quad \text{Eq. (2.2.3)}$$

To compare the corrosion risk due to carbonation with that due to chloride ingress, the diffusion coefficient was used to calculate the chloride penetration depth according to Eq. (2.6), derived from Fick's second law of diffusion (Eq. 2.2.4).

In this equation, $x_{Cl,lim}$ represents the depth at which the chloride concentration reaches the critical value C_{lim} (m).

$$x_{Cl,lim} = 2 \cdot \sqrt{D_{nss(t)}} \cdot \sqrt{t} \cdot erfc^{-1}\left(\frac{C_{lim} - C_0}{C_s - C_0}\right) \quad \text{Eq. (2.2.4)}$$

The apparent diffusion coefficient may vary over time due to factors such as simplifications in the transport process, changes in moisture content during exposure, chloride binding reducing the amount of free mobile chlorides, redistribution and depletion effects, and ongoing hydration. It is therefore often represented by a time-dependent function, $D_{app(t)}$.

Furthermore, the maximum chloride concentration may be located below the concrete surface due to wash-off effects, variations in material composition, or surface leaching. In such cases, the surface concentration C_s is replaced by C_x, where C_x denotes the maximum chloride concentration and x the corresponding depth. The depth x is derived from x_{Cl} and $x_{Cl,lim}$ using Eqs. (2.2.3) and (2.2.4), respectively.

For the determination of Cl_{WS}, Ca, and pH by ISE analysis, an ex-situ leaching (ESL) method was applied. For this purpose, 10 g of oven-dried concrete powder were dissolved in 10 g of deionized water. During dissolution, the solution was continuously stirred for 10 minutes. Nitrogen was injected during stirring to prevent further carbonation of the leachate.

Since water was added to the samples during the ESL procedure, the ion concentrations were corrected for dilution using Eq. (2.2.5) according to [163]. In this equation, C_{ESL} represents the ion concentration in the pore solution, C_{ESL} the measured ion concentration in the solvent, V_{ESL} the volume of solvent used in the ESL method, and V_{PSE} the volume of pore solution.

The volumes of solvent and pore solution were calculated from the mass of added water m_w, the sample mass m_{sample}, and the fraction of evaporable water determined after oven drying at 105 °C, divided by the density of water.

$$c_{PSE} = C_{ESL}\frac{V_{ESL}}{V_{PSE}} \quad \rightarrow \quad V_{ESL} = \frac{m_w + {m_{sample}\cdot\%m_{w,evap}}/{100}}{\rho_w} \quad \rightarrow \quad V_{PSE} = \frac{{m_{sample}\cdot\%m_{w,evap}}/{100}}{\rho_w} \qquad \text{Eq. (2.2.5)}$$

Water-soluble chlorides were determined using a chloride ion-selective electrode (Cl^--ISE, Ag/AgCl). The total calcium content (free and bound Ca in solution) was measured using a Ca^{2+} ion-selective electrode (Ca-ISE), and the pH of the solution was determined using a pH electrode (Mettler Toledo).

Calibration of the electrodes and data acquisition were performed using an InLab Seven Excellence instrument (Mettler Toledo), as shown in Fig. 27.

***Fig. 27** Measurement of Ion concentration and pH by means of ISE.*

The OH^- concentration was calculated from the measured pH values using Eq. (2.2.6).

$$pOH = 14 - pH \quad \leftrightarrow \quad [OH^-] = 10^{-pOH} \qquad \text{Eq. (2.2.6)}$$

2.2.3 Photos of preparation

Fig. 28 shows photographs of the concrete specimens under Wf conditions: (a) boxes, (b) sealing, (c) installation of the boxes, (d) final specimens without MRE, and (e) final specimens with installed MRE.

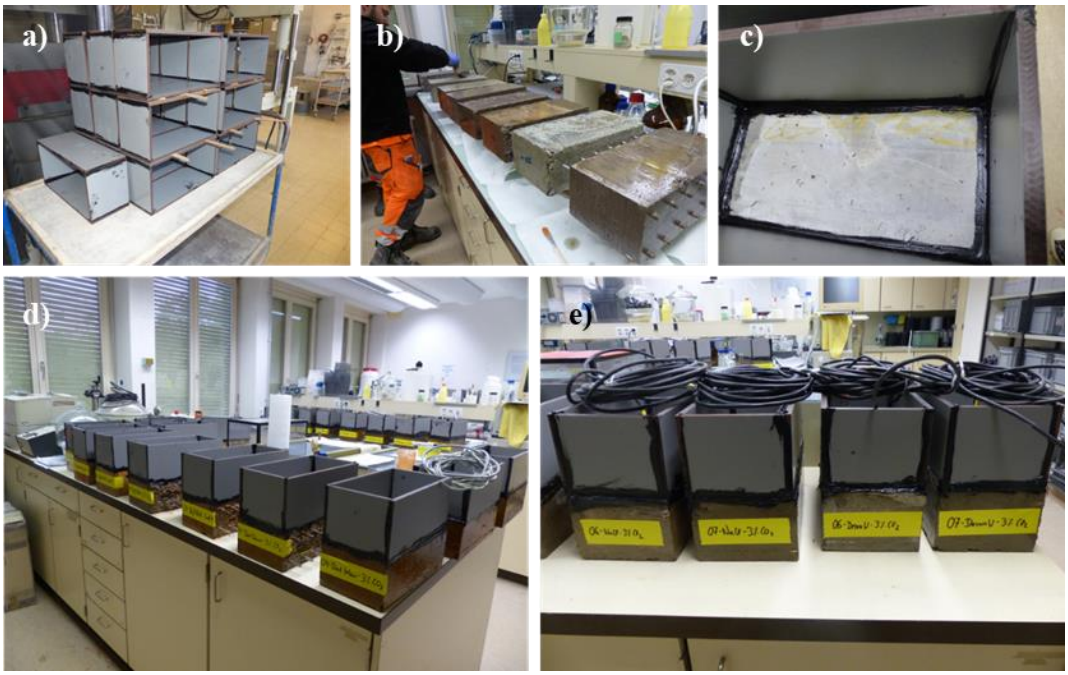

Fig. 28 *Wf specimen preparation: (a) box placed on top of the specimens, (b) sealing, (c) installation, (d) finished specimens, and (e) finished specimens with installed MRE.*

2.3 Monitoring

2.3.1 Moisture monitoring

In some of the Wf-CO_2 and Wf-Cl-CO_2 specimens, multi-ring electrodes (MRE) from Sensortec GmbH were installed to monitor depth-dependent water uptake and release by measuring electrical resistance. Fig. 29 shows (a) a cross-section with MRE placement and (b) a top view of the specimen.

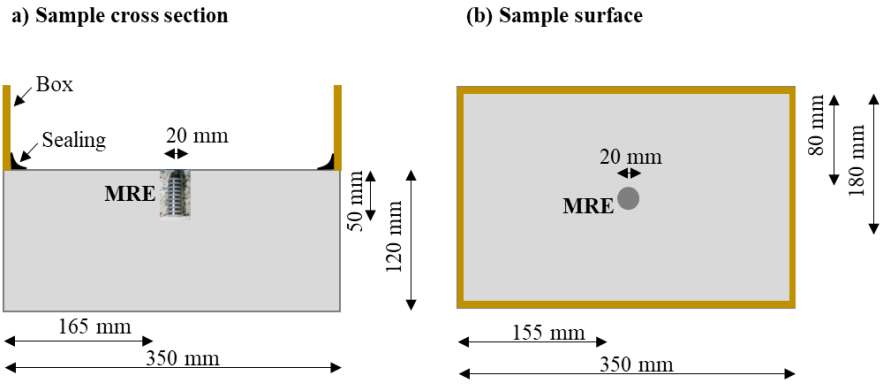

Fig. 29 *Durability samples for Wf conditions with the position of the MRE.*

The MRE sensor consists of stainless-steel ring electrodes positioned at different depths and connected by non-conductive plastic rings (cf. Fig. 30). The electrical resistance is measured between two stainless-steel rings by applying an alternating current across the electrodes.

The total length of the MRE is 42 mm, the diameter is 20 mm, and the spacing between two consecutive stainless-steel rings is 5 mm. The geometry factor (cell constant) k used to calculate the specific electrolytic resistivity is reported as k ≈ 0.07 m [164] and k ≈ 0.1 m according to Sensortec GmbH.

The electrical resistivity ρ (Ω·m) is calculated by multiplying the cell constant k by the measured resistance R (Ω).

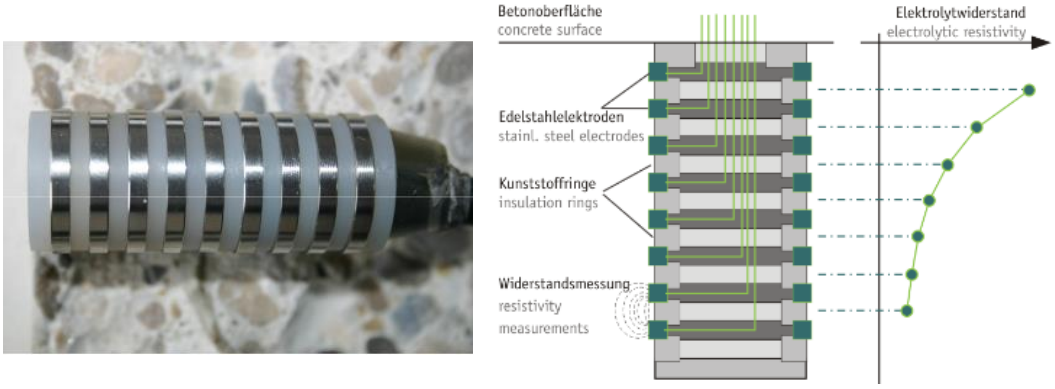

Abb. 30 *MRE according to Sensortec GmbH.*

The electrolytic resistivity was monitored using the wireless data acquisition system DSLog4.0 based on impedance measurements. Data transmission to the PRTG network monitoring system was carried out via a Raspberry Pi (IoT).

2.3.2 Corrosion monitoring

Fig. 31 shows the corrosion specimens. As for the durability specimens, three specimens were prepared for each concrete type and exposed to three different cyclic conditions.

At a distance of 20 mm from the bottom of the specimen, seven stainless steel bars with a diameter of 10 mm and material grade 1.4462 were installed. In addition, ordinary ribbed carbon steel reinforcement bars with a diameter of 10 mm were installed at depths of 10 mm, 20 mm, and 30 mm.

Prior to installation, the transition zone between the concrete and air at the reinforcement bars (total length 30 mm) was coated. The coating consisted of an initial cement–lime layer, followed by two layers of epoxy coating.

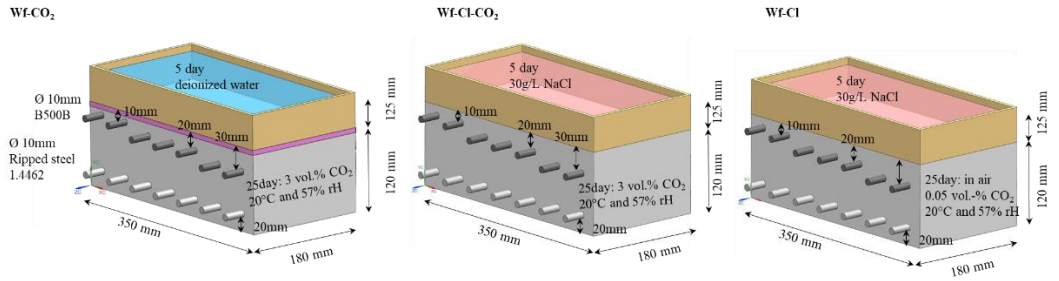

Fig. 31 *Corrosion samples for Wf conditions (a) Wf-CO_2, (b) Wf-Cl-CO_2 and (c) Wf-Cl.*

For corrosion monitoring, all black steel reinforcement bars within one concrete cover were electrically connected and served as the working electrode (WE). The electrically connected stainless steel bars on the opposite side served as the counter electrode (CE). Consequently, an anode-to-cathode area ratio of approximately A/C ≈ 1:1 was achieved for each concrete cover (see Fig. 32).

For data logging and transmission, a DSLog 3.0 system was used with hourly file transfer to the workstation. At the workstation, the individual files were automatically combined into a single data file.

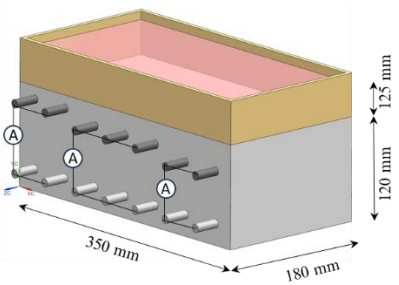

Fig. 32 *Corrosion current measurement.*

From the measured short-circuit current I, the corrosion rate v_{corr}, expressed as the volumetric loss per unit area and unit time (equivalent diameter loss), was calculated using Eq. (2.3.1), assuming a linear current density over time.

The calculation of corrosion loss is based on Faraday's law (Eq. 2.3.1) and was extended by incorporating the density of the corroding material in Eq. (2.3.2).

In these equations, M denotes the atomic mass, z the number of electrons involved in the corrosion reaction, F Faraday's constant (96 485 C/mol), and t the exposure time (s).

$$v_{corr}\left[\frac{\mu m}{year}\right] = 11.6 \cdot i \quad with\ i\ [\frac{\mu A}{cm^2}] = \frac{I\ [\mu A]}{A\ [cm^2]} \qquad \text{Eq. (2.3.1)}$$

$$G = \frac{M[g/mol]}{z[-]F[\frac{As}{mol}]} \cdot I[A] \cdot t[s] \qquad \text{Eq. (2.3.2)}$$

Due to the limited number of available data loggers, corrosion currents were monitored for 14 out of 18 specimens. The monitored specimens were selected based on the expectation of early depassivation caused either by carbonation or by chloride ingress.

2.4 Manual and Supplementary Investigations

2.4.1 Manual corrosion investigations

The microcell corrosion rate was determined by linear polarization resistance measurements during the 16th and 18th cycles. The specimens were configured as three-electrode corrosion cells, in which the electrically connected stainless-steel bars of all rebars under short-circuit conditions served as the counter electrode (surface area A = 351.86 cm²), the uncoated part of the selected carbon steel rebar served as the working electrode (surface area A = 50.27 cm²), and an Ag/AgCl electrode served as the reference electrode, as shown in Fig. 33.

Electrochemical measurements were performed using a Gamry Interface 1010 potentiostat/galvanostat/ZRA. All potentials are reported with respect to the saturated Ag/AgCl reference electrode (SSE).

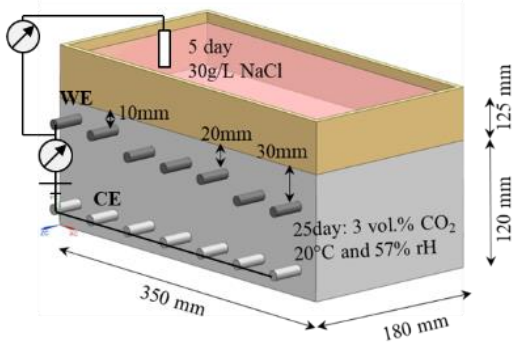

Fig. 33 *LPR measurement configuration*

The electrochemical tests consisted of a minimum stabilization period of 24 hours at open-circuit potential (OCP), followed by linear polarization resistance measurements at a scan rate of 0.1 mV/s within ±20 mV relative to the OCP. For selected specimens, electrochemical impedance spectroscopy (EIS) measurements were additionally performed over a frequency range of 0.001 Hz to 10 kHz, using a polarization amplitude of ±10 mV around the OCP with five points per decade.

The free corrosion potential (OCP) was measured during cycles 5, 12, and 17 using a silver/silver chloride reference electrode (SSE). Approximately half a day prior to the measurements, the short circuit was opened to allow depolarization of the corroding reinforcement bars. Measurements were carried out on the third day of the wetting phase and during the final week of the drying phase. The measurement setup is shown in Fig. 34.

Potential measurements were performed using a high-input-impedance voltmeter (Fluke 87V MAX, 50 GΩ input resistance).

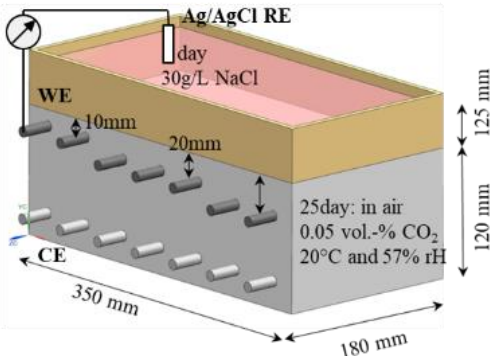

Fig. 34 *Free corrosion potential measurement.*

2.4.2 Supplementary investigations

Cubes with an edge length of 150 mm were prepared for compressive strength and density testing in accordance with SN EN 12390-3. Cylindrical specimens were used for chloride migration testing according to SIA 262/1 Annex B and EN 12390-18, as well as for capillary absorption and total porosity measurements according to SIA 262/1 Annexes A and K, respectively.

The specimens were tested in the unexposed state, as well as after full carbonation or chloride loading (30 g/L NaCl). Tab. 8 summarizes the preconditioning procedures, the number of specimens per mix, and the specimen dimensions.

Tab. 8 *Samples for pore structure, adsorption isotherm & resistivity, capillary adsorption*

Name (precondition)	Prec.1 at 20°C		Prec. 2 at 20°C		Prec. 3 at 20°C		No. of samples per mix	Sample size Ø x H
	day	type	day	type	day	type	-	mm
Ref28 (water cured)	28	water	-	-	-	-	3	50 x 50
Ref (long term water cured)	250	water	-	-	-	-	3	50 x 50
Chloride (Chloride loaded)	91	water	≥ 20	30g/L NaCl, 20V Migration	≤ 230	30g/L NaCl	5	50 x 50
Carb (carbonated)	91	water	250	57% rh, 3% CO_2	-	-	3	50 x 10

To ensure complete carbonation (condition: carb), fourth and fifth specimens of the CEM I mix (02) and the CEM II/B-M (S-T) mix (06) were used to verify the carbonation depth by indicator spraying.

To ensure maximum possible chloride loading (including both bound chlorides in hydrated samples and free chlorides), three cylindrical specimens of each mix were saturated and chloride-loaded using the steady-state chloride migration method according to SIA 262/1 Annex B (20 V, 30 g/L NaCl, 20 °C) until an increase in chloride concentration was detected in the analytical compartment (verified by ISE measurements). A fourth specimen was used to verify chloride ingress by spraying $AgNO_3$ indicator solution on the fractured cross-section.

After migration conditioning, the specimens were stored in a 30 g/L NaCl solution for three months to ensure chloride redistribution and binding.

Hydration pores, total porosity, and air pores were determined according to the protocol specified in SIA 262/1 Annex A. Porosity was calculated from the mass differences between oven-dried specimens at 110 °C (m_{110}), water-saturated specimens (m_E), and vacuum-saturated specimens (m_{TOT}). The specimen volume was determined by hydrostatic weighing using overwater (O) and underwater (U) measurements.

Equations (2.4.1), (2.4.2), and (2.4.3) describe the determination of hydration pores (φ_{hyd}), total porosity (n), and air pores (LP), respectively. Alternatively, the specimen volume can be obtained from geometric measurements. In this case, ($m_{EO} - m_{EU}$) is replaced by the measured volume multiplied by the density of water.

$$\Phi_h = \frac{(m_{Eo} - m_{110})}{(m_{EO} - m_{EU})} \quad \text{Eq. (2.4.1)}$$

$$\Phi_{tot} = \frac{(m_{TOT} - m_{110})}{(m_{EO} - m_{EU})} \quad \text{Eq. (2.4.2)}$$

$$\Phi_{air} = \phi_{tot} - \phi_h \quad \text{Eq. (2.4.3)}$$

For the determination of adsorption isotherms, the specimens were stored in a climate chamber at relative humidities of 57 %, 65 %, 75 %, 85 %, and 95 % until mass constancy was reached (weight change < 0.1 mass%/h). The mass was then recorded, and the degree of saturation (w/w_{sat}) was determined by dividing the specimen mass at a given relative humidity by the difference between the mass after vacuum saturation and that after oven drying at 105 °C, in accordance with Eq. (2.4.4).

$$w/w_{sat} = \frac{(m_{rh} - m_{105°C})}{(m_{Vac} - m_{105°C})} \quad \text{Eq. (2.4.4)}$$

The coefficient of capillary absorption was determined following the protocol specified in SIA 262/1 Annex K. After oven drying at 50 °C until mass constancy, the specimens were transferred to a desiccator and allowed to cool to room temperature. The mass was measured to the nearest 0.01 g before exposure and after 1 h, 2 h, 3 h, 5 h, and 24 h of one-sided exposure to a 3 mm water layer.

The coefficient of capillary absorption was determined by linear regression of the measured water uptake per unit front surface area as a function of the square root of time. From the slope, the capillary absorption coefficient S_c (kg/m²·h$^{0.5}$) was obtained.

Electrical resistivity was determined by two-electrode measurements (TEM). The cylindrical specimens were connected to electrodes on each end surface using conductive sponges. Electrical resistance was measured using a “GEOM” earth ground tester (Fluke). From the measured resistance R (Ω), the resistivity ρ (Ω·m) was calculated using Eq. (2.4.5), where A is the cross-sectional area (m²) and L is the specimen length (m).

Alternatively, geometric effects can be accounted for using a cell constant k (m), which depends on the measurement geometry.

$$\rho = \frac{A}{L} \cdot R = k \cdot R \quad \text{Eq. (2.4.5)}$$

In addition, two binder types - CEM II/B-LL (Mix 07) and CEM III/B (Mix 05) - were tested for their migration coefficients in different electrolytes, as summarized in Tab.9.

***Tab. 9** Additional migration tests*

Condition	Water curing [day]	Precondition	Exposure condition	Exposure duration [day]
SIA 262/1 B Chloride migration	91	24h partly in water; 5 days under water	force: 20 V T: 20°C Anolyte: 30g/l NaCl in 0.2 N KOH Catholyte: 0.2 Mol KOH	2
EN 12390-18 Similar but 20 V Chloride migration	91	24h partly in water; 5 days under water	Force: 20 V T: 20°C Anolyte: 50g/l NaCl in 0.2 N KOH () Catholyte: 0.2 N KOH	2
NT Build 492 Similar but 20 V Chloride migration	91	24h partly in water; 5 days under water but excluding vacuum saturation	Force: 20 V T: 20°C Anolyte: 100g/l NaCl in deionized water (2N Cl) Catholyte: 0.3 N NaOH	2

The chloride migration specimens (SIA 262/1 Annex B) were split, and the penetration depth was determined by spraying 0.1 % fluorescein in 70 % ethanol, followed by application of a 0.1 N silver nitrate solution, prior to oven drying. After oven drying, the depth corresponding to the color change was measured.

The color change depends, among other factors, on the w/c ratio and the $Ca(OH)_2$ content. For the 0.1 N $AgNO_3$ indicator, color change occurs when the water-soluble chloride concentration ranges between 0.01 and 0.06 wt.-% relative to concrete (0.1–0.35 wt.-% relative to cement), or when the total chloride concentration ranges between 0.025 and 0.1 wt.-% relative to concrete (0.25–0.7 wt.-% relative to cement), as reported in [165], and up to 1.45 wt.-% relative to cement according to [166]. The draft standard prEN 12390-18 indicates that the color change corresponds to a chloride concentration of 0.07 mol/L for OPC concrete.

The chloride migration coefficient was calculated using Eq. (2.4.6). In this equation, D_{Cl} (or M_{nss}) denotes the migration coefficient (10^{-12} m²/s), R is the gas constant (8,314 J/(K·mol)), T is the absolute temperature during the migration test (K), z is the ionic charge of the chloride ion (z = 1), F is Faraday's constant (96,485 J/(V·mol)), U is the applied electrical voltage (V), h is the specimen thickness (m), x_d is the depth corresponding to the color change (chloride penetration depth, m), erf^{-1} is the inverse error function, c_d is the chloride concentration at which the color change occurs (mol/L), c_0 is the chloride concentration of the catholyte solution (mol/L), and t is the test duration (s).

$$D_{Cl} = M_{nss} = \frac{RTL}{zFE\left(\frac{U}{h}\right)} \cdot \frac{x_d - 2 \cdot \sqrt{\frac{RTL}{zF\left(\frac{U}{h}\right)}} erf^{-1}\left(1-\frac{2c_d}{c_0}\right)\sqrt{x_d}}{t} \qquad \text{Eq. (2.4.6)}$$

SIA 262/1 Annex B provides a simplified formula applicable to the specific testing protocol defined therein. For all investigations conducted in accordance with SIA 262/1, this simplified formula was used, including cases in which the exposure duration was modified to ensure sufficiently large, but not excessive, chloride penetration depths.

For all other tests involving different NaCl concentrations, Eq. (2.4.6) was applied.

3 Mortar investigations

3.1 Mix design

Four of the six cements were selected to investigate corrosion initiation under decalcification conditions. The mortar was prepared using 1350 g of CEN standard sand, 450 g of cement, and 225 g of water. The specimens were produced using deuterium oxide (D_2O) instead of H_2O to enable neutron investigations.

The selected cements comply with the chemical compositions presented in Tab. 10. For each cement type, five mixes were prepared, each containing a different amount of NaCl (> 99 % purity). The NaCl contents added to the mixing water corresponded to 0, 0.4, 0.6, 1.0, and 4.0 wt.-% Cl relative to the binder mass. Specimen preparation followed EN 196-1. The mix compositions are summarized in Tab. 10.

***Tab. 10** Mortar mix*

Cement type	CEM I 42.5N	CEM II/B-LL	CEM III/B	ZN/D
w/c = D_2O/c	0.5	0.5	0.5	0.5
Cement [kg/m³]	505	501	500	501
Aggregate [kg//m³]	1514	1503	1500	1503
Max grain [mm]	2	2	2	2
NaCl [g/L]	3.3, 5.0, 8.3, 33	3.3, 5.0, 8.3, 33	3.3, 4.9, 8.2, 33	3.3, 4.9, 8.2, 33
Cl [%/cem]	0, 0.4, 0.6, 1.0, 4.0			

3.2 Artificial carbonation in 6M NH_4NO_3

For “artificial” carbonation, decalcification using a 6 M NH_4NO_3 solution was selected. In water, ammonium nitrate dissociates readily due to its high solubility (24 mol/L at 20 °C). In a basic environment, NH_4^+ is further transformed into NH_3 (gas) and H^+, as described in Eq. (3.2.1).

Ammonium nitrate reacts with hydration products such as CH, C–S–H, AFt, AFm, and CC, according to Eqs. (3.2.2–3.2.7).

$$NH_4NO_3 \leftrightarrow NH_4^+ + NO_3^- \rightarrow NH_4^+ \leftrightarrow NH_{3,gas} + H^+ \quad \text{Eq. (3.2.1)}$$

$$CH: Ca(OH)_2 + 2NH_4NO_3 \rightarrow Ca(NO_3)_2 + 2NH_{3g} + 2H_2O \quad \text{Eq. (3.2.2)}$$

$$CSH: C_xS_yH_z + 2NH_4NO_3 \rightarrow C_{x-1}S_yH_{z-2} + Ca(NO_3)_2 + 2NH_{3g} + 2H_2O \quad \text{Eq. (3.2.3)}$$

$$AFt: Ca_6Al_2(SO_4)_3(OH)_{12} \cdot 26H_2O + 12NH_4NO_3 \xrightarrow{z.B.} 3CaSO_4 + 3Ca(NO_3)_2 + 2Al(NO_3)_3 + 38H_2O + 12NH_3(\uparrow) \quad \text{Eq. (3.2.4)}$$

$$AFm: Ca_4Al_2O_6(SO_4) + 14H_2O + 12NH_4NO_3 \xrightarrow{z.B.} CaSO_4 + 3\mathrm{Ca}(NO_3)_2 + 2Al(NO_3)_3 + 20H_2O + 12NH_3(\uparrow) \quad \text{Eq. (3.2.5)}$$

$$CC: CaCO_3 + 2NH_4NO_3 \rightarrow Ca(NO_3)_2 + H_2O + 2NH_3(\uparrow) + CO_2(\uparrow) \quad \text{Eq. (3.2.6)}$$

In this simulated carbonation process, calcium reacts to form $Ca(NO_3)_2$, which diffuses into the solution instead of being bound as $CaCO_3$, resulting in increased porosity due to decalcification.

When chlorides are present, physically bound chlorides in C-(A)-S-H are expected to be gradually released during decalcification, while chemically bound chlorides are released through the decomposition of Friedel’s salt, for example, according to Eq. (3.2.8).

$$Friedel`s: Ca_2Al(OH)_6(Cl, OH) \cdot 2H_2O + 7NH_4NO_3 \rightarrow 2Ca(NO_3)_2 + Al(NO_3)_3 + 9H_2O + 7NH_3(\uparrow) \quad \text{Eq. (3.2.7)}$$

3.3 Samples and investigation

Cylindrical specimens with a diameter of 43 mm were prepared and exposed to a 6 M NH_4NO_3 solution for chloride monitoring and deterioration measurements, as shown in Fig. 35 (left and right). Fig. 35 (right) also illustrates the measurement of Cl^- concentration and pH using ion-selective electrodes (ISE).

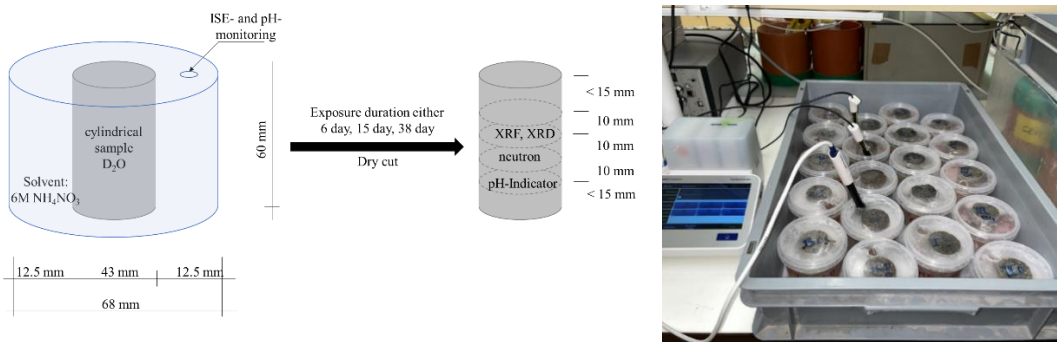

Fig. 35 *In 6M NH_4NO_3 exposed samples measurement scheme (left) and photo of the sample exposure and monitoring (right).*

In addition to the cylindrical specimens, a series of prismatic specimens was prepared to determine compressive strength, density, and initial water-soluble chloride contents of the reference samples. Tab. 11 summarizes the prepared specimen types (geometries), their preconditioning procedures and durations, as well as the exposure types and durations. Furthermore, the investigations performed on each specimen type are listed.

Tab. 11 *Samples, curing, exposure and investigations*

Sample	Curing type	Curing duration	Exposure	Exposure duration	Investigation
Prisms length x width x height = 40 x 40 x 160 mm	Cling film at 97% RH and 20±2°C	40 & 91 day	SN EN 12390-3		Compressive strength, raw density
Cylinder Ø 43 mm h = 45 mm	Cling film at 97% RH and 20±2°C	91 day	6M NH_4NO_3	6, 15, 38 day	Phenolphthalein Indicator depth, Neutron image (PSI), μXRF, μXRD (PSI)
Solvent	-	-	6M NH_4NO_3	0-38 day	Cl-concentration* (ISE Mettler Toledo) pH** (pH-Electrode Mettler Toledo)

3.4 Neutron Imaging

The aim of neutron radiography (NR) was to investigate the depth-dependent dissolution of hydrous phases during leaching in saturated ammonium nitrate solution. Leaching occurs as a reactive transport process in which water containing ammonium nitrate diffuses into the D_2O-filled pore space and reacts with D_2O-bound hydrous phases.

Because different hydrogen isotopes exhibit different neutron attenuation properties—hydrogen (H) shows high attenuation and therefore appears dark in NR images, whereas deuterium (D) shows low attenuation and appears bright - it is possible to distinguish between D_2O and H_2O in NR images.

During NR measurements, the neutron flux passes through the 10 mm thick mortar specimen and reaches a sensitive detector. Due to radiation attenuation while passing through the specimen, the detector records a projection of the object averaged over its

thickness. This attenuation results from the interaction of neutrons with the nuclei of atoms within the material.

The attenuation of the incident neutron radiation intensity I_0 by a material of thickness t is described by the transmitted intensity I after passage through the specimen, following the Beer–Lambert law (Eq. 3.4.1). In this formulation, the sum in the exponential term accounts for all isotopes present in the sample.

$$\frac{I}{I_0} = e^{-kt} \quad with \quad k = \sum \frac{n\sigma_i}{V} \qquad or \qquad k = \sum \left[g\left(\frac{\mu}{\rho}\right) \right] \qquad \text{Eq. (3.4.1)}$$

Herein, I_0 denotes the intensity of the incident radiation, I the intensity of the transmitted beam, k the attenuation coefficient, t the specimen thickness (cm), V the volume, n the number of atoms of a given type with total microscopic cross section σ_t, and g the mass fraction of the atom with mass attenuation coefficient μ/σ.

For each neutron image, 20 projections and 20 black-body projections were acquired. In addition, five black-beam (closed-field) images with all beamline shutters closed, five open-beam images, and 20 open-beam black-body images were recorded.

Image processing was performed using the software ImageJ and included the following steps: generation of averaged projection and reference image stacks, removal of bright spots using a median filter (3-pixel kernel, 15 % threshold), normalization with respect to open- and closed-beam images to correct for background noise according to Eq. (3.4.2), minimization of background scattering effects using a constant value estimated from the mean greyscale intensity behind boron-rich material in the black-body images, selection of regions of interest (ROI), and calculation of greyscale values.

$$I_{corrected} = \frac{I_{projection} - I_{dark\ field}}{I_{flat\ field} - I_{dark\ field}} \qquad \text{Eq. (3.4.2)}$$

Herein, $I_{corrected}$ denotes the corrected radiation intensity of the leached or reference specimen, $I_{projection}$ the intensity of the projection image of the leached or reference specimen, $I_{dark\ field}$ the intensity recorded in closed-beam images, and $I_{flat\ field}$ the intensity recorded in open-beam images.

From each image, a region of interest (ROI) or a line of interest (LoI) can be selected, as shown in Fig. 36 (a) and (b), respectively. Within the ROI or LoI, the greyscale profile is determined, as illustrated below the neutron images.

The thinner the ROI, the larger the scatter of greyscale values. However, thinner ROIs also lead to increased uncertainty at the specimen edges due to the radial geometry of the samples. In the present investigations, an ROI thickness of 5 mm was selected, as shown in Fig. 36 (a).

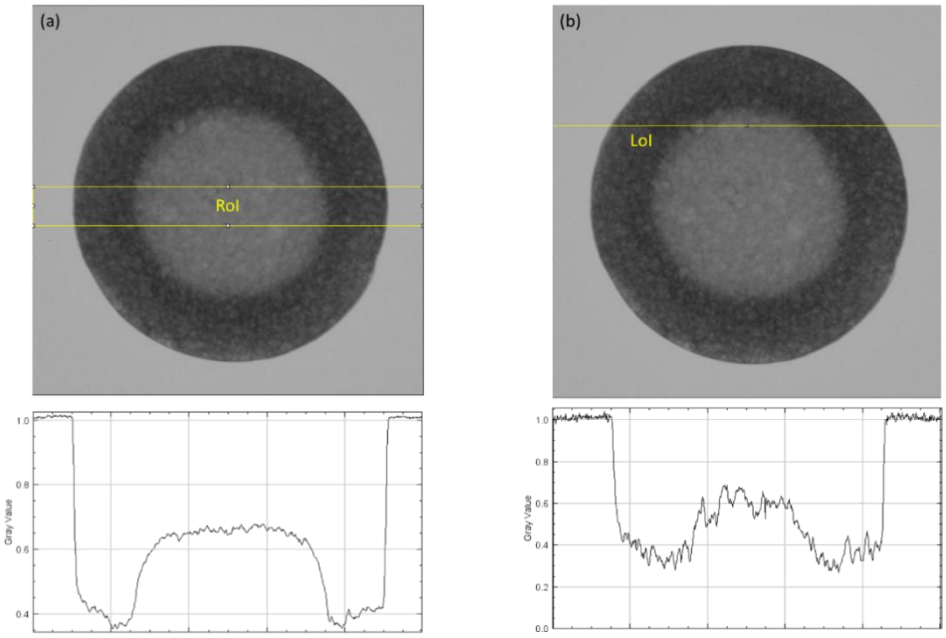

Fig. 36 *(a) Region of Interest (RoI) for average grey value analyses of all investigated samples and (b) Line of Interest (LoI) for interesting spots.*

For comparison Fig. 37 shows the greyscale values of different elements (a) and their visualization in different shades of grey for different isotopes (b).

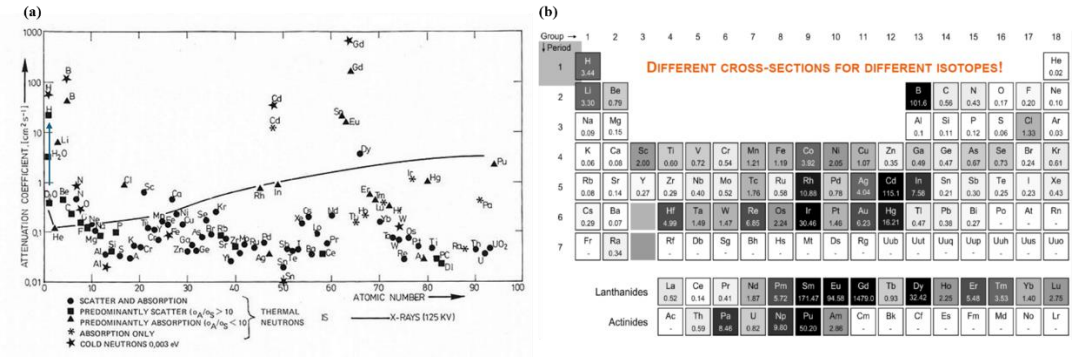

Fig. 37 *Attenuation by specific elements (a) shown through the different results in grey values (b).*

3.5 Corrosion investigation

For monitoring corrosion onset, reinforced specimens were prepared as shown in Fig. 38. A centrally positioned hot-rolled ribbed carbon steel bar B500B (material number 1.0439) with a diameter of 12 mm was used as the working electrode (rebar).

The rebar surface exposed to the solution and the rebar ends were coated with one layer of Portland cement paste followed by two layers of epoxy. The mortar cover thickness was 15.5 mm.

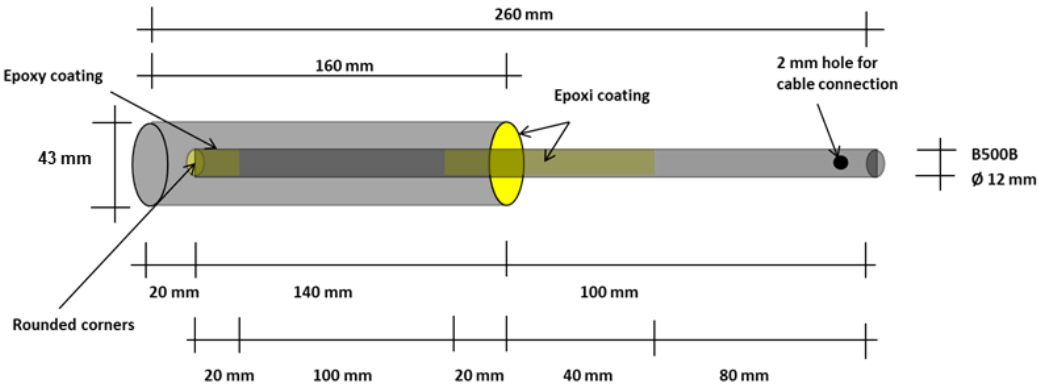

Fig. 38 *Lollipop sample geometry and coating.*

The specimens were stored in a 6 M NH_4NO_3 solution in parallel with the non-reinforced specimens. Each cement type and chloride content was stored in a separate container.

The free corrosion potential (OCP) was measured against a saturated silver/silver chloride reference electrode. The macrocell current was measured using an L-shaped counter electrode made of stainless steel (material number 1.4404). The anode (exposed rebar) to cathode (exposed counter electrode) area ratio was approximately 1:8.

The free corrosion potential and the short-circuit current (macrocell current) were measured manually using a high-resistance ammeter. The corrosion rate was calculated from the macrocell corrosion current density using Faraday's law, taking the total uncoated rebar surface area into account.

3.6 Thermodynamic modelling

Thermodynamic modelling was carried out using the Gibbs free energy minimization software GEMS 3.3, which calculates equilibrium phase assemblages in chemical systems based on their bulk elemental composition. The default databases were extended with the CEMDATA18 database [167-168], which includes solubility products of solids relevant to cementitious materials. For the C–S–H phase, the CSHQ model proposed by [169-171] was applied. Full hydration was assumed in all calculations.

Changes in phase assemblages upon exposure to a 6 M NH_4NO_3 solution were modelled by incrementally adding fractions of the solvent consisting of 1000 g deionized water and 480 g NH_4NO_3. Activity coefficients were calculated using the extended Debye-Hückel equation.

All calculations were performed for systems containing 100 g cement, 50 g deionized water, and 0.1 g O_2, with NaCl contents of either 0 g, 0.7 g (0.4 wt.-% Cl), 1.0 g (0.6 wt.-% Cl), 1.6 g (1.0 wt.-% Cl), or 6.6 g (4.0 wt.-% Cl).

4 Concrete results

4.1 Fresh concrete properties

Tab. 12 summarizes the fresh concrete properties determined during mixing. Fresh concrete density, air content, slump, and consistency were within the expected ranges for all concrete mixes.

***Tab. 12** Fresh concrete properties*

Property [Unit]	CEM I 42.5N	CRCF* (ZN/D 42.5N)	CEM II/B-M (T-LL)	05: CEM III/B	06: CEM II/B-M (S-T)	07: CEM I + 33%LS
Temperature [°C]	20	22.8	22	23.2	22.1	22.1
Raw density SN EN 12350-6 [kg/m^3]	2390	2370	2410	2390	2390	2360
Fresh concrete air SN EN 12350-7 [%]	2.1	2.0	1.4	1.4	0.9	1.7
Slump (flow table) SB EB 12350-5 [mm]	420	420	430	490	470	420
Flow table spread after 45 min [mm]	350	350	390	380	350	350
Consistency class [-]	F2	F2	F2	F3	F2	F2

* Cement with recycles concrete fines and oil shale

4.2 Compressive strength

Tab. 13 summarizes the measured compressive strength according to SN EN 12390-3.

Tab. 13 Compressive strength

Cement type	CEM I	CRCF	CEM II/B-M(T-LL)	CEM III/B	CEM II/B-M(S-T)	CEM I + 33%LS
28-day compressive strength f_{c28} [MPa]	57.3	46.7	52.1	49.5	61.9	37.9
56-day compressive strength f_{c56} [MPa]	61.4	49.9	56.2	55.4	66.5	40.7
91-day compressive strength f_{c91} [MPa]	63.3	50.9	58.4	56.7	68.0	42.8

Fig. 39 (a) compares the development of compressive strength over time, while Fig. 39 (b) shows the increase in compressive strength relative to the 28-day compressive strength, expressed as $r = f_{cx}/f_{c28}$. Where f_{cx} is the compressive strength at age x (days).

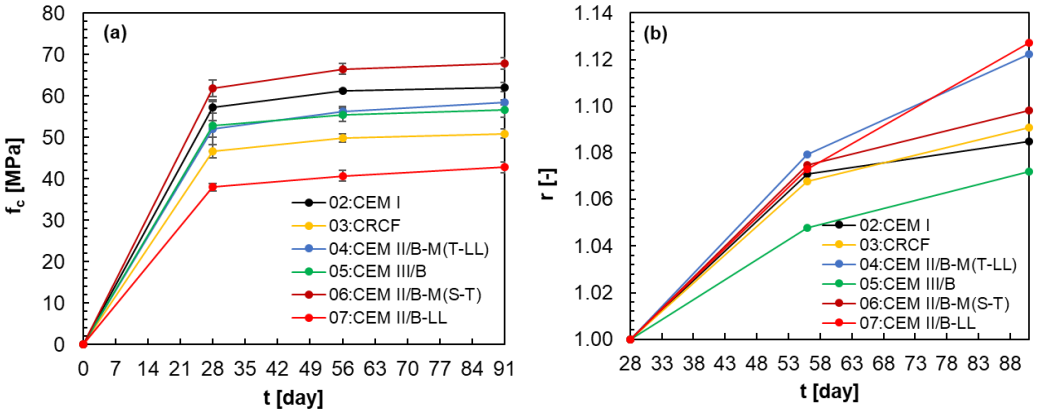

***Fig. 39** Time-dependent development of compressive strength: (a) absolute values and (b) increase relative to the 28-day compressive strength.*

The highest compressive strength was observed for CEM II/B-M (S-T) 42.5R concretes, while the lowest was found for CEM II/B-LL 32.5N. As expected, the compressive strength of CEM III/B 32.5N was significantly higher than that of CEM II/B-LL with the same cement strength class.

The addition of limestone or recycled concrete fines in CEM II/B-M (T-LL) and CRCF, respectively, resulted in slightly lower compressive strengths compared to CEM I with the same cement strength class. However, an unexpected increase in cement strength was observed for CEM II/B-M (T-LL) and CEM II/B-LL.

4.3 Raw density

Tab. 14 summarizes the density determined in accordance with SN EN 12390-3.

Tab. 14 Raw density

Cement type	02	03	04	05	06	07
28-day raw density ρ_{28} [kg/m³]	2403	2373	2410	2367	2407	2360
56-day raw density ρ_{56} [kg/m³]	2400	2380	2410	2353	2407	2380
91-day raw density ρ_{91} [kg/m³]	2400	2383	2410	2360	2403	2380

Fig. 40 shows (a) the fresh concrete density of each concrete type after 28, 56, and 91 days of curing, and (b) the relationship between chloride contents expressed in wt.-% relative to concrete and wt.-% relative to cement.

In the subsequent investigations, chloride contents are reported with respect to the concrete mass. Using the relationship shown in Fig. 40 (b), these values can be converted to chloride contents relative to the cement mass.

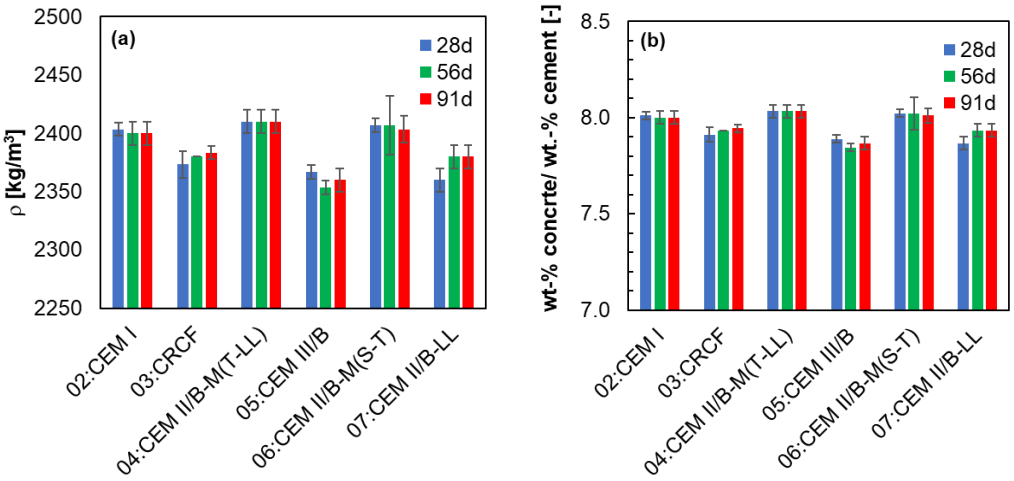

***Fig. 40** Raw density (a) and ratio of concrete versus cement (b).*

The density of all concretes ranged between 2350 and 2400 kg/m³, which is within the expected and comparable range. Slightly lower densities were observed for CRCF, CEM II/B-M (T-LL), and CEM II/B-LL concretes.

Accordingly, the mass of concrete was approximately eight times the mass of cement and about 7.9 times for concretes containing limestone or recycled concrete fines in the present investigations.

4.4 Carbonation

4.4.1 Carbonation depth and rates

Fig. 41 shows photographs of the Wf specimens after indicator spraying. Regardless of the binder type, the carbonation depth increases from Wf-Cl to Wf-Cl-CO_2 and further to Wf-CO_2.

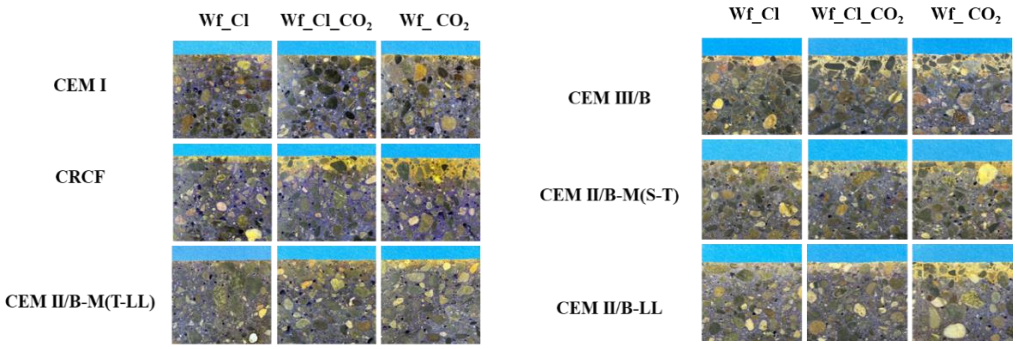

Fig. 41 *Carbonation depth of Wf samples.*

Fig. 42 It shows the development of carbonation depth over time for all specimens, including standard conditions, reference conditions, and cyclic wet–dry exposure.

The investigated exposure regimes were as follows:

- Wf-Cl: cyclic wetting and drying with sodium chloride solution under natural CO_2 concentration;
- Wf-Cl-CO_2: cyclic wetting and drying with sodium chloride solution at 3 % CO_2;
- Wf-CO_2: cyclic wetting and drying at 3 % CO_2;
- R0-CO_2 (R-CO_2): exposure at 3 % CO_2 and 57 % relative humidity;
- EN 12390-12: exposure at 3 % CO_2 and 57 % relative humidity after 28 days of curing;
- SIA 262/1: exposure at 4 % CO_2 and 57 % relative humidity after 3 days of curing.

Regression analysis was performed in accordance with ISO 16204. In this analysis, the slope of the regression corresponds to the product k·W.

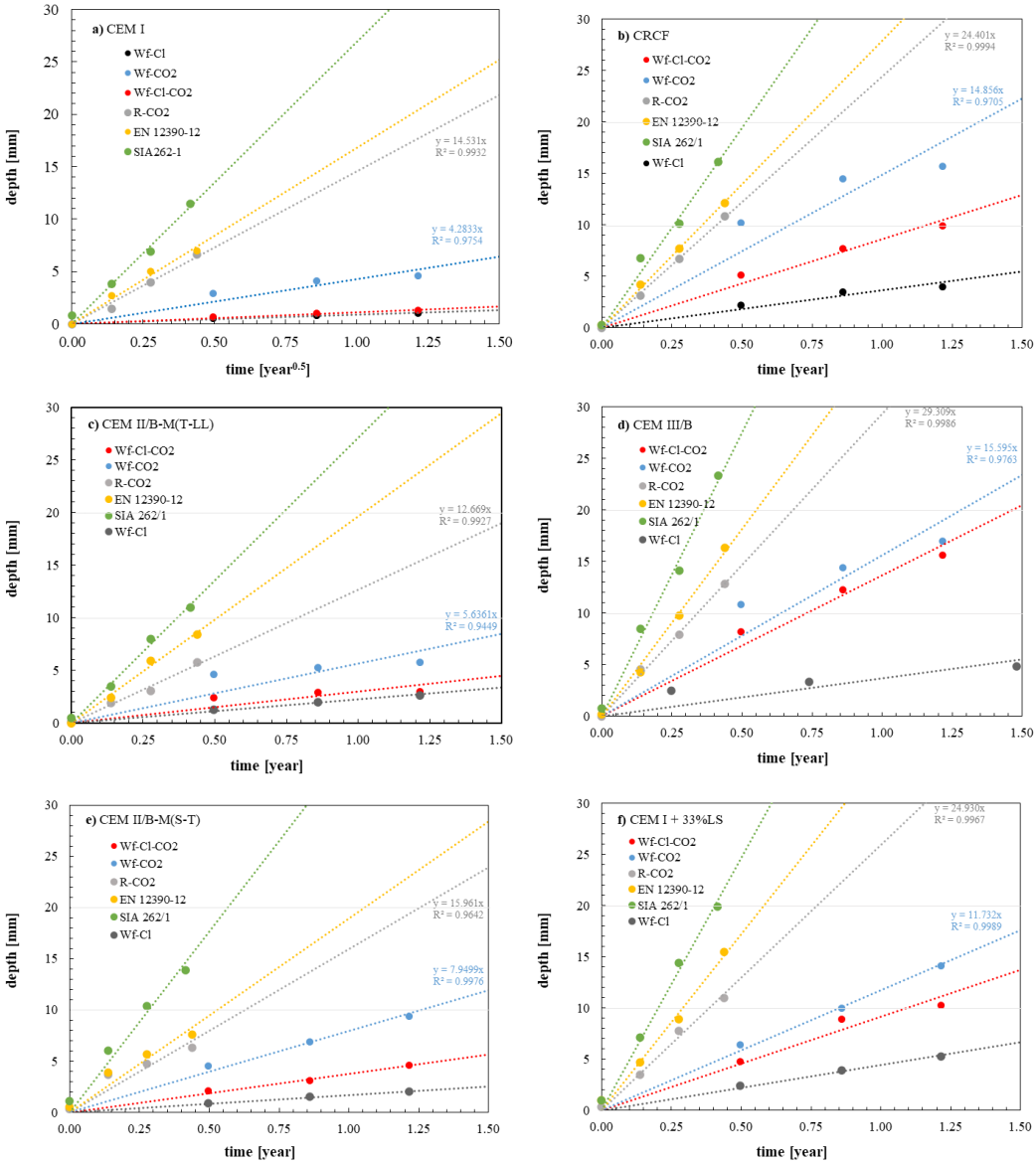

Fig. 42 *Carbonation depth as a function of exposure time for each binder type and test condition: (a) CEM I, (b) CRCF, (c) CEM II/B-M (T-LL) with an unintended additional 15 days of water exposure under Wf-CO_2 and Wf-Cl-CO_2 conditions, (d) CEM III/B, (e) CEM II/B-M (S-T), and (f) CEM I + 33 % LS.*

The carbonation depth increases from Wf-Cl to Wf-Cl-CO_2 and further to Wf-CO_2, followed by R0-CO_2 and EN 12390-11, and finally SIA 262/1. The largest carbonation depths were observed for specimens tested according to SIA 262/1, owing to both the higher CO_2 concentration and the shorter curing period compared to EN 12390-11 and R-CO_2, as well as the constant moderate humidity conditions compared to Wf exposures.

Carbonation depths determined according to EN 12390-11 were generally higher than those determined under R-CO_2 conditions.

Under constant exposure conditions, linear regression following the square-root-of-time law through the origin is commonly applied, as is conventional linear regression. However, linear regression generally provides slightly higher coefficients of determination. Moreover, linear regression is typically less conservative than regression through the origin.

For carbonation under cyclic conditions, the extended curing period of 91 days was considered sufficient to comply with ISO 16204 and to derive parameters comparable to those used for chloride ingress. Although the coefficients of determination appear acceptable, it should be noted that models using a time exponent b provide improved goodness of fit and less conservative long-term predictions.

Tab. 15 summarizes the carbonation rates determined under constant exposure conditions according to SIA 262/1 Annex B (linear regression, Model 3, and regression forced through the origin, Model 2), SN EN 12390-11 (regression forced through the origin, Model 2), and R-CO_2 (regression forced through the origin, Model 2).

The accelerated carbonation rates k_{AC} were converted to natural carbonation rates at 0.04 vol.-% CO_2. Conversion factors of 1.36 for 4 % CO_2 and 1.28 for 3 % CO_2 were applied.

***Tab. 15** Carbonation rates, constant exposure conditions*

Test type	**SIA 262**	**SIA 262/1-I**	**SN EN 12390-12**		**R0-CO_2**
CO_2	0.04%CO_2	0.04%CO_2	3%CO_2	0.04%CO_2	3%CO_2
Regression type	through origin (Model 2)	linear regression (Model 3)	through origin (Model 2)	through origin (Model 2)	through origin (Model 2)
Parameter	k_{NA} [mm/year$^{0.5}$]	k_N [mm/year$^{0.5}$]	k_{AC} [mm/year$^{0.5}$]	k_{NA} [mm/year$^{0.5}$]	k_{AC} [mm/year$^{0.5}$]
CEM I	1.4	3.5	16.8	2.5	14.5
CRCF	2.0	5.0	27.9	4.1	24.4
CEM II/B-M(T-LL)	1.4	3.5	19.6	2.9	12.7
CEM III/B	2.9	7.2	36.3	5.4	29.3
CEM II/B-M(S-T)	1.8	4.2	18.9	2.8	16.0
CEM I + 33%LS	2.6	6.3	32.9	4.9	26.0

Tab. 16 summarizes the carbonation rates determined under cyclic exposure conditions using the conservative linear regression forced through the origin in accordance with ISO 16402 (Model 2) and a potential function regression with time exponent b. The former yields lower predicted carbonation depths at early ages (less than one year) but higher depths for exposure periods exceeding one year.

***Tab. 16** Carbonation progress parameter, cyclic exposure conditions, accelerated rates with 3% CO_2 (k_{AC})*

Test type	**Wf-CO_2**			**Wf-Cl-CO_2**		
Regression	Linear origin (Model 2)	With time exponent (Model 1)		Linear origin (Model 2)	With time exponent (Model 1)	
Parameter	k_{AC} [mm/year$^{0.5}$]	k_{AC} [mm/year$^{0.5}$]	b [-]	k_{AC} [mm/year$^{0.5}$]	k_{AC} [mm/year$^{0.5}$]	b [-]
CEM I	4.3	4.5	0.22	1.1	1.2	0.32
CRCF	14.9	15.5	0.26	8.6	9.3	0.31
CEM II/B-M(T-LL)	5.6	5.8	0.12	3.0	3.0	0.11
CEM III/B	15.6	16.3	0.21	13.6	14.6	0.30
CEM II/B-M(S-T)	7.9	8.6	0.34	3.8	3.6	0.33
CEM I + 33%LS	11.7	12.9	0.49	9.2	11.0	0.45

4.4.2 Correlation with natural conditions (Model 2 & 3)

In general, the natural carbonation rates k_n determined according to SIA 262/1 Annex I (Model 3) are comparable to carbonation rates measured for specimens exposed under sheltered conditions in Switzerland, as reported in [5,6]. Accordingly, k_n determined according to SIA 262/1 Annex I can be considered representative of carbonation rates under sheltered conditions.

Fig. 43 (a) compares the natural carbonation rates under sheltered conditions (equivalent to k_n according to SIA 262/1) with the accelerated carbonation rates determined under the reference condition R0-CO_2 (Model 2) at elevated CO_2 concentration (3 % CO_2). The accelerated R0-CO_2 exposure resulted in carbonation rates approximately four times higher than those expected under natural sheltered conditions ($k_{AC,R0\text{-}CO_2} \approx 4.16 \cdot k_n$).

The carbonation rates under artificial unsheltered (cyclic) conditions in this study were compared with carbonation rates determined under natural unsheltered conditions reported in [6] (Model 2). To estimate natural carbonation rates, the carbonation rates obtained under unsheltered laboratory conditions (Wf-CO_2) were divided by a factor of 4.16, as shown in Fig. 43 (b).

In [6], similar water-to-cement ratios and cement contents were used as in the present study. In two cases, the same cement from the same production plant was used. In two additional cases, cements from the same plant with comparable w/CaO ratios but different cement types were applied. These four concretes were compared with the present experimental results.

Both investigations show comparable carbonation rates determined using Model 2 (cf. Fig. 43 (b)).

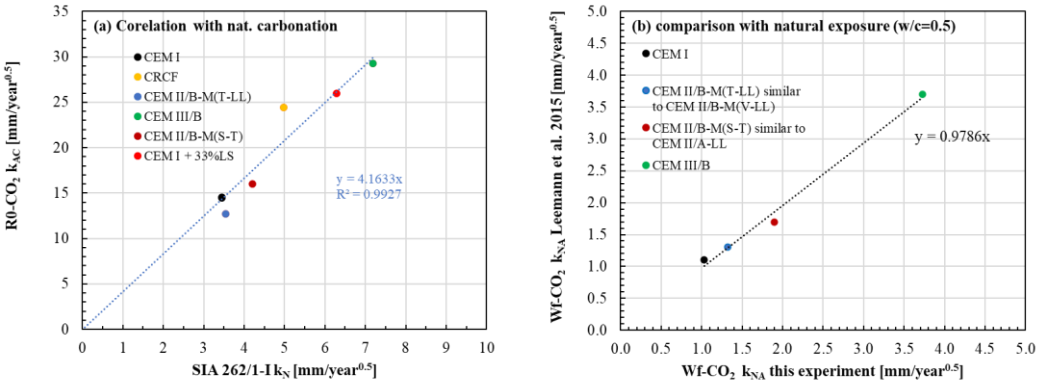

Fig. 43 *Comparison of carbonation rates: (a) k_{NA} according to SIA 262/1 and R0-CO_2, and (b) $k_{NA,Wf\text{-}CO_2}$ (= $k_{AC,Wf\text{-}CO_2}$ / 4.16) compared with exposure test data from [6] with similar w/c ratios, using carbonation rates determined by Model 2.*

Based on Fig. 43, natural carbonation rates can be derived from the accelerated tests conducted in this study by applying an acceleration factor of 4.16 to convert accelerated carbonation rates to natural carbonation rates for the R0-CO_2, Wf-CO_2, and Wf-Cl-CO_2 conditions, as summarized in Tab. 15 and Tab. 16.

The resulting natural carbonation rates are presented in Tab. 17. It should be noted that, for the same exposure duration, [13] proposes carbonation rates that are approximately 1.2 times higher for structural elements exposed vertically to rain. These values are indicated in brackets.

Tab. 17 *Carbonation rates and parameter cyclic exposure conditions, natural rates (k_{NA}) Model 2*

Test type	**R0-CO_2**	**Wf-CO_2**	**Wf-Cl-CO_2**
Parameter	k_{NA} [mm/year$^{0.5}$]	k_{NA} [mm/year$^{0.5}$]	k_{NA} [mm/year$^{0.5}$]
CEM I	3.5	1.0 (1.2)	0.3 (0.4)
CRCF	5.9	3.5 (4,2)	2.1 (2.5)
CEM II/B-M(T-LL)	3.1	1.3 (1.6)	0.7 (0.8)
CEM III/B	7.0	3.7 (4.4)	3.3 (4.0)
CEM II/B-M(S-T)	3.8	1.9 (2.3)	0.9 (1.1)
CEM I + 33%LS	6.3	2.8 (3.4)	2.2 (2.6)

4.4.3 Correlations between standardized test conditions

Fig. **44** (a) compares the natural carbonation rate k_n determined according to SIA 262/1-I (Model 3) with the accelerated carbonation rate k_{AC} determined according to EN 12390-12 (Model 2). Fig. **44** (b) illustrates the influence of prolonged curing from 28 days (EN 12390-12) to 91 days (R0-CO_2, Model 2) on the carbonation rate.

The test conditions in Fig. 44 (b) were identical and followed EN 12390-12, with curing duration being the only variable.

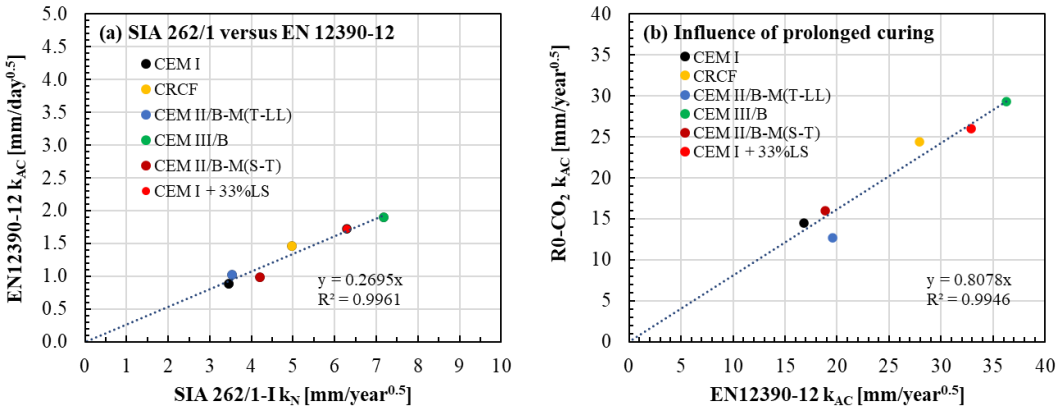

Fig. 44 *Correlation between k_N according to SIA 262/1-I and k_{AC} according to EN 12390-12 (a), and the effect of curing for 91 days instead of 28 days on carbonation progress under EN 12390-12 conditions (b).*

According to Fig. 44 (a), the carbonation rate determined according to EN 12390-12 (mm/day$^{0.5}$, regression forced through the origin) is, on average, 0.27 times the value of k_N determined according to SIA 262/1 Annex I.

The extended curing period of 91 days instead of 28 days resulted in carbonation rates that were approximately 0.81 times lower. No significant differences were observed for slowly reacting concretes.

4.4.4 Correlations between different exposure conditions (Model 2)

Fig. 45 illustrates (a) the influence of cyclic wetting and drying on the carbonation rate and (b) the effect of chlorides on the carbonation rate. In both figures, the carbonation rate determined according to ISO 16204 (linear regression forced through the origin, Model 2) is shown.

The natural carbonation rate was obtained by dividing the accelerated carbonation rate by a factor of 4.16.

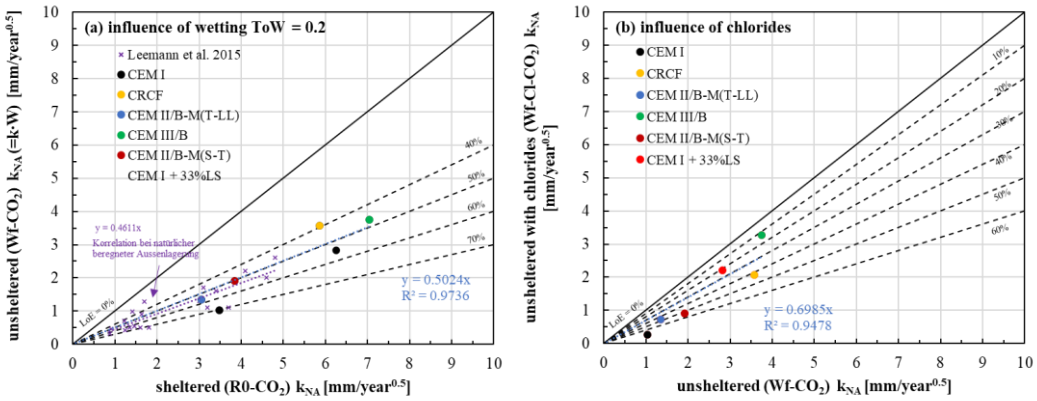

Fig. 45 *Comparison of carbonation rates: (a) sheltered and unsheltered conditions (R0-CO_2 and Wf-CO_2) together with data from real exposure tests reported by Leemann et al. (2015), and (b) unsheltered conditions without and with simultaneous chloride ingress (Wf-CO_2 and Wf-Cl-CO_2).*

For the Wf experiments, a time of wetness (ToW) of 0.2 was selected. This value corresponds well to average conditions in Switzerland for horizontal structural elements [13,172].

As shown in Fig. 44 (a), the carbonation rate under cyclic wetting and drying conditions (Wf-CO_2) is approximately half that observed under sheltered conditions (R0-CO_2). These results are in good agreement with exposure test data reported in [6] for specimens in Dübendorf, Switzerland.

According to Fig. 44 (b), the carbonation rate is further reduced by approximately 30 % when simultaneous chloride ingress occurs (Wf-Cl-CO_2). For binders in which a denser pore structure is expected to form upon carbonation, such as CEM I, this deceleration is more pronounced than for concretes exhibiting a less dense pore structure after carbonation, such as CEM III/B.

4.4.5 Correlation between different exposure conditions (Model 1)

Fig. 46 compares the natural carbonation rates determined under constant sheltered conditions (R0-CO_2, Model 2 by definition) without chloride exposure (Wf-CO_2) with the time-dependent carbonation behaviour determined under Wf-Cl-CO_2 conditions using a time exponent (Wf: Model 1).

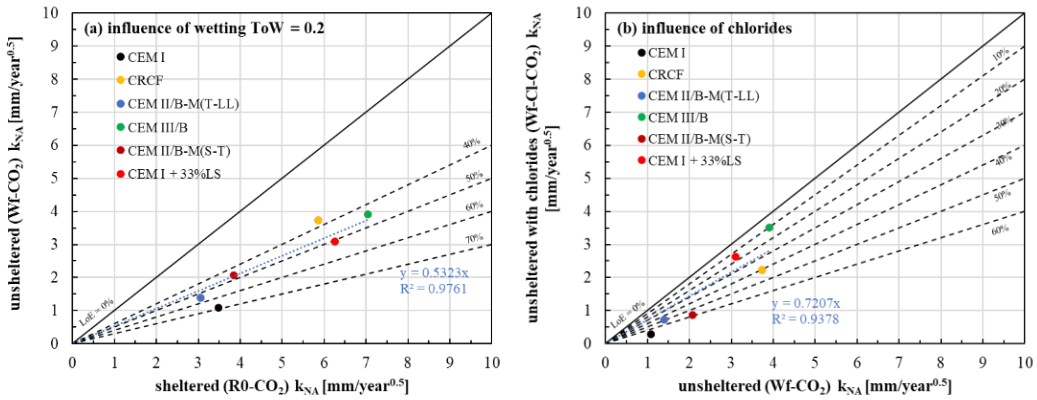

Fig. 46 *Correlation between time exponent in R0-CO_2 and Wf-CO_2 (a) or Wf-CO_2 and Wf-Cl-CO_2 (b) condition.*

The deceleration from sheltered reference conditions (R0-CO_2) to unsheltered conditions (Wf-CO_2), and further to unsheltered conditions with chlorides (Wf-Cl-CO_2), is slightly less pronounced to similar when using Model 1 with a time exponent at an exposure age of one year.

Fig. 47 compares the time exponent determined under unsheltered conditions without chlorides (Wf-CO_2) with that determined under Wf-Cl-CO_2 conditions.

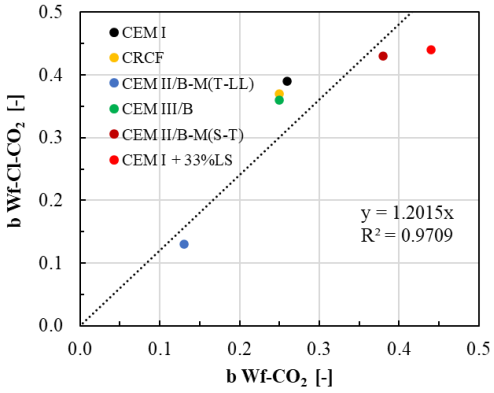

Fig. 47 *Correlation between the time exponent under Wf-CO_2 and Wf-Cl-CO_2 condition.*

In these experiments, the time exponent generally ranged between 0.25 and 0.45. The combination of similar carbonation rates and lower time exponents results in less conservative predictions of carbonation depth for long-term exposure (50 years) when using Model 1 with a time exponent. In contrast, predictions based on Model 2 lead to higher estimated carbonation depths and can therefore be considered conservative.

The time exponent was higher under unsheltered conditions in the presence of chlorides (Wf-Cl-CO_2), which is somewhat unexpected. Due to the higher degree of saturation in salt-contaminated specimens, a lower time exponent would be anticipated under Wf-Cl-CO_2 conditions compared to Wf-CO_2 conditions.

One possible explanation is that the smaller convection zone in salt-contaminated specimens, resulting from their higher degree of saturation, leads to reduced carbonation rates and depths but has a smaller influence on the square-root-of-time behaviour than the more pronounced convection zone observed in solely carbonated specimens under cyclic wetting and drying conditions.

4.4.6 Correlation with w/CaO

Fig. 48 comparison of carbonation rates as a function of w/CaO_r according to (a) SIA 262/1 (Model 3), (b) EN 12390-12 (Model 2), (c) R-CO_2 (Model 2), (d) Wf-CO_2 (Model 2), and (e) Wf-Cl-CO_2 (Model 2).

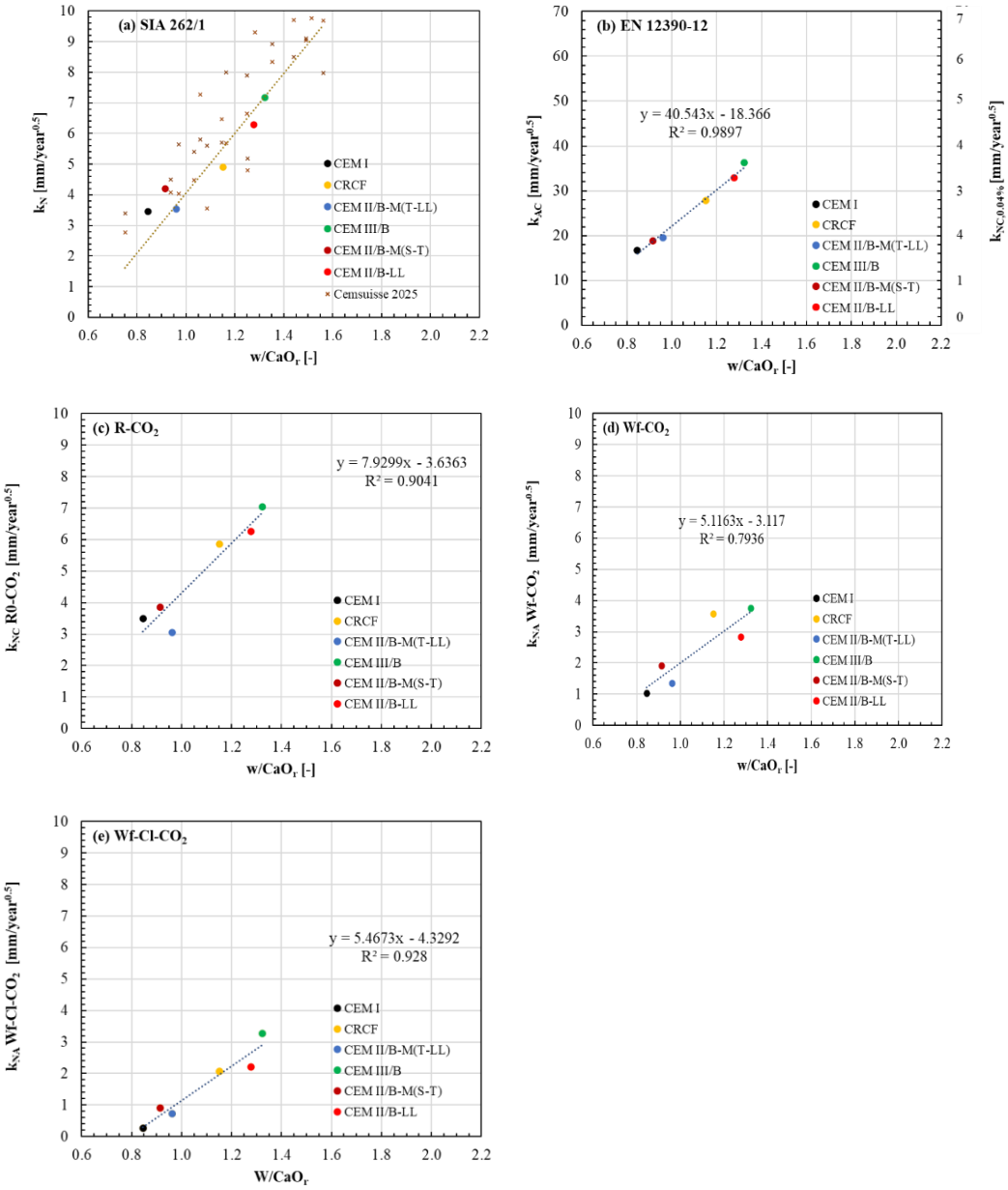

Fig. 48 *Carbonation rate as a function of w/CaO_r under different exposure conditions.*

The correlation between the carbonation rate determined according to SIA 262/1 Annex I and w/CaO_r is consistent with the results reported in [6]. Furthermore, similar and reasonable correlations with w/CaO_r were observed for EN 12390-12, R0-CO_2, Wf-CO_2, and Wf-Cl-CO_2 conditions.

Fig. 49 compares the time exponents under Wf-CO_2 (a) and Wf-Cl-CO_2 (b) conditions as a function of w/CaO_r.

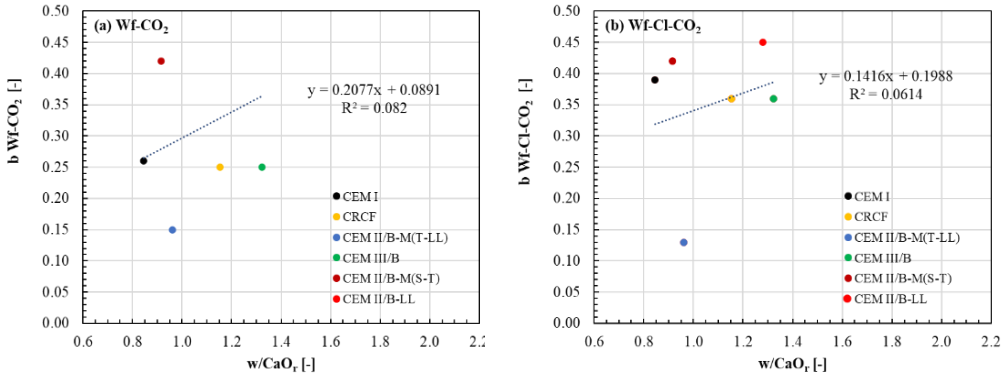

Fig. 49 *Time exponent as a function of w/CaO_r under different exposure conditions.*

The correlation between w/CaO_r and the time exponent is weak. This confirms that diffusion is the dominant factor governing carbonation progress over time. The main reasons for the decrease in carbonation rate with increasing exposure time are related to the pore structure of the concrete, the depth of the influential zone, and the frequency of moisture fluctuations.

4.4.7 Change in pore solution composition

For the Wf-CO_2 specimens, pH and Ca profiles were measured in addition to carbonation depth using ion-selective electrodes (ISE). The results are shown in Fig. 50 for (a1) CEM I, (c1) CEM II/B-M (T-LL), (d1) CEM III/B, (e1) CEM II/B-M (S-T), and (f1) CEM I + 33 % LS.

Fig. 50 (right) presents the thermodynamically calculated concentrations as a function of added CO_2, obtained using the GEMS software. It should be noted that the right-hand side of the calculated profiles corresponds to the exposed surface of the mortar specimens.

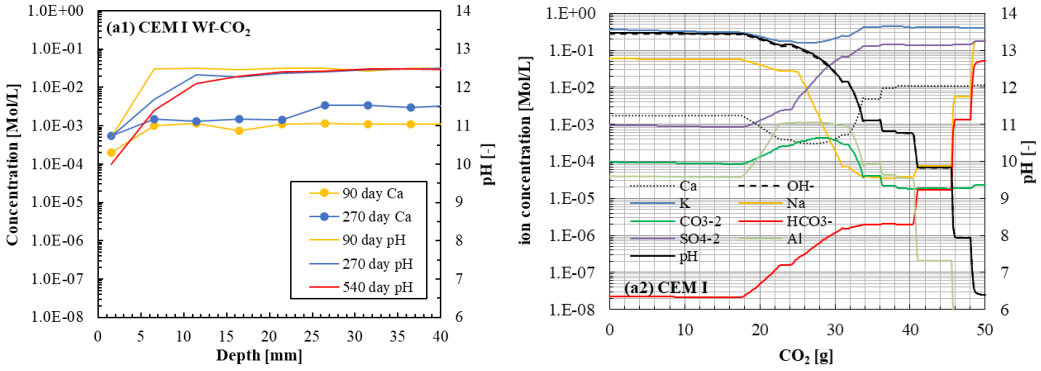

Fig. 50 *pH and Ca profiles determined by ISE (left) after 90, 270, and 540 days under Wf-CO_2 conditions, and (right) obtained from thermodynamic modelling with incremental addition of up to 40 g CO_2 for (a) CEM I, (b) CRCF, (c) CEM II/B-M (T-LL), (d) CEM III/B, (e) CEM II/B-M (S-T), and (f) CEM I + 33 % LS.*

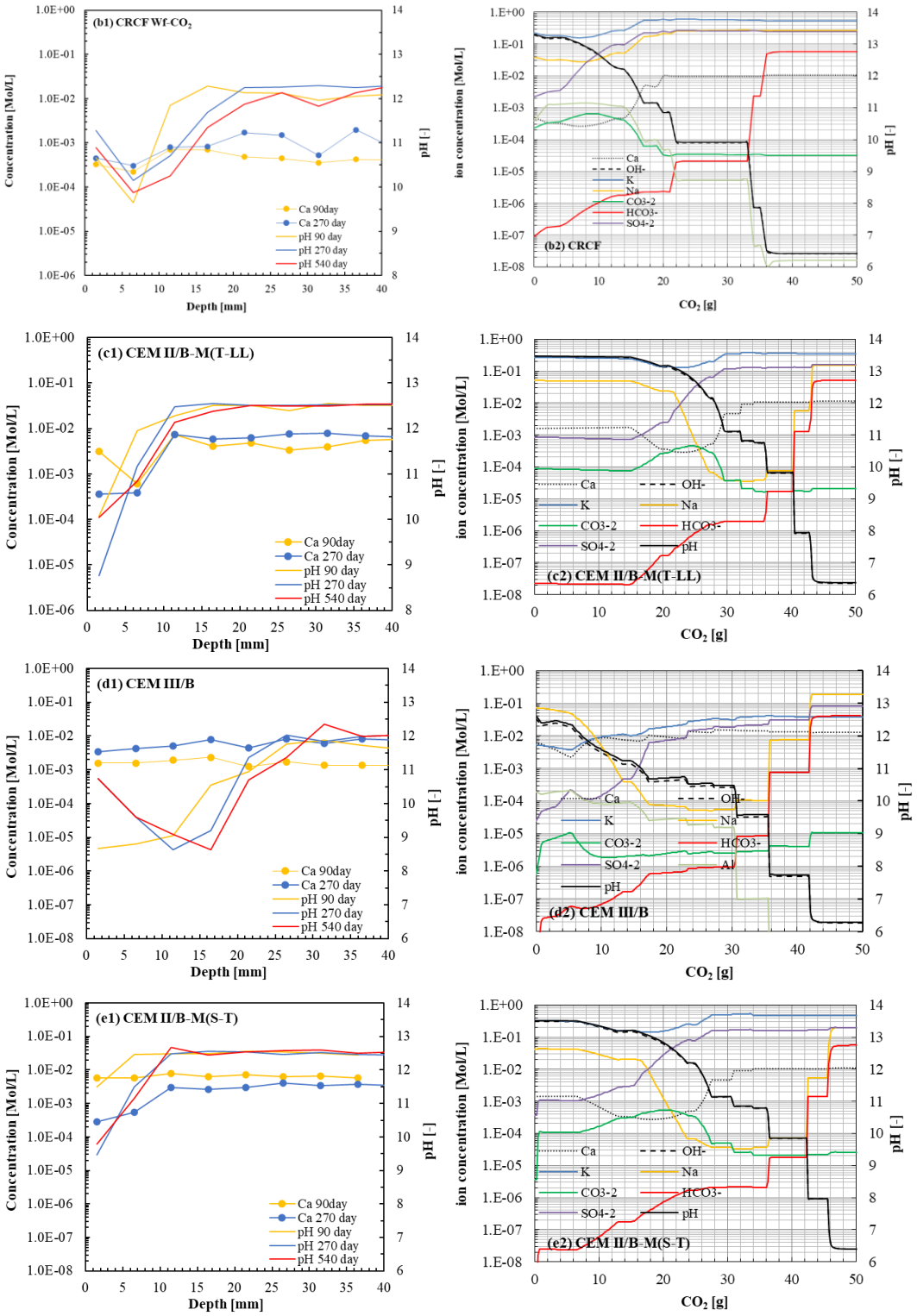

Follow up Fig. 50 *pH and Ca profiles determined by ISE (left) after 90, 270, and 540 days under Wf-CO_2 conditions, and (right) obtained from thermodynamic modelling with incremental addition of up to 40 g CO_2 for (a) CEM I, (b) CRCF, (c) CEM II/B-M (T-LL), (d) CEM III/B, (e) CEM II/B-M (S-T), and (f) CEM I + 33 % LS.*

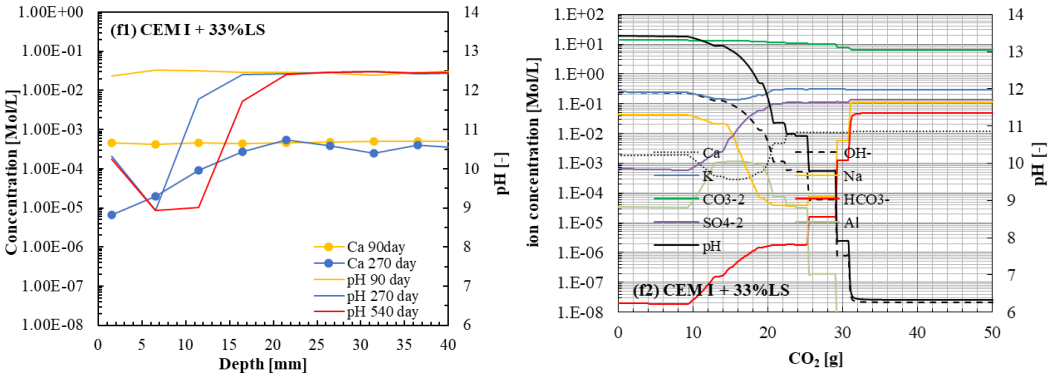

Follow up Fig. 50 *pH and Ca profiles determined by ISE (left) after 90, 270, and 540 days under Wf-CO_2 conditions, and (right) obtained from thermodynamic modelling with incremental addition of up to 40 g CO_2 for (a) CEM I, (b) CRCF, (c) CEM II/B-M (T-LL), (d) CEM III/B, (e) CEM II/B-M (S-T), and (f) CEM I + 33 % LS.*

In general, higher pH values were predicted (pH ≈ 13.5 for CEM I) than those measured experimentally (pH ≈ 12.5 for CEM I). This discrepancy is attributed to the ex-situ leaching method, which typically results in lower measured pH values. Similar differences were observed for the other cement types, except for slag-containing CEM III/B, where larger discrepancies occurred, likely due to the presence of reduced sulfur species.

Consistent with the experimental results, the model predicted a decrease in pH with increasing CO_2 exposure, corresponding to the exposed surface of the mortar specimens. However, the pH decrease predicted by the model was more pronounced than that observed experimentally.

Although thermodynamic modelling using GEMS predicted a decrease in Ca concentration from the surface (depth 0) onwards at high CO_2 contents (e.g., 50 g CO_2), followed by an increase behind the carbonation front, this trend was not clearly observed in the ISE measurements. This suggests that the degree of carbonation in the carbonated zone is less than 100 %. Alternatively, the expected increase may be masked by averaging the Ca concentration over a depth interval of 5 mm.

Furthermore, an increase in pH at the surface was observed for the CEM III/B specimens, which cannot be explained by the thermodynamic modelling. Nevertheless, the overall trends observed in the ISE measurements are well captured by the thermodynamic simulations.

4.4.8 Phase change during carbonation

Fig. 51 shows the calculated phase changes during carbonation for (a) CEM I, (b) CRCF, (c) CEM II/B-M(T-LL), (d) CEM III/B, (e) CEM II/B-M(S-T) and (f) CEM I + 33% LS.

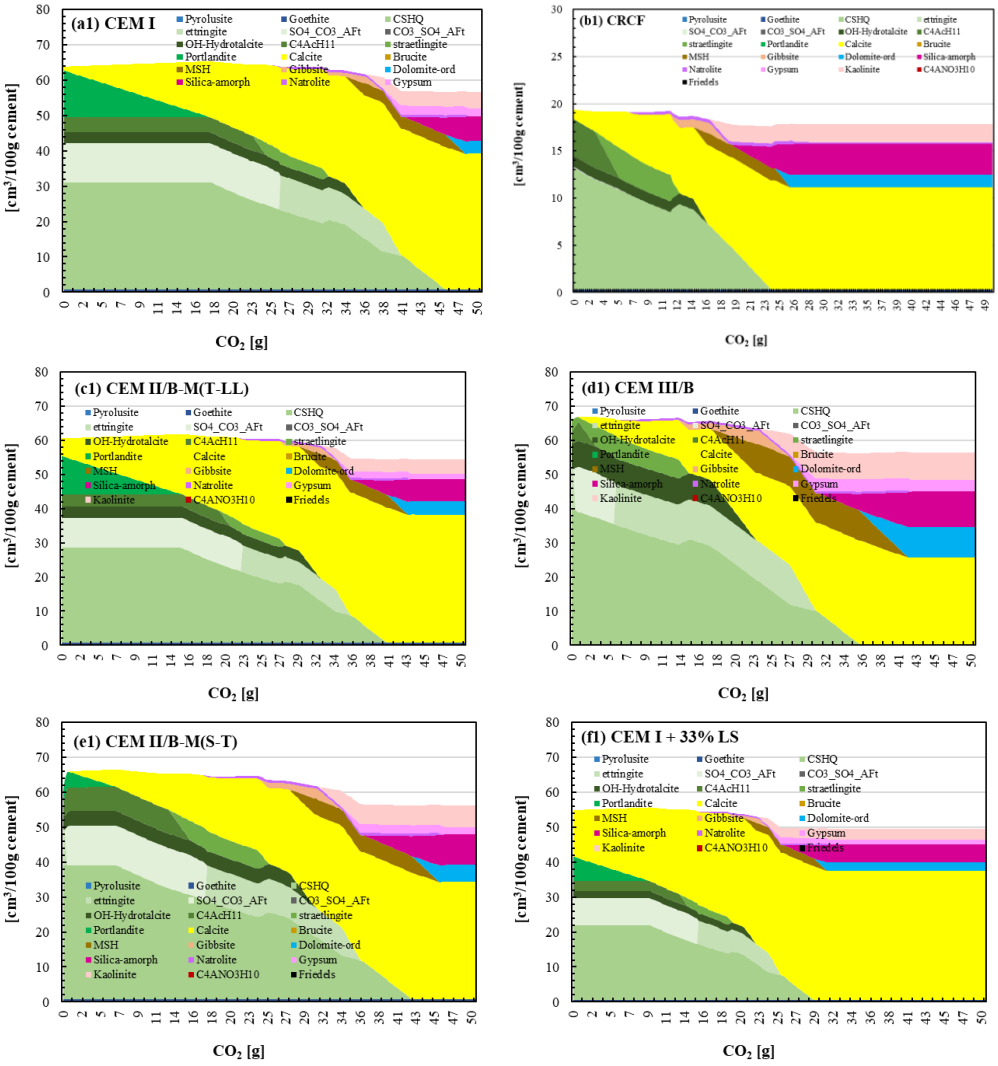

Fig. 51 *Phase changes (in grams) during carbonation for (a) CEM I, (b) CRCF, (c) CEM III/B, and (d) CEM I + 33 % LS.*

Fig. 51 shows the calculated phase evolution during progressive carbonation of the investigated cement types. Carbonation initially consumes portlandite and AFm phases, leading to calcite formation. After depletion of portlandite, C-(A)-S-H becomes the main Ca source and undergoes progressive decalcification, accompanied by dissolution of strätlingite, ettringite and OH-hydrotalcite (in slag systems). Advanced carbonation results in the formation of secondary phases such as gypsum, gibbsite and amorphous silica, marking the transition toward a silica-rich, low-pH assemblage.

The CO_2 demand for complete decalcification decreases from CEM I to blended systems and is lowest for CEM I + 33% LS, reflecting dilution of CaO and initial calcite presence. Although CEM III/B contains less portlandite, its high C-(A)-S-H volume contributes substantially to total CO_2 binding. Overall, carbonation is governed by the total reactive Ca reservoir (portlandite + AFm + C-(A)-S-H), not by portlandite alone.

4.5 Chloride ingress

4.5.1 Chloride ingress depth and rates Model 2

Fig. 52 shows the chloride profiles determined after approximately 60, 90, and 365 days of exposure for the concrete mixes containing (a) CEM I, (b) CRCF, (c) CEM II/B-M (T-LL), (d) CEM III/B, (e) CEM II/B-M (S-T), and (f) CEM I + 33 % LS. It should be noted that Cl (wt.-% relative to cement) is approximately eight times higher than Cl (wt.-% relative to concrete).

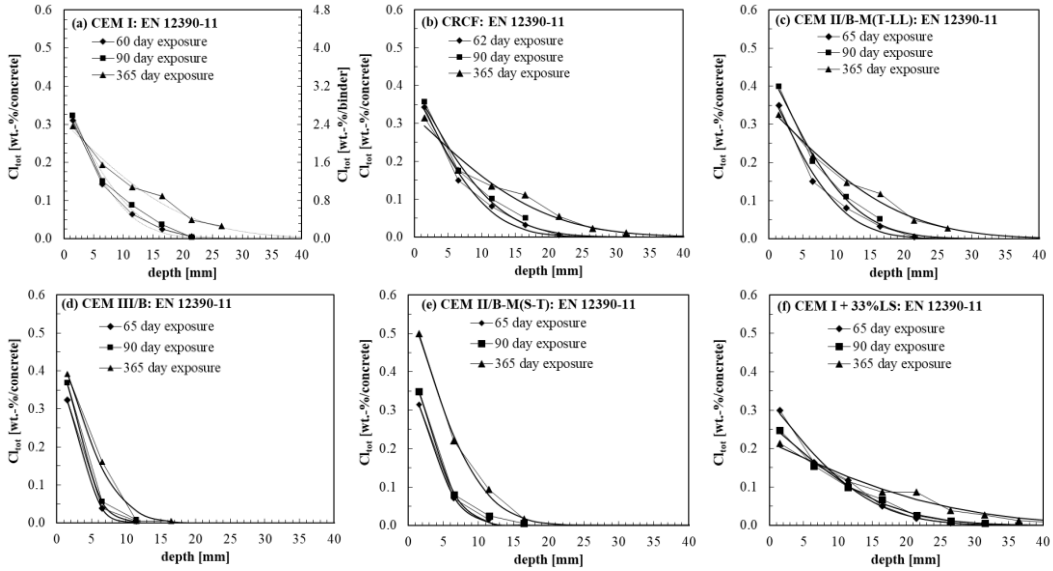

Fig. 52 *Chloride profiles determined according to SN EN 12390-11 at samples water cured for 28 days.*

From Fig. 52, it can be observed that chloride concentrations decrease less pronouncedly with depth for CEM I, CEM I + 33 % LS, CRCF, and CEM II/B-M (T-LL) concretes, and more pronouncedly for CEM III/B and CEM II/B-M (S-T) concretes. The maximum chloride concentrations (surface chloride concentrations) are lowest for CEM I + 33 % LS and CEM I, and highest for CEM II/B-M (S-T) concretes.

The surface chloride concentrations are similar or slightly lower after 60 and 90 days of exposure, but are generally lower after one year of exposure, except for CEM III/B and CEM II/B-M (S-T) concretes. In particular, concretes exhibiting rapid and deep chloride ingress show a decrease in maximum chloride concentration over time. This behaviour may be attributed to a limited availability of chlorides in the surrounding solution, suggesting that the chloride concentration should be renewed more frequently. Alternatively, cutting and grinding procedures may affect chloride concentrations in the near-surface layer.

Fig. 53 shows the chloride profiles determined after 90, 270, and 540 days of exposure under (a) constant NaCl solution exposure, (b) cyclic NaCl exposure with drying phases under Wf-Cl conditions, and (c) cyclic NaCl exposure with drying phases in a climate chamber at an increased CO_2 concentration of 3 vol.-% (Wf-Cl-CO_2).

From top to bottom (1–6), the profiles correspond to the different cement types: (1) CEM I, (2) CRCF, (3) CEM II/B-M (T-LL), (4) CEM III/B, (5) CEM II/B-M (S-T), and (6) CEM I + 33 % LS.

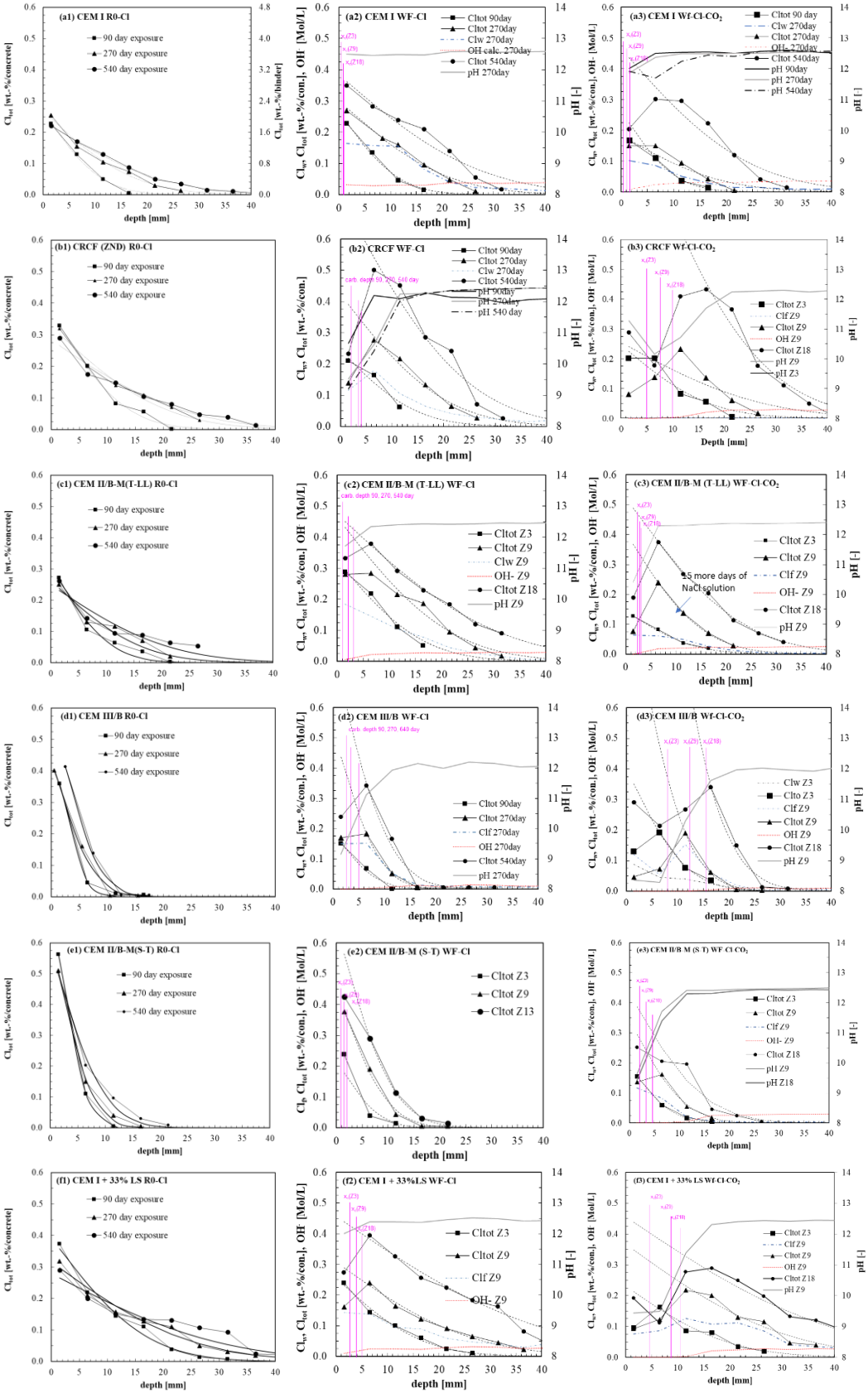

Fig. 53 *Chloride profiles determined (1) in accordance with EN 12390-11 after 91 days of curing prior to exposure, (2) during exposure following 91 days of curing under cyclic wet–dry and atmospheric conditions (Wf-Cl), and (3) during exposure following 91 days of curing under cyclic wet–dry conditions with increased CO_2 concentration (Wf-Cl-CO_2) for (a) CEM*

I, (b) CRCF, (c) CEM II/B-M (T-LL), (d) CEM III/B, (e) CEM II/B-M (S-T), and (f) CEM II/B-LL concretes.

From Fig. 53 (left), the maximum chloride concentration tends to remain similar or slightly decrease with increasing exposure time. This behaviour may be attributed to partial depletion of chlorides in the exposure solution, although Cl^--ISE measurements of the solution indicate only minor changes.

In most cyclic experiments without accelerated carbonation, a maximum chloride concentration develops at some distance from the sample surface from the third cycle onwards. Under Wf-Cl conditions, the depth of this maximum does not increase with exposure time, suggesting that it is related to the influential depth. The maximum chloride concentration tends to increase with exposure time, particularly after the 18th cycle for non-slag cements, but remains lower for slag-blended cements compared to R-Cl conditions.

Since chloride wash-off is negligible in these experiments, it can be assumed that drying phases lead to increased chloride concentrations in the reduced pore solution, thereby enhancing chloride binding.

Under cyclic conditions with accelerated carbonation (Wf-Cl-CO_2), a pronounced chloride concentration peak occurs away from the sample surface in all concretes. The maximum chloride concentrations are generally lower than under constant exposure (R-Cl) or cyclic exposure without accelerated carbonation (Wf-Cl). This behaviour is likely related to reduced chloride binding in the carbonated zone. Moreover, the depth of the chloride concentration maximum correlates well with the carbonation depth.

Fig. 54 illustrates, as an example, the chloride profiles of CEM III/B concretes under (a) constant NaCl exposure, (b) cyclic wet–dry exposure to NaCl solution, and (c) cyclic wet–dry exposure to NaCl solution with accelerated carbonation during the drying phase. The depth corresponding to a chloride content of 1 wt.-% is indicated by arrows. This depth was used to determine the chloride ingress rate, as described in Chapter 1.

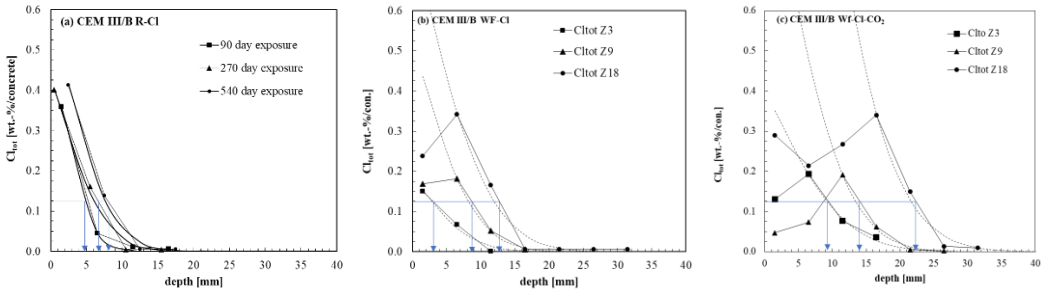

Fig. 54 *Chloride profiles of CEM III/B concretes under (a) constant NaCl exposure, (b) cyclic wet–dry exposure, and (c) cyclic wet–dry exposure with accelerated carbonation. Arrows indicate the depth at 1 wt.-% chloride used to determine the chloride ingress rate.*

The depth corresponding to a chloride content of 1 wt.-% relative to cement is shown in Fig. 55. As a curing period of 91 days was applied prior to exposure, the specimens were approximately 180 days old at the time of the first measurement, in accordance with the recommendations in [19,20]. The chloride ingress rate was determined using Chloride Model 2.

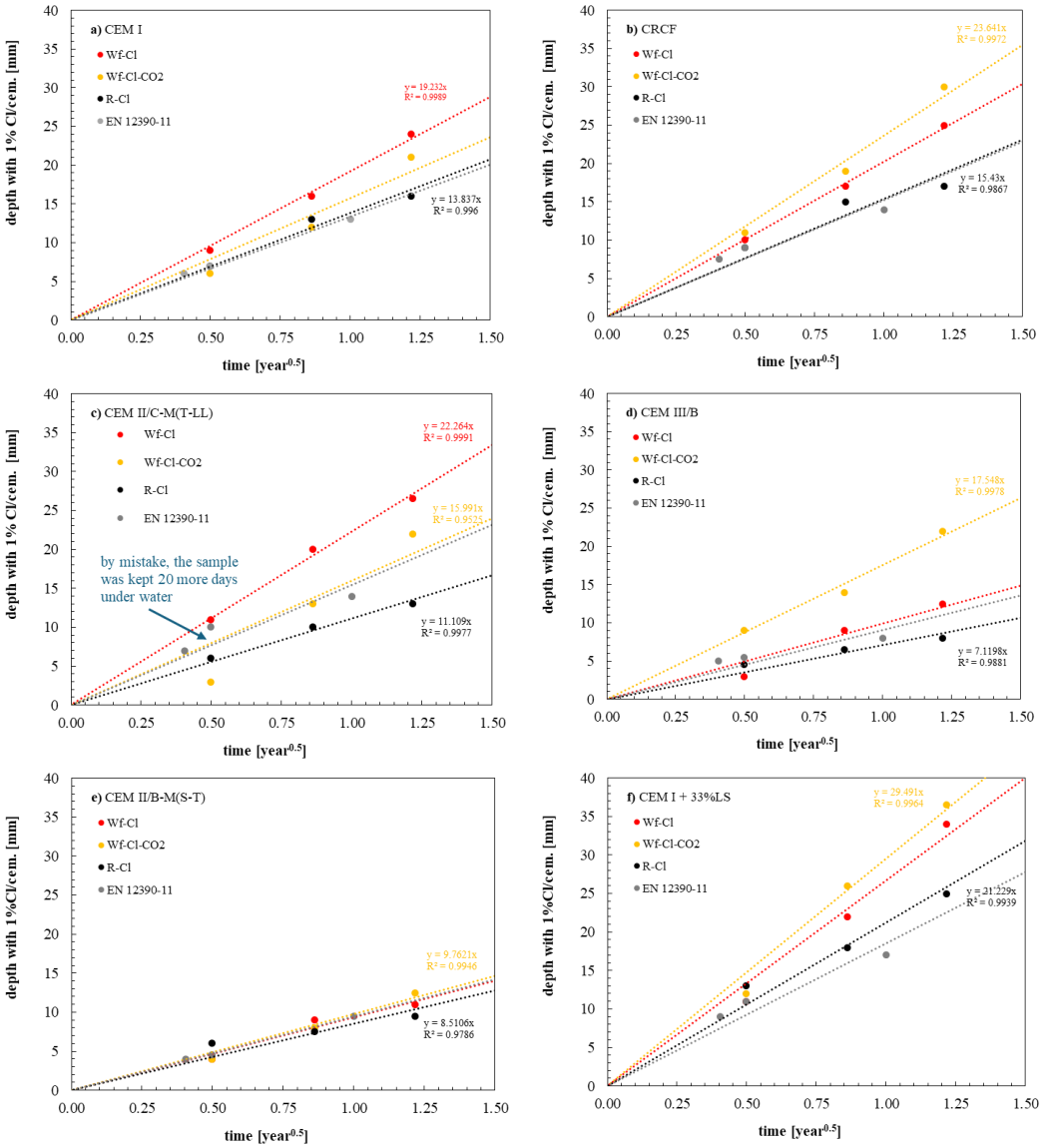

Fig. 55 *Ingress depth corresponding to a chloride content of 1 wt.-% relative to cement over time for (a) CEM I, (b) CRCF, (c) CEM II/B-M (T-LL) with an additional 15 days of water exposure under Wf-CO_2 and Wf-Cl-CO_2 conditions, (d) CEM III/B, (e) CEM II/B-M (S-T), and (f) CEM I + 33 % LS.*

In all specimens, chloride ingress was faster under cyclic exposure conditions than under constant exposure. Chloride ingress was generally further accelerated under simultaneous accelerated carbonation, except for CEM I concretes. This behaviour may be attributed to pore structure densification during carbonation of CEM I.

Although the coefficients of determination are acceptable, it should be noted that unconstrained regression models or approaches incorporating time-dependent ingress rates (accounting for ageing of the diffusion coefficient) yield higher coefficients of determination and less conservative ingress rates. Nevertheless, linear regression forced through the origin according to [19] was adopted to ensure comparable ingress parameters for both deterioration processes, namely carbonation and chloride ingress.

Tab. 15 summarizes the chloride ingress rates corresponding to 1 wt.-% Cl relative to cement under constant exposure conditions (SN EN 12390-11 and R0-Cl) and under cyclic exposure without (Wf-Cl) and with carbonation (Wf-Cl-CO_2). The ingress rates were determined using Chloride Model 2.

Tab. 18 *Chloride ingress rates 1% chloride/cement constant exposure conditions all regression through the origin, in brackets the chloride ingress rate at 0.4 wt.-% chloride/cement is added ($V_{Cl1\%}$ respectively $v_{Cl0,4\%}$)*

Test type	SN EN 12390-11	R0-Cl	Wf-Cl	Wf-Cl-CO_2
Parameter	$V_{Cl1\%}$ [mm/year$^{0.5}$] ($V_{Cl0,4\%}$ [mm/year$^{0.5}$])			
CEM I	14.5 (24.3)	13.8 (19.5)	19.2 (25.9)	15.8 (20.1)
CRCF	15.2 (23.8)	15.4 (23.5)	20.3 (28.3)	23.6 (30.4)
CEM II/B-M(T-LL)	15.5 (24.6)	11.1 (18.2)	22.3 (32.6)	16.0 (25.4)
CEM III/B	9.0 (11.1)	7.1 (8.9)	9.9 (13.1)	17.5 (20.8)
CEM II/B-M(S-T)	9.5 (15.1)	8.5 (11.5)	9.5 (13.8)	9.8 (16.8)
CEM I + 33%LS	18.5 (29.0)	21.2 (29.7)	26.7 (35.7)	29.5 (43.0)

4.5.2 Parameter of Model 1

Fig. 56 shows the non-steady-state diffusion coefficients (D_{nss}) calculated from the chloride profiles in Fig. 52 as a function of exposure time. For the non-steady-state diffusion coefficients determined using a single investigation protocol (EN 12390-11 or R0-Cl), a potential curve with parameters A and n was fitted.

Parameter A represents the normalized apparent diffusion coefficient at t = 1, while n corresponds to the age exponent α expressed with a negative sign.

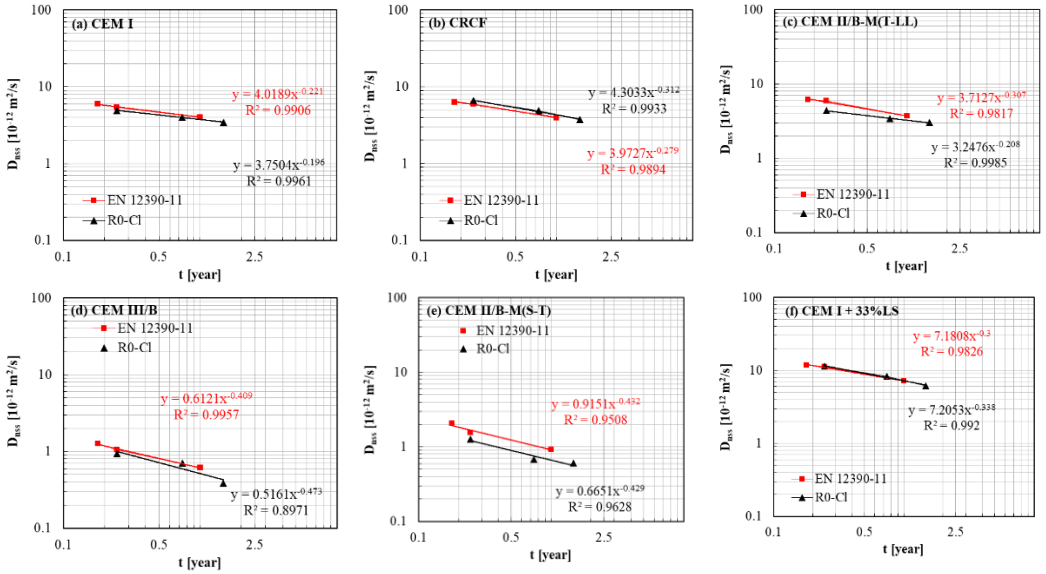

Fig. 56 *Non-steady-state diffusion coefficients (D_{nss}) calculated from chloride profiles determined according to the EN 12390-11 and R0-Cl protocols at three different exposure times for (a) CEM I concrete, (b) CRCF concrete, (c) CEM II/B-M (T-LL) concrete, (d) CEM III/B concrete, (e) CEM II/B-M (S-T) concrete, and (f) CEM I + 33 % LS.*

The diffusion coefficients determined for concretes cured for 91 days prior to exposure to NaCl solution are similar or slightly lower than those determined after shorter curing periods. Comparable diffusion coefficients were obtained for concretes containing no or only small amounts of pozzolanic or latent hydraulic additions (CEM I, CRCF, CEM I + 33 % LS). Lower diffusion coefficients were observed for concretes incorporating higher amounts of latent hydraulic (CEM III/B, CEM II/B-M (S-T)) or pozzolanic additions (CEM II/B-M (T-LL)).

This behaviour indicates that a higher degree of hydration leads to an increased chloride binding capacity, mainly through physical binding in C-(A)-S-H and AFm phases and through the formation of Friedel's salt.

Tab. 19 summarizes the diffusion coefficients, age exponents, and maximum chloride concentrations (maximum over time and depth) determined under constant exposure conditions according to SN EN 12390-11 and R0-Cl using Model 1, as well as the chloride migration coefficients determined according to SIA 262/1 Annex B.

Tab. 19 *Chloride diffusion coefficients, age exponents and maximum chloride concentration of constant exposure conditions*

Test type	**SIA 262/1-B**	**SN EN 12390-11**			**R0-Cl**		
Parameter	**D_{Cl} [10^{-12} m^2/s]**	**$D_{app}(t)$ [10^{-12} m^2/s]**	**α [-]**	**C_{max} [wt.-%/cem.]**	**$D_{app}(t)$ [10^{-12} m^2/s]**	**α [-]**	**C_{max} [wt.-%/cem.]**
CEM I	7.6	3.8	-0.20	2.9	3.8	-0.19	2.2
CRCF	13.05	4.0	-0.31	3.2	4.3	-0.31	3.0
CEM II/B-M(T-LL)	9.05	3.7	-0.21	3.3	3.2	-0.21	2.5
CEM III/B	1.05	0.6	-0.52	4.0	0.5	-0.47	4.9
CEM II/B-M(S-T)	5.2	0.9	-0.67	5.4	0.7	-0.43	6.1
CEM I + 33%LS	19.45	7.2	-0.34	2.4	7.2	-0.34	3.1

Fig. 57 shows the non-steady-state diffusion coefficients (D_{nss}) calculated from the chloride profiles in Fig. 53 as a function of exposure time. For the diffusion coefficients determined using a single investigation protocol, a potential curve with parameters A and n was fitted.

Parameter A represents the normalized apparent diffusion coefficient at t = 1, while n corresponds to the age exponent α expressed with a negative sign.

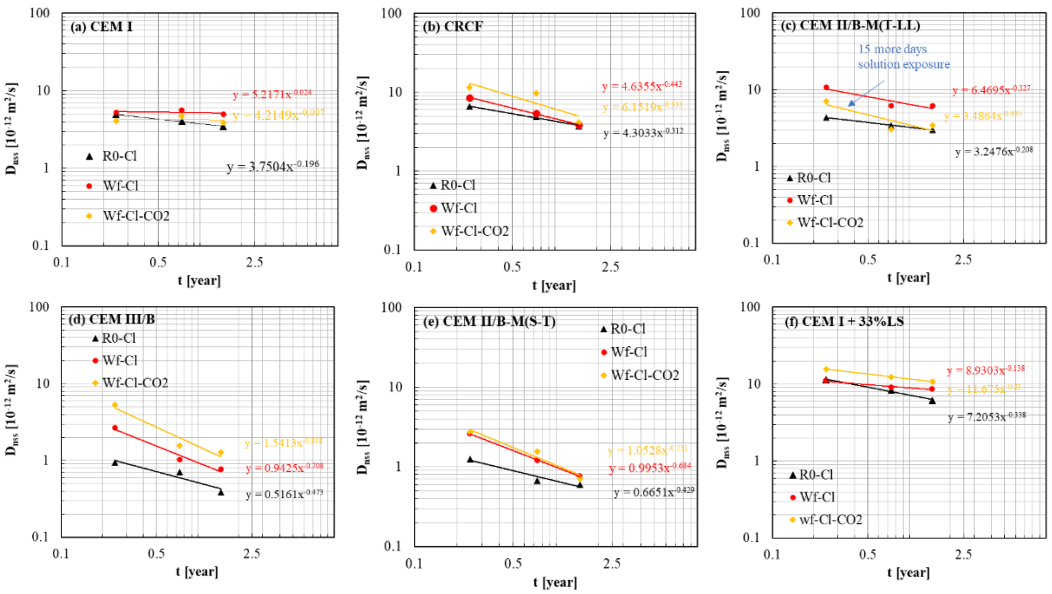

Fig. 57 *Non-steady-state diffusion coefficients (D_{nss}) calculated from chloride profiles determined according to the R0-Cl, Wf-Cl, and Wf-Cl-CO_2 protocols at three different exposure times for (a) CEM I concrete, (b) CRCF concrete, (c) CEM II/B-M (T-LL) concrete, (d) CEM III/B concrete, (e) CEM II/B-M (S-T) concrete, and (f) CEM I + 33 % LS.*

Under cyclic wet–dry exposure conditions, chloride ingress initially proceeds more rapidly, while further ingress by diffusion is subsequently slowed. This behaviour is reflected by the initially increased D_{nss} values under cyclic exposure, leading to higher age exponents for most concretes under Wf-Cl conditions compared to R-Cl conditions.

Where carbonation has a stronger influence on chloride ingress, as indicated by greater carbonation depths, the non-steady-state diffusion coefficients are generally higher. However, differences in moisture conditions are expected to cause a stronger decline in D_{nss} over time, resulting in higher age exponents.

For concretes exhibiting negligible carbonation depths (CEM I and CEM II/B-M (S-T)), D_{nss} values are similar under both exposure conditions.

Tab. 20 summarizes the diffusion coefficients, age exponents, maximum chloride concentrations (maximum over time and depth), and the depths corresponding to the maximum chloride concentrations determined under cyclic Wf-Cl and Wf-Cl-CO_2 conditions using Model 1.

Tab. 20 *Chloride diffusion coefficients, age exponents, maximum chloride concentration and depth with maximum concentration of cyclic exposure conditions*

Testtype	**Wf-Cl**				**Wf-Cl-CO_2**			
Parameter	**$D_{app}(t)$ [10^{-12} m^2/s]**	**α [-]**	**C_{max} [wt.-%/cem.]**	**Δx [mm]**	**$D_{app}(t)$ [10^{-12} m^2/s]**	**α [-]**	**C_{max} [wt.-%/cem.]**	**Δx [mm]**
CEM I	5.2	-0.02	3.1	0	4.2	-0.01	2.4	6.5
CRCF	4.6	-0.44	4.0	6.5	6.2	-0.54	3.4	17.5
CEM II/B-M(T-LL)	6.5	-0.33	3.8	6.5	3.5	-0.45	3.0	6.5
CEM III/B	0.9	-0.71	2.8	6.5	1.5	-0.82	2.7	17.5
CEM II/B-M(S-T)	1.0	-0.68	4.0	0	1.1	-0.73	1.8	2.5
CEM I + 33%LS	8.9	-0.14	3.2	7.5	11.7	-0.21	2.6	15.0

4.5.3 Correlation with natural conditions

Fig. 58 (a) presents chloride profiles from concrete specimens with compositions similar to those used in this study (same cement type and production plant, same aggregate type and source, and comparable mix proportions) that were exposed to a road environment at the Naxberg tunnel, as reported in [136,173]. It should be noted that this site represents a particularly severe exposure condition in Switzerland, with chloride loads at the upper end of the exposure spectrum.

Fig. 58 (b) compares the depth corresponding to 1 wt.-% chloride relative to cement (0.125 wt.-% relative to concrete) from the Naxberg exposure with that of CEM I specimens from this study over time. Since carbonation depths were negligible under both Wf-Cl (approximately 1 mm) and Wf-Cl-CO_2 (approximately 2 mm) conditions, the influence of carbonation can be neglected, similar to the Naxberg exposure (approximately 2 mm carbonation depth).

It should be noted that the Naxberg site represents an exceptionally harsh environment in Switzerland for XD3 exposure.

In addition, Fig. 58 (c) shows chloride profiles obtained from a bridge in the Canton of Schwyz (Horgenberg Street). The profiles were collected at a height of 1 m above ground and at a horizontal distance of 0.5 m from the road at the same abutment location [174].

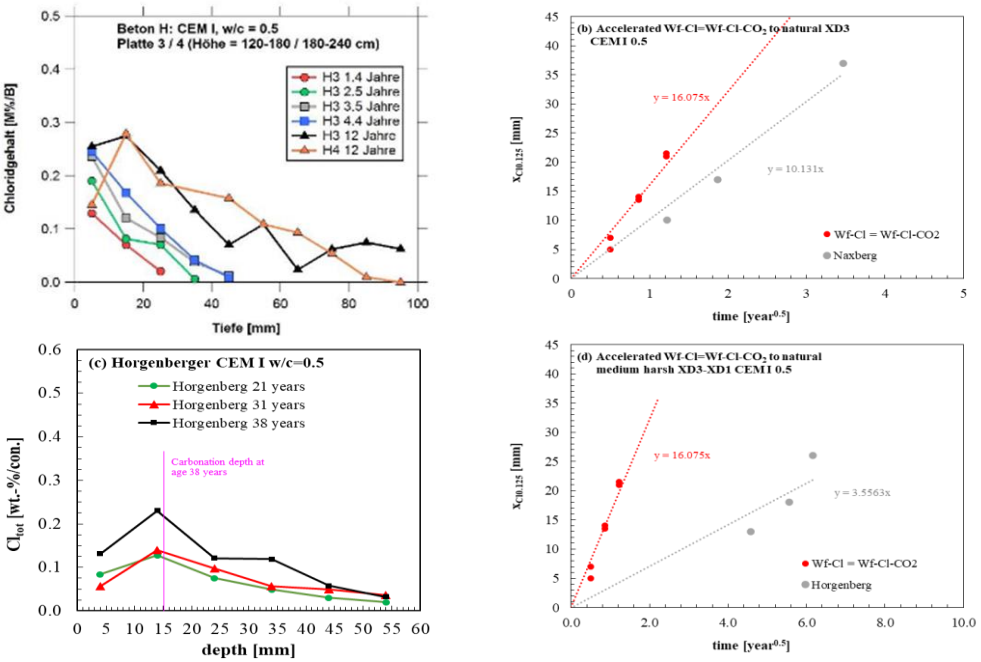

Fig. 58 *Chloride profiles of CEM I concretes (w/c = 0.5) exposed to road environments: (a) chloride profiles from Naxberg tunnel [136,173], (b) ingress depth corresponding to 1 wt.-% chloride relative to cement at the Naxberg site, (c) chloride profiles from Horgenberg Street, and (d) corresponding ingress depth at 1 wt.-% chloride relative to cement [174].*

Chloride ingress observed in this study was faster than that measured under the severe natural exposure conditions at the Naxberg road site. The regression curves (Model 2) provide the chloride ingress rate $v_{Cl,1\%}$. Based on the comparison of ingress rates, it can be concluded that using a time of wetness (ToW) of 0.2 with NaCl solution (equivalent to approximately 12 months of NaCl exposure per year), instead of only 4-6 months of exposure, results in chloride ingress rates that are approximately 1.6 times higher.

Furthermore, the chloride ingress rate determined in this study is substantially higher than that observed under typical natural XD3 exposure conditions in the road environment (Horgenberg Street, Canton of Schwyz). In this case, the regression curves (Model 2) indicate chloride ingress rates that are approximately 4.5 times higher.

Overall, chloride ingress under cyclic laboratory conditions (Wf) is, on average, about four times faster than under natural XD3 road exposure. A similar acceleration factor is observed between sheltered XC3 exposure and accelerated carbonation. In contrast, a direct correlation between constant submerged chloride exposure and natural submerged exposure, analogous to carbonation testing, is neither reasonable nor currently available.

The differences between accelerated cyclic laboratory exposure (Wf) and natural XD3 road exposure result from a combination of several factors, including temperature effects, frequency and intensity of chloride loading, moisture conditions, and potential material-related variations.

Tab. 21 summarizes the calculated natural chloride ingress rates. These values were obtained by dividing the accelerated ingress rates $v_{Cl,1\%,AC}$ under Wf conditions by a factor of 4.26.

Tab. 21 *Ingress rate of 1% Cl/cement cyclic exposure conditions, natural rates ($v_{Cl,1\%}$) Model 2*

Test type	**Wf-Cl**	**Wf-Cl-CO_2**
Parameter	$v_{Cl1\%,NA}$ [mm/year$^{0.5}$]	$v_{Cl1\%,NA}$ [mm/year$^{0.5}$]
CEM I	4.5	3.7
CRCF	4.8	5.5
CEM II/B-M(T-LL)	5.2	3.8
CEM III/B	2.3	4.1
CEM II/B-M(S-T)	2.2	2.3
CEM I + 33%LS	6.3	6.9

If the chloride load differs, for example under XD1 conditions where chloride contents of approximately 1–2 wt.-% relative to cement are expected [13], instead of 3–5 wt.-% typical for XD3 conditions as investigated in this study, the chloride ingress rate is lower (Fig. 59, left).

Conversely, when the reference level for determining the chloride ingress rate, namely the critical chloride content, is reduced (here assumed as 1 wt.-% relative to cement, $v_{Cl,1\%}$), the calculated ingress rate increases (see values in brackets in Tab. 18). This behaviour is reflected by the multiplicative factor derived from Model 1, which can be used to assess the increase or reduction of chloride ingress rates. This factor depends on the ratio between the critical chloride content and the surface chloride concentration (C_{Crit}/C_s).

In addition, a lower degree of saturation leads to reduced diffusivity. According to [91] (Fig. 59, right), a decrease in relative humidity from 95 % to 80 % results in a reduction in diffusivity of approximately 50 %. This reduction is smaller than that proposed in [13,176], where an increase in ageing from 0.3 to 0.65 over a 50-year service life is assumed to reduce diffusivity by approximately 75 %.

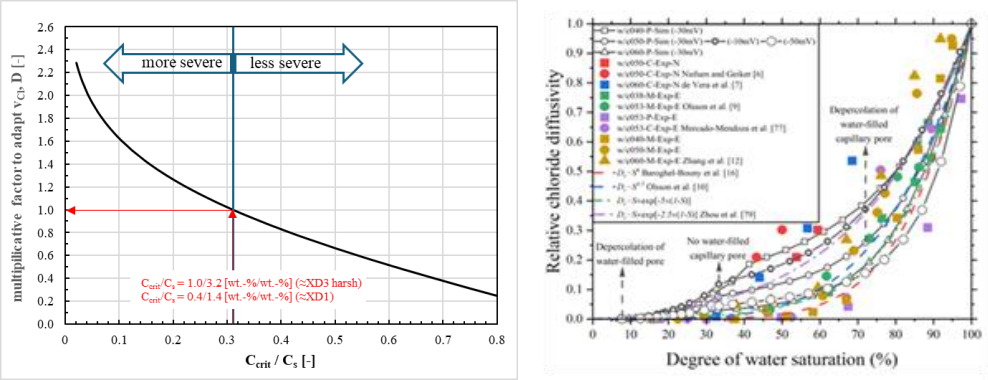

Fig. 59 *Multiplicative factors used to increase or reduce v_{Cl} as a function of (a) the ratio C_{crit} / C_s and (b) the degree of saturation [91], to assess the effect of changing boundary conditions on v_{Cl}.*

4.5.4 Correlation between different exposure conditions (Model 2)

Fig. 60 compares the chloride ingress rates $v_{Cl,1\%}$ under different exposure conditions. In Fig. 60 (a), the chloride ingress rate under constant chloride exposure (R-Cl) is compared with that under cyclic chloride exposure without carbonation influence (Wf-Cl). Fig. 60 (b) compares the chloride ingress rates under Wf-Cl conditions with those under Wf-Cl-CO_2 conditions.

To evaluate the effect of cyclic wetting and drying on chloride ingress, the accelerated ingress rates reported in Tab. 18 were used.

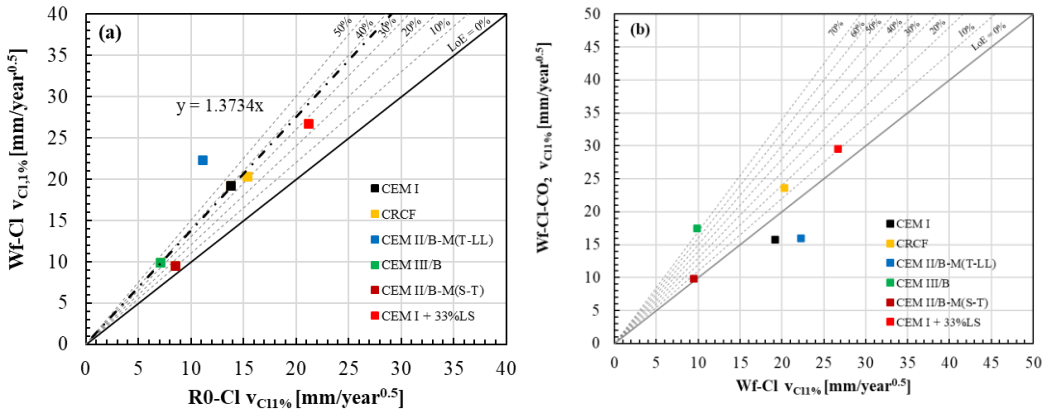

Fig. 60 *Comparison of chloride ingress rates corresponding to 1 wt.-% Cl relative to binder (0.125 wt.-% relative to concrete): (a) constant chloride exposure under reference conditions (R-Cl) versus cyclic chloride exposure without carbonation influence (Wf-Cl), and (b) cyclic chloride exposure without carbonation influence versus cyclic chloride exposure with carbonation influence (Wf-Cl-CO_2).*

Under cyclic exposure conditions, chloride ingress is accelerated. This acceleration is more pronounced for specimens exhibiting higher initial capillary water absorption and larger initial volumes of hydration pores. However, this acceleration is valid only for the present series of consecutive laboratory tests.

It is expected that concrete exposed continuously to the same chloride load will exhibit higher chloride ingress rates than concrete exposed to the same chloride solution only a few times per year. Consequently, the acceleration factor determined between cyclic laboratory conditions and structural elements cannot be directly applied to reference conditions.

When comparing chloride ingress under cyclic conditions with and without carbonation, no clear trend is observed. Therefore, Fig. 61 (a) compares the carbonation rate with the chloride ingress rate (1 wt.-% Cl relative to cement) obtained from the consecutive experiments. This comparison allows identification of mixes in which carbonation progresses faster than, or at a similar rate to, chloride ingress.

Fig. 61 (b) compares the chloride ingress rates for mixes in which carbonation progresses faster than, or at a similar rate to, chloride ingress.

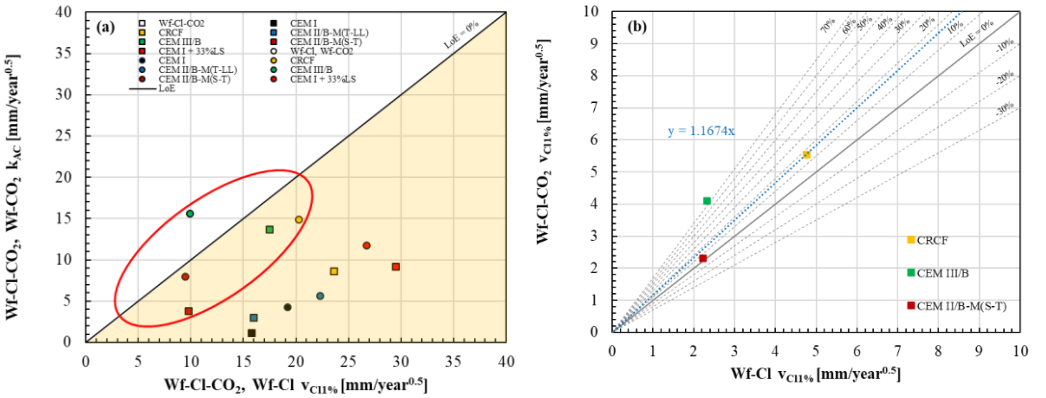

Fig. 61 *Comparison of (a) the chloride ingress rate corresponding to 1 wt.-% Cl relative to binder (0.125 wt.-% relative to concrete) with the carbonation rate under cyclic conditions (squares: combined exposure, dots: single-process exposure), and (b) the influence of carbonation on chloride ingress under cyclic conditions for mixes exhibiting faster or similar carbonation rates compared to chloride ingress rates.*

Carbonation rates exceeding chloride ingress rates are observed only when single-process tests (Wf-Cl versus Wf-CO_2) are compared, as shown in Fig. 61 (a). Since carbonation progress is generally decelerated in the presence of chlorides, while chloride ingress tends to be accelerated in carbonated concrete, the number of samples exhibiting simultaneous dominance of carbonation decreases, as illustrated in Fig. 61 (b).

4.5.5 Correlation between different exposure conditions (Model 1)

Fig. 62 correlates the migration coefficients determined according to SIA 262/1-B with the apparent diffusion coefficients determined according to SN EN 12390-11 (a) and R0-Cl (b). In addition, Fig. 62 correlates the apparent diffusion coefficients determined under (c) SN EN 12390-11 and R0-Cl, (d) R0-Cl and Wf-Cl, and (e) Wf-Cl and Wf-Cl-CO_2 conditions.

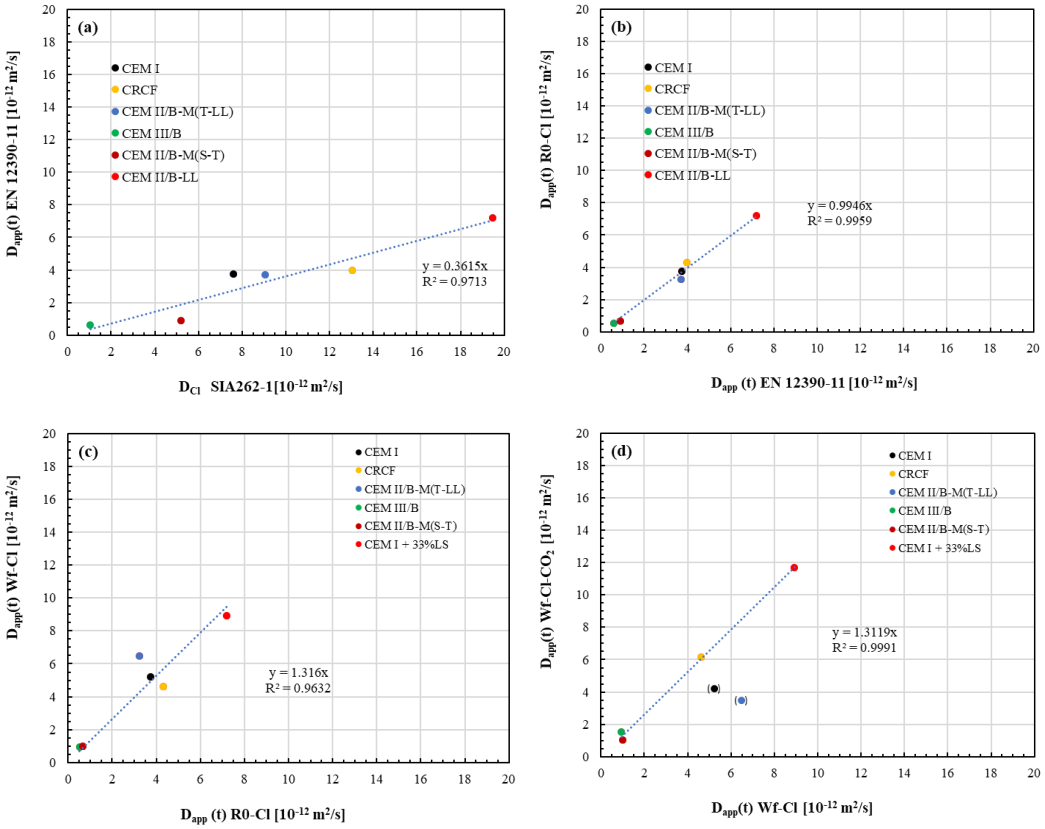

Fig. 62 *Correlation between (a) the chloride migration coefficient according to SIA 262/1 Annex B and the apparent diffusion coefficient according to EN 12390-11, (b) the apparent diffusion coefficients according to EN 12390-11 and R0-Cl, (c) the apparent diffusion coefficients according to R0-Cl and Wf-Cl, and (d) the apparent diffusion coefficients according to Wf-Cl and Wf-Cl-CO_2.*

The apparent diffusion coefficient determined according to EN 12390-11 is, on average, 0.36–0.37 times the migration coefficient (Fig. 62 a), which is slightly higher than reported in [4]. Since prolonged curing had no significant effect on the solvent-exposed diffusion specimens, extending the curing period prior to chloride diffusion testing to 91 days (as applied in the R0-Cl experiments) had no measurable influence on the apparent diffusion coefficient. Consequently, the correlation shown in Fig. 62 (b) is approximately unity.

Compared to constant diffusion conditions according to EN 12390-11, cyclic wetting and drying increases the apparent chloride diffusion coefficient. Accordingly, in Fig. 62 (c), the apparent diffusion coefficient is, on average, about 1.3 times higher than that determined under continuous saturation without intermediate drying.

For mixes exhibiting similar carbonation and chloride ingress rates, higher apparent diffusion coefficients were observed under Wf-Cl-CO_2 conditions compared to Wf-Cl conditions (Fig. 62 d).

Fig. 63 compares the non-steady-state diffusion coefficients determined according to EN 12390-11 after 90 days of exposure with the migration coefficients determined according to SIA 262/1.

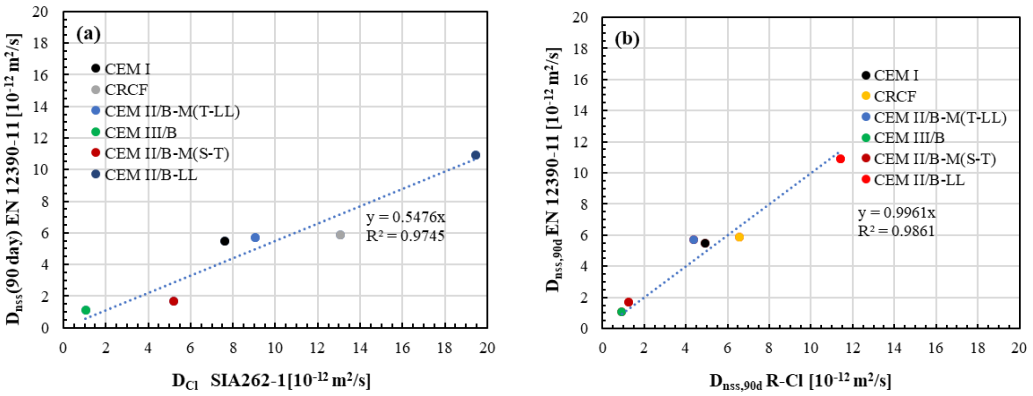

Fig. 63 *Comparison of D_{Cl} determined according to SIA 262/1 Annex B with the diffusion coefficient determined according to EN 12390-11 after 90 days of exposure to NaCl (a), and comparison of diffusion coefficients determined according to EN 12390-11 for concretes exposed under identical conditions but cured for 91 days prior to exposure (b).*

The diffusion coefficient is lower than the migration coefficient determined according to SIA 262/1 Annex B, as shown in Fig. 63 (a). The observed correlation is similar to that reported in [4]. The apparent diffusion coefficient is even lower due to further ageing effects. Concretes containing slag exhibit a larger difference between migration and diffusion coefficients than binders with higher proportions of ordinary Portland cement. Prolonged curing was found to result in similar diffusion coefficients (Fig. 63 b).

Fig. 64 shows (a) the age exponents determined according to EN 12390-11 and (b) those determined under cyclic wet–dry exposure conditions.

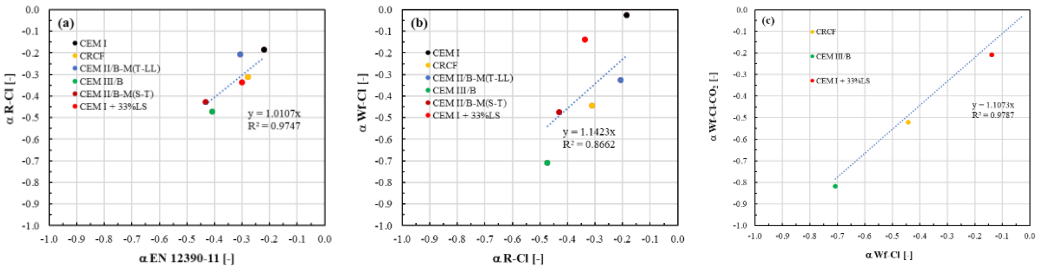

Fig. 64 *Age exponent determined according to (a) EN 12390-11, (b) under saturated conditions and (c) determined in cyclic wet and dry conditions.*

The age exponents determined according to EN 12390-11 and R0-Cl are similar. Consequently, prolonged curing has no significant effect on the age exponent (Fig. 64a). From R-Cl to Wf-Cl and further to Wf-Cl-CO_2, the age exponents become larger in magnitude (more negative) for most mixes, except for CEM I and CEM I + 33 % LS.

This behaviour may be attributed to partial saturation, which reduces the pore volume available for chloride transport. In addition, the shift towards more negative age exponents supports the hypothesis of increased chloride binding capacity with decreasing moisture content.

Fig. 65 shows the correlation between the maximum chloride concentration $C_s\Delta x$ after long-term exposure (540 days) under (a) EN 12390-11 and R0-Cl, (b) R0-Cl and Wf-Cl, and (c) Wf-Cl and Wf-Cl-CO_2 conditions.

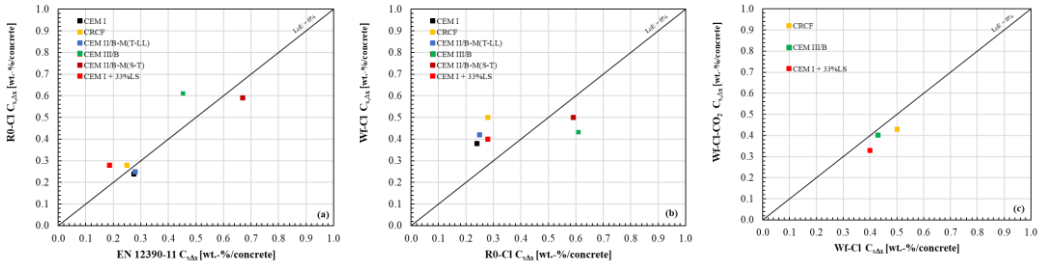

Fig. 65 *Chloride maximum concentration determined after long term exposure in (a) EN 12390-11 and R0-Cl, (b) R0-Cl and Wf-Cl and (c) Wf-Cl and Wf-Cl-CO_2.*

The maximum chloride concentration in Fig. 68 (a) strongly depends on the chloride binding capacity of the binder. Binders with high chemical binding capacity (associated with substantial amounts of AFm phases) and high physical binding capacity (due to significant contents of C-(A)-S-H), such as CEM III/B and CEM II/B-M (S-T), exhibit higher surface chloride concentrations.

Under cyclic exposure conditions, with or without carbonation, these binder-specific differences largely disappear, and the maximum chloride concentration depends mainly on the chloride concentration in the surrounding solution. One reason for this behaviour is carbonation and calcium leaching, which transform or dissolve phases responsible for chloride binding. Nevertheless, under carbonated conditions (Fig. 68c), the maximum chloride concentration is systematically lower than under conditions without accelerated carbonation.

The correlation between Model 1 and Model 2 is illustrated in Fig. 66. In theory, for identical measurements, the apparent diffusion coefficient $D_{app}(t_0)$ determined according to EN 12390-11 should be equivalent to the chloride ingress rate v_{Clx} according to Eq. (4.5.1). In this equation, the factor 31.536 accounts for unit conversion, v_{Clx} represents the ingress rate at chloride concentration x, C_s is the surface chloride concentration, and $erfc^{-1}$ denotes the inverse complementary error function.

The resulting correlation function incorporates all parameters of Eq. (4.5.1). However, this correlation represents a simplification, as it neglects cement-specific variations in C_s and the time dependency of the diffusion coefficient. In particular, the time dependency of diffusion is conservatively neglected in the determination of v_{Cl}.

$$D_{app}(t0) = \left(\frac{v_{ClX}}{4}\right)^2 \cdot \frac{1}{\text{inverfc}\left(\frac{x}{Cs}\right)\cdot 31.536} \qquad \text{Eq.(4.5.1)}$$

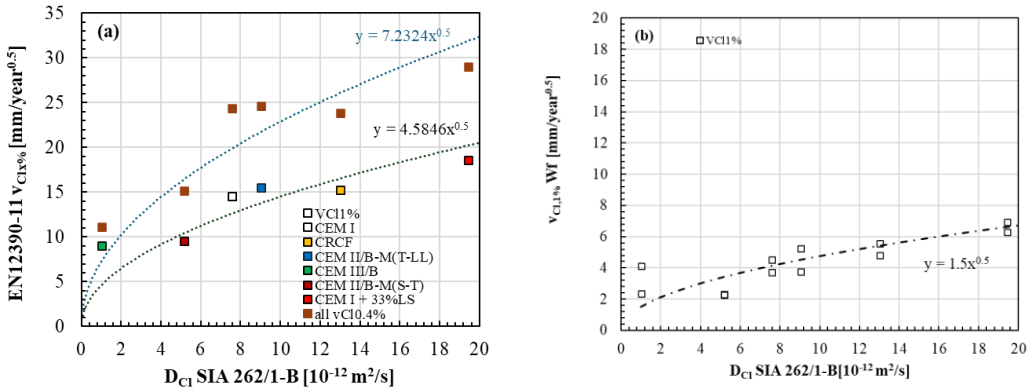

Fig. 66 *Correlation between $v_{Cl,x\%}$ for x = 1% and 0.4 wt.-% relative to cement and (a) D_{Cl} determined according to SIA 262/1-B or (b) $D_{app}(t_0)$ determined according to EN 12390-11.*

In Fig. 66 (a), a clear positive correlation is observed between $v_{Cl,x\%}$ and the migration coefficient D_{Cl}. Higher migration coefficients are consistently associated with higher chloride ingress rates. This confirms that D_{Cl} provides a reasonable indicator of the chloride transport capacity of concrete under steady-state migration conditions. However, a certain scatter is visible, reflecting the influence of additional factors such as chloride binding, moisture state, and microstructural differences that are not fully captured by the migration test.

The relationship in Fig. 66 (a) is slightly non-linear, indicating that the increase in chloride ingress rate becomes less pronounced at higher migration coefficients. This behaviour suggests that, at high transport capacities, other limiting mechanisms such as chloride binding and partial saturation increasingly control chloride ingress.

In Fig. 66 (b), the correlation between $v_{Cl,x\%}$ and the apparent diffusion coefficient $Dapp(t_0)$ is more pronounced and shows less scatter than in Fig. 66 (a). This indicates that $Dapp(t_0)$, which is derived from long-term diffusion measurements under realistic exposure conditions, better reflects the effective chloride transport behaviour governing chloride ingress.

The improved correlation in Fig. 66 (b) can be attributed to the fact that both $v_{Cl,x\%}$ and $D_{app}(t_0)$ are obtained from diffusion-based experiments and therefore incorporate ageing effects, moisture conditions, and chloride binding more consistently than migration tests.

Overall, Fig. 66 demonstrates that both D_{Cl} and $Dapp(t_0)$ correlate with chloride ingress rates, but $Dapp(t_0)$ provides a more reliable predictor of long-term chloride penetration under service-relevant exposure conditions. Migration coefficients according to SIA 262/1 Annex B tend to overestimate transport capacity and show larger variability when used to assess long-term chloride ingress.

4.5.6 Correlation with w/SiO_2 and w/(SiO_2+Al_2O_3)

Fig. 67 correlates the w/SiO_2 with (a) D_{Cl} according to SIA 262/1-B, (b) $D_{nss,90d}$ according to SN EN 12390-11, (c) Dapp(t_0) according to SN EN 12390-11, (d) $D_{app}(t_0)$ under R0 condition, (e) $D_{app}(t_0)$ under Wf-Cl condition and (e) $D_{app}(t_0)$ under Wf-Cl-CO_2.

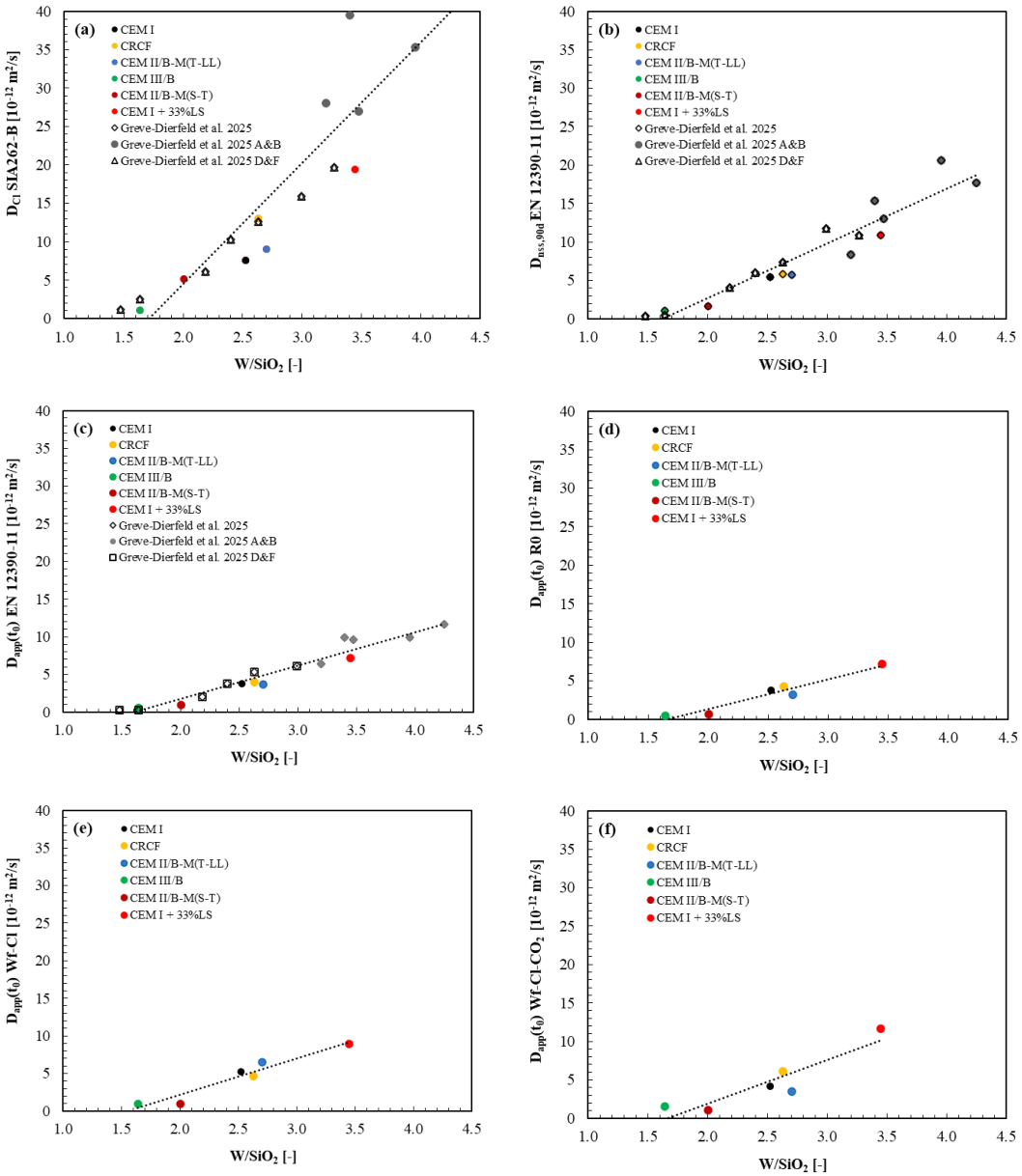

Fig. 67 *Correlation between w/SiO_2 and (a) D_{Cl} according to SIA 262/1-B, (b) $D_{nss,90d}$ according to SN EN 12390-11, (c) Dapp(t_0) according to SN EN 12390-11, (d) $D_{app}(t_0)$ under R0 condition, (e) $D_{app}(t_0)$ under Wf-Cl condition and (e) $D_{app}(t_0)$ under Wf-Cl-CO_2.*

As expected from [67], the chloride migration coefficient determined according to SIA 262/1 Annex B, as well as the chloride diffusion coefficients determined under diffusion conditions, correlate well with w/SiO_2. It should be noted that, for recycled concrete fines (CRCF = CEM II/C-M (F-T)), the non-reactive SiO_2 fraction was subtracted from the total SiO_2 content for these correlations.

However, as indicated by the results reported in [4], caution is required for low-performance concretes with high migration coefficients (25-40 × 10^{-12} m²/s). These concretes exhibited w/c ratios of approximately 0.65 and cement contents of about 280 kg/m³. For such concretes, the relationship between the SIA 262/1 Annex B results and w/SiO_2 is less clear.

Fig. 68 correlates w/(SiO_2 + Al_2O_3) with (a) D_{Cl} according to SIA 262/1-B, (b) $D_{nss,90d}$ according to SN EN 12390-11, (c) Dapp(t_0) according to SN EN 12390-11, (d) $D_{app}(t_0)$ under R0 condition, (e) $D_{app}(t_0)$ under Wf-Cl condition and (e) $D_{app}(t_0)$ under Wf-Cl-CO_2.

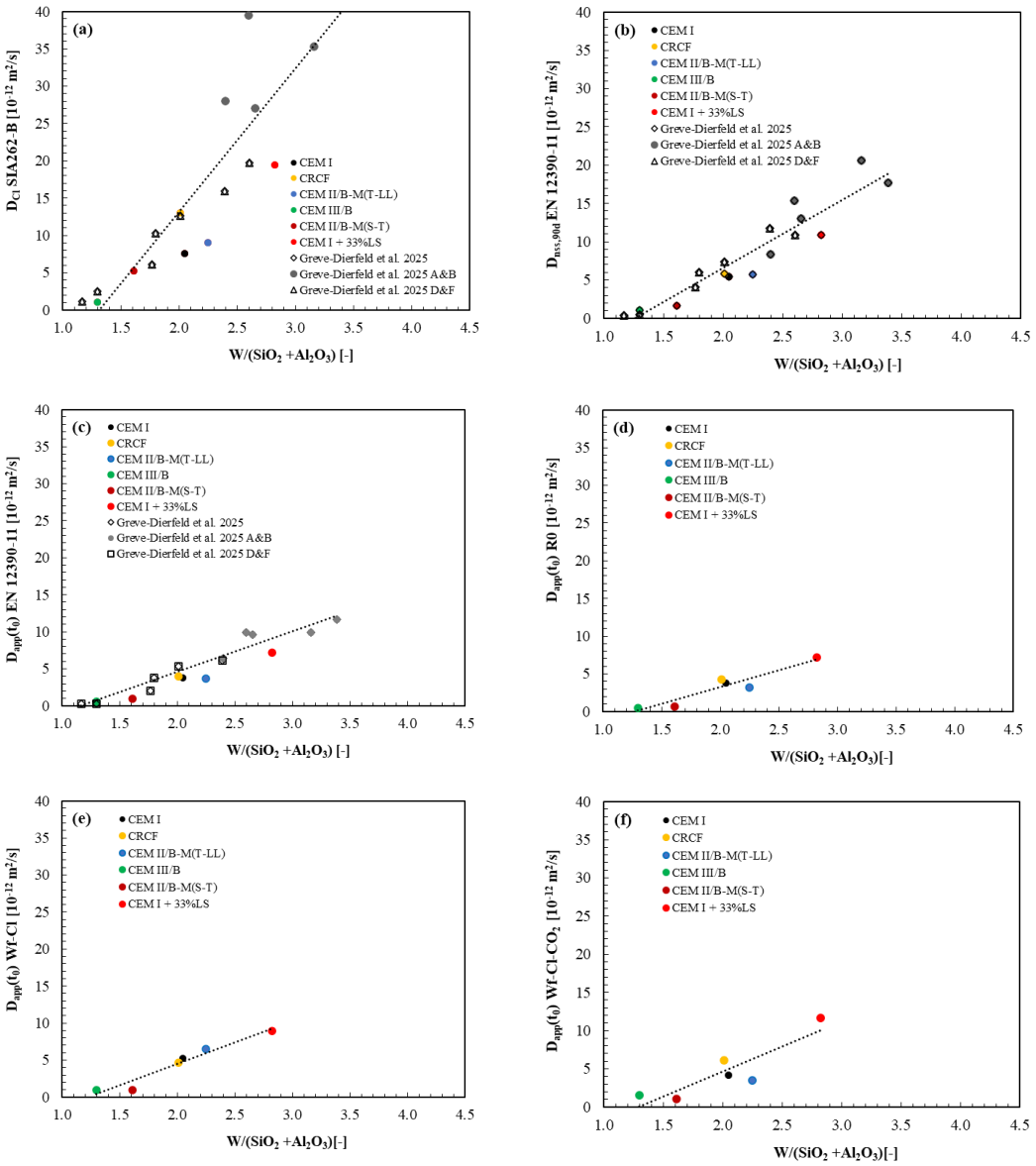

Fig. 68 *Correlation between w/(SiO_2 + Al_2O_3)$_r$* and (a) D_{Cl} according to SIA 262/1-B, (b) $D_{nss,90d}$ according to SN EN 12390-11, (c) Dapp(t_0) according to SN EN 12390-11, (d) $D_{app}(t_0)$ under R0 condition, (e) $D_{app}(t_0)$ under Wf-Cl condition and (e) $D_{app}(t_0)$ under Wf-Cl-CO_2.

The w/(SiO_2 + Al_2O_3) ratio correlates equally well with the diffusion coefficients as w/SiO_2. A slight improvement in correlation is observed for the migration coefficients (Fig. 71a). However, it was expected that the w/SiO_2 relationship would be particularly relevant for migration tests, in which there is insufficient time for extensive chemical chloride binding.

Fig. 69 shows the correlation between w/SiO_{2r} and the age exponent determined under (a) R0-Cl, (b) Wf-Cl, and (c) Wf-Cl-CO_2 conditions. Similarly, the correlation between w/(SiO_2 + Al_2O_3)$_r$ and the age exponent is presented for (d) R0-Cl, (e) Wf-Cl, and (f) Wf-Cl-CO_2 conditions.

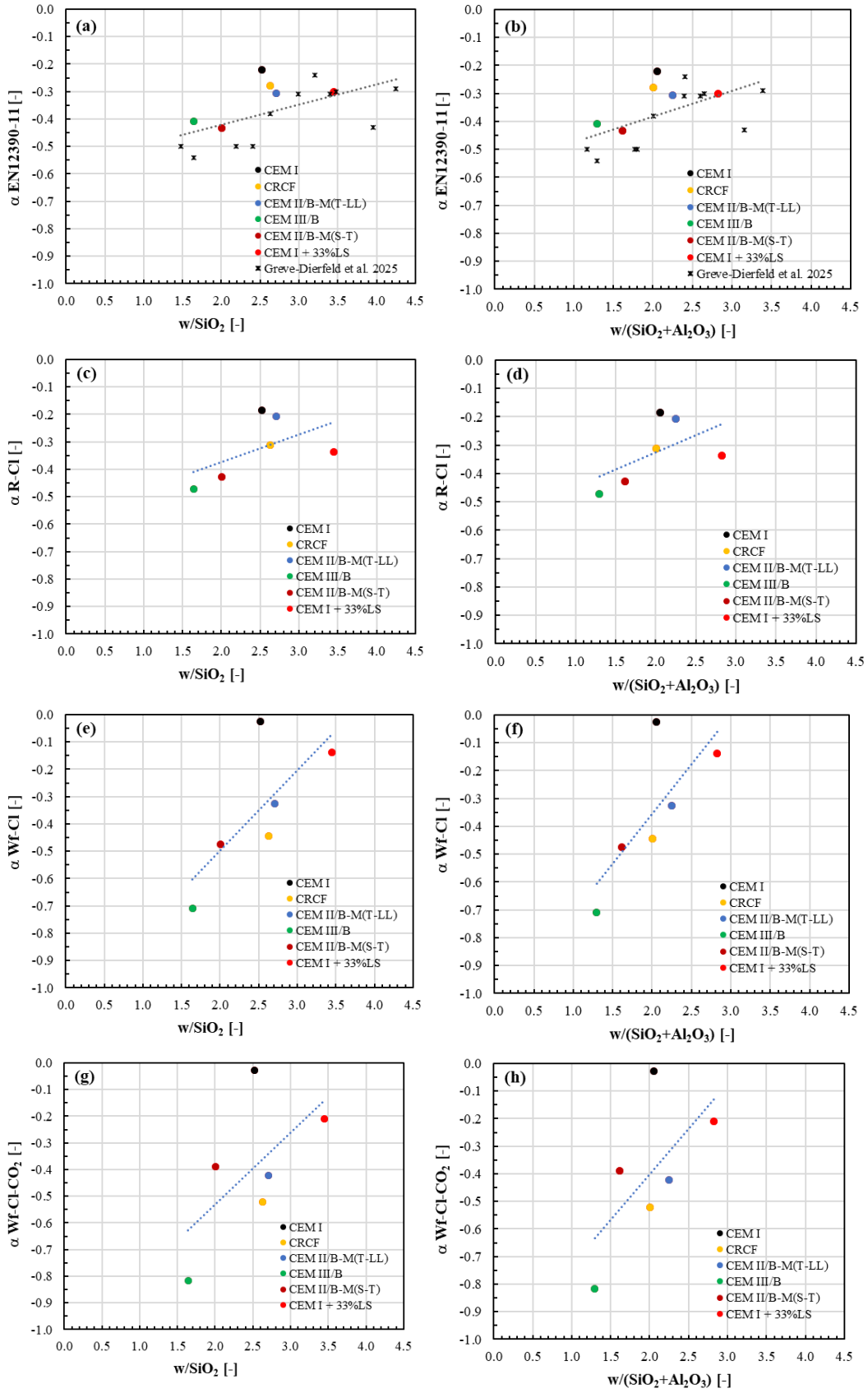

Fig. 69 *Correlation of the age exponent with w/SiO_2, and $w/(SiO_2 + Al_2O_3)_r$ determined under (a) EN 12390-11, (c) R0-Cl, (e) Wf-Cl, and (g) Wf-Cl-CO_2 conditions, and with $w/(SiO_2 + Al_2O_3)_r$ determined under (b) EN 12390-11, (d) R0-Cl, (f) Wf-Cl, and (h) Wf-Cl-CO_2 conditions.*

It is evident that the correlation between the age exponent and concrete composition is relatively weak, mainly due to the large uncertainties associated with the determination of the age exponent. A slightly better correlation is observed for $w/(SiO_2 + Al_2O_3)_r$ and under cyclic exposure conditions.

Fig. 70 presents the correlation between the chloride ingress depth $x_{Cl,x\%}$ corresponding to a chloride concentration of x = 1.0 wt.-% relative to binder under Wf-Cl and Wf-Cl-CO_2 conditions and (a, b) w/SiO_{2r} and (c, d) $w/(SiO_2 + Al_2O_3)_r$, respectively.

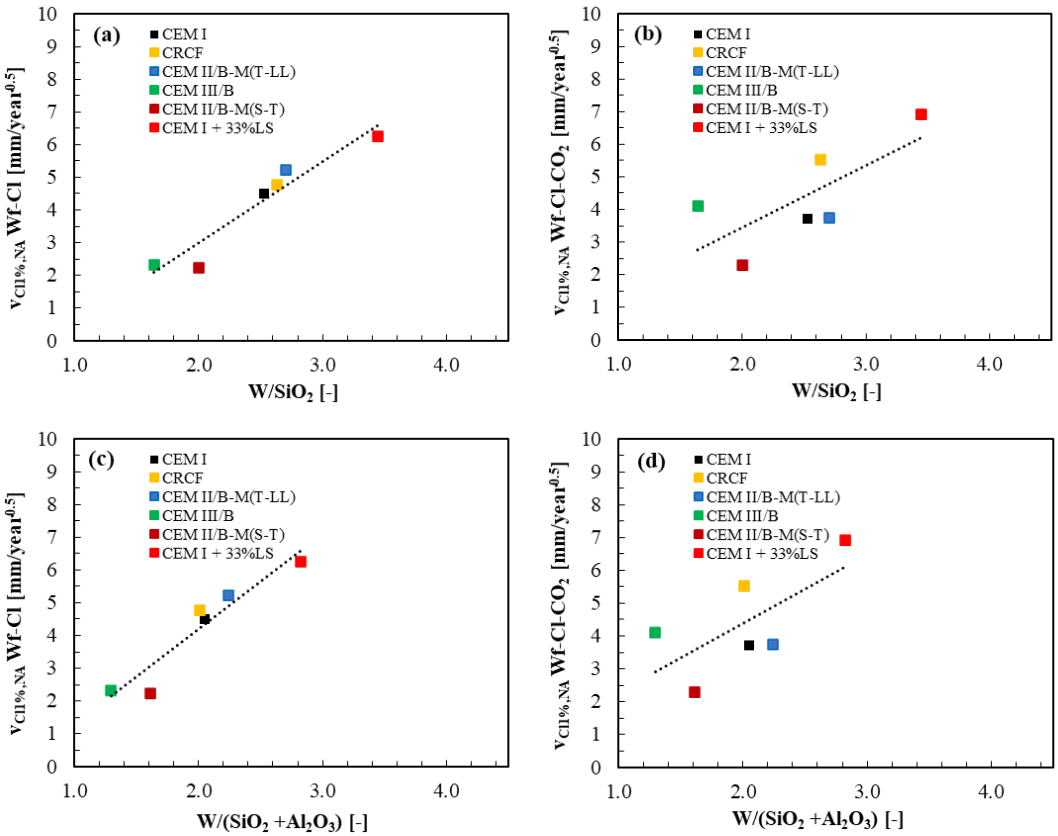

Fig. 70 *Correlation between $v_{Cl1\%}$ determined under Wf-Cl and w/SiO_2 (a), Wf-Cl-CO_2 and w/SiO_2 (b), Wf-Cl $w/(SiO_2 + Al_2O_3)$ (c) and Wf-Cl-CO_2 and $w/(SiO_2$ and $Al_2O_3)$ (d).*

Both correlations give reasonable coefficients of determination.

Fig. 70 shows that the chloride ingress rate $v_{Cl,1\%}$ exhibits a clear positive correlation with both w/SiO_{2r} and $w/(SiO_2 + Al_2O_3)_r$ under Wf-Cl and Wf-Cl-CO_2 conditions. In all four subfigures, an increase in the water-to-reactive-oxide ratio is associated with higher chloride ingress rates, indicating reduced resistance to chloride penetration.

For both exposure regimes, concretes with lower w/SiO_{2r} and $w/(SiO_2 + Al_2O_3)_r$ ratios generally show lower ingress rates, reflecting their denser microstructure and higher chloride binding capacity. In contrast, mixes with higher ratios exhibit increased scatter and systematically higher $v_{Cl,1\%}$ values, consistent with a more open pore structure and reduced binding potential.

The correlations obtained using $w/(SiO_2 + Al_2O_3)_r$ (Fig. 70c and d) are slightly stronger than those obtained using w/SiO_{2r} (Fig. 70a and b). This suggests that the combined contribution of silica and alumina, which governs the formation of C-(A)-S-H and AFm phases, plays a more comprehensive role in controlling chloride transport and binding than silica alone.

Under Wf-Cl-CO_2 conditions, a slightly larger scatter is observed compared to Wf-Cl conditions. This increased variability can be attributed to the additional influence of carbonation, which alters pore structure and reduces chloride binding phases.

Nevertheless, the general trend remains similar, indicating that binder composition remains a dominant factor governing chloride ingress even under combined carbonation and chloride exposure.

Overall, the results demonstrate that both w/SiO_{2r} and $w/(SiO_2 + Al_2O_3)_r$ are suitable parameters for describing chloride ingress behaviour under cyclic exposure conditions, with a slight advantage for the combined oxide ratio.

4.5.7 Pore solution composition

Fig. 71 shows the measured molar concentrations of Cl^- (free chlorides in the pore solution), Ca^{2+}, and pH (top). The measurements were performed using the ex-situ leaching (ESL) method on powdered samples taken in 5 mm depth intervals and therefore tend to be somewhat lower than the actual concentrations in the in-situ pore solution.

In addition to the measured values, the calculated total ion concentrations for non-carbonated samples as a function of the added sodium chloride content are presented (middle). Furthermore, the calculated ion concentrations for carbonated samples, assuming exposure to 30 g CO_2, as a function of Cl^- concentration are shown (bottom).

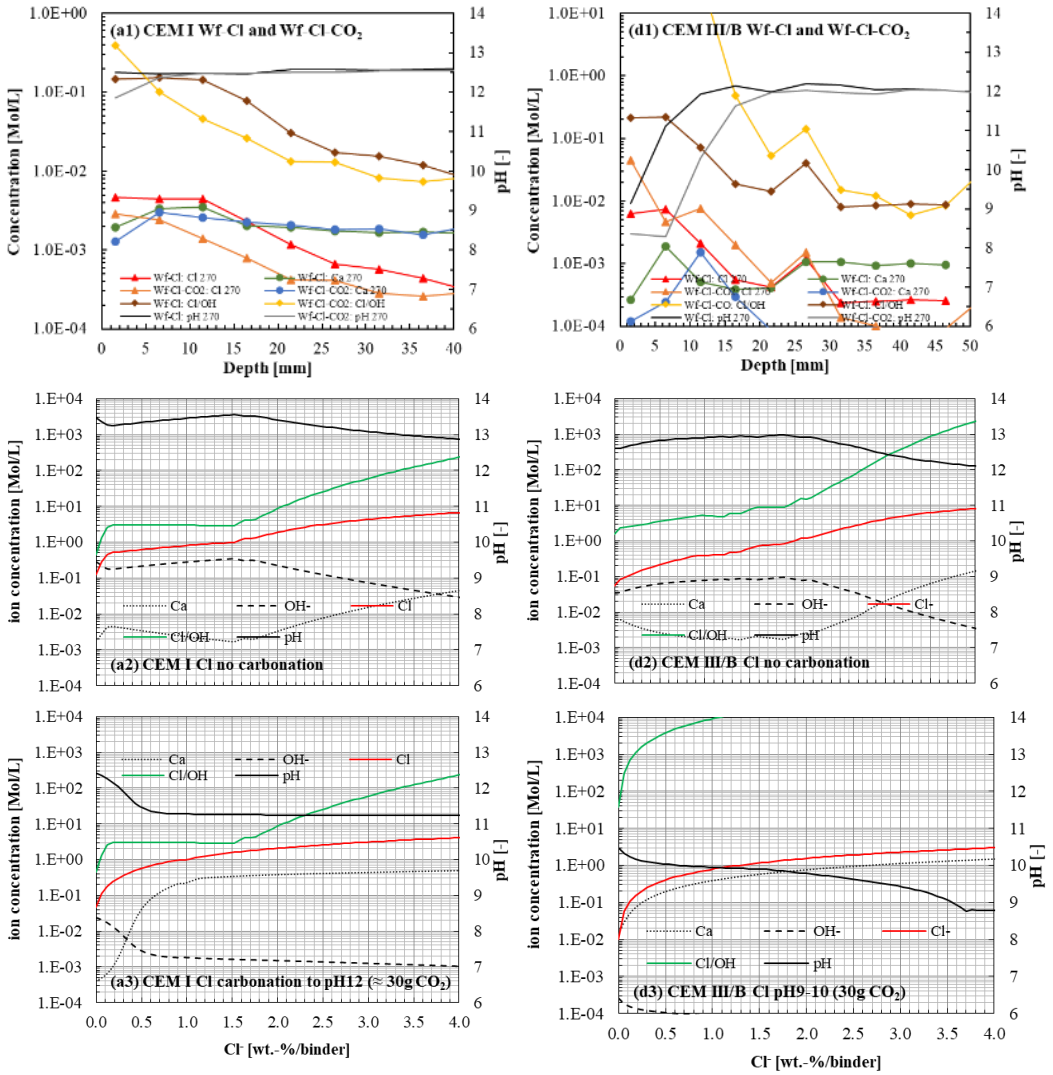

Fig. 71 *Chloride Ion concentration (C_f), Ca concentration and pH determined with ISE and pH Electrode after 270 days of cyclic exposure (top) in comparison with the GEMS modelling results for pore solution composition of the respective ions without carbonation influence (middle) with a certain carbonation influence corresponding to the surface pH (bottom) for (a) CEM I and (b) CEM III/B.*

When comparing cyclic exposure conditions without and with accelerated carbonation, systematic changes in pore solution composition are observed. In the carbonated zone, free chloride concentrations increase, while Ca^{2+} concentrations decrease. This indicates that $CaCO_3$ formed during carbonation is not dissolved during the ESL procedure and that the ISE measurements reflect Ca^{2+} concentrations in equilibrium with calcite, as expected for carbonated concrete.

Carbonation therefore leads to a redistribution of chlorides and calcium within the concrete cover. The release of previously bound chlorides during decalcification, combined with the reduction of alkaline buffering capacity, results in locally increased free chloride concentrations.

Consequently, the critical $[Cl^-/OH^-]$ ratio governing steel passivation is strongly increased in the carbonated zone compared to Wf-Cl samples with little or no carbonation. This demonstrates that carbonation significantly enhances the corrosivity of chloride-contaminated concrete by simultaneously reducing alkalinity and increasing chloride availability.

Thermodynamic calculations indicate a non-linear increase of $[Cl^-/OH^-]$ with chloride content. At approximately 4 wt.-% Cl relative to binder, the ratio is highest for slag-containing cements and lowest for CEM I, reflecting differences in chloride binding and buffering behaviour. After carbonation, this increase becomes much more pronounced, while the same ranking among cement types is preserved.

These trends are confirmed by ISE measurements. Although absolute values obtained by ESL are lower than in-situ pore solution concentrations, the same systematic dependencies on binder type, chloride content, and carbonation are observed.

A comparison between CEM I and CEM III/B reveals distinct differences in pore solution chemistry. In the non-carbonated state, CEM III/B exhibits lower Ca^{2+} concentrations and slightly lower pH values due to its lower portlandite content. Under accelerated carbonation, these differences become more pronounced, with a stronger reduction in Ca^{2+} concentration and pH in CEM III/B, indicating a lower buffering capacity against decalcification.

As a result, OH^- concentrations decrease more strongly in CEM III/B, leading to markedly higher $[Cl^-/OH^-]$ ratios. Both thermodynamic modelling and ISE measurements consistently show that this increase is more pronounced in CEM III/B than in CEM I.

Overall, CEM III/B is more sensitive to combined chloride ingress and carbonation than CEM I. The stronger alkalinity loss and higher $[Cl^-/OH^-]$ ratios indicate an increased risk of corrosion initiation in slag-containing concretes under simultaneous exposure conditions.

4.5.8 Phase change during chloride ingress

Fig. 72 shows the calculated phase changes during chloride ingress in hydrated, non-carbonated binders as a function of added sodium chloride (wt.-% relative to binder) for (a) CEM I, (b) CRCF, (c) CEM II/B-M(T-LL), (d) CEM III/B, (e) CEM II/B-M(S-T), and (f) CEM I + 33% LS.

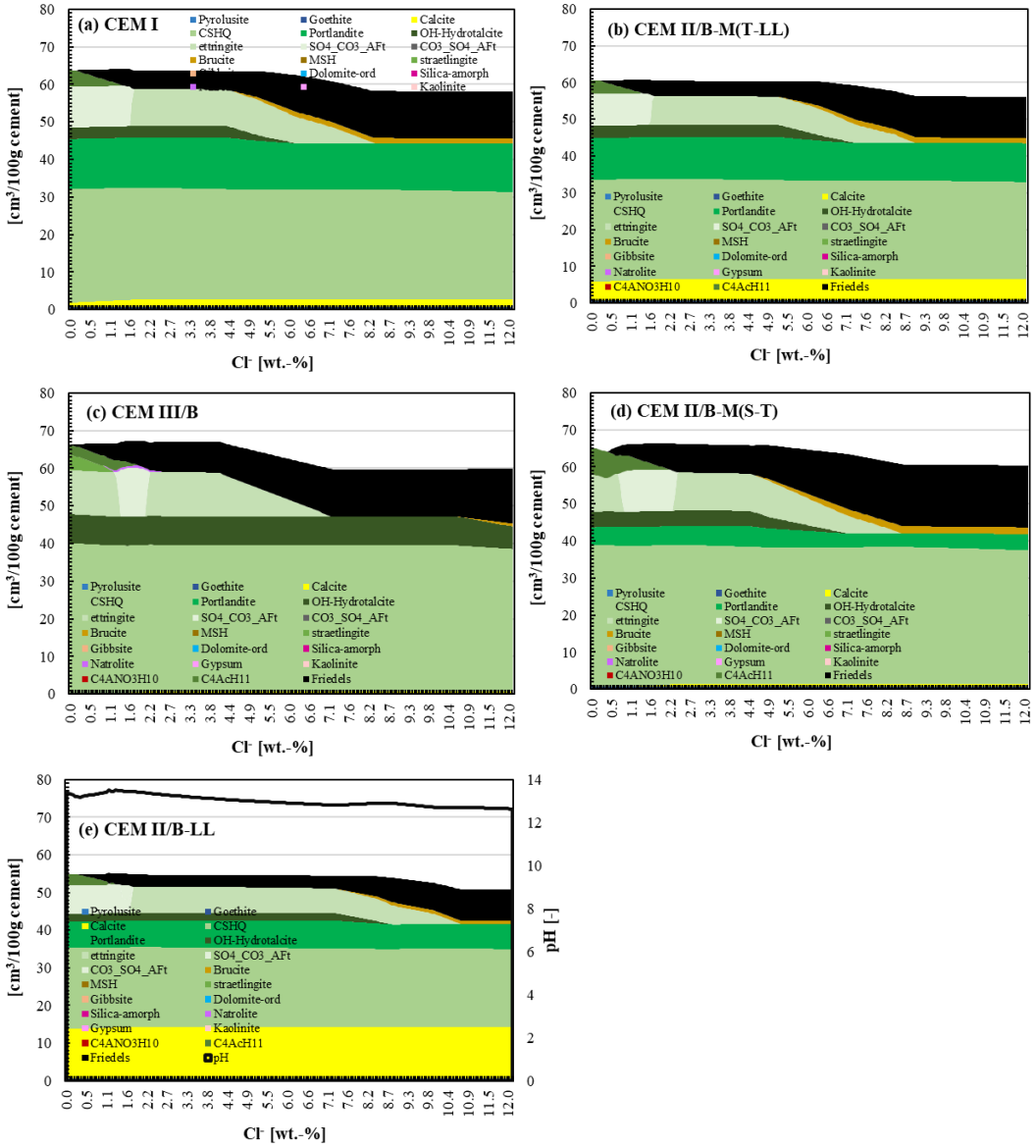

Fig. 72 *Phase change in g during chloride ingress for (a) CEM I, (b) CRCF, (c) CEM III/B, (d) CEM II + 33% LS from left.*

Fig. 72 illustrates the calculated evolution of hydrate phases in hydrated, non-carbonated binders with increasing chloride content. For all investigated binders, initial chloride ingress leads to the transformation of monocarbonate and other AFm phases into ettringite and Friedel's salt through anion exchange and phase transformation reactions.

At low to moderate chloride contents (up to approximately 1.6 wt.-% relative to binder, and up to more than 3 wt.-% for CRCF), Friedel's salt formation increases significantly, enhancing the effective chloride binding capacity. The upper limit of this capacity depends mainly on the initial amount of monocarbonate and related AFm phases.

With further chloride addition, Friedel's salt formation slows down, indicating progressive depletion of AFm phases and saturation of chloride binding. Additional chlorides are then increasingly present in the pore solution rather than being chemically bound.

The extent of this saturation range strongly depends on binder composition, particularly on the contents of ettringite and OH-hydrotalcite. Binders with lower amounts of these phases exhibit a wider chloride range with limited additional binding.

For CRCF, a renewed increase in Friedel's salt is predicted only at very high and practically unrealistic chloride contents, accompanied by destabilization of ettringite.

Overall, the results demonstrate that chloride binding in hydrated, non-carbonated systems is primarily controlled by the availability and stability of AFm phases. Initial chloride ingress enhances binding, whereas at higher chloride contents binding becomes saturated and increasingly governed by binder-specific phase assemblages, explaining the observed differences between cement types. The results indicate that chloride binding through Friedel's salt formation can temporarily delay corrosion initiation at low to moderate chloride loads. Binders with higher AFm contents therefore show improved initial resistance to chloride ingress.

However, this effect is limited, as chloride binding capacity becomes saturated once the available AFm phases are depleted. Beyond this point, additional chlorides increasingly remain in the pore solution, leading to a rapid increase in corrosion risk. Chloride binding should therefore be regarded as a temporary buffer rather than a long-term protective mechanism.

4.6 Results of accompanying investigations

4.6.1 Phase assemblage combined action

Fig. 73 shows the calculated phase changes during carbonation of chloride-contaminated concrete. As an example, a chloride content of 2 wt.-% relative to binder, introduced by NaCl addition, was selected for the calculations. This chloride level corresponds to intermediate concentrations observed in the present investigations (approximately 0.25 wt.-% relative to concrete).

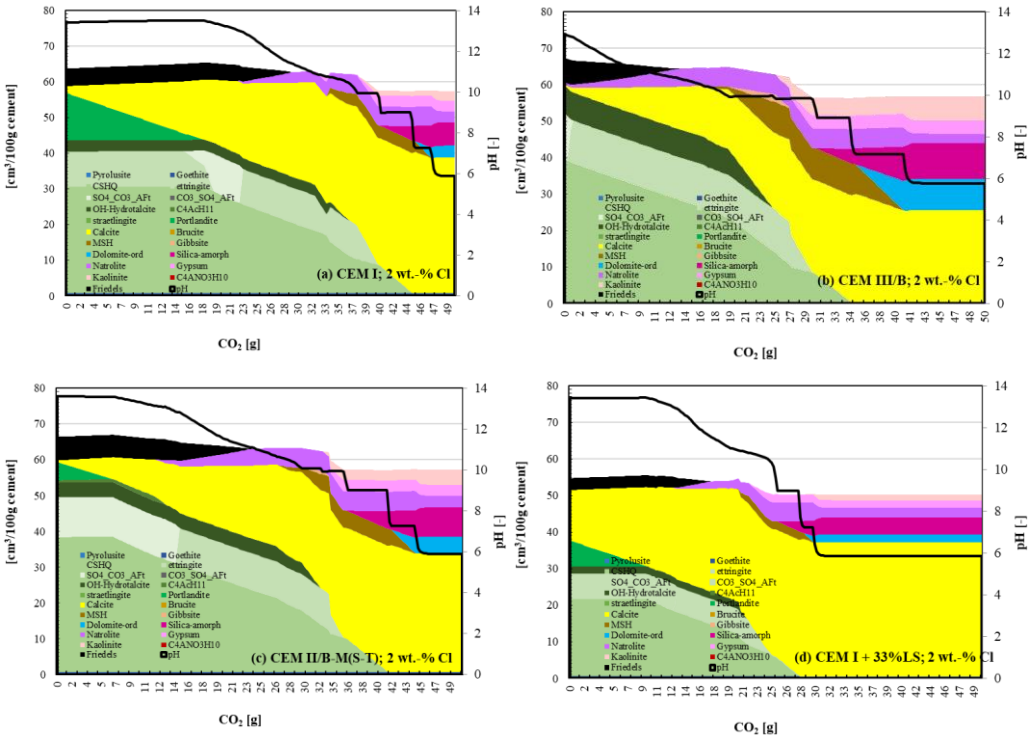

Fig. 73 *Phase change in during carbonation of paste w/b 0.5 with 2 wt.-%Cl/binder (a) CEM I (b) CEM III/B (c) CEM II/B-M(S-T) (d) CEM I + 33% LS.*

Fig. 73 illustrates the calculated evolution of hydrate phases for selected binders at a chloride content of 2 wt.-% relative to binder during progressive carbonation. For all investigated systems, carbonation initially leads to the depletion of portlandite, followed by the destabilization of AFm and AFt phases.

The modelling results show that the release of chemically bound chlorides from Friedel's salt starts upon portlandite depletion and is largely completed before significant dissolution of ettringite occurs. This indicates that chloride remobilization begins at an early stage of carbonation, when the alkaline buffering capacity is already reduced but AFt phases are still present.

With further carbonation, ettringite progressively dissolves, which is accompanied by a pronounced decrease in pore solution pH to values around 10. This phase transition marks a critical stage, as both chemical chloride binding and alkalinity are strongly reduced.

As a consequence, a significant increase in free, corrosion-relevant chloride concentration occurs already at pH values around 11. At this stage, the concrete is typically not yet identified as carbonated when using conventional phenolphthalein indicators. This implies that chloride-induced depassivation may occur before visible carbonation is detected in practice.

Binder-dependent differences are observed in the stability ranges of Friedel's salt and ettringite. Slag-containing binders and blended cements generally exhibit earlier phase transformations and more pronounced alkalinity loss compared to CEM I, reflecting their lower portlandite content and buffering capacity.

Overall, the results demonstrate that the combined action of carbonation and chloride ingress leads to an early remobilization of bound chlorides and a rapid reduction of alkalinity. This creates critical pore solution conditions for corrosion initiation at an early stage of carbonation, well before complete decalcification of the cement matrix.

4.6.2 Elemental distribution combined action

Micro XRF images have been taken from selected samples with CEM III/B concrete and samples with CEM II/B-LL after 270 days of exposure. The samples have been selected due to their high chloride content and deep carbonation depths. Fig. 74 shows pictures of the CEM III/B samples as well as the distribution of calcium, chloride and titanium. The sample width was 50 mm. The brighter the yellow color the larger is the Ca concentration. If no Ca is available, the figure appears blue. The darker the red color the higher the chloride concentration is. If no chlorides are visible, the figure appears blue. Similarly, the brighter the color the higher the titanium concentration.

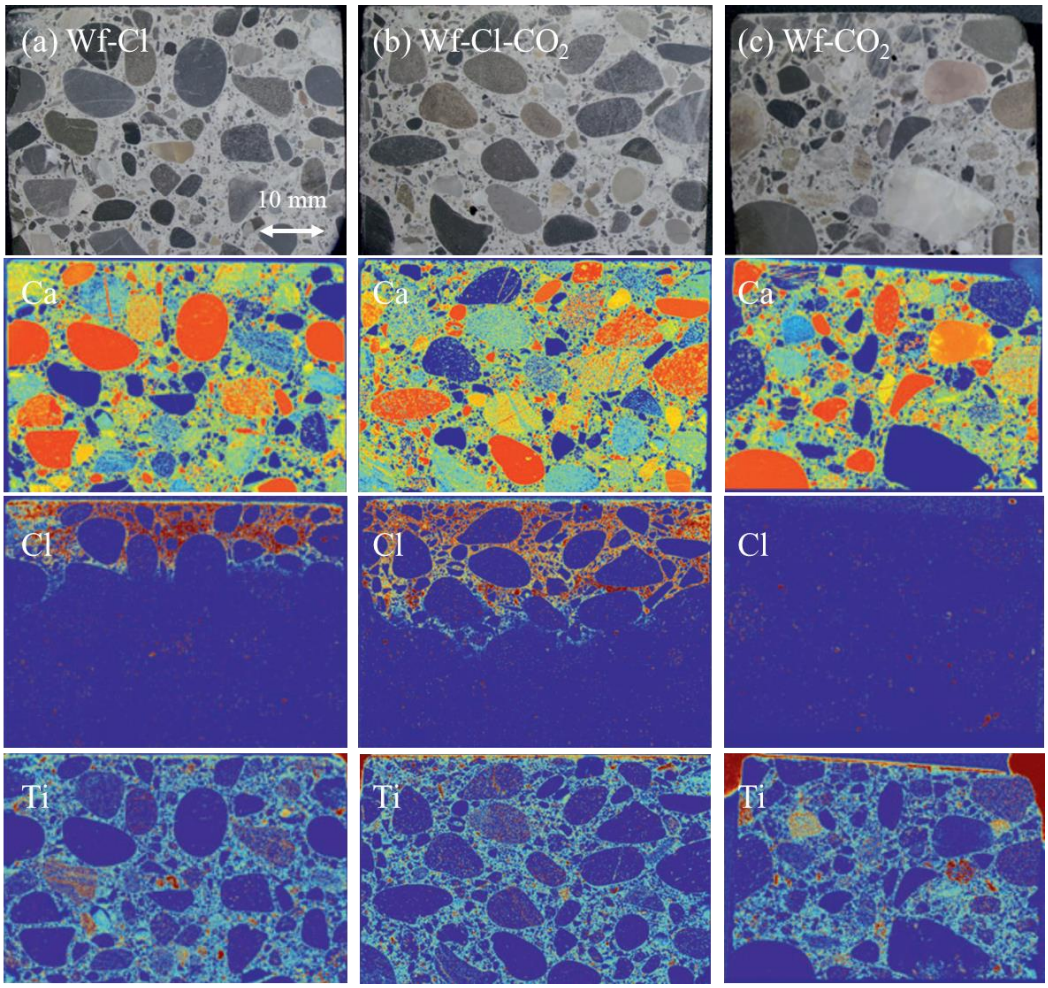

Fig. 74 *μXRF image for CEM III/B concretes after 270 days in cyclic (a) Wf-Cl, (b) Wf-Cl-CO_2 and (c) Wf-CO_2 condition.*

From Fig. 74 it is apparent, that no Ca depletion occurs in all exposure condition i.e. in Wf-Cl condition where cyclic exposure to 30g/L NaCl in deionized water solution upon storage in air occurs as well as in Wf-Cl-CO_2 condition, where the samples are carbonated at 4 vol.-

% CO_2 during dry out and in Wf-CO_2 condition, where the samples are cyclic exposed to deionized water and exposed to 4 vol.-% CO_2 during dry out. It must be stated that the samples, in all conditions, suffered from carbonation. In Wf-Cl the carbonation depth was around 4 mm, in Wf-Cl-CO_2 around 12 mm and in Wf-CO_2 around 15 mm. Hence no Ca was available because Ca-bearing phases in the surface region were already transformed to calcium carbonate polymorphs and these calcium carbonate polymorphs are less likely to dissolve Ca in this close to neutral solution, although carbonic acid (Wf-Cl-CO_2 and Wf-CO_2 exposure) would be able to dissolve calcite.

No chlorides have accidentally entered the Wf-CO_2 samples. The chloride ingress is clearly visible in Wf-Cl and Wf-Cl-CO_2 condition. In Wf-Cl condition the color changes from a small bright yellow front to dark red. The depth with dark red (chloride content ≈> 0.18 wt.-%/concrete) corresponds to the carbonation depth (≈ 4 mm depth). This peak concentration corresponds well with the chloride profile determined, except that the peak concentration was smeared in the depth profiles to 6.5 mm depth, cp. Fig. 53 (d2). The peak concentration is less than the influential depth. Upon this peak concentration depth, the chloride concentration strongly declines to bright red at around 10 mm depth. The chloride distribution in the Wf-Cl-CO_2 sample shows two layers of lower chloride concentration but also two layers of higher chloride concentration. The highest concentration (peak) is in app. 15 mm depth which corresponds with the carbonation depth of this sample. The intermediate layer with higher chloride concentration may be due to incoming new chlorides from the latest NaCl exposure cycle that precipitate during drying process. These two layers of lower and higher concentration can also be found in the measured chloride contents in Fig. 53 (d3).

The µXRF elemental maps of CEM I + 33% limestone (LS) concrete after exposure to Wf-Cl, Wf-Cl-CO_2 and Wf-CO_2 are presented in Fig. 75, showing the distribution of calcium (Ca), chloride (Cl) and titanium (Ti).

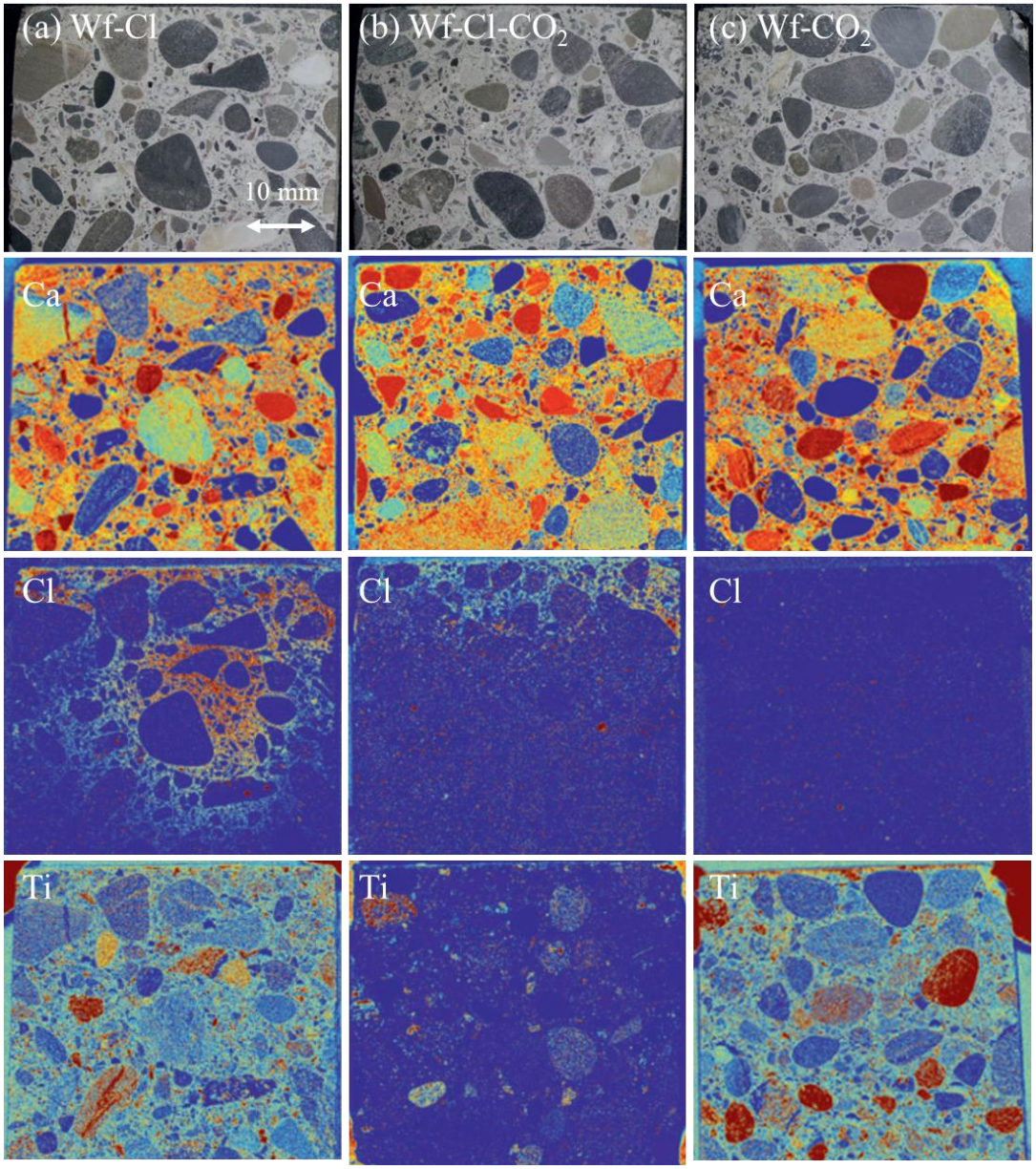

Fig. 75 *µXRF elemental maps of CEM I + 33% LS concrete after 270 days of cyclic exposure to (a) Wf-Cl, (b) Wf-Cl-CO_2 and (c) Wf-CO_2.*

Although the overall calcium content is expected to be comparable across all exposure conditions, regions of Ca enrichment associated with $CaCO_3$ formation appear more pronounced in the Wf-Cl-CO_2 condition. No evidence of calcium depletion is observed.

Elevated chloride concentrations are evident in the Wf-Cl condition. In the Wf-Cl-CO_2 condition, chloride enrichment is observed at the exposed surface, with concentrations decreasing to a depth of approximately 7 mm, consistent with the measured chloride profiles. This behaviour is clearly reflected in the corresponding µXRF Cl map. As expected, no chloride ingress is detected in the Wf-CO_2 condition (Fig. 75c).

The titanium distribution appears largely unaffected under isolated cyclic chloride or cyclic carbonation exposure. However, a localised depletion is observed in the Wf-Cl-CO_2 condition. In addition to chloride dissolution processes, a possible wash-out of titanium bearing phases may have occurred. As titanium is reported to accelerate cement hydration and promote C-S-H formation [Neto et al., 2022], partial decalcification of hydration products could explain the observed depletion. Nevertheless, such a mechanism would be

expected to occur in all exposure conditions, and the reason for the selective depletion under combined chloride–carbonation exposure therefore remains unclear.

Figure 76 presents the μXRF elemental maps of sulphur (S), aluminium (Al), sodium (Na), magnesium (Mg), iron (Fe) and potassium (K) for CEM I + 33% limestone (LS) concrete after 270 days of cyclic exposure to (a) Wf-Cl and (b) Wf-CO_2.

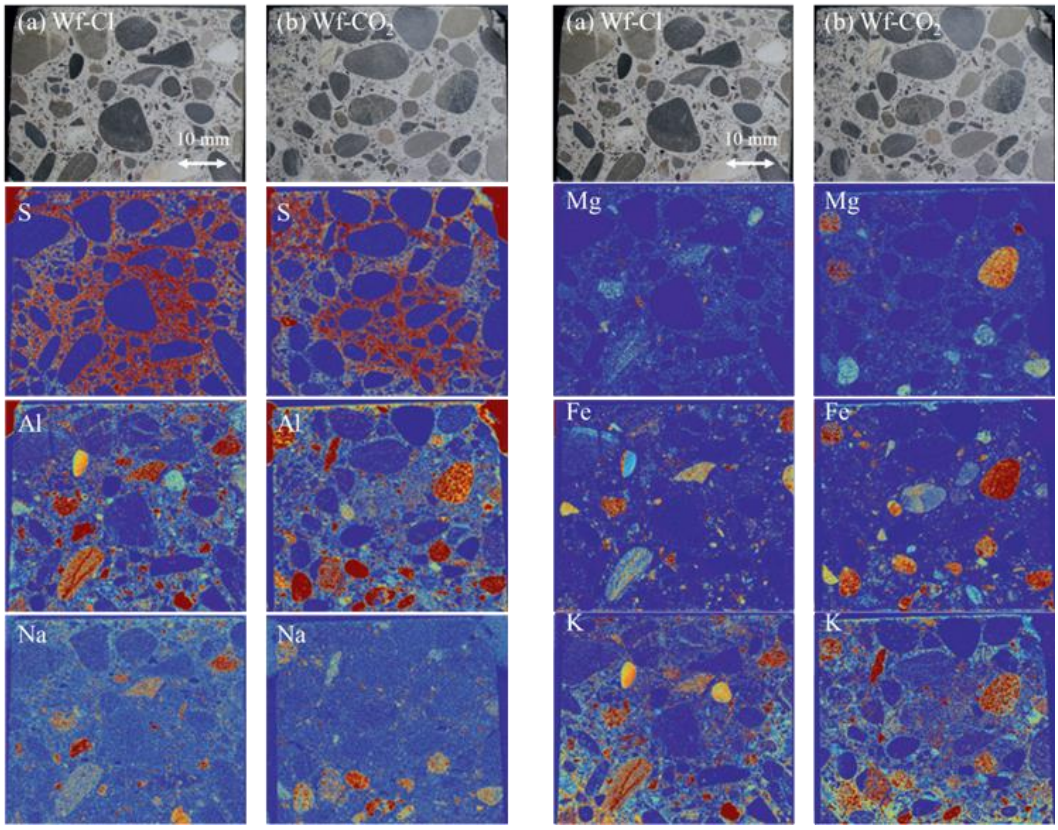

***Fig. 76** μXRF elemental maps of S, Al, Na, Mg, Fe and K in CEM I + 33% LS concrete after 270 days of cyclic exposure to (a) Wf-Cl and (b) Wf-CO_2.*

The sulphur distribution appears largely unaffected by the exposure conditions. No distinct enrichment or depletion zones are observed.

In contrast, aluminium and iron show surface-near enrichment in the carbonated specimens (Wf-CO_2). This may indicate the formation of secondary alumina- and iron-rich phases during carbonation, potentially associated with silica-rich gel formation.

Sodium concentrations are elevated in the chloride-exposed specimens (Wf-Cl), consistent with the NaCl exposure solution and the ingress of alkali ions.

Potassium and magnesium exhibit localised enrichment near the exposed surface in the Wf-CO_2 condition. This behaviour may be related to the formation of sparingly soluble carbonate phases or the transformation of hydration products under reduced pH conditions. However, thermodynamic modelling did not confirm the formation of stable carbonate or zeolitic phases under the investigated conditions.

4.6.3 Pore structure

Fig. 77 (a–i) presents the measured total porosity (φ_n), hydration pore porosity (φUE) and air porosity (φair) of reference samples, fully chloride-loaded samples and carbonated samples.

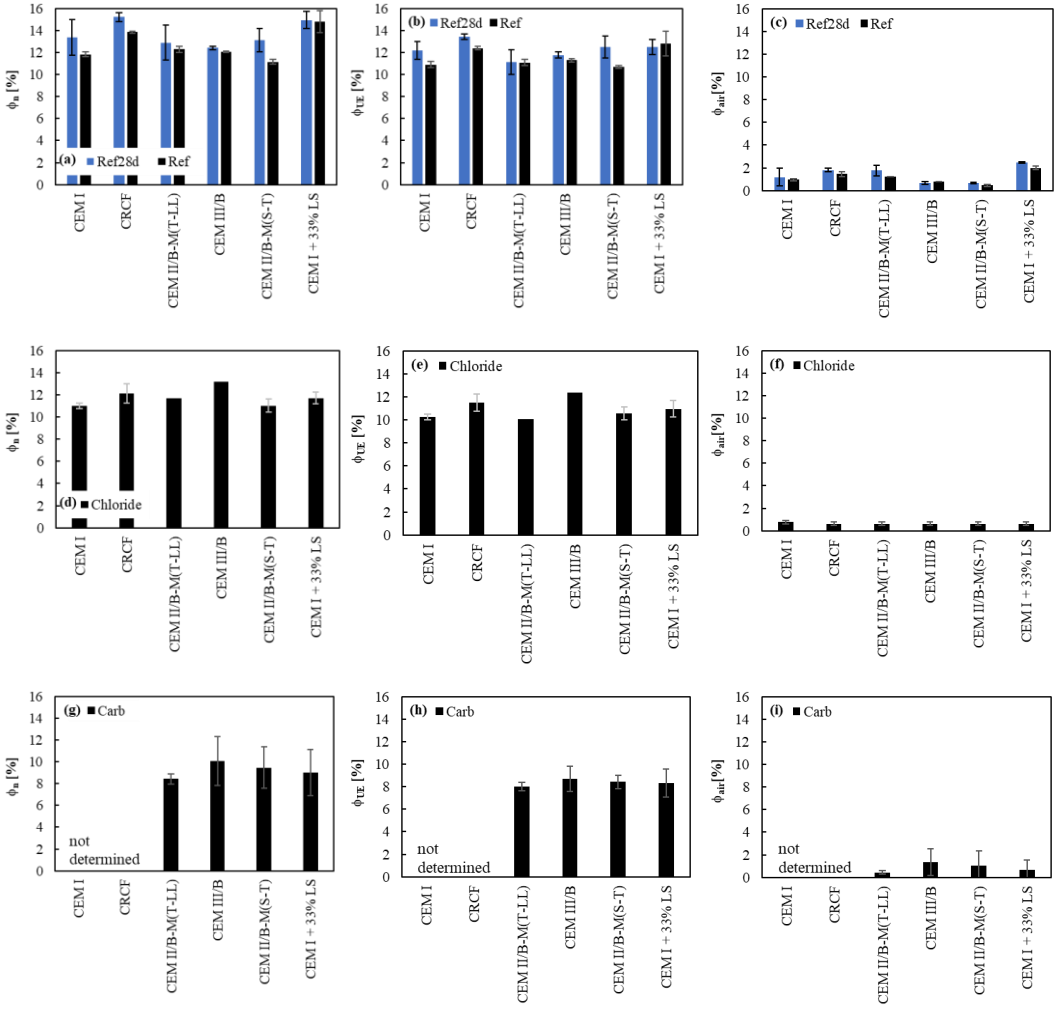

***Fig. 77** Total porosity φ_n (a, d, g), hydration pore porosity φ_{UE} (b, e, h) and air porosity φ_{air} (c, f, i) of reference samples after 28 and 91 days of water curing (a–c), fully chloride-loaded samples (d–f) and carbonated samples (g–i).*

The total porosity (φ_n) and hydration pore porosity (φ_{UE}) decrease with increasing hydration time (28 to 91 days), as shown in Fig. 77a and Fig. 77b, reflecting continued hydration. This effect is more pronounced for the slag-containing cements. In contrast, the air porosity (φair) remains essentially unchanged with further hydration (Fig. 80c).

Compared with the reference concrete, the incorporation of sodium chloride leads to a reduction in both total and hydration pore porosity to approximately 0.9 times the original value, particularly for CEM I and CRCF concretes (Fig. 77d–e). This is consistent with the findings of Shi et al. (2016), who reported reductions in the range of 0.89–0.91. The decrease in total porosity is slightly greater than that of the hydration pores, resulting in a minor reduction in calculated air porosity upon chloride ingress.

CEM III/B is capable of binding larger amounts of chlorides due to its higher content of carbonate- and alumina-bearing phases. Therefore, a reduction in porosity upon chloride exposure was expected. In the present experiments, however, the hydration pore volume remains largely unchanged.

Compared with the reference concrete, carbonation results in a reduction in total porosity. This decrease is less pronounced for CEM III/B samples. These observations are in agreement with previous studies (e.g. [79, 112, 175]). The reduction in total porosity is more pronounced under carbonation than under chloride ingress, as also reported in [114–115].

4.6.4 Capillary adsorption

Fig. 78 compares the coefficients of capillary absorption of reference concrete cured in water for 28 days (Ref28) and for 90 days (Ref) (Fig. 78a). The rate of capillary water absorption (S_c, in $mm \cdot m^{-2} \cdot h^{-0.5}$) was calculated based on the hydration pore volume (φUE) of the respective samples. No coefficient of capillary absorption was determined for the carbonated specimens due to their limited sample height (Fig. 78b).

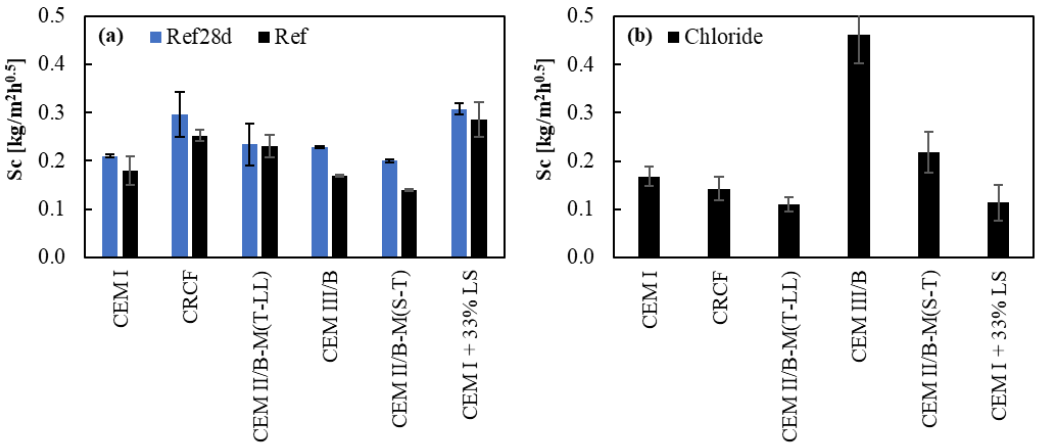

Fig. 78 *Coefficient of capillary absorption of (a) reference samples and (b) fully chloride-loaded samples.*

As shown in Fig. 78a, the coefficient of capillary absorption is slightly higher at early age (28 days) compared with approximately seven months of curing. This behaviour is consistent with the higher total and hydration pore porosity at early age.

Most chloride-loaded samples (Fig. 78b) exhibit lower coefficients of capillary absorption than the corresponding reference specimens, except for the slag-containing binders (CEM III/B and CEM II/B-M (S-T)). Although slag cements possess a higher chemical chloride binding capacity, their total porosity remained comparable, while the coefficient of capillary absorption increased after chloride exposure.

This behaviour may indicate that long-term migration under high voltage induced microstructural alterations, particularly in the slag-containing systems, which were exposed for longer durations. Possible mechanisms include pore structure modification, phase transformation during chloride binding, or changes in pore connectivity affecting capillary transport.

Fig. 79 presents the coefficients of capillary absorption of chloride-contaminated concrete subsequently tested in water (Fig. 79a). The samples were exposed to 30 g/L NaCl solution by migration until chloride dilution occurred in the anode compartment. The capillary absorption coefficient (S_c) was calculated from the hydration pore volume (φ_{UE}) of each specimen. As in Fig. 79, no coefficient was determined for carbonated specimens due to their limited sample height (Fig. 79b).

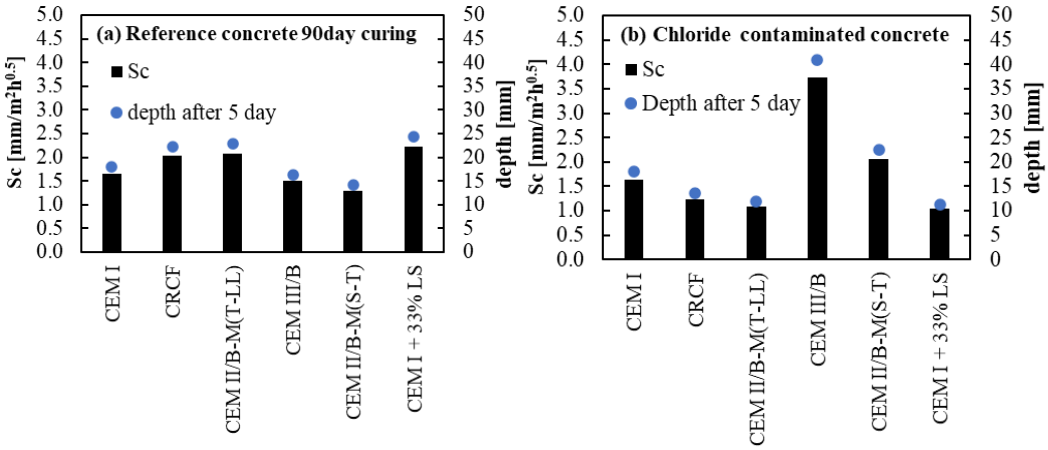

Fig. 79 *Coefficient of capillary absorption and corresponding theoretical water ingress depth of (a) reference samples and (b) fully chloride-loaded samples.*

In the absence of chloride contamination (Fig. 79a), CRCF, CEM II/B-M (T-LL) and CEM I + 33% LS exhibit the highest calculated theoretical ingress depths, ranging from approximately 20 to 25 mm. In contrast, CEM III/B and CEM II/B-M (S-T) show the lowest theoretical ingress depths, between 10 and 15 mm.

Following chloride contamination (Fig. 79b), CRCF, CEM II/B-M (S-T) and CEM I + 33% LS display the smallest theoretical ingress depths (approximately 10–15 mm). Conversely, CEM III/B and CEM II/B-M (S-T) exhibit increased theoretical ingress depths, ranging from approximately 25 to 40 mm.

Thus, for most binder systems, chloride contamination leads to a reduction in the coefficient of capillary absorption and the associated theoretical water ingress depth. However, the slag-containing mixes deviate from this trend, showing an increase in calculated ingress depth despite their higher chemical chloride binding capacity.

4.6.5 Resistivity

Fig. 80 presents the measured electrical resistivity as a function of relative humidity (RH) for (a) reference specimens, (b) fully chloride-loaded specimens and (c) fully carbonated specimens. The graphs on the left show resistivity over the entire RH range, whereas the graphs on the right compare resistivity at 57% RH and under water-saturated conditions. It should be noted that 100% RH in the left-hand figures corresponds to fully water-saturated samples.

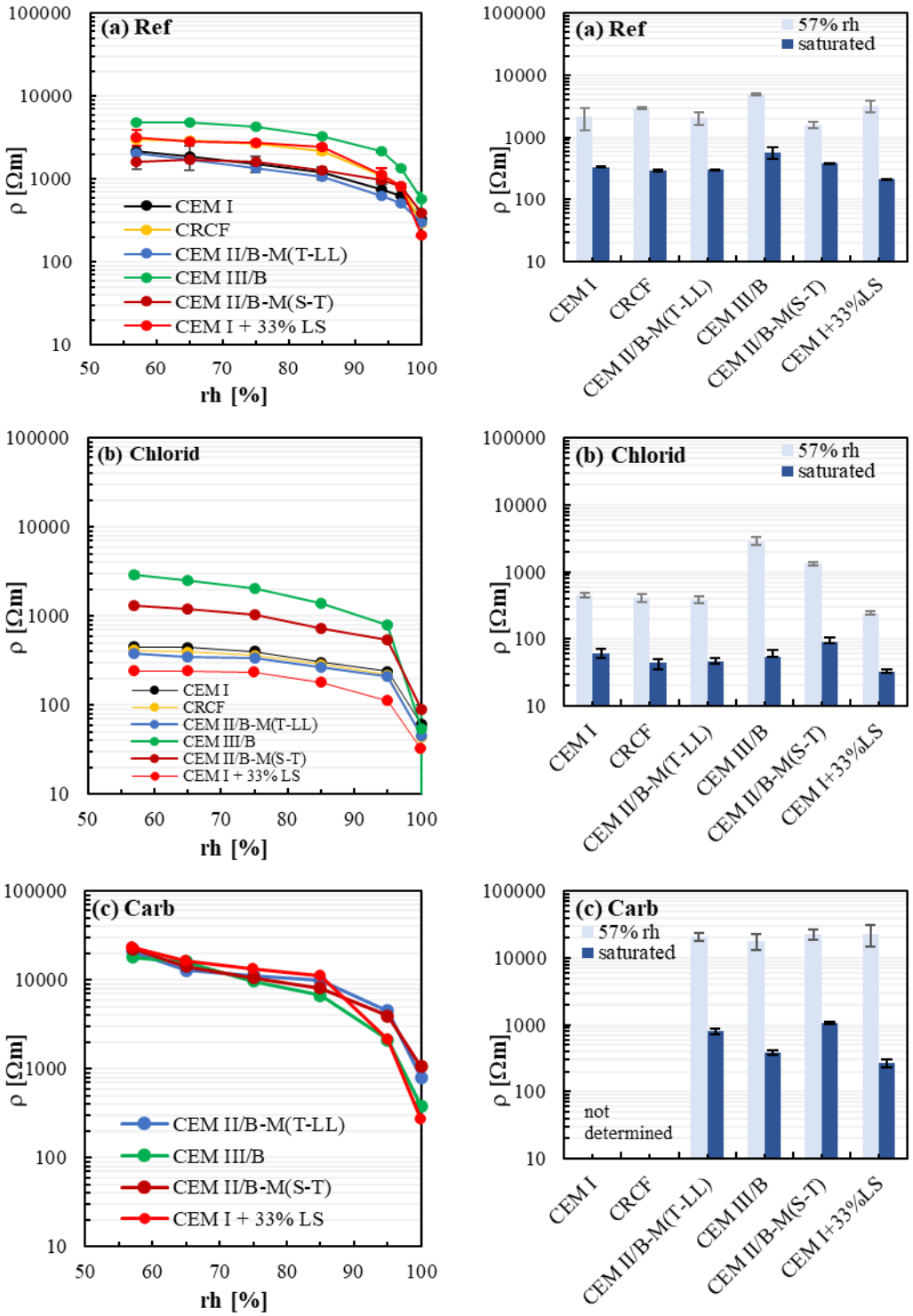

Fig. 80 *Electrical resistivity as a function of relative humidity (left) and comparison of resistivity at 57% RH and under water-saturated conditions (right) for (a) reference samples, (b) fully chloride-loaded samples and (c) fully carbonated samples.*

Across all binder types and throughout the full range of relative humidity, resistivity increases in the following order: chloride-contaminated samples (approximately 20–2000 Ω·m), reference samples (approximately 200–6000 Ω·m) and carbonated samples (approximately 300–20,000 Ω·m). Thus, chloride contamination leads to the lowest resistivity values, whereas carbonation results in the highest resistivity.

For all mixtures, resistivity decreases with increasing relative humidity. The decrease is moderate up to approximately 85% RH and becomes more pronounced towards full saturation, reflecting the increasing connectivity of the pore solution and enhanced ionic transport.

CEM III/B exhibits the highest resistivity under reference and chloride-contaminated conditions. However, this distinction becomes less pronounced after carbonation, where resistivity values of the different binders converge.

Under water-saturated conditions, CEM I + 33% LS shows the lowest resistivity across all exposure regimes. In contrast, slag-containing binders (CEM III/B and CEM II/B-M (S-T)) show the highest resistivity as long as the concrete is not carbonated.

The higher resistivity of slag-containing concretes cannot be explained solely by total porosity. Although a refined pore structure would normally increase the degree of saturation and thereby reduce resistivity, slag systems are characterised by altered pore solution chemistry and reduced ionic strength, which decrease ionic conductivity and thus increase resistivity.

Carbonation significantly increases resistivity in all binder systems. This increase is attributed not only to pore refinement due to $CaCO_3$ precipitation but also to substantial changes in pore solution composition, including reduced hydroxide concentration and altered alkali distribution. After carbonation, the resistivity differences between binders diminish, suggesting that carbonation leads to a more uniform pore solution chemistry and transport behaviour across the different cement types.

Under dry reference and dry carbonated conditions, CEM I + 33% LS exhibits higher resistivity than most other binders, except for the slag-containing systems. This behaviour is consistent with its comparatively higher total porosity, which leads to a lower degree of saturation under dry conditions. Under water-saturated conditions, however, the higher ionic conductivity of its pore solution results in lower resistivity. This trend is consistent with the porosity data presented in Fig. 81.

4.6.6 Degree of saturation versus resistivity

Fig. 81 presents the degree of saturation, expressed as the ratio of actual mass to mass at water saturation (w/w_{sat}), as a function of relative humidity for (a) reference samples, (b) fully chloride-loaded samples and (c) fully carbonated samples.

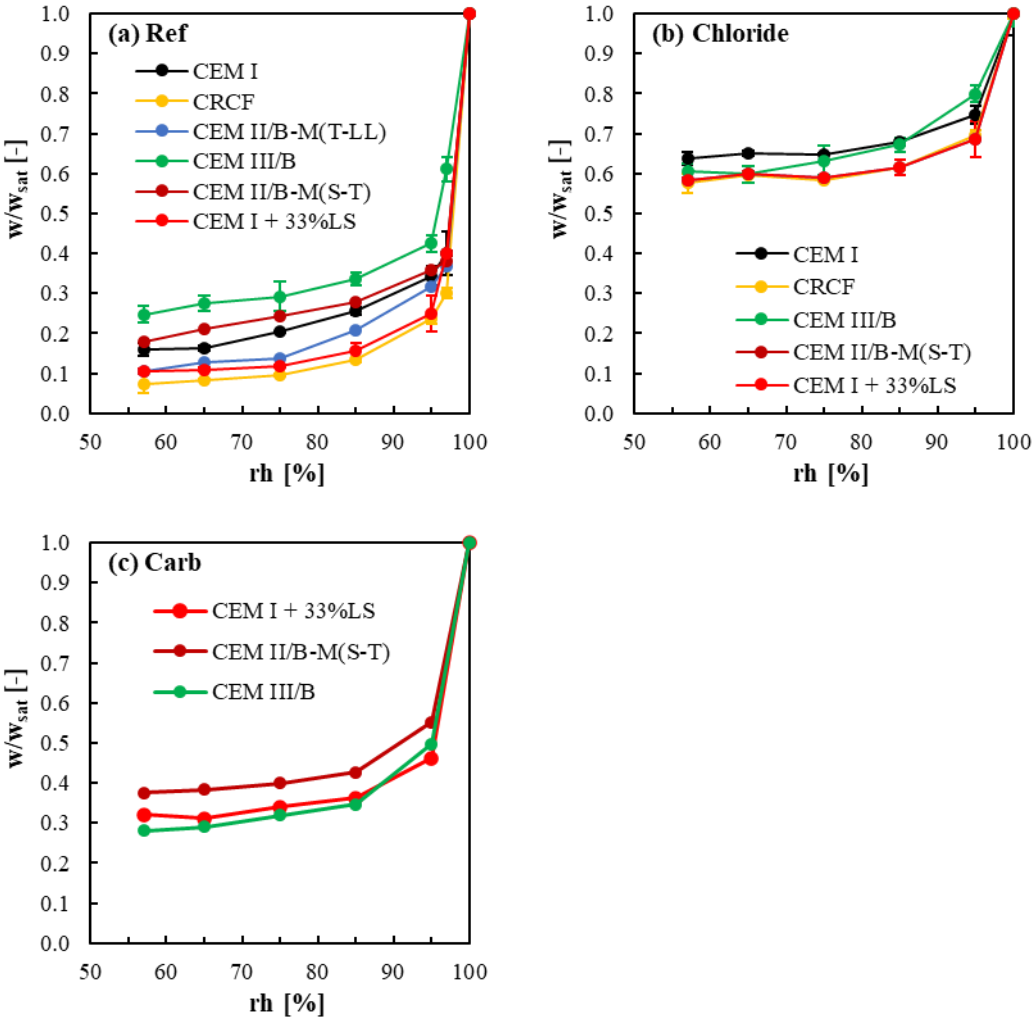

Fig. 81 *Ratio w/w_{sat} versus relative humidity for (a) reference samples, (b) fully chloride-loaded samples and (c) fully carbonated samples.*

For all binder systems, the degree of saturation increases progressively with increasing relative humidity and approaches unity under water-saturated conditions.

Compared with the reference specimens (Fig. 81a), chloride-loaded samples (Fig. 81b) exhibit noticeably higher degrees of saturation across the entire humidity range. This increase occurs despite only minor changes in total porosity. The behaviour can be attributed primarily to the hygroscopic nature of sodium chloride, which promotes moisture retention and increases equilibrium water content at a given relative humidity.

Carbonated specimens (Fig. 81c) generally show slightly higher degrees of saturation than reference samples but lower values than chloride-contaminated specimens. The moderate increase compared with the reference condition is consistent with the reduced porosity observed after carbonation and the associated refinement of the pore structure.

Across all exposure regimes, CEM II/B-LL consistently exhibits the lowest degree of saturation. In contrast, slag-containing binders (CEM III/B and CEM II/B-M (S-T)) generally display the highest degrees of saturation, reflecting their refined pore structure and higher moisture retention capacity. An exception is observed for the chloride-contaminated CEM

l mixture, which also shows elevated saturation levels due to the presence of dissolved salts.

Fig. 82 illustrates the relationship between degree of saturation (w/w_{sat}) and electrical resistivity for (a) reference samples, (b) fully chloride-loaded samples and (c) fully carbonated samples.

To maintain clarity, the x-axis scale differs between the reference and chloride conditions (a, b) and the carbonated condition (c), due to the substantially higher resistivity values observed after carbonation.

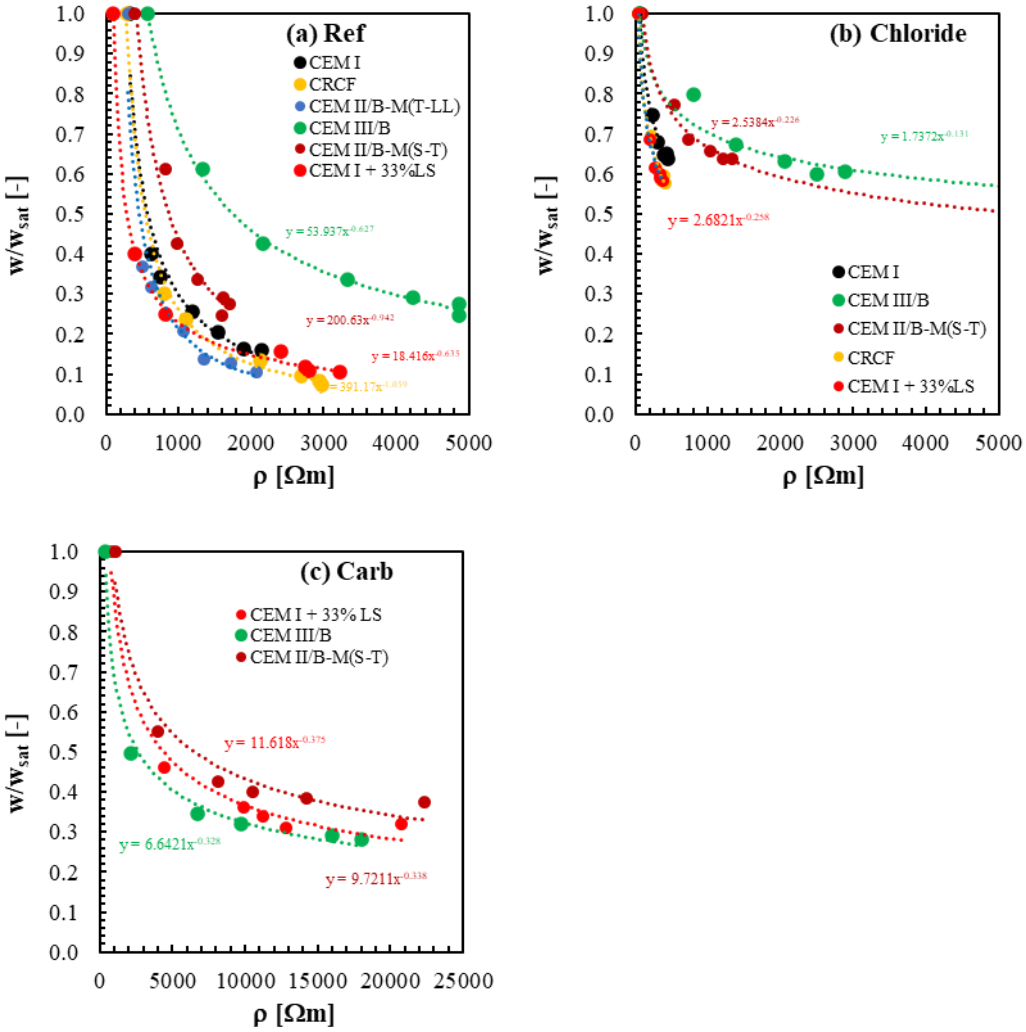

Fig. 82 *Ratio w/w_{sat} versus electrical resistivity for (a) reference samples, (b) fully chloride-loaded samples and (c) fully carbonated samples.*

For all exposure regimes, resistivity decreases non-linearly with increasing degree of saturation. The relationship can be approximated by a power-law function of the form in Eq. (4.6.1)

$$\rho = A \cdot \left(\frac{w}{w_{sat}}\right)^{-n} \qquad \text{Eq. (4.6.1)}$$

where A is a material-dependent coefficient and n is an empirical exponent. Representative fitting parameters are indicated for selected curves.

Under reference and chloride-contaminated conditions, CEM III/B generally exhibits higher degrees of saturation at comparable resistivity values compared with the other binders. This behaviour reflects the combined influence of pore structure and pore solution chemistry.

In contrast, under carbonated conditions, the relative position of the curve's changes. The large increase in resistivity observed for slag-containing binders upon carbonation leads to a steeper shift of the resistivity–saturation relationship, reducing the difference between binders at higher saturation levels.

4.6.7 Electrical resistance monitoring

The multi-ring electrode (MRE) system monitors electrical resistance. Electrical resistivity is calculated by multiplying the measured resistance by the cell constant.

Sensortec GmbH and reference [164] propose slightly different cell constants for the MRE, ranging from 0.07 m to 0.10 m. To validate these proposed cell constants, the resistivity determined from MRE measurements on Wf specimens was compared with resistivity values obtained from water-saturated laboratory specimens of known geometry using the two-electrode measurement (TEM) method.

Tab. 22 presents the resistance R measured with the MRE in the Wf specimens at a depth of 5 mm between the first two electrode rings on the fifth day of saturation. Measurements were taken before the first exposure cycle (cycle 0) and during the final wet condition. For comparison, the resistivity determined by TEM under water-saturated conditions for reference, fully carbonated and chloride-loaded laboratory specimens is also included.

Based on these values, the effective cell constant required to obtain identical resistivity values for the Wf specimens (MRE) and the water-saturated laboratory specimens (TEM) was calculated. The resulting cell constants are listed alongside the measured resistances in Tab. 22.

***Tab. 22** Cell constants and corresponding resistivity of MRE*

Binder	**CEM III/B**			**CEM II/B-M(S-T)**			**CEM I + 33%LS**		
Parameter	**R**	**k**	**ρ**	**R**	**k**	**ρ**	**R**	**k**	**ρ**
Unit	**[Ω]**	**[m]**	**[Ωm]**	**[Ω]**	**[m]**	**[Ωm**	**[Ω]**	**[m]**	**[Ωm]**
Wf_CO_2 (cycle 0)	6544	0.09	567	2122	0.18	388	705	0.30	212
Wf_Cl_CO_2 (cycle 0)	8143	0.07	567	2349	0.18	388	705	0.30	212
Ref182 (saturate)	-	-	567	-	-	388	-	-	212
Wf_CO_2 wet	4901	0.08	383	6719	0.16	1062	5090	0.05	268
Carb (saturated)	-	-	383	-	-	1062	-	-	268
Wf_Cl_CO_2 wet	766	0.07	55	1338	0.07	88	413	0.08	32
Chloride (saturated)	-	-	55	-	-	88	-	-	32

Fig. 83 presents the long-term resistance monitoring of CEM III/B specimens over 18 wet–dry cycles. Exposure was terminated on 25 April 2023. After removing sections of the specimens for further investigations, drying was continued and monitored.

Fig. 83a shows the resistance development of Wf-CO_2 specimens, and Fig. 83b that of Wf-Cl-CO_2 specimens. Manual calibration measurements indicated slight deviations in the effective cell constant. For consistency in further analysis, the cell constant proposed by the MRE manufacturer (k = 0.10 m) was adopted, resulting in resistivity calculated as $\rho = R \cdot 10^{-1}$.

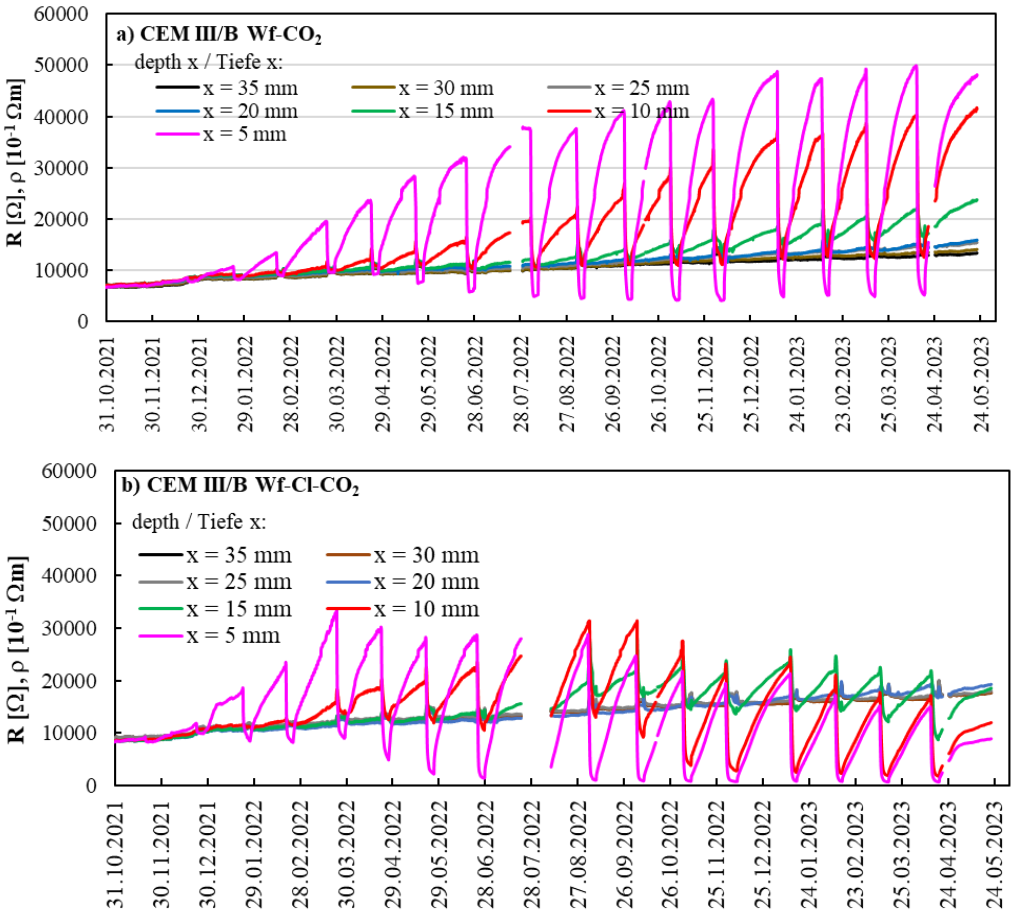

Fig. 83 *Resistivity monitoring of CEM III/B samples: (a) Wf-CO_2 and (b) Wf-Cl-CO_2.*

At the beginning of the monitoring period, the resistance values measured at depths between 5 mm and 35 mm were relatively similar and at a comparatively low level. The first two wet–dry cycles had only a minor influence on resistance at all measurement depths.

Subsequently, a clear cyclic behaviour developed: resistance increased during drying phases (without water application) and decreased immediately upon rewetting. This cyclic effect is most pronounced at shallow depths (5–15 mm) and becomes progressively less visible at depths of 30–35 mm.

For Wf-CO_2 specimens (Fig. 83a), the amplitude of the wet–dry resistance fluctuations increase over time, particularly at depths of 5–10 mm. During drying phases, resistance at shallow depth exceeds that of the non-carbonated core concrete (30–35 mm), whereas during wetting phases it decreases rapidly. This behaviour becomes more pronounced with increasing exposure time and carbonation depth.

In the Wf-Cl-CO_2 specimens (Fig. 83b), the average resistance decreases progressively over time, indicating the influence of chloride ingress on pore solution conductivity. During wetting phases, resistance at 5–10 mm depth is lower than that of the chloride-free core concrete (30–35 mm depth), reflecting increased ionic conductivity. After drying, the resistance at shallow depth approaches values similar to those of the inner concrete.

Fig. 84 presents the long-term resistance monitoring of CEM II/B-M (S-T) specimens over 18 wet–dry cycles. Exposure was terminated on 2 May 2023. After removing selected sample sections for further investigations, drying was continued and monitored.

Fig. 84a shows the resistance development of Wf-CO_2 specimens, and Fig. 84b that of Wf-Cl-CO_2 specimens.

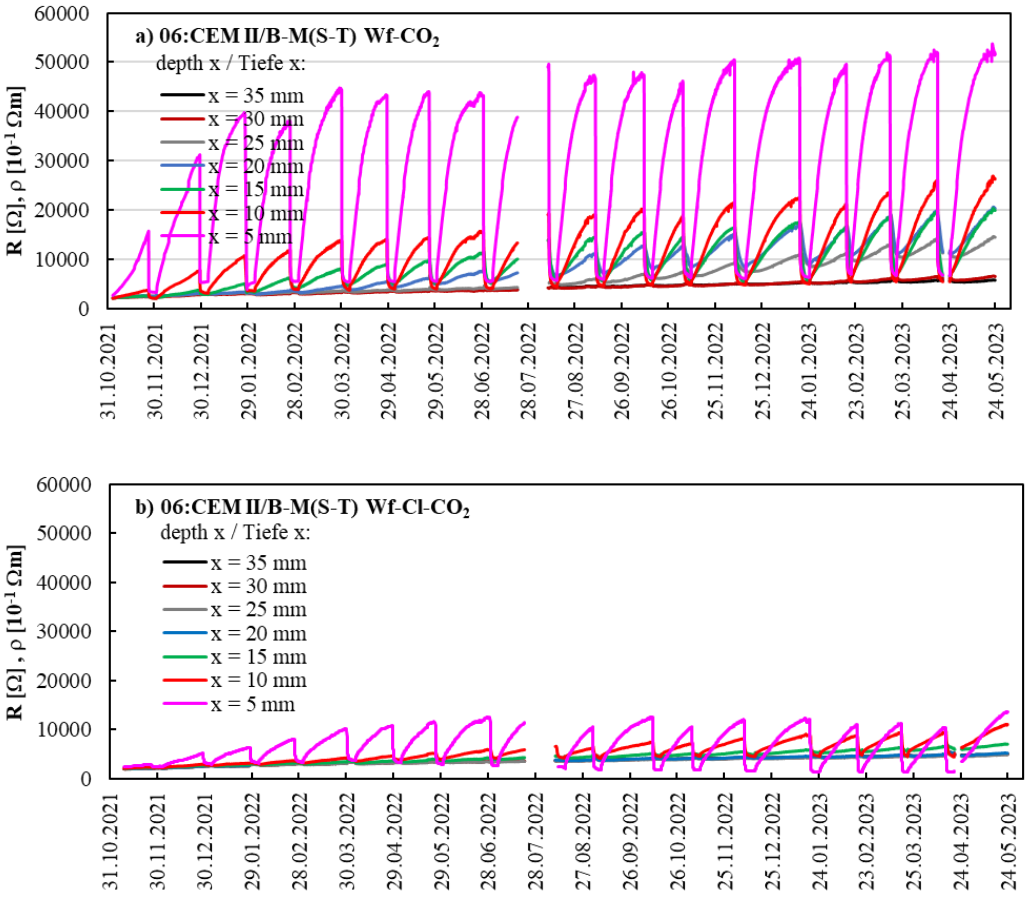

Fig. 84 *Resistivity monitoring of CEM II/B-M (S-T) samples: (a) Wf-CO_2 and (b) Wf-Cl-CO_2.*

Compared with the CEM III/B specimens (Fig. 83), the initial electrical resistance of the CEM II/B-M (S-T) concrete is lower. From the first wet–dry cycle onwards, distinct drying phases are visible at shallow depth (5 mm). The pronounced cyclic behaviour at this depth suggests a stronger sensitivity to surface moisture fluctuations, which may be related to differences in cover quality or electrode positioning relative to the surface.

Under CO_2 exposure (Fig. 84a), the long-term increase in resistance is less pronounced than observed for CEM III/B. This behaviour is consistent with a smaller carbonation depth and therefore a more limited alteration of pore solution chemistry and microstructure.

When chlorides are present (Fig. 84b), the overall resistance remains significantly lower throughout the monitoring period. Although cyclic wet–dry fluctuations are still visible, the baseline resistance does not increase over time, indicating that the conductivity-enhancing effect of chloride ingress dominates over any carbonation-induced resistivity increase.

Fig. 85 presents the long-term resistance monitoring of CEM II/B-LL specimens over 18 wet–dry cycles. Exposure was terminated on 2 May 2023. After removing selected sections for further investigations, drying was continued and monitored.

Fig. 85a shows the resistance development of Wf-CO_2 specimens, and Fig. 85b that of Wf-Cl-CO_2 specimens.

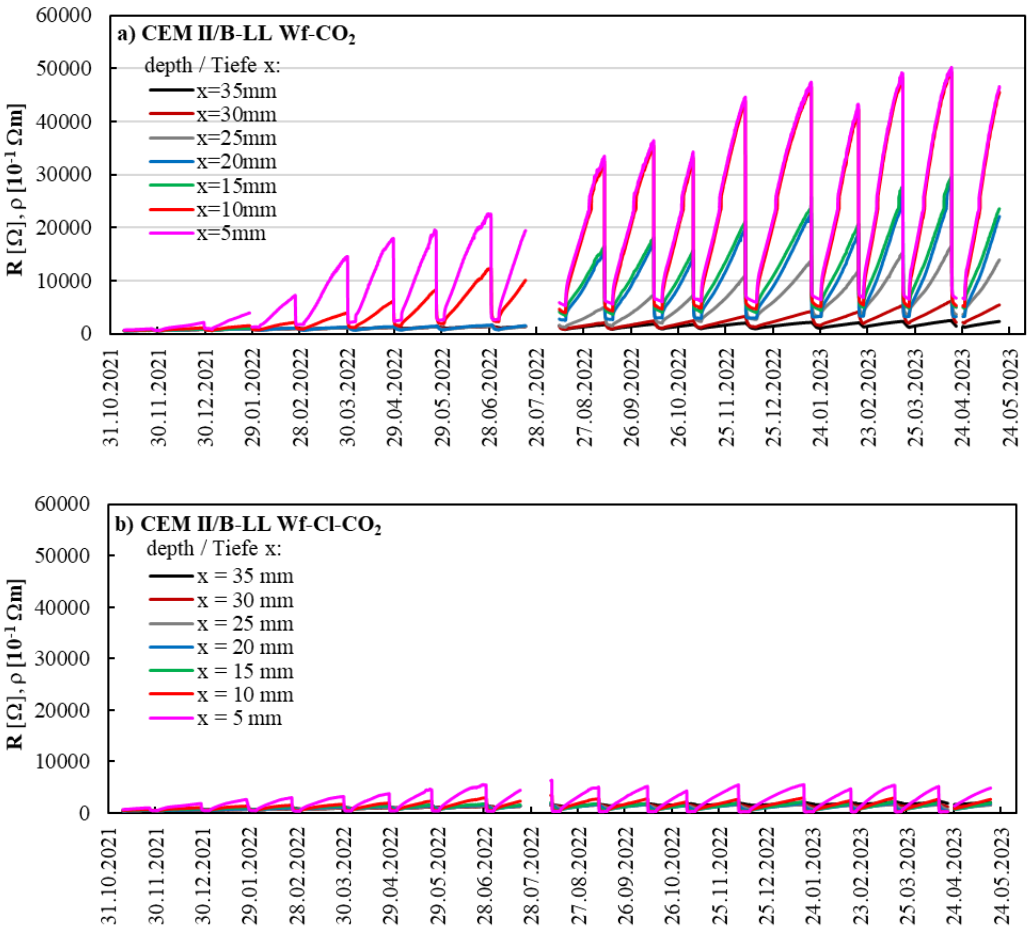

Fig. 85 *Resistivity monitoring of CEM II/B-LL samples: (a) Wf-CO_2 and (b) Wf-Cl-CO_2.*

At the beginning of monitoring, the electrical resistance of CEM II/B-LL is lower than that of CEM III/B and CEM II/B-M (S-T) concretes. Under CO_2 exposure (Fig. 85a), resistance increases progressively during drying phases. At shallow depths (5–10 mm), the maximum resistance reached during dry-out becomes comparable to the values observed in the other binder systems.

In the presence of chlorides (Fig. 85b), the overall resistance remains at a comparatively low level throughout the monitoring period. The cyclic wet–dry fluctuations are visible but less pronounced than in CEM III/B. The baseline resistivity does not exhibit a substantial long-term increase.

For CEM III/B, carbonated concrete under wet conditions exhibits resistivity values below those of the uncarbonated core concrete. For CEM II/B-M (S-T), the near-surface resistivity under wet conditions is similar to that of the core concrete. In contrast, for CEM II/B-LL, the near-surface resistivity under wet conditions remains higher than that of the core concrete.

4.6.8 Influential depth

The depth-dependent resistivity was evaluated by plotting the resistivity measured at discrete depths (5, 10, 15, 20, 25, 30 and 35 mm) as smoothed profiles over the concrete cover depth. Profiles showing a decrease in resistivity at the exposed surface (depth = 0 mm) correspond to measurements taken during the wetting phase of a cycle (first 5 days). Profiles showing an increase in resistivity at the surface correspond to measurements performed at the end of the cycle (approximately day 30), after the drying phase.

Fig. 86 presents the depth-dependent resistivity of CEM III/B specimens exposed to Wf-CO_2 during (a) the 3rd cycle, (b) the 9th cycle and (c) the 18th cycle. In addition, the corresponding profiles for Wf-Cl-CO_2 specimens are shown for (d) the 3rd cycle, (e) the 9th cycle and (f) the 18th cycle. The 3rd, 9th and 18th cycles correspond to approximately 90, 270 and 540 days of total exposure, respectively (one cycle consists of 5 days of wetting followed by 25 days of drying).

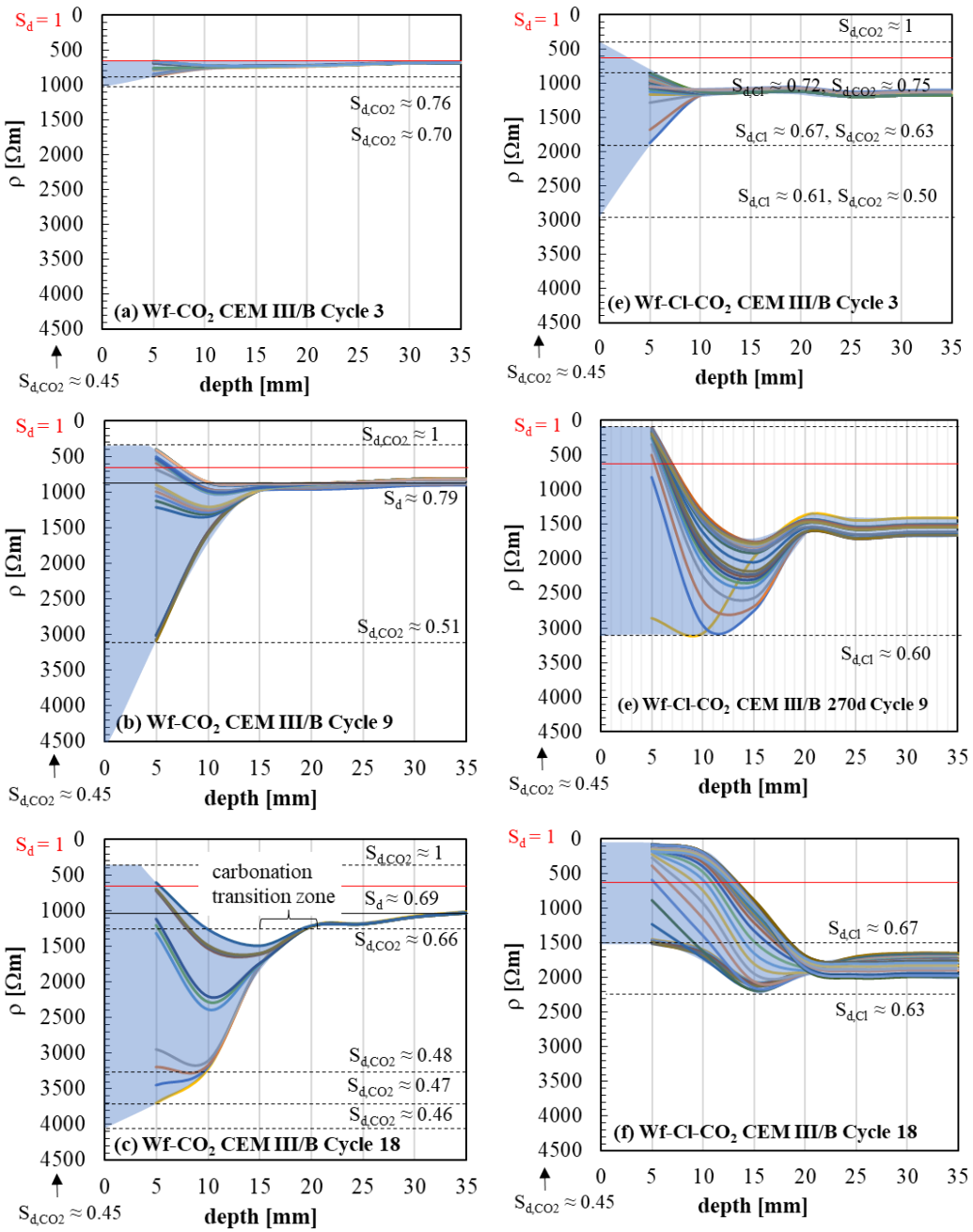

Fig. 86 *Depth-dependent resistivity of CEM III/B specimens exposed to Wf-CO_2 during the (a) 3rd cycle, (b) 9th cycle and (c) 18th cycle, and of CEM III/B specimens exposed to Wf-*

Cl-CO_2 during the (d) 3rd cycle, (e) 9th cycle and (f) 18th cycle. The 3rd, 9th and 18th cycles correspond to approximately 90, 270 and 540 days of total exposure, respectively. One cycle consists of 5 days of wetting followed by 25 days of drying.

In all figures, resistivity varies strongly near the exposed surface (depth = 0 mm) due to cyclic wetting and drying. High resistivity corresponds to low degree of saturation (drying phase), whereas low resistivity corresponds to high degree of saturation (wetting phase). The red horizontal line in each figure represents the resistivity of the non-carbonated reference concrete at full saturation (Sd = 1), serving as a baseline without carbonation or wetting effects.

At early age (Cycle 3), the influence of cyclic wetting and drying is similar for Wf-CO_2 and Wf-Cl-CO_2 specimens. In fact, the amplitude of resistivity variation is slightly lower for the Wf-CO_2 condition at this stage.

With increasing exposure time (Cycles 9 and 18), the resistivity fluctuations become significantly more pronounced under Wf-CO_2 exposure. In particular, during the 18th cycle, a clear transition between non-carbonated and carbonated concrete is visible, forming a distinct carbonation transition zone. This is characterised by a local maximum in resistivity at intermediate depth, reflecting carbonation-induced changes in pore solution chemistry and microstructure.

Under Wf-Cl-CO_2 exposure, the resistivity fluctuations remain less pronounced compared with the corresponding Wf-CO_2 condition. The baseline resistivity is generally lower, and the transition zone is less sharply defined. This behaviour indicates that chloride-induced increases in ionic conductivity partially counteract the resistivity increase associated with carbonation.

The influential depth can be defined as the depth from the exposed surface at which the resistivity profile converges towards the baseline behaviour of the inner concrete (i.e. where cyclic fluctuations become negligible and the resistivity approaches the reference level).

- For Wf-CO_2 specimens at the 18th cycle, the influential depth is approximately 15 mm.
- For Wf-Cl-CO_2 specimens at the 18th cycle, the influential depth increases to approximately 20 mm.

Thus, the presence of chlorides increases the depth over which cyclic moisture and chemical effects influence the electrical response of the concrete.

This observation is consistent with the higher degree of saturation observed in chloride-contaminated specimens and with the increased coefficient of capillary absorption measured for slag-blended cements under chloride exposure.

The increase in influential depth under Wf-Cl-CO_2 exposure can be explained by the combined effect of:

- enhanced moisture retention due to the hygroscopic nature of chlorides,
- increased ionic conductivity of the pore solution,
- and modified capillary transport behaviour.

In contrast, under Wf-CO_2 exposure without chlorides, the resistivity increase is primarily governed by carbonation-induced pore refinement and changes in pore solution chemistry, leading to a sharper and more localised transition zone.

The data therefore demonstrate that chloride presence not only affects absolute resistivity values but also modifies the spatial extent of moisture- and carbonation-induced electrical changes within the concrete cover.

Fig. 87 presents the depth-dependent resistivity profiles of CEM II/B-M (S-T) specimens under Wf-CO_2 and Wf-Cl-CO_2 exposure. In all figures, resistivity varies near the exposed surface (depth = 0 mm) as a result of cyclic wetting and drying. High resistivity corresponds to low degree of saturation (drying phase), whereas low resistivity corresponds to high degree of saturation (wetting phase). The red horizontal line represents the resistivity of the non-carbonated reference concrete at full saturation (Sd = 1).

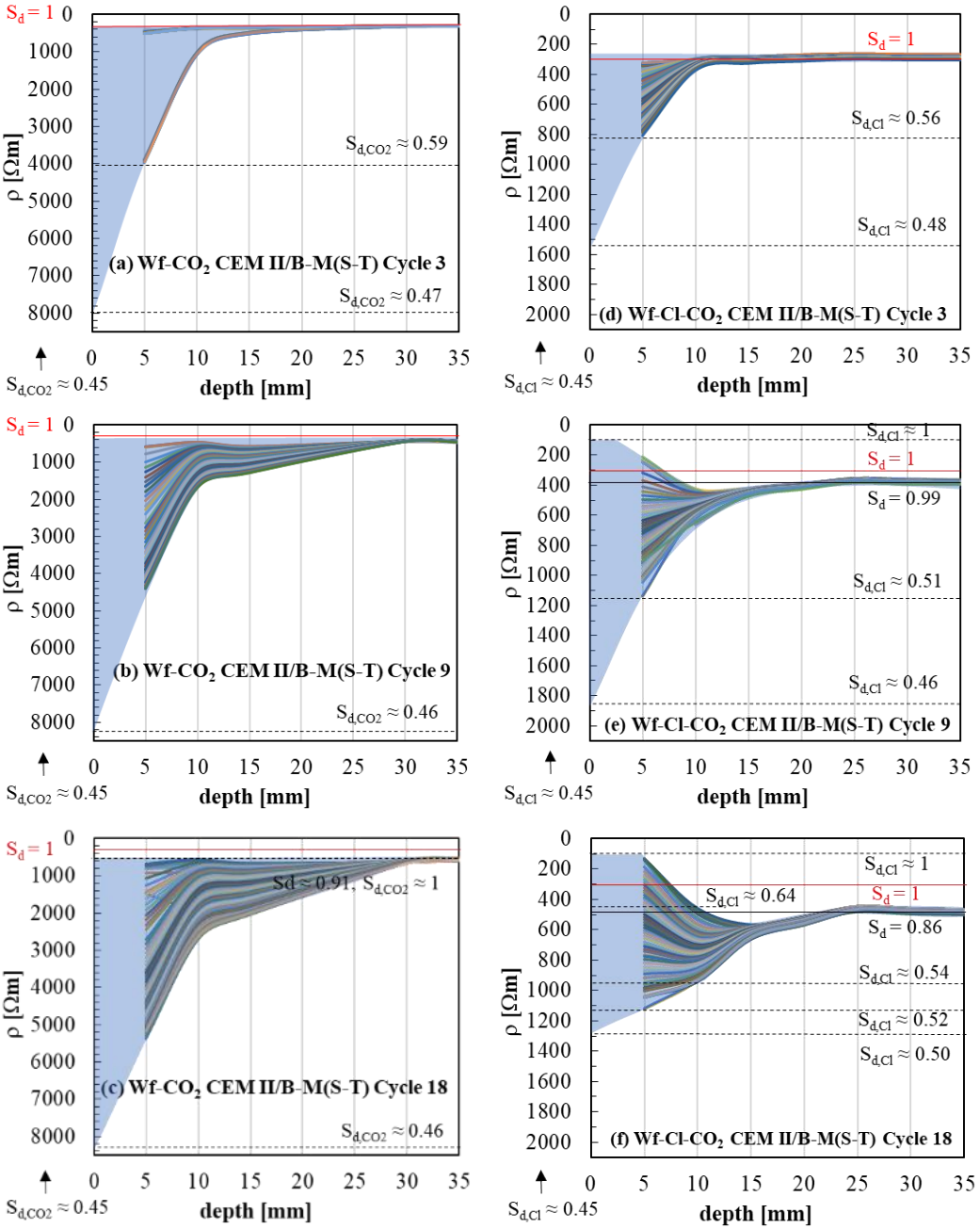

Fig. 87 *Depth-dependent resistivity of CEM II/B-M (S-T) specimens exposed to Wf-CO_2 during the (a) 3rd cycle, (b) 9th cycle and (c) 18th cycle, and of CEM II/B-M (S-T) specimens exposed to Wf-Cl-CO_2 during the (d) 3rd cycle, (e) 9th cycle and (f) 18th cycle.*

During the 3rd cycle (Fig. 87a and Fig. 87d), the influential depth — defined as the depth at which cyclic resistivity fluctuations become negligible — is slightly larger under Wf-CO_2 exposure compared with Wf-Cl-CO_2 exposure. At this stage, both carbonation and chloride ingress primarily affect the near-surface region (approximately 5–10 mm).

With increasing exposure time (9th and 18th cycles), the influential depth increases under both exposure regimes. However, the increase is more pronounced under Wf-CO_2 exposure than under Wf-Cl-CO_2 exposure.

Under Wf-CO_2 exposure, the depth profiles show progressive deviation from the reference line (Sd = 1) not only at the surface but also in the inner regions. This indicates gradual drying of the inner concrete and progressive carbonation-induced modification of pore structure and pore solution chemistry.

In contrast, under Wf-Cl-CO_2 exposure, the degree of saturation remains slightly higher throughout the profile. The resistivity curves show less pronounced upward deviation from the reference line at larger depths, indicating enhanced moisture retention in the presence of chlorides.

For CEM II/B-M (S-T), carbonation and chloride ingress appear to progress at comparable rates but remain largely confined to the cover zone (5–10 mm). The presence of chlorides increases the degree of saturation due to their hygroscopic nature and enhances ionic conductivity, which counteracts the resistivity increase associated with carbonation.

- Under Wf-CO_2 exposure, resistivity increases more strongly and the influential depth becomes larger over time.
- Under Wf-Cl-CO_2 exposure, higher moisture retention limits the resistivity increase and reduces the apparent influential depth.

The data indicate that in this binder system, chloride-induced moisture retention partially offsets carbonation-induced pore refinement effects, leading to a more moderate spatial extension of resistivity changes.

Fig. 88 presents the depth-dependent resistivity profiles of CEM II/B-M (S-T) specimens under Wf-CO_2 and Wf-Cl-CO_2 exposure. In all figures, resistivity varies near the exposed surface (depth = 0 mm) as a result of cyclic wetting and drying. High resistivity corresponds to low degree of saturation (drying phase), whereas low resistivity corresponds to high degree of saturation (wetting phase). The red horizontal line represents the resistivity of the non-carbonated reference concrete at full saturation (Sd = 1).

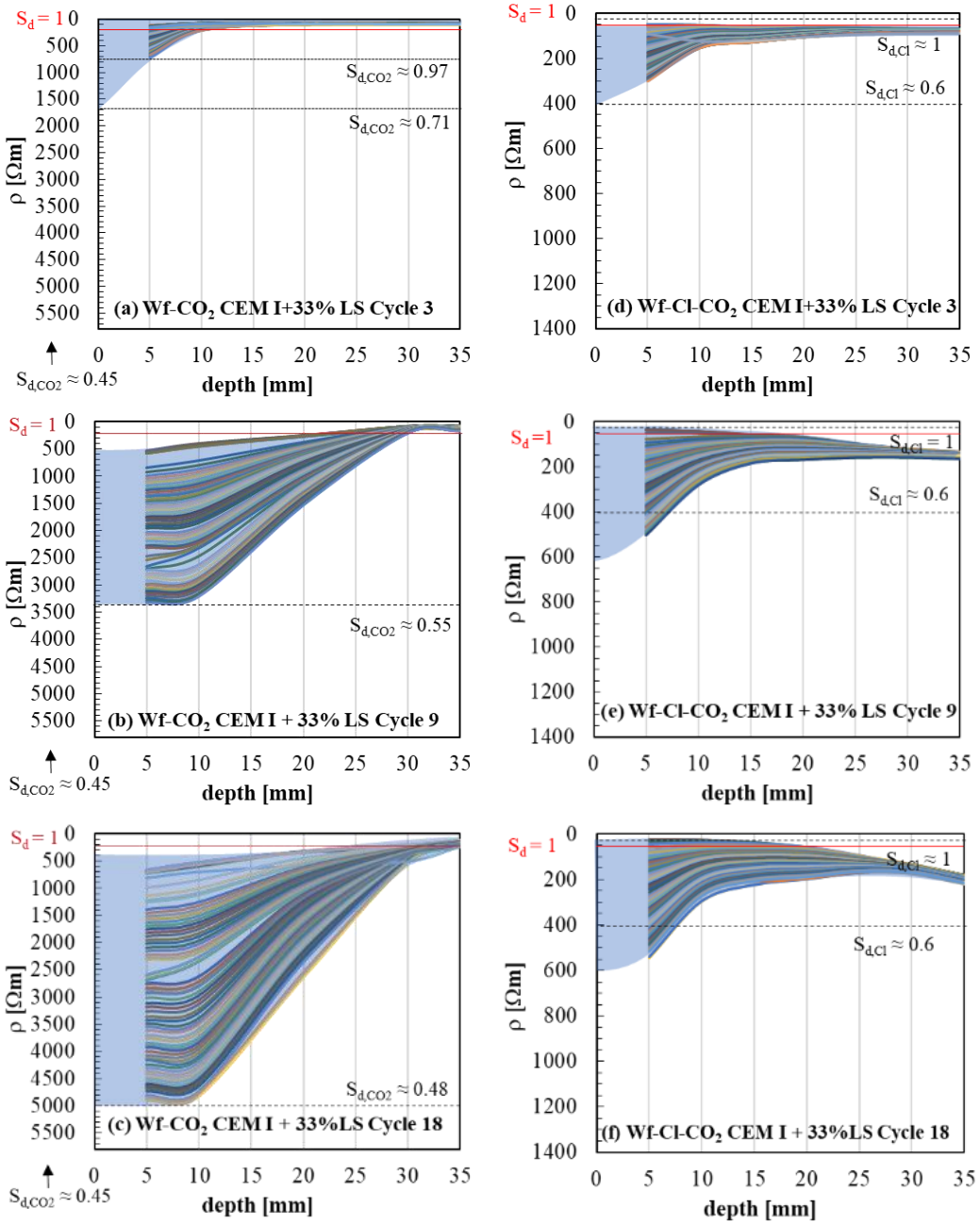

Fig. 88 *Depth dependent resistivity of CEM I + 33% LS Wf-CO_2 samples during the (a) 3rd cycle (b) 9th cycle and (c) 18th cycle as well as CEM II/B-M(S-T) Wf-Cl-CO_2 samples during the (d) 3rd cycle (e) 9th cycle and (f) 18th cycle.*

During the 3rd cycle (Fig. 88a and Fig. 88d), the influential depth — defined as the depth at which cyclic resistivity fluctuations become negligible — is slightly larger under Wf-CO_2 exposure compared with Wf-Cl-CO_2 exposure. At this stage, both carbonation and chloride ingress primarily affect the near-surface region (approximately 5–10 mm).

With increasing exposure time (9th and 18th cycles), the influential depth increases under both exposure regimes. However, the increase is more pronounced under Wf-CO_2 exposure than under Wf-Cl-CO_2 exposure.

Under Wf-CO_2 exposure, the depth profiles show progressive deviation from the reference line (Sd = 1) not only at the surface but also in the inner regions. This indicates gradual drying of the inner concrete and progressive carbonation-induced modification of pore structure and pore solution chemistry.

In contrast, under Wf-Cl-CO_2 exposure, the degree of saturation remains slightly higher throughout the profile. The resistivity curves show less pronounced upward deviation from the reference line at larger depths, indicating enhanced moisture retention in the presence of chlorides.

The depth-dependent resistivity profiles reveal a pronounced binder-dependent moisture redistribution under coupled wetting–drying, carbonation and chloride exposure. For all binders, cyclic moisture fluctuations originate at the exposed surface and progressively propagate inward with increasing exposure time. However, the spatial extent and magnitude of this moisture-affected zone differ significantly. In CEM III/B, chloride presence increases the influential depth, extending moisture-related resistivity fluctuations deeper into the cover zone compared with pure carbonation exposure. This behaviour reflects enhanced moisture retention and ionic conductivity in the slag-rich system. In contrast, for CEM II/B-M (S-T) and CEM I + 33% LS, chloride exposure reduces the influential depth relative to Wf-CO_2 conditions. In these binders, carbonation-driven drying and pore refinement dominate spatial resistivity evolution, while chloride-induced hygroscopic effects mainly stabilise near-surface moisture without promoting deeper penetration. The results demonstrate that influential depth is not governed solely by capillary transport but by a chemo-transport interaction controlled by binder chemistry. Consequently, the spatial evolution of moisture profiles under combined exposure cannot be generalised across cement types but must be interpreted in the context of binder-specific carbonation kinetics, chloride binding capacity and pore structure modification.

4.7 Dominating process carbonation or chloride?

Based on the established correlations between chloride migration coefficients (D_{Cl}) and chloride ingress velocities (v_{Cl}), and between accelerated test conditions and natural exposure conditions (cf. previous chapters), a relationship between the natural carbonation rate (k_N) and the natural chloride ingress rate ($v_{Cl,x\%,NA}$) under XD1 conditions was derived. XD1 represents exposure scenarios with an elevated risk of simultaneous carbonation and chloride-induced corrosion.

Fig. 89 illustrates combinations of k_N and D_{Cl} associated with a higher probability of simultaneous ingress. The previously established transfer functions between laboratory and natural conditions are summarised therein.

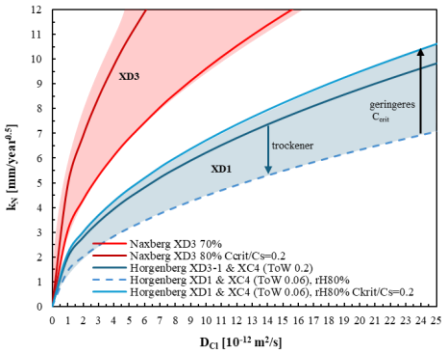

Basis	Wf-CO_2 test condition k_A	Exposure XC4		Influence of chlorides
		moist (ZH) ToW = 0.2	dry (ZH) 65-85% ToW = 0.06	
k_{NA}	1/4.16=0.24	1	1.3 - 1.2	0.7

Basis	Wf-Cl Test condition V_{Cl}	XD3	XD1-3	Exposure XD1		
		C_{crit}/C_s=0.41 Naxberg	C_{crit}/C_s=0.5 Horgenberg	C_{crit}/C_s=0.2 rel. Hum. 95 to 70%	C_{crit}/C_s=0.2 rel. Hum. 80 to 70%	Influence of carbonation
DC1	$1.5*DCl^{0.45}$	0.63	0.22	0.63*0.45*1.6	0.22*0.6*1.8	1.0 - 1.17

Fig. 89 *Schematic representation of the interaction between carbonation and chloride ingress under different exposure classes (XD1 and XD3). The left diagram illustrates the relative balance between drying and chloride surface concentration, while the right schematics show the resulting moisture and transport mechanisms within the concrete cover under cyclic wetting and drying.*

Carbonation rate can be approximated as proportional to w/CaO, whereas chloride ingress rate correlates with w/SiO_2 (or more precisely w/(SiO_2 + Al_2O_3)). Based on this, a compositional dominance criterion can be derived, see Eq. (4.7.1)

$$\frac{k}{v_{Cl,x}} = \frac{w/CaO}{w/(SiO_2+Al_2O_3)} \approx \frac{w/CaO}{w/SiO_2} \quad \text{Eq. (4.7.1)}$$

For a given concrete mixture (constant w), the water content cancels, see Eq. (4.7.2).

$$\frac{k}{v_{Cl,x}} = \frac{SiO_2+Al_2O_3}{CaO} \approx \frac{SiO_2}{CaO} \quad \text{Eq. (4.7.2)}$$

Here, CaO does not include CaO bound in $CaCO_3$, and SiO_2 excludes silica bound in recycled fines.

Thus, the ratio SiO_2/CaO (or (SiO_2 + Al_2O_3)/CaO) serves as a compositional indicator for the dominant ingress mechanism.

Fig. 90a and Fig. 90b compare the ratio of natural carbonation rate to natural chloride ingress rate $k_{NA} : v_{Cl,x\%,NA}$ for:
- Wf-Cl-CO_2 samples (squares)
- Wf-Cl and Wf-CO_2 samples (dots)

These ratios are plotted against:
- (w/CaO)/(w/SiO_2) ≈ SiO_2/CaO (Fig. 90a)
- (w/CaO)/(w/(SiO_2 + Al_2O_3)) ≈ (SiO_2 + Al_2O_3)/CaO (Fig. 90b)

Two exposure scenarios were assessed. One for XD3 & XC4 condition and one for XD1 & XC4 condition.

XD3 & XC4 (Severe Deicing Conditions)
- C_{crit} = 1.0 wt.-% Cl/cement
- C_s ≈ 3.2 wt.-% Cl/cement
- Time of wetness (ToW) = 0.2
- Reference: Naxberg exposure [136, 173]
- Additionally, a reduced Ccrit = 0.4 wt.-% was evaluated using the multiplicative factor derived in Chapter 4.5.3.

XD1 & XC4 (Moderate Combined Exposure)
- Ccrit = 0.4 wt.-% Cl/cement
- Cs = 1.3 wt.-% Cl/cement
- ToW = 0.06 (vertical elements) [172, 176]

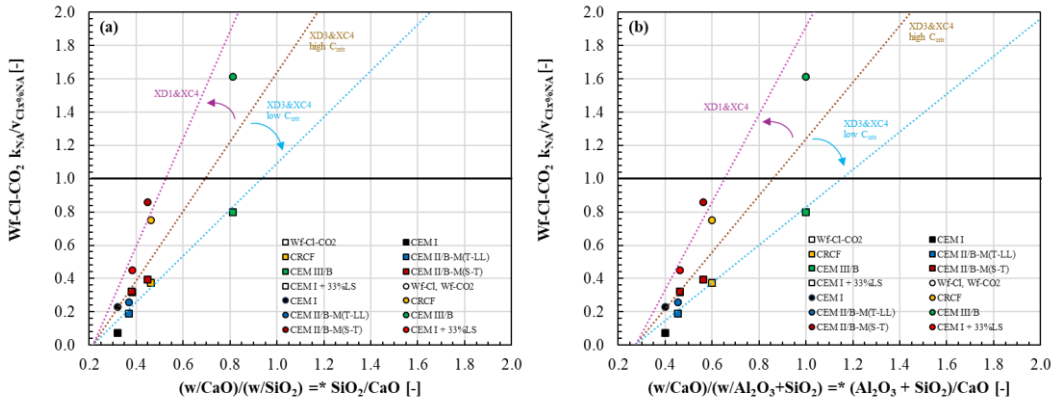

Fig. 90 *Correlation between natural carbonation rate (k_{NA}) and natural chloride ingress rate ($v_{Cl,x\%,NA}$) for different binders and exposure conditions. The diagonal line represents equal rates (k_{NA} = $v_{Cl,x\%,NA}$); points above indicate carbonation-dominated behaviour and points*

below chloride-dominated ingress. Trend lines illustrate the compositional dependence and identify regions with increased risk of simultaneous depassivation under XD1/XD2a/XC4 and XD3/XC4 exposure.

Only CEM III/B exhibits a carbonation rate exceeding or approaching the chloride ingress rate. CRCF and CEM II/B-M (S-T) show nearly equal carbonation and chloride ingress rates under isolated exposure (Wf-CO_2 or Wf-Cl). All other mixes show chloride ingress as the clearly dominating mechanism at x% = 1%.

Importantly, under combined Wf-Cl-CO_2 exposure, carbonation rates are reduced in chloride-contaminated concrete. As a result, chloride ingress exceeds carbonation even in compositions where carbonation would otherwise dominate.

From the derived correlations a risk zones based on SiO_2/CaO ratio can be derived.

Under XD1 & XC4 conditions higher risk of simultaneous corrosion occurs for:
- SiO_2/CaO ≈ 0.5 – 0.6

Under XD3 & XC4 conditions higher risk of simultaneous corrosion occurs for:
- SiO_2/CaO ≈ 0.7 – 0.9

The results demonstrate that:
- The relative dominance of carbonation vs. chloride ingress can be predicted from binder chemistry.
- The ratio SiO_2/CaO provides a mechanistic compositional indicator for simultaneous ingress risk.
- Combined exposure does not represent a linear superposition of single mechanisms.
- Chloride contamination can decelerate carbonation kinetics.
- Risk zones depend strongly on exposure class (XD1 vs. XD3).

These correlations are derived from accelerated exposure experiments and calibrated to natural exposure sites.

They provide a mechanistic estimation framework but require further validation under long-term natural exposure conditions.

4.8 Corrosion and corrosion initiation

4.8.1 General Methodology and Overview

This section presents the corrosion behaviour of reinforced concrete specimens exposed to cyclic wetting and drying under three exposure regimes:

- Wf-Cl (chloride exposure),
- Wf-CO_2 (carbonation exposure),
- Wf-Cl-CO_2 (combined exposure).

The objective is to relate corrosion initiation and propagation to chloride ingress, carbonation depth and moisture variations identified in previous sections.

The macrocell corrosion rate was determined using an anode-to-cathode ratio (A:K) of 1:1. The measured corrosion current was converted into corrosion rate using Faraday's law.

For the calculation, the entire exposed reinforcement surface (excluding coated areas) was assumed to be anodic. No pitting factor was applied. Therefore, the reported corrosion rates represent uniform corrosion rates. In reality, corrosion is likely localised, and the true local corrosion rate may be up to an order of magnitude higher when applying a pitting factor (e.g. according to [153]).

Manual A:K = 1:1 measurements from [177] are included for comparison.

For each binder system (Fig. 91 - Fig. 96):

- Subfigure (a) shows the corrosion rate over time under cyclic exposure.
- Subfigure (b) shows: Chloride content at reinforcement depth (left y-axis), Distance between carbonation front and reinforcement, Δdc (right y-axis).

In subfigures (a):

- Blue columns indicate wetting periods,
- White intervals represent drying phases.

In subfigures (b):

- Full symbols and solid lines represent chloride content at reinforcement depth.For example:

  Cl(dc = 10 mm) denotes chloride content at 10 mm cover depth.

  Cl(dc = 20 mm) denotes chloride content at 20 mm depth.

- Empty symbols and dotted lines indicate Δdc (distance between carbonation front and reinforcement).

Where corrosion is governed exclusively by chlorides, Wf-Cl and Wf-Cl-CO_2 results are presented together in one diagram and distinguished by labels "Cl" and "Cl-CO_2". The same procedure was applied when corrosion was governed exclusively by carbonation.

- Cl(dc = 10 mm) denotes chloride content at 10 mm cover depth (red symbols)
- Cl(dc = 20 mm) denotes chloride content at 20 mm depth (blue symbols)

4.8.2 Behaviour of CEM I

Fig. 91a presents the corrosion rate development of CEM I concrete exposed to cyclic wetting and drying in the presence of chlorides (Wf-Cl and Wf-Cl-CO_2). Carbonation progressed only slowly in both conditions, and the carbonation depth remained limited (≤ 4 mm in Wf-CO_2). Consequently, corrosion initiation and propagation were governed exclusively by chloride ingress. No corrosion was detected in specimens exposed to Wf-CO_2 without chlorides; therefore, these results are not shown.

Fig. 91b combines the evolution of chloride content at reinforcement depth with the distance between the carbonation front and the reinforcement (Δdc).

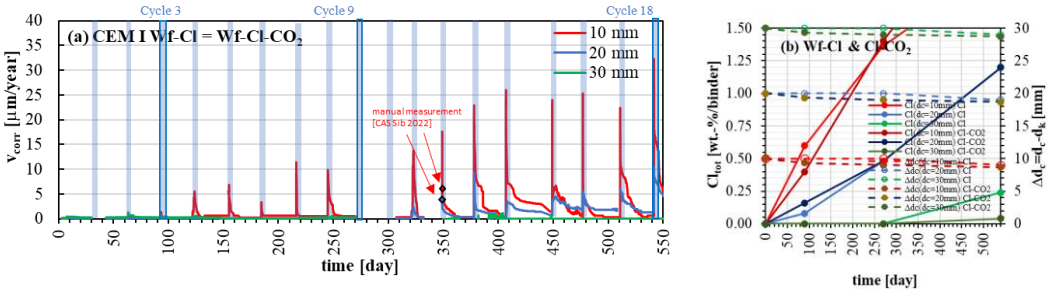

Fig. 91 *Corrosion behaviour of CEM I concrete under cyclic chloride exposure: (a) corrosion rate over time (Wf-Cl and Wf-Cl-CO_2) and (b) chloride content at reinforcement depth together with the distance between carbonation front and reinforcement (Δdc).*

Corrosion initiation in chloride-exposed specimens occurred first at 10 mm concrete cover after approximately 90 days. At that time, the chloride content at reinforcement depth (Fig. 94b) was about 0.6 wt.-% Cl/binder. For 20 mm cover, corrosion initiated after approximately 350 days at a chloride content of about 0.7 wt.-% Cl/binder. The similar initiation times and corrosion rates in Wf-Cl and Wf-Cl-CO_2 confirm that corrosion was governed by chloride ingress and that carbonation did not measurably contribute to depassivation for CEM I within the investigated exposure duration.

The Δdc curves remain relatively large throughout exposure, indicating that the carbonation front did not approach the reinforcement sufficiently to control corrosion initiation. Consequently, differences in corrosion rate between Wf-Cl and Wf-Cl-CO_2 are mainly attributable to scatter in chloride content at reinforcement depth rather than differences in carbonation depth.

After initiation, corrosion rates fluctuate with the wet–dry cycles (Fig. 94a). The response is more pronounced for reinforcement at 20 mm cover depth, indicating that cyclic moisture variations affect the steel environment at least to this depth. The maximum corrosion rate increases with exposure time, which is consistent with the assumption of a uniform anodic area; if corrosion is localised, local penetration rates would be higher. Average corrosion rates tend to be higher during drying phases than during wetting, consistent with improved oxygen availability under partially saturated conditions.

Finally, although no corrosion was expected under Wf-CO_2 exposure alone, minor corrosion activity observed after approximately 450–500 days may reflect local scatter in carbonation depth or depassivation within the carbonation gradient zone (where pH may remain above the phenolphthalein indicator threshold).

4.8.3 Behaviour of CRCF

Fig. 92 presents the corrosion rate development of CRCF concretes under cyclic exposure in Wf-Cl, Wf-Cl-CO_2 and Wf-CO_2 conditions, together with the corresponding chloride contents at reinforcement depth and the distance between carbonation front and reinforcement (Δdc).

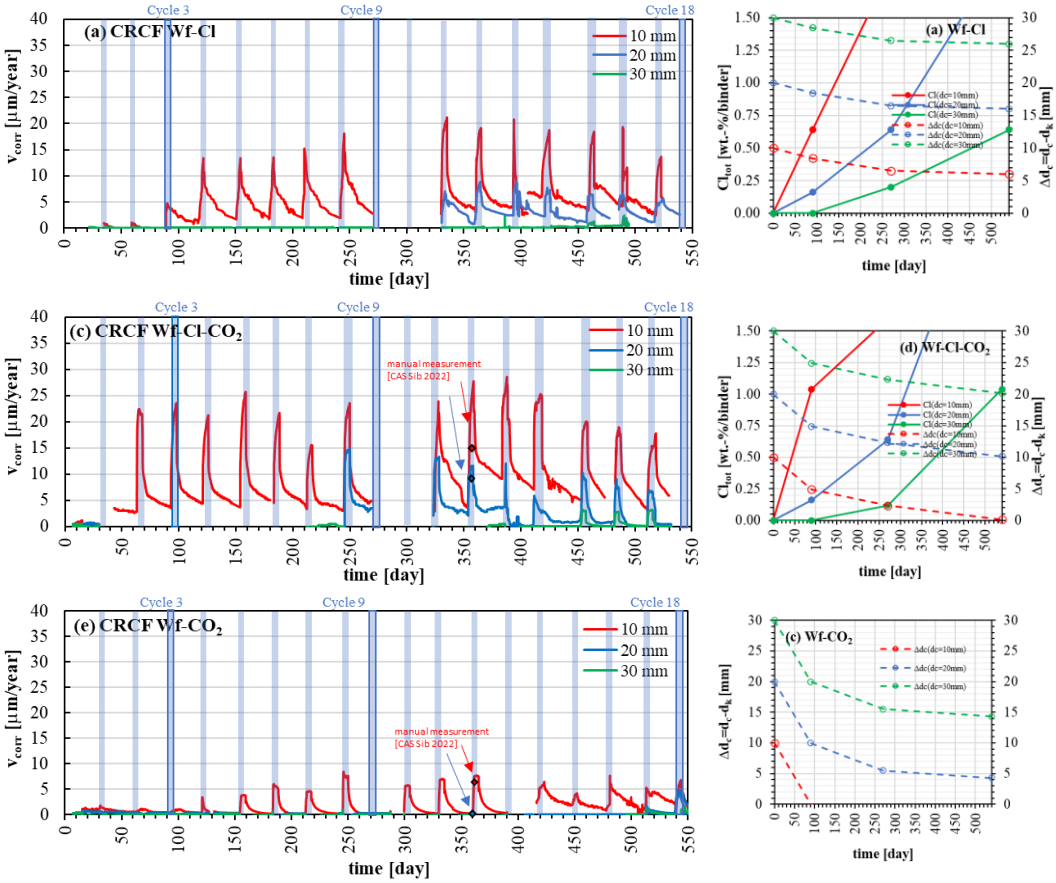

Fig. 92 *Corrosion rate development of CRCF concretes under cyclic exposure: (a) Wf-Cl, (c) Wf-Cl-CO_2, and (e) Wf-CO_2. Corresponding chloride content at reinforcement depth and distance between carbonation front and reinforcement (Δdc) are shown in (b), (d), and (f), respectively.*

In the Wf-Cl condition (Fig. 92a,b), corrosion initiates early at 10 mm cover depth. First corrosion peaks are visible after approximately 30 days of exposure, with pronounced maxima around 90 days.

At 20 mm cover, corrosion initiation occurs between approximately 270 and 330 days. For 30 mm cover, first significant corrosion activity is observed at around 450 days.

Cyclic wetting effects are clearly visible in all reinforcement layers. Corrosion rates increase during wetting phases and decrease during drying. Despite a high degree of saturation at intermediate depths (notably 20 mm), drying phases systematically reduce the corrosion rate.

Under combined exposure (Fig. 92c,d), the corrosion rate is similar or slightly higher than under pure chloride exposure. Carbonation reaches the 10 mm reinforcement shortly before the final cycle (≈540 days). The slightly increased corrosion rate in Wf-Cl-CO_2 compared to Wf-Cl is therefore primarily attributed to the somewhat higher chloride content at 10 mm depth rather than to carbonation-induced depassivation.

After approximately 420 days, corrosion rates decrease, which may indicate redistribution of moisture and chlorides or partial reduction of macrocell activity.

In the carbonation-only condition (Fig. 92e,f), corrosion develops progressively at 10 mm cover once the carbonation front exceeds the reinforcement (after approximately 120 days). Corrosion rates increase with exposure time and show cyclic fluctuations corresponding to wetting events.

At 20 mm and 30 mm cover depths, measurable corrosion currents appear after approximately 500 days, although the reinforcement remains nominally passive according to manual measurements and visual inspection. These currents are therefore likely related to moisture-induced macrocell effects rather than fully developed depassivation.

4.8.4 Behaviour of CEM II/B-M(T-LL)

Fig. 93 presents the evolution of chloride content at reinforcement depth and the corresponding distance between the carbonation front and the reinforcement (Δdc) for CEM II/B-M(T-LL) concretes under (a) Wf-Cl, (b) Wf-Cl-CO_2 and (c) Wf-CO_2 exposure.

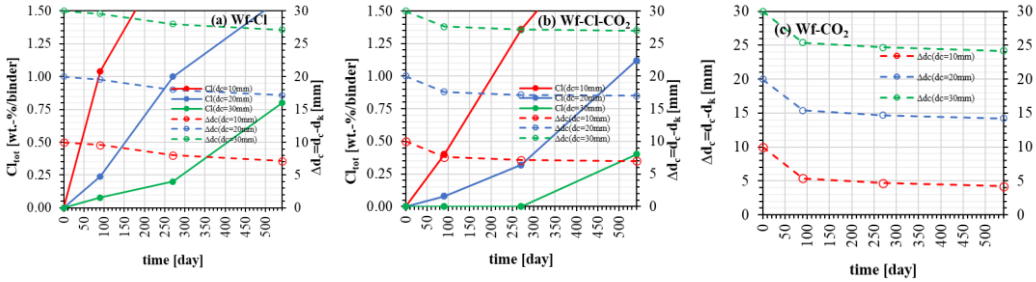

Fig. 93 *Chloride content at reinforcement depth and distance between carbonation front and reinforcement (Δdc) for CEM II/B-M(T-LL) concretes under (a) Wf-Cl, (b) Wf-Cl-CO_2 and (c) Wf-CO_2 exposure. Note: Wf-Cl-CO_2 and Wf-CO_2 specimens experienced an unintended additional 15 days of water exposure.*

Short-circuit measurements confirm active corrosion in both Wf-Cl and Wf-Cl-CO_2 conditions. In contrast, no corrosion was detected in the Wf-CO_2 specimens throughout the entire exposure period. Under Wf-CO_2 conditions, the carbonation front remained at least 6 mm from the reinforcement, indicating that depassivation did not occur.

These results demonstrate that corrosion initiation and propagation in CEM II/B-M(T-LL) concretes were predominantly governed by chloride ingress. Carbonation alone was insufficient to induce reinforcement depassivation within the investigated exposure duration.

4.8.5 Behaviour of CEM III/B

Fig. 94 presents the corrosion rate development of CEM III/B concretes under cyclic wetting and drying, together with the corresponding chloride contents at reinforcement depth and the distance between the carbonation front and reinforcement (Δdc).

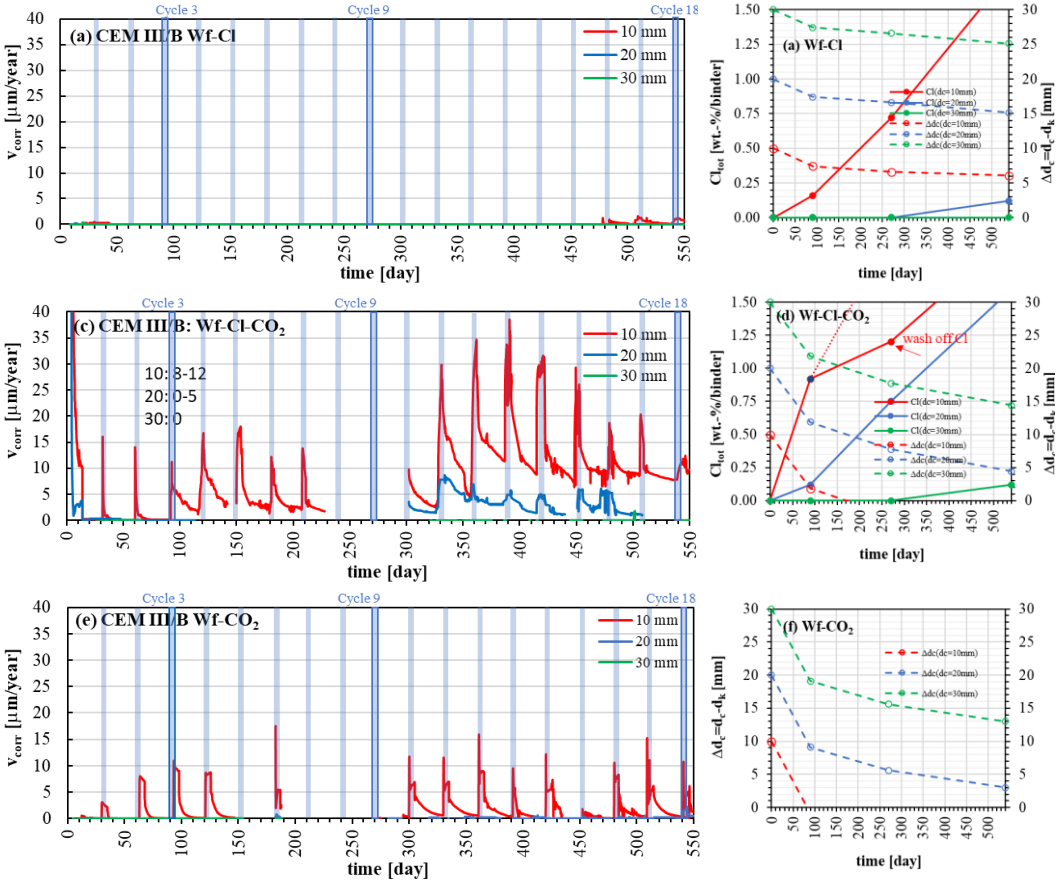

Fig. 94 *Corrosion rate over time of CEM III/B concretes under cyclic wet–dry exposure: (a) Wf-Cl, (c) Wf-Cl-CO_2 and (e) Wf-CO_2. Corresponding chloride content at reinforcement depth and distance between carbonation front and reinforcement (Δdc): (b) Wf-Cl, (d) Wf-Cl-CO_2 and (f) Wf-CO_2.Corrosion.*

Under pure chloride exposure (Wf-Cl), corrosion initiation at 10 mm cover occurs relatively late, at approximately 450 days. At initiation, the chloride content at reinforcement depth is about 1.4 wt.-%/binder, while the carbonation depth remains limited to approximately 6 mm and therefore does not contribute to depassivation. The measured corrosion currents remain comparatively low, indicating slow corrosion propagation.

No corrosion is observed at 20 mm and 30 mm cover within the investigated exposure duration.

Under combined chloride and carbonation exposure (Wf-Cl-CO_2), corrosion at 10 mm cover initiates significantly earlier, between 30 and 60 days of exposure. At that time, the chloride content ranges between 0.3 and 0.5 wt.-%/binder, while the carbonation front is located 3–5 mm from the reinforcement.

After approximately 160 days, the carbonation front reaches the reinforcement depth (10 mm). Beyond ~300 days, corrosion rates increase markedly and remain elevated even during drying phases. This sustained activity is attributed to the higher degree of saturation observed after the 9th cycle (see resistivity/moisture analysis), which maintains electrolyte continuity.

Corrosion at 20 mm cover initiates between 250 and 300 days at chloride contents between 0.2 and 0.5 wt.-%/binder. This earlier initiation compared to Wf-Cl indicates a clear synergistic effect of carbonation and chloride ingress in CEM III/B concretes.

Under carbonation-only exposure (Wf-CO_2), measurable corrosion currents are detected early, even during the first cycles. More significant currents appear after approximately 60 days, when the average carbonation front remains approximately 2 mm from the reinforcement.

This apparent early initiation is attributed to local variability in carbonation depth and possible depassivation within the carbonation gradient. However, corrosion activity decreases during drying phases and does not develop into sustained propagation.

For 20 mm and 30 mm cover depths, no stable corrosion propagation is observed within the investigated period.

4.8.6 Behaviour of CEM II/B-M(S-T)

Fig. 95 compares the evolution of chloride content at reinforcement depth and the corresponding distance between the carbonation front and the reinforcement (Δdc) for CEM II/B-M(S-T) concretes under (a) Wf-Cl, (b) Wf-Cl-CO_2 and (c) Wf-CO_2 exposure.

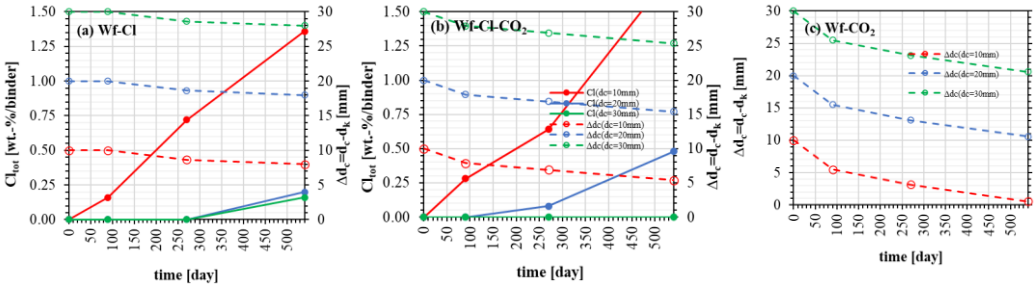

Fig. 95 *Chloride content at reinforcement depth (left axis) and distance between carbonation front and reinforcement (Δdc, right axis) for CEM II/B-M(S-T) concretes under (a) Wf-Cl, (b) Wf-Cl-CO_2 and (c) Wf-CO_2 exposure. Note: Wf-Cl-CO_2 and Wf-CO_2 specimens experienced an unintended additional 15 days of water exposure.*

Under Wf-Cl exposure, chloride contents at 10 mm cover increase steadily over time, reaching values above 1 wt.-%/binder at later ages. However, carbonation depth remains limited, and Δdc remains clearly positive for all reinforcement depths.

Under combined Wf-Cl-CO_2 exposure, carbonation progresses more rapidly, reducing Δdc at 10 mm cover. Nevertheless, chloride contents at reinforcement depth remain comparatively moderate, and the carbonation front does not consistently exceed the reinforcement level during the investigated period.

Under Wf-CO_2 exposure, carbonation advances progressively, particularly at 10 mm cover, but no chlorides are present. Even when the carbonation front approaches the reinforcement, no corrosion initiation is detected.

Across all exposure conditions, no corrosion initiation occurred in CEM II/B-M(S-T) specimens. This indicates a comparatively high resistance against both chloride-induced and carbonation-induced depassivation. The results suggest that either the critical chloride threshold is higher than the measured chloride contents or that the dense microstructure and refined interfacial transition zone delay corrosion initiation despite carbonation advance.

4.8.7 Behaviour of CEM I +33% LS

Fig. 96 presents the corrosion rate development of CEM I + 33% LS concretes subjected to cyclic wetting and drying under (a) Wf-Cl, (b) Wf-Cl-CO_2 and (c) Wf-CO_2 exposure.

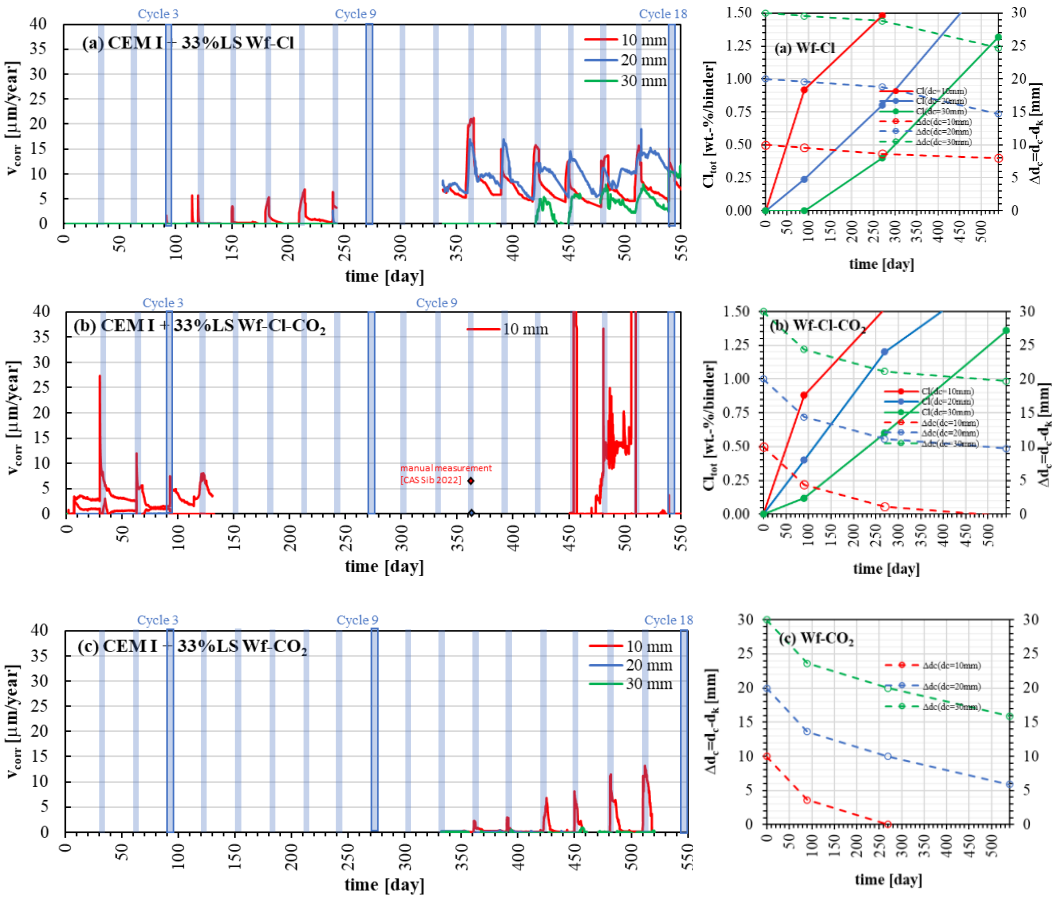

Fig. 96 *Corrosion rate development of CEM I + 33% LS concretes under cyclic exposure: (a) Wf-Cl, (b) Wf-Cl-CO_2 and (c) Wf-CO_2.*

Under Wf-Cl exposure, corrosion initiates at 10 mm cover at an early stage. The corrosion rate shows pronounced cyclic fluctuations corresponding to wetting events, indicating strong moisture control of the electrochemical response. The high degree of saturation limits drying of the cover zone, resulting in sustained corrosion activity once initiation has occurred. Corrosion at 20 mm cover occurs significantly later and remains at a lower level. At 30 mm cover, corrosion remains negligible within the investigated period.

Under Wf-Cl-CO_2 exposure, corrosion behaviour is broadly similar but with slightly higher peak currents at 10 mm cover during later cycles. This can be attributed to the combined effect of chloride accumulation and progressive carbonation in the near-surface region. Carbonation reduces the buffering capacity and may facilitate depassivation once sufficient chloride content is present. The corrosion response becomes more irregular in the later cycles, indicating localised corrosion processes. At greater cover depths (20 mm and 30 mm), corrosion remains limited during most of the exposure period.

Under Wf-CO_2 exposure, drying of the surface zone is more pronounced compared to Wf-Cl. Corrosion currents at 10 mm cover increase during later cycles, consistent with carbonation-induced depassivation once the carbonation front reaches the reinforcement. However, corrosion rates remain strongly dependent on moisture state, decreasing during drying phases. Due to the delayed start of corrosion monitoring (limited data logger availability), the exact initiation time cannot be determined. At 20 mm and 30 mm cover, corrosion activity is low and occurs only in later stages, consistent with the slower carbonation progress at greater depth.

4.8.8 Critical chloride content at corrosion initiation

Fig. 97 summarises the critical total chloride contents at corrosion initiation (C_{Crit}) as a function of (a) the distance between carbonation front and reinforcement (Δd_c) and (b) the measured pH at reinforcement depth.

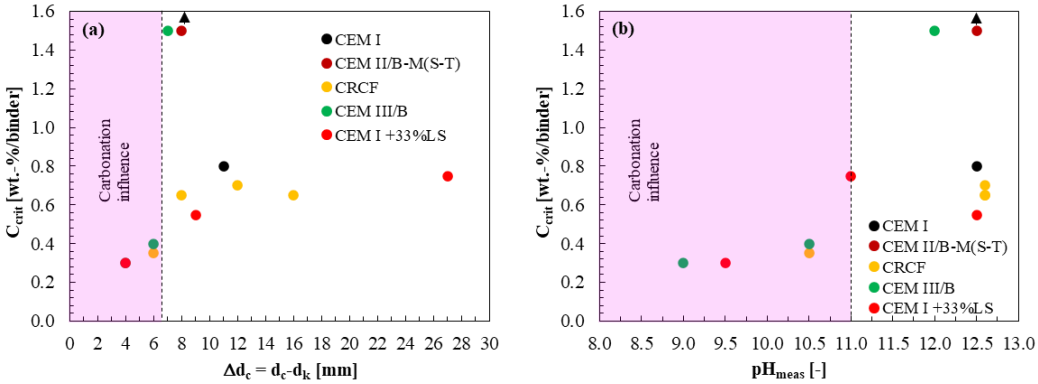

Fig. 97 *Critical total chloride content at corrosion initiation (C_{Crit}) in relation to (a) distance between carbonation front and reinforcement (Δd_c) and (b) measured pH at reinforcement depth.*

Fig. 97 (a) shows that when the carbonation front approaches the reinforcement to within approximately 6 mm (based on phenolphthalein colour change at pH ≈ 8.5), the critical chloride content decreases markedly to approximately 0.3–0.4 wt.-%/binder. In this near-carbonated zone, no pronounced binder-dependent differences are observed; the reduction in alkalinity dominates the depassivation behaviour.

For larger distances between carbonation front and reinforcement (Δd_c > 6–8 mm), the influence of carbonation becomes negligible. Under these conditions, C_{Crit} varies between approximately 0.6 and >1.5 wt.-%/binder, depending on binder type. The lowest values in this range correspond to Portland cement-based systems, while slag-containing systems exhibit the highest chloride thresholds.

Fig. 97 (b) confirms that the reduction in C_{Crit} correlates directly with decreasing pH. At measured pH values around 10–11, C_{Crit} falls into the range of 0.3–0.4 wt.-%/binder, whereas at pH ≈ 12.5, C_{Crit} ranges from 0.6 up to >1.5 wt.-%/binder. This demonstrates that alkalinity at reinforcement depth is a governing parameter for chloride-induced depassivation.

Overall, the data indicate two distinct regimes:

- Carbonation-influenced regime ($\Delta d_c \leq 6$ mm, pH ≤ 11): C_{Crit} ≈ 0.3–0.4 wt.-%/binder, largely independent of binder type.
- Non-carbonated regime (Δd_c > 6–8 mm, pH ≈ 12.5): C_{Crit} ≈ 0.6 to >1.5 wt.-%/binder, strongly binder-dependent.

Fig. 98 presents the calculated phase assemblage of the investigated binders (a) without chlorides and (b) with 2.0 wt.-% Cl/binder.

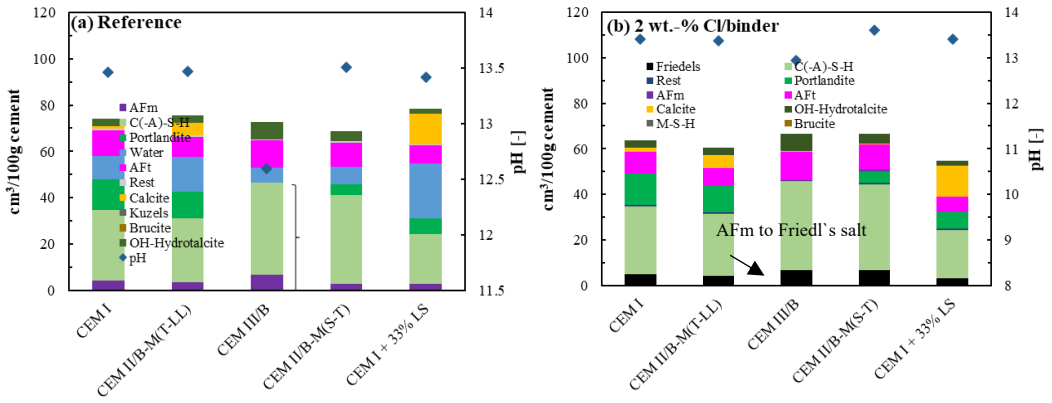

Fig. 98 *Calculated phase assemblage of the investigated binders (a) without chloride and (b) with 2.0 wt.-% Cl/binder.*

The slag-containing binders (CEM III/B and CEM II/B-M(S-T)) exhibit the highest calculated volumes of C-(A-)S-H and Friedel's salt. This corresponds well with the experimentally observed higher critical chloride contents (C_{Crit}) under non-carbonated conditions (Table 23). In contrast, CEM I + 33% LS shows lower volumes of chloride-binding phases and correspondingly lower C_{Crit} values.

The higher chloride thresholds in slag-rich binders can therefore be attributed to:

- Increased chemical binding via Friedel's salt formation,
- Higher Al-bearing hydrates contributing to chloride uptake,
- Larger volumes of C-(A-)S-H capable of physical and chemical chloride incorporation.

Upon carbonation, the experimentally observed convergence of C_{Crit} values (≈0.3–0.4 wt.-%/binder) suggests partial release of previously bound chlorides. Although pH measurements indicate that only part of the C-(A-)S-H is decalcified, even moderate alkalinity reduction significantly lowers the chloride threshold. This implies that chloride binding capacity becomes less decisive once alkalinity drops below approximately pH 11.

A clearer description of C_{Crit} under non-carbonated conditions is obtained when plotting C_{Crit} as a function of Al_2O_3 content (Fig. 99).

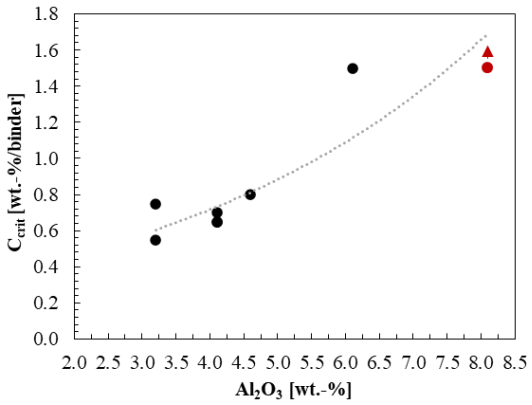

Fig. 99 *Al_2O_3. Critical chloride content (C_{Crit}) of non-carbonated samples as a function of Al_2O_3 content.*

Fig. 99 shows a positive correlation between Al_2O_3 content and C_{Crit}. This supports the mechanistic interpretation that chloride threshold in highly alkaline systems is primarily governed by the availability of Al-bearing hydrates capable of forming Friedel's salt. Under purely chloride exposure, binder composition - particularly Al_2O_3 content — is therefore a controlling parameter for corrosion initiation.

However, this compositional control weakens significantly under partial carbonation, where alkalinity becomes the dominant parameter.

Based on the measured and calculated results, corrosion initiation can be summarised as follows:

- Strong reduction of C_{Crit} when pH ≤ 11 or when the carbonation front approaches within ≤ 6 mm of the reinforcement.
- Under carbonation influence, corrosion initiation occurs at total chloride contents C_{tot} ≥ 0.3 wt.-%/binder, largely independent of binder type.
- Under non-carbonated conditions, C_{Crit} increases with increasing Al_2O_3 content and chloride-binding capacity.

4.8.9 Carbonation induced corrosion initiation

Carbonation-induced corrosion was observed only in selected systems and occurred primarily when the carbonation front approached the reinforcement to within a few millimetres. Under carbonation-only exposure (Wf-CO_2), corrosion was detected in CRCF, CEM III/B and CEM I + 33% LS, whereas no carbonation-induced corrosion occurred in CEM I within the investigated period.

Across the affected systems, corrosion initiation consistently occurred when the distance between the carbonation front and the reinforcement (Δdc) was approximately 3–5 mm. At this stage, the measured pore solution pH ranged between about 9.0 and 9.5. These values correspond to substantial decalcification of portlandite and partial decalcification of C-(A)-S-H phases. In CEM III/B, corrosion under both carbonation-only and combined carbonation–chloride exposure initiated already after 30 days (third cycle), indicating comparatively high sensitivity to pH reduction in the near-reinforcement zone.

Overall, carbonation-induced depassivation was governed primarily by local pH reduction and proximity of the carbonation front rather than by pronounced binder-specific effects. The absence of carbonation-induced corrosion in CEM I reflects its slower carbonation advance and sustained alkaline buffering at reinforcement depth.

Fig. 100 presents the calculated evolution of pore solution pH as a function of CO_2 concentration for the different binders and chloride contents.

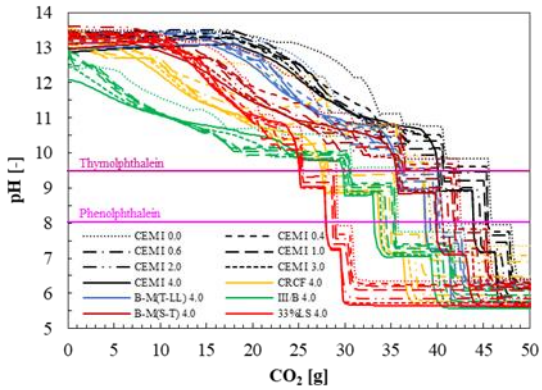

Fig. 100 *Calculated pore solution pH as a function of CO_2 concentration for different binders and total chloride contents (added as NaCl). Carbonation leads to dissolution of portlandite and progressive decalcification of hydrates, reducing pH toward the depassivation range.*

Initially, portlandite and alkalis buffer the pore solution at pH ≈ 13.5 (slightly lower for CRCF and CEM III/B). Upon portlandite dissolution, pH decreases continuously due to decalcification of ettringite, AFm phases, hydrotalcite, strätlingite and C-(A)-S-H until calcite becomes the dominant Ca phase. Complete decalcification results in pH values near 8 and below.

The calculations further indicate that increasing chloride content reduces pH at a given CO_2 concentration across the entire carbonation range. However, the experimentally observed carbonation rates do not strictly follow the thermodynamic ranking, demonstrating that kinetic effects and transport properties dominate carbonation progression.

To relate pH reduction to electrochemical stability, Fig. 101 shows the evolution of the ionic ratios $[CO_3^{2-}]/[HCO_3^-]$ and $[SO_4^{2-}]/[OH^-]$ during carbonation.

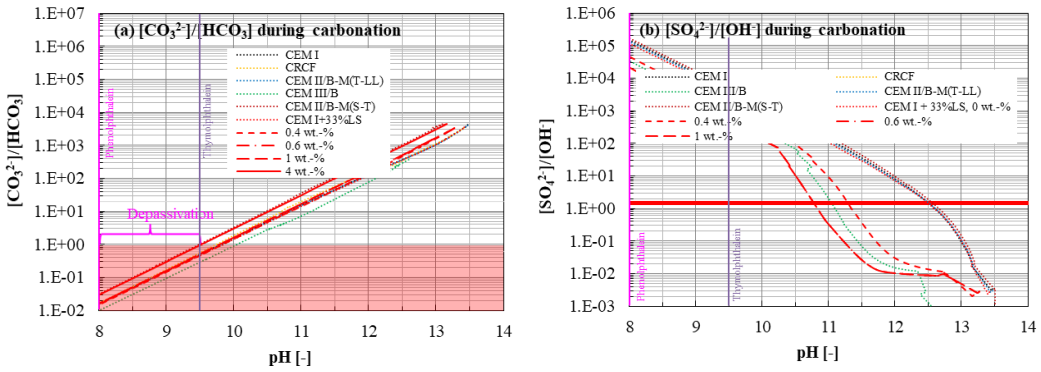

Fig. 101 *Evolution of (a) $[CO_3^{2-}]/[HCO_3^-]$ and (b) $[SO_4^{2-}]/[OH^-]$ ratios during pH reduction due to carbonation (chloride-free systems). Horizontal lines indicate proposed depassivation limits from literature. Vertical lines mark colour-change pH of phenolphthalein and thymolphthalein.*

The binder type exerts only minor influence on depassivation thresholds when expressed in terms of the carbonate ratio. For chloride-free systems, depassivation according to the $[CO_3^{2-}]/[HCO_3^-]$ criterion occurs at pH ≈ 9.7–10 for most binders, and slightly higher for CEM III/B.

Addition of chlorides shifts depassivation to lower pH values (≈ 9.0), consistent with the experimental observations. Comparison with the $[Cl^-]/[OH^-]$ criterion suggests that chloride-induced depassivation would theoretically occur earlier than predicted by carbonate ratio limits. Conversely, the $[SO_4^{2-}]/[OH^-]$ threshold appears overly conservative, predicting depassivation at unrealistically high pH values (~12.5).

Combining experimental observations and thermodynamic modelling, carbonation-induced corrosion initiation can be characterised by:

- Local pH reduction to pH ≤ 9.0–9.5
- Carbonation front located within Δdc ≈ 3 mm
- Complete dissolution of portlandite and Friedel's salt
- Partial decalcification of C-(A)-S-H

Thus, depassivation during carbonation is governed by progressive buffering exhaustion and near-reinforcement chemical transformation rather than by abrupt indicator colour change or binder-specific phase assemblage alone.

4.8.10 Microcell corrosion rate

Linear polarization resistance (LPR) measurements were performed using a Gamry Interface 1010 potentiostat/galvanostat/ZRA. All specimens were tested after completion of the cyclic exposure during the final wet phase. After stabilization for > 24 h, polarization curves were recorded at a scan rate of 0.1 mV/s over an exposed steel area of 40.21 cm².

Fig. 102 presents the current density–potential curves obtained during the last wet period for all investigated binders: (a) CEM I, (b) CRCF, (c) CEM II/B-M(T-LL), (d) CEM III/B, (e) CEM II/B-M(S-T), and (f) CEM II/B-LL.

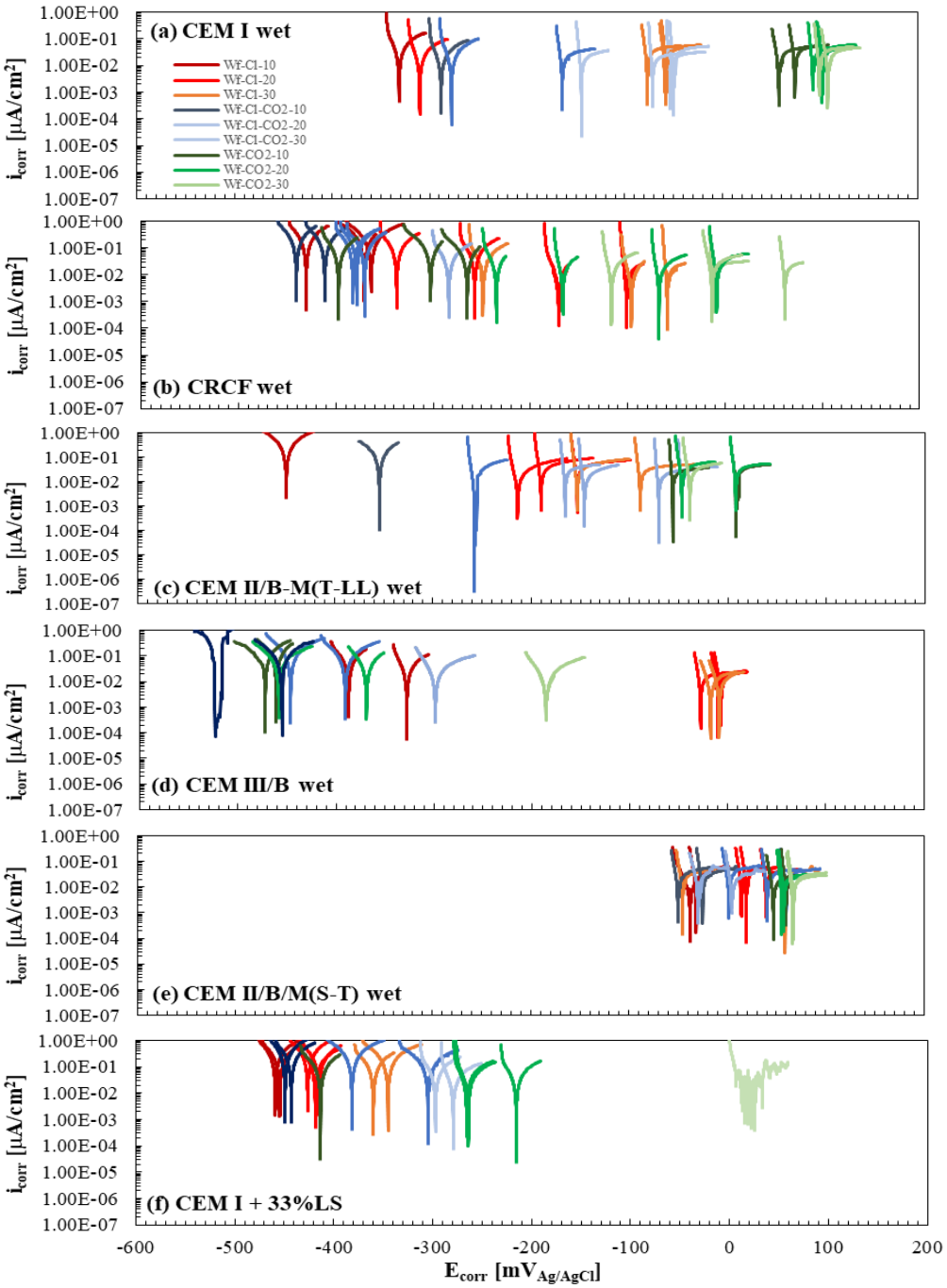

Fig. 102 *Current density–potential curves determined by linear polarization resistance during the final wet period for (a) CEM I, (b) CRCF, (c) CEM II/B-M(T-LL), (d) CEM III/B, (e) CEM II/B-M(S-T), and (f) CEM II/B-LL.*

In specimens without active corrosion, free corrosion potentials (E_{corr}) remain relatively noble, typically between –100 mV and +100 mV (vs. reference), and corrosion current densities are low, largely independent of cover depth. These curves exhibit limited polarization slopes, indicating passive behaviour.

In systems where corrosion is governed purely by chlorides (e.g. Wf-Cl and Wf-Cl-CO_2 for CEM I; CRCF at 20 and 30 mm; CEM II/B-M(T-LL); CEM I + 33% LS at 10 mm), E_{corr} shifts to more negative values in the range of approximately –300 to –450 mV. Correspondingly, corrosion current densities increase, reflecting active chloride-induced depassivation.

Where corrosion occurs in carbonated concrete, E_{corr} is generally even more negative (< –450 mV), particularly in systems where carbonation and chlorides act synergistically. These samples show steeper polarization behaviour and higher corrosion current densities, consistent with reduced alkalinity and sustained electrochemical activity.

Across all binders, a clear relationship is observed: decreasing free corrosion potential is accompanied by increasing corrosion current density. The microcell measurements therefore confirm the trends derived from macrocell monitoring—passive behaviour at noble potentials, chloride-induced activation at intermediate negative potentials, and intensified corrosion under combined carbonation–chloride exposure.

Fig. 103 illustrates the relationship between polarization resistance and free corrosion potential for different corrosion regimes.

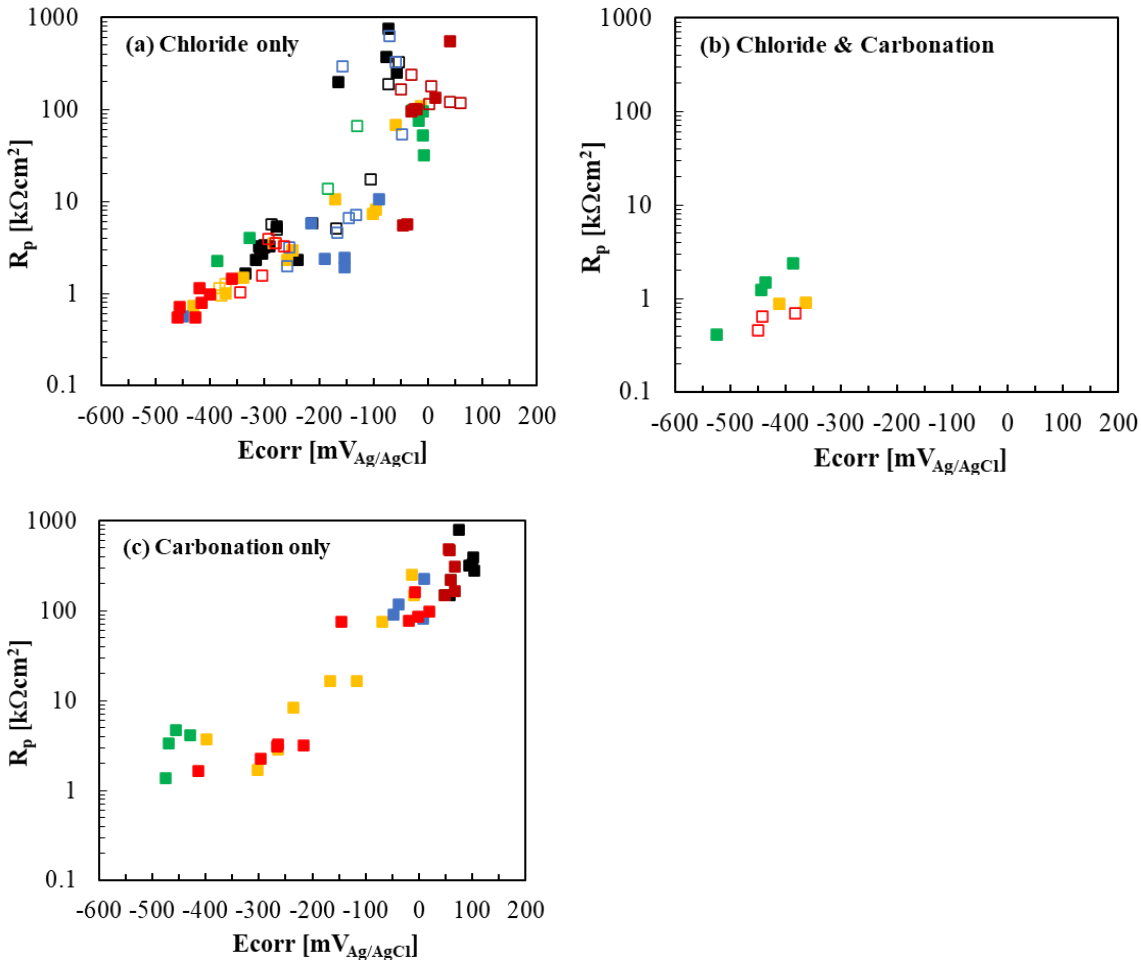

Fig. 103 *Polarization resistance (R_p) versus free corrosion potential (Ag/AgCl) for (a) chloride-governed corrosion without carbonation influence (Δdc ≥ 5 mm), (b) combined carbonation–chloride exposure (Δdc ≤ 3 mm or carbonation front at reinforcement), and (c) carbonation-only exposure.*

In the case of purely chloride-induced corrosion (Fig. 103a), R_p decreases with increasingly negative potentials, but values generally remain above approximately 0.5 kΩ·cm².

Under combined carbonation–chloride exposure (Fig. 103b), the lowest polarization resistances are observed at the most negative free corrosion potentials, indicating intensified electrochemical activity when chloride ingress and pH reduction act simultaneously.

In contrast, carbonation-only exposure (Fig. 103c) results in comparatively higher polarization resistances; none of the measured values fall below 1 kΩ·cm². Although measurable corrosion currents may occur in carbonated concrete, the electrochemical response remains less severe than in chloride-containing systems.

Overall, decreasing (more negative) free corrosion potentials correspond to reduced polarization resistance and increased corrosion activity, with the most pronounced effect occurring under combined carbonation and chloride action.

Fig. 104 compares the microcell corrosion rates derived from polarization resistance measurements. The anodic area was assumed to correspond to the entire exposed reinforcement surface; current confinement within pits was not considered. Results are grouped into (i) chloride-induced corrosion without carbonation influence, (ii) combined chloride and carbonation exposure, and (iii) carbonation-induced corrosion only. Data are shown for (a) 10 mm and (b) 20 mm concrete cover.

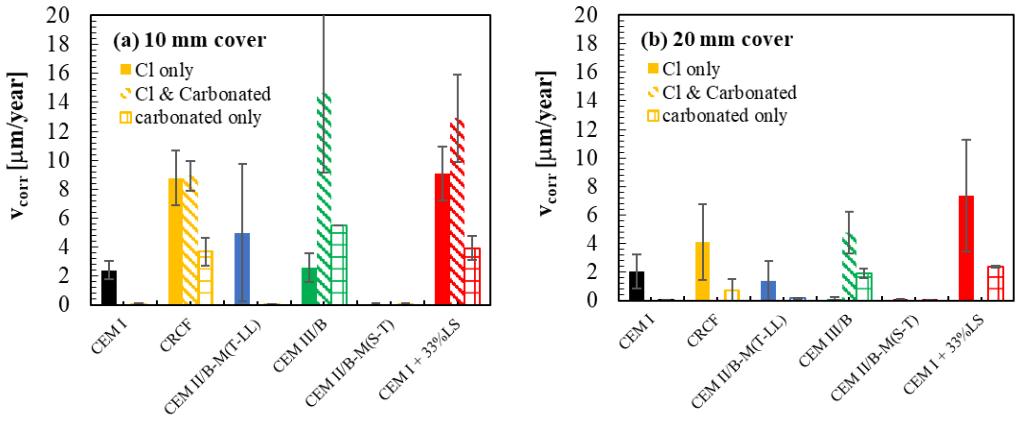

Fig. 104 *Microcell corrosion rate only influenced by chlorides with no carbonation effect, in the presence of chlorides with carbonation influence and only carbonation induced corrosion for rebars with (a) 10 mm cover and (b) 20 mm cover.*

At 10 mm cover (Fig. 104a), the highest average corrosion rates occur under combined chloride–carbonation exposure, reaching approximately 12 µm/year (mean over all binders). Purely chloride-induced corrosion yields intermediate rates of approximately 7 µm/year, while carbonation-only exposure results in lower values of approximately 5 µm/year.

At 20 mm cover (Fig. 104b), corrosion rates under chloride-only and combined exposure converge to similar levels of approximately 5 µm/year. In contrast, carbonation-only exposure leads to clearly lower corrosion rates of approximately 2 µm/year. Although measurements were conducted during wetting phases, resistivity results indicate that the average moisture state at reinforcement depth remained below full saturation, which explains the moderate absolute corrosion rates observed.

Overall, combined chloride and carbonation exposure produces the most severe microcell corrosion response, particularly at low cover depth, whereas carbonation alone results in comparatively limited corrosion activity.

4.8.11 Microcell & Macrocell corrosion rate

Fig. 105 compares the macrocell corrosion rates determined during wet conditions (a) with the corresponding microcell corrosion rates (b). Both manually measured and continuously monitored values are included.

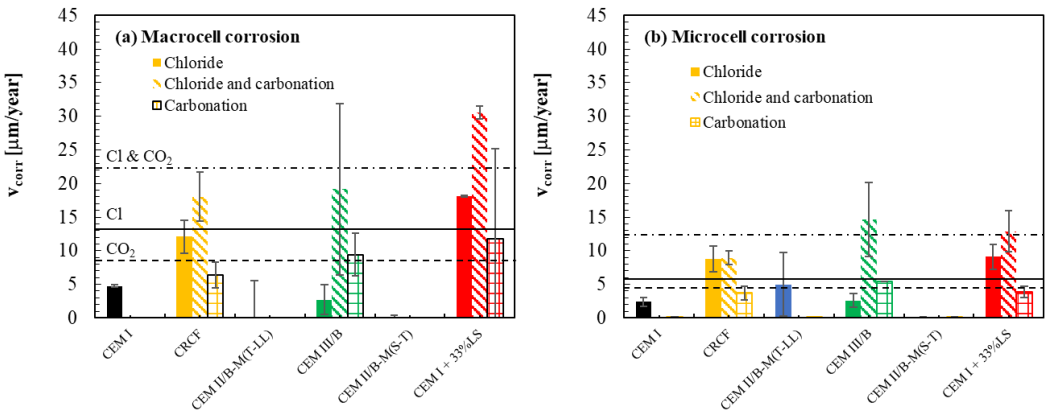

Fig. 105 *Macrocell corrosion rate manually measured during wetting (a) and microcell corrosion rates (right); concrete cover 10 mm.*

A clear and systematic difference between macrocell and microcell corrosion rates is observed.

Under carbonation-induced corrosion, the microcell corrosion rate is approximately 50% of the macrocell corrosion rate. In contrast, for purely chloride-induced corrosion and for chloride-induced corrosion in carbonated concrete, the microcell corrosion rate is only about one third of the macrocell corrosion rate.

This demonstrates that:

- Macrocell activity significantly amplifies corrosion propagation, particularly in chloride-contaminated systems.
- The contribution of macrocell corrosion is more pronounced in chloride-driven systems than in carbonation-only systems.
- Lower resistivity in chloride-contaminated concrete enhances macrocell currents and thus increases the discrepancy between macrocell and microcell rates.

5 Mortar results

5.1 Mechanical properties

5.1.1 Compressive strength

Fig. 106 (a) compares the 91-day compressive strength of the mortars after sealed curing with the corresponding concretes produced using the same binders.

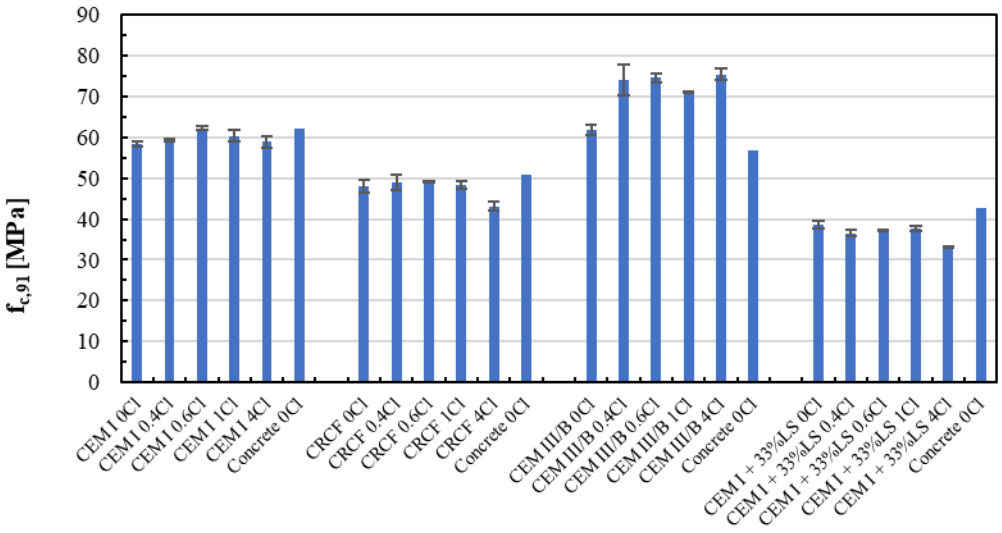

Fig. 106 *Compressive strength of mortar specimens after 91 days of sealed curing compared with corresponding concretes.*

With the exception of CEM III/B, the 91-day compressive strengths of mortar and concrete are comparable for the same binder type. Minor differences can be attributed to variations in aggregate grading, interfacial transition zone effects, and specimen geometry. Overall, the binder-controlled strength development appears consistent between mortar and concrete systems.

For CEM III/B, however, mortars containing NaCl exhibit a noticeably higher compressive strength compared to the corresponding chloride-free mix. This effect was not observed for the other binders.

In contrast to $CaCl_2$, which is known to accelerate hydration and increase early strength, NaCl is generally not expected to significantly enhance compressive strength. However, in slag-containing systems (CEM III/B), chloride ions may:

- Promote slag activation by increasing ionic strength of the pore solution,
- Enhance early formation of C-(A)-S-H phases,
- Modify aluminate reactions and potentially increase the formation of Friedel's salt.

These mechanisms may contribute to a denser microstructure and thus slightly higher later-age strength in the chloride-containing CEM III/B mortars.

No systematic strength increase due to NaCl addition was observed in Portland cement–dominated systems (CEM I, CEM I + 33% LS, CEM II/B-M), indicating that the chloride–slag interaction is likely responsible for the observed strength enhancement.

5.1.2 Raw density

Fig. 107 presents the raw density of the mortar specimens after 91 days of sealed curing in comparison with the corresponding concretes.

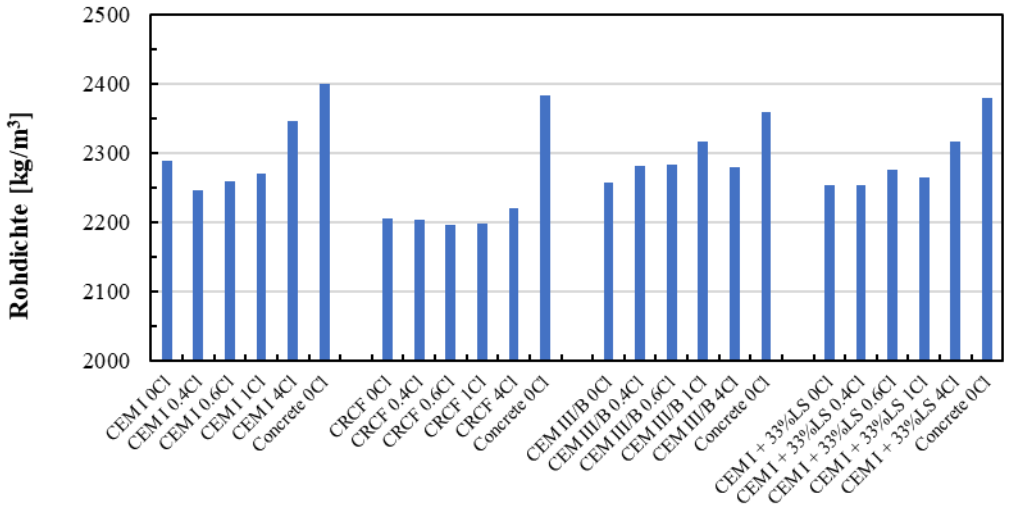

Fig. 107 *Raw density of mortar specimens after 91 days of sealed curing compared with the corresponding concretes.*

As expected, the mortars exhibit lower raw densities than the corresponding concretes. This difference is primarily attributable to the absence of coarse aggregates in the mortar mixtures. Coarse aggregates typically possess higher intrinsic density and reduce the overall paste volume fraction; consequently, concretes generally show higher bulk densities than mortars produced with the same binder.

A slight increase in raw density with increasing NaCl content is observed across most binder systems. This effect can be explained by:

- The higher solid mass introduced by NaCl addition,
- Possible changes in hydration products (e.g. formation of Friedel's salt),
- A marginal reduction in porosity due to modified hydration kinetics, particularly in slag-containing systems.

However, the density changes remain small and do not indicate significant microstructural densification. The primary controlling parameter for raw density remains the aggregate composition rather than binder type or chloride content.

5.2 Durability

5.2.1 Decalcification progress

Fig. 108 presents the neutralization depth determined by phenolphthalein spraying after exposure to 6 M NH_4NO_3 for different durations for (a) CEM I, (b) CRCF, (c) CEM III/B and (d) CEM I + 33% LS mortars. Each mix contained 0, 0.4, 0.6, 1.0 or 4.0 wt.-% Cl/binder, added as NaCl.

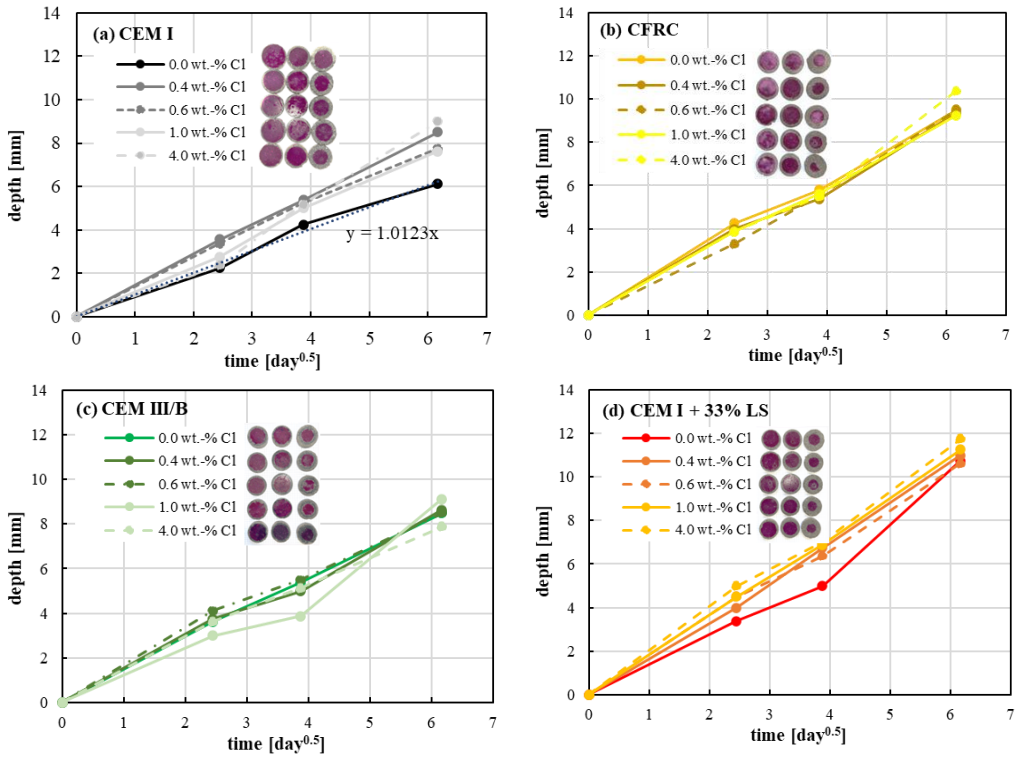

Fig. 108 *Neutralization depth after leaching in 6 M NH_4NO_3 for (a) CEM I, (b) CRCF, (c) CEM III/B and (d) CEM I + 33% LS mortars containing 0–4.0 wt.-% Cl per binder added as NaCl.*

For all binders, neutralization depth increases approximately linearly with the square root of time, indicating diffusion-controlled decalcification.

The influence of binder type is more pronounced than that of admixed NaCl:

- Highest leaching depths: CEM I + 33% LS
- Followed by: CRCF
- Lowest depths: CEM I and CEM III/B

The addition of NaCl does not systematically reduce neutralization depth, although a slight porosity reduction might have been expected. In CEM I and CEM I + 33% LS, leaching depths tend to increase with increasing chloride content. In CRCF and CEM III/B, the influence of chloride addition is minor and within scatter.

Leaching rates were determined from the slope of neutralization depth versus √time (example shown in Fig. 108a). The resulting rates are summarized in Tab. 23.

***Tab. 23** Leaching (neutralisation) rates*

Wt.-% Cl / cement (mixed in NaCl)	CEM I [mm/day$^{0.5}$]	CRCF [mm/day$^{0.5}$]	CEM III/B [mm/day$^{0.5}$]	CEM I + 33% [mm/day$^{0.5}$]
0.0	1.01	1.55	1.39	1.59
0.4	1.39	1.50	1.39	1.76
0.6	1.30	1.50	1.42	1.72
1.0	1.24	1.50	1.33	1.81
4.0	1.38	1.61	1.31	1.89

The data confirm:

- CEM I + 33% LS exhibits the highest leaching rates, increasing systematically with chloride content.
- CRCF shows consistently high but relatively stable rates, largely independent of chloride content.
- CEM III/B displays moderate rates with minimal chloride influence.
- CEM I shows the lowest rates at 0% Cl but a noticeable increase at elevated chloride contents.

Overall, binder composition governs decalcification kinetics more strongly than admixed chloride content. Chloride addition does not reduce leaching resistance and may slightly accelerate decalcification in selected systems, particularly those with limestone addition.

5.2.2 Chloride depletion into solvent

The increase in chloride concentration in the surrounding 6 M NH_4NO_3 solution was monitored periodically using an ion-selective electrode (ISE). The temporal evolution of chloride concentration is presented in Fig. 109. Although expected, No pronounced initial wash-off was observed, indicating that chloride release was governed by progressive matrix decalcification rather than by rapid dissolution of loosely bound surface chlorides.

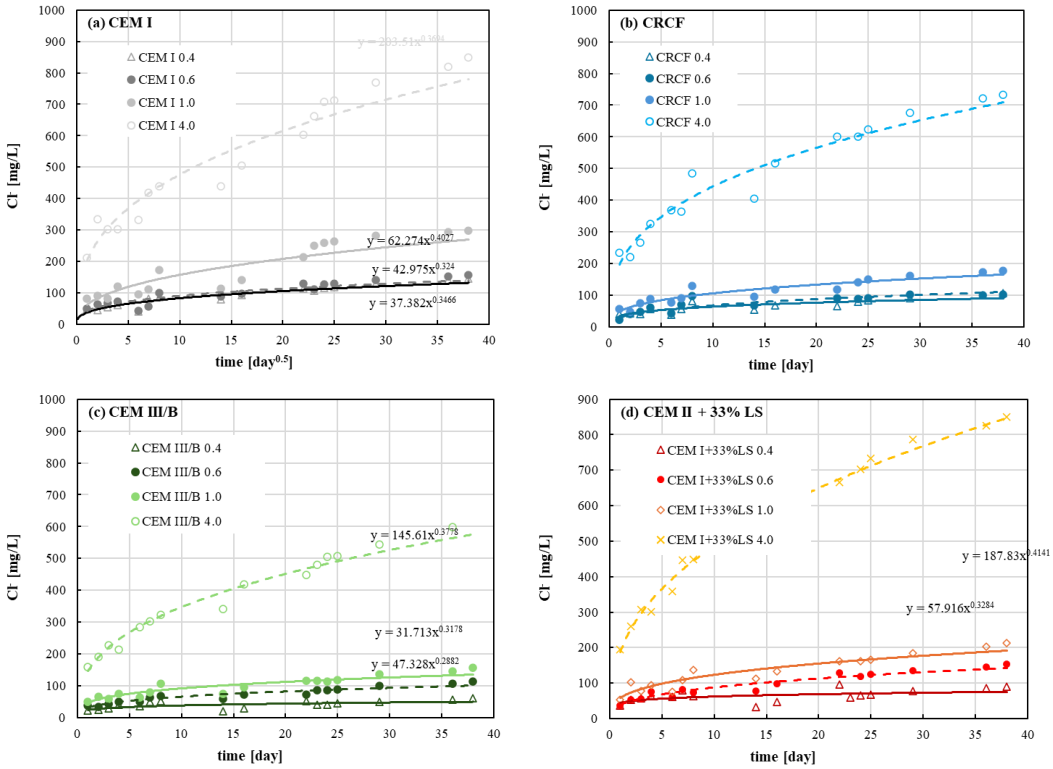

Fig. 109 *Chloride concentration in the leaching solution (6 M NH_4NO_3) over time for mortars based on (a) CEM I, (b) CRCF, (c) CEM III/B and (d) CEM I + 33% LS with 0.4–4.0 wt.-% Cl/binder added as NaCl.*

The highest cumulative chloride concentrations in the solvent were measured for CEM I + 33% LS, followed by CRCF, which corresponds well with the larger neutralization depths determined previously. The lowest chloride release was observed for CEM III/B, consistent with its comparatively lower decalcification depth and higher chloride binding capacity.

The increase in chloride concentration over time deviates from a classical $\sqrt{t}$ behaviour and is better described by a power function, reflecting the coupling between ongoing decalcification and progressive release of chemically and physically bound chlorides.

Tab. 24 summarizes the total mixed-in chloride content (Cl_tot), the measured chloride concentration in the solvent after 38 days (Cl_meas), and the derived leaching rate parameters. The time exponent n ranges between approximately 0.16 and 0.41, confirming non-Fickian release kinetics. Lower exponents (e.g., CEM I + 33% LS at 0.4 wt.-% Cl, n = 0.16) indicate a stronger initial release tendency, whereas values around 0.35–0.40 suggest more sustained chloride mobilization over time.

***Tab. 24** total chloride content Cl^-_{tot}, measured chloride concentration in solvent before sample removal Cl^-_{meas} and chloride leaching rate as well as time exponent n of leaching rate*

Sample	Cl^-_{tot} [mg/sample]	$Cl^-_{meas.}$ after 38 day [mg/L]	Cl^- leach. rate [mg/day^n]	n leach. Rate [-]
CEM I 0.4	196	83	37.4	0.35
CEM I 0.6	294	95	43.0	0.32
CEM I 1.0	490	106	62.3	0.40
CEM I 4.0	1959	751	203.5	0.37
CRCF 0.4	194	107	34.7	0.26
CRCF 0.6	292	102	29.8	0.36
CRCF 1.0	486	178	49.2	0.33
CRCF 4.0	1943	732	197.3	0.35
CEM III/B 0.4	194	61	24.2	0.20
CEM III/B 0.6	291	115	31.7	0.31
CEM III/B 1.0	485	156	47.3	0.29
CEM III/B 4.0	1940	598	145.6	0.38
CEM I+33%LS 0.4	194	91	44.2	0.16
CEM I+33%LS 0.6	291	153	38.0	0.36
CEM I+33%LS 1.0	485	213	57.9	0.33
CEM I+33%LS 4.0	1940	851	187.8	0.41

For all binders and chloride levels, the theoretically available chloride content exceeded the measured amount in the solvent at the end of the test period. This demonstrates that only a fraction of the total chloride inventory was mobilized within 38 days, even under aggressive leaching conditions. The remaining chlorides are either still physically trapped within the pore structure or chemically bound in hydration phases that were not fully decalcified during the investigated period.

The pH of the 6 M NH_4NO_3 solution was monitored throughout the leaching period. All chloride levels (0–4.0 wt.-% Cl/binder) of a given cement are plotted in the same colour in Fig. 110.

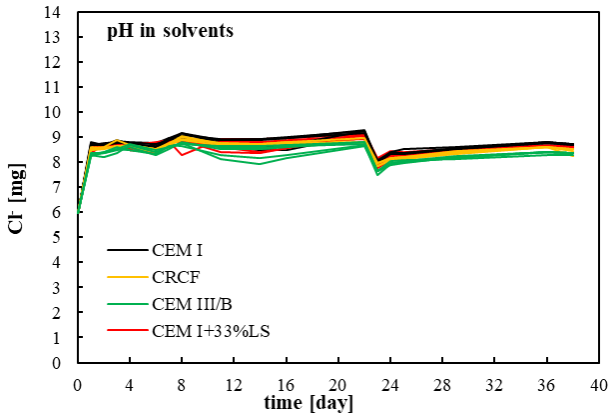

***Fig. 110** Evolution of pH in the leaching solution (6 M NH_4NO_3) over time for all investigated binders and chloride contents.*

An initial increase in pH is observed during the first days of exposure, reflecting the rapid dissolution of alkaline species released during early decalcification. Subsequently, the pH

stabilizes below 9 for all systems, indicating limited buffering capacity of the leaching solution despite ongoing matrix degradation.

After approximately 25 days, the solvent was replaced in all containers due to an accidental cross-contamination. This exchange is clearly visible as a sudden drop in pH. Following renewal, the pH stabilizes at approximately 8.5 and remains nearly constant until the end of the measurement period.

5.2.3 Neutron images

From selected specimens, neutron radiographs were obtained after exposure. The images are shown in Fig. 111.

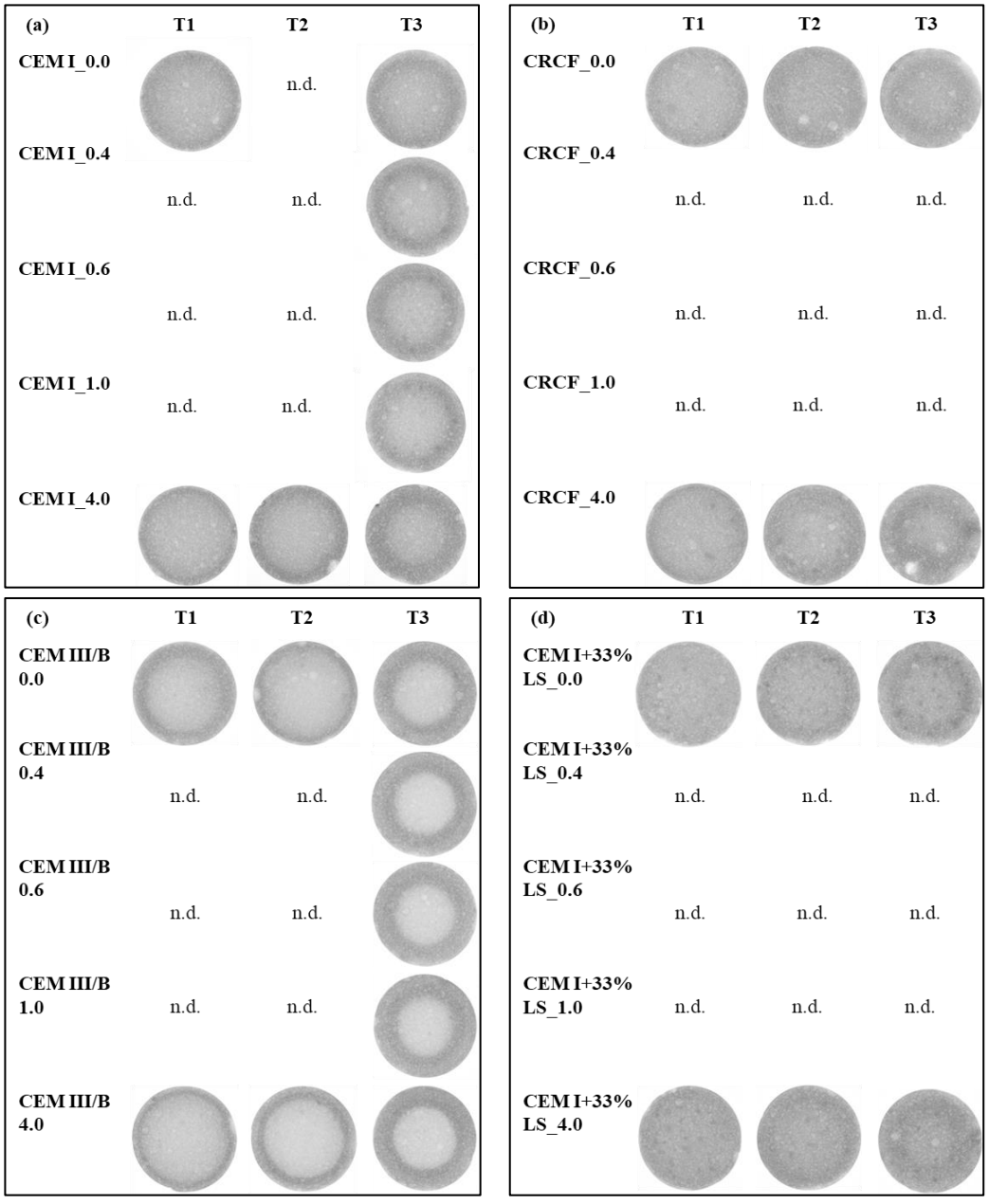

Fig. 111 *Neutron radiographs of leached mortar specimens: (a) CEM I, (b) CRCF, (c) CEM III/B and (d) CEM I + 33% LS.*

The grey-scale contrast reflects differences in hydrogen distribution and thus pore water content and transport processes. A brighter central region indicates limited exchange

between pore solution and the external NH_4NO_3 solvent, i.e. reduced dissolution of water-bearing hydration phases.

CEM I and CEM III/B exhibit a pronounced grey-scale gradient from the surface towards the core, indicating progressive leaching and solvent ingress. In contrast, CRCF and especially CEM I + 33% LS show a less distinct brightness gradient, suggesting a more heterogeneous or locally restricted exchange.

In CEM I + 33% LS, distinct dark spots are visible throughout the specimen cross-section. These may indicate locally increased hydrogen content (retained water) or phases with higher neutron attenuation originating from the raw materials.

A thin, bright outer rim is visible in several samples. This layer is most likely associated with rapid surface drying during handling and may correspond to a silica gel- and Al-/Fe-hydroxide-rich zone formed after extensive decalcification.

Fig. 112 presents the neutron grey-value profiles for the CEM I mortar series. The symbols indicate the carbonation depth determined by pH indicator, while the pink band marks the grey-value range corresponding to the indicator color change.

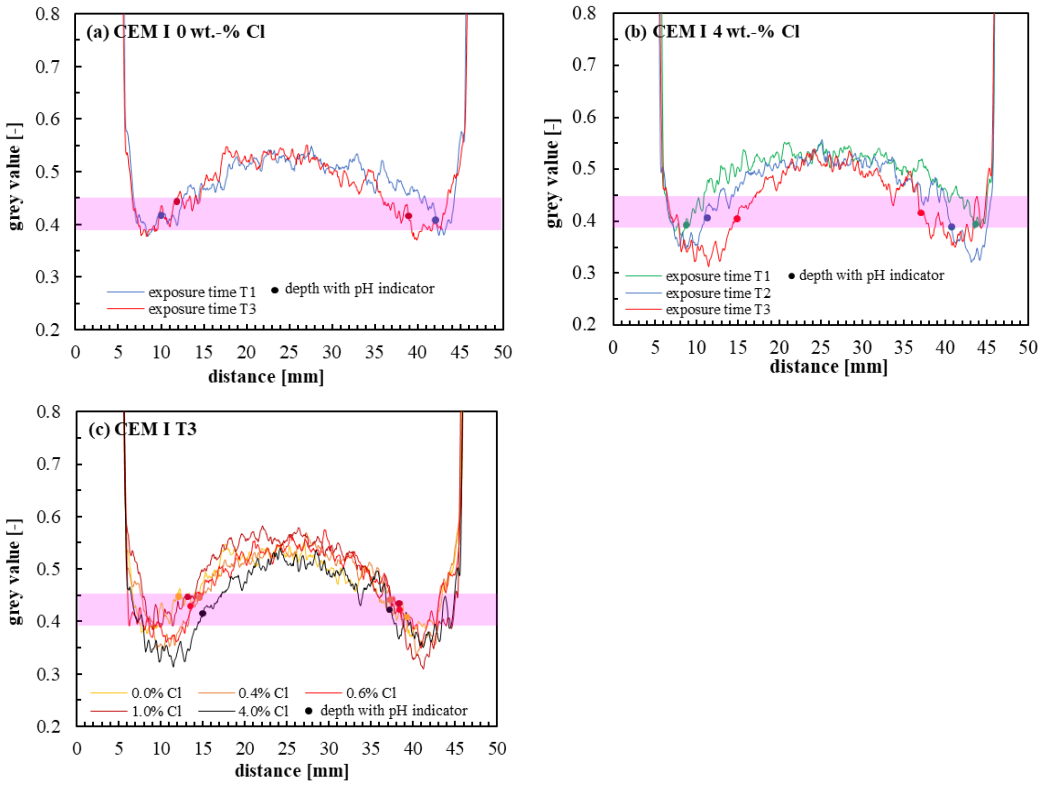

Fig. 112 *Neutron grey-value profiles of CEM I mortars: (a) 0 wt.-% Cl (T1 and T2), (b) T3 with 0–4 wt.-% Cl/binder, and (c) 4 wt.-% Cl (T1, T2, T3). Symbols denote carbonation depth from pH indicator; pink band indicates corresponding grey-value range.*

The sharp increase in grey value at both edges marks the specimen boundaries. Immediately beneath the surface, reduced grey values (higher neutron attenuation) indicate regions where pore solution exchange and dissolution of hydration products occurred. Towards the specimen centre, grey values increase, reflecting limited solvent penetration and thus no significant decalcification.

For both chloride-free and 4 wt.-% Cl samples, the zone of reduced grey values expands progressively with exposure time (T1 < T2 < T3), confirming the continuous advance of decalcification depth.

A notable observation is the systematic decrease in grey values in the central region with increasing NaCl content. This behaviour is attributed to the higher chloride binding (e.g., formation of Friedel's salt), which alters the hydrogen distribution and attenuation characteristics. Thus, chloride addition influences not only chemical stability but also the internal moisture and phase distribution detectable by neutron imaging.

Fig. 113 presents the neutron grey value profiles of CRCF mortars for (a) 0 wt.-% Cl and (b) 4 wt.-% Cl at exposure times T1, T2 and T3. The symbols indicate the carbonation (neutralization) depth determined by phenolphthalein, while the pink band marks the corresponding grey value range associated with the indicator colour change.

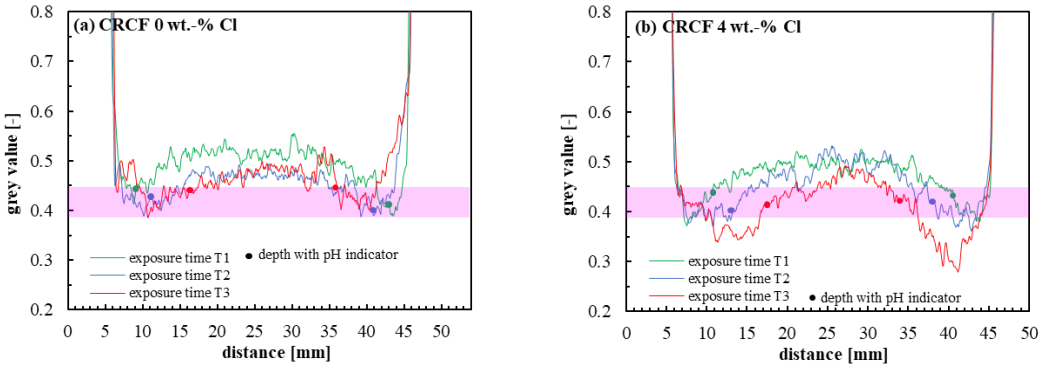

Fig. 113 *Neutron grey value profiles of CRCF mortars after leaching in 6M NH_4NO_3: (a) 0 wt.-% Cl and (b) 4 wt.-% Cl at exposure times T1, T2 and T3. Symbols indicate the neutralization depth determined by phenolphthalein; the pink band represents the grey value range corresponding to the indicator colour change.*

Compared to CEM I, the contrast between decalcified and non-decalcified regions is less pronounced in CRCF. The grey value difference between the outer leached zone (low grey values due to higher attenuation and water exchange) and the inner intact core is smaller. This reduced contrast is likely related to the higher initial calcite content originating from carbonated recycled fines, which decreases the relative mineralogical change during leaching.

Nevertheless, a progressive inward shift of the low-grey-value region is clearly visible from T1 to T3, confirming the increase in decalcification depth with exposure time. For the 4 wt.-% Cl specimens, the central grey values are slightly lower than for the chloride-free specimens, indicating higher attenuation in the core region, possibly associated with increased bound chlorides (e.g. Friedel's salt) and modified pore solution chemistry.

Fig. 114 presents the grey value profiles across CEM III/B mortar specimens after leaching exposure. The symbols indicate the neutralization depth determined by phenolphthalein, while the pink band marks the grey value range corresponding to the indicator color change.

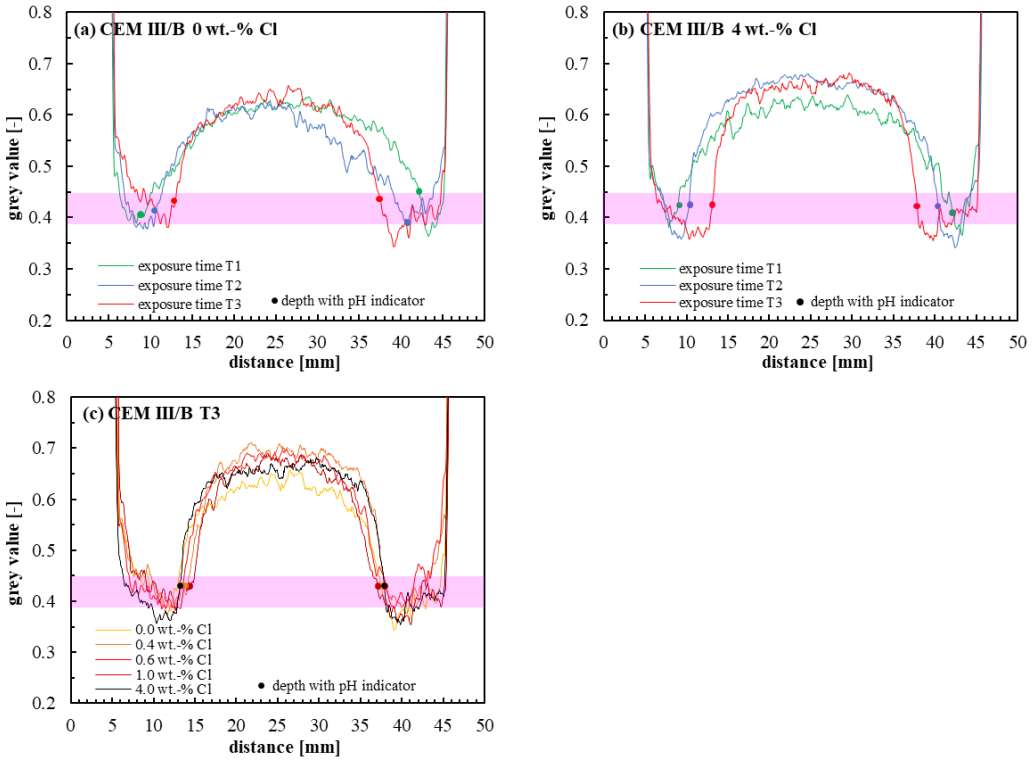

Fig. 114 *Grey value profiles of CEM III/B mortars after leaching in 6 M NH_4NO_3: (a) 0 wt.-% Cl (T1–T3), (b) T3 for all mixed-in chloride contents (0, 0.4, 0.6, 1.0 and 4.0 wt.-% Cl/binder), and (c) 4 wt.-% Cl (T1–T3). Symbols denote the phenolphthalein color-change depth; the shaded band indicates the corresponding grey value range.*

Compared to CEM I and CRCF, CEM III/B exhibits a more pronounced contrast between the decalcified outer zone and the unaffected inner core, reflected by a steeper grey value gradient. The difference in grey values increases further for specimens containing 4 wt.-% mixed-in chlorides, indicating stronger changes in phase assemblage and water distribution within the leached region.

Fig. 115 shows the grey values determined for each tested series of CEM III/B samples. The symbols show the depth at color change with pH indicator of the corresponding sample, and the pink beam shows the grey value range corresponding to the depth of color change with pH indicator.

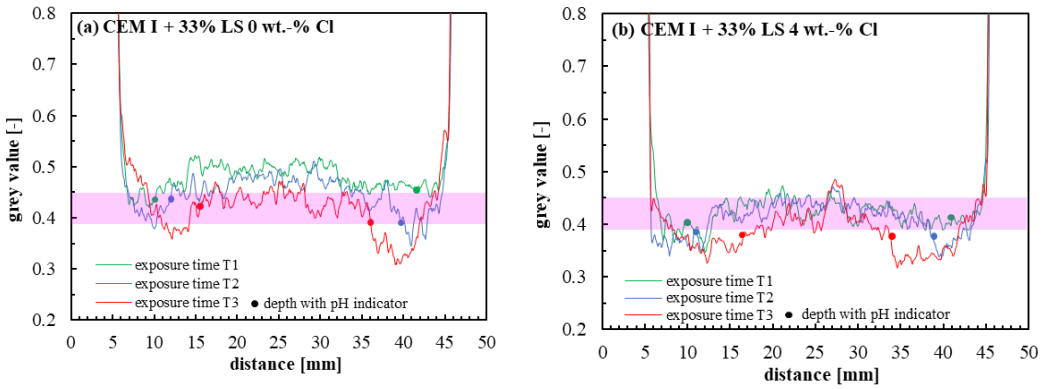

Fig. 115 *Grey value profiles of CEM I + 33% LS mortars after leaching in 6M NH_4NO_3: (a) 0 wt.-% Cl at T1, T2 and T3; (b) T3 for all chloride additions (0, 0.4, 0.6, 1.0 and 4.0 wt.-% Cl/binder); (c) 4 wt.-% Cl at T1, T2 and T3. Symbols indicate the phenolphthalein color-change depth; the pink band marks the corresponding grey-value range.*

In contrast to CEM I and CEM III/B, the unaffected core of CEM I + 33% LS specimens exhibits generally lower grey values, i.e. a darker appearance in neutron imaging. This behavior is attributed to the high calcite content introduced via limestone as well as to locally darker regions, which may indicate retained water or phases with increased neutron attenuation independent of decalcification.

Despite this lower baseline grey value in the core, a progressive expansion of the decalcified outer zone is clearly visible. With increasing exposure time (T1 < T2 < T3), the region of reduced grey values at the specimen edges widens, indicating increasing depth of water exchange and dissolution of Ca-bearing phases. The correspondence between the grey-value transition and the phenolphthalein indicator depth confirms that neutron imaging reliably captures the advance of the decalcification front in CEM I + 33% LS mortars.

Fig. 116 presents neutron images of mortar samples with 4 wt.-% Cl/binder (added as NaCl) after exposure time T3 for the four investigated binders. Fig. 119b compares the corresponding grey value profiles across the sample diameter. The symbols indicate the neutralization depth determined by phenolphthalein, while the pink band represents the grey value range associated with the indicator color change.

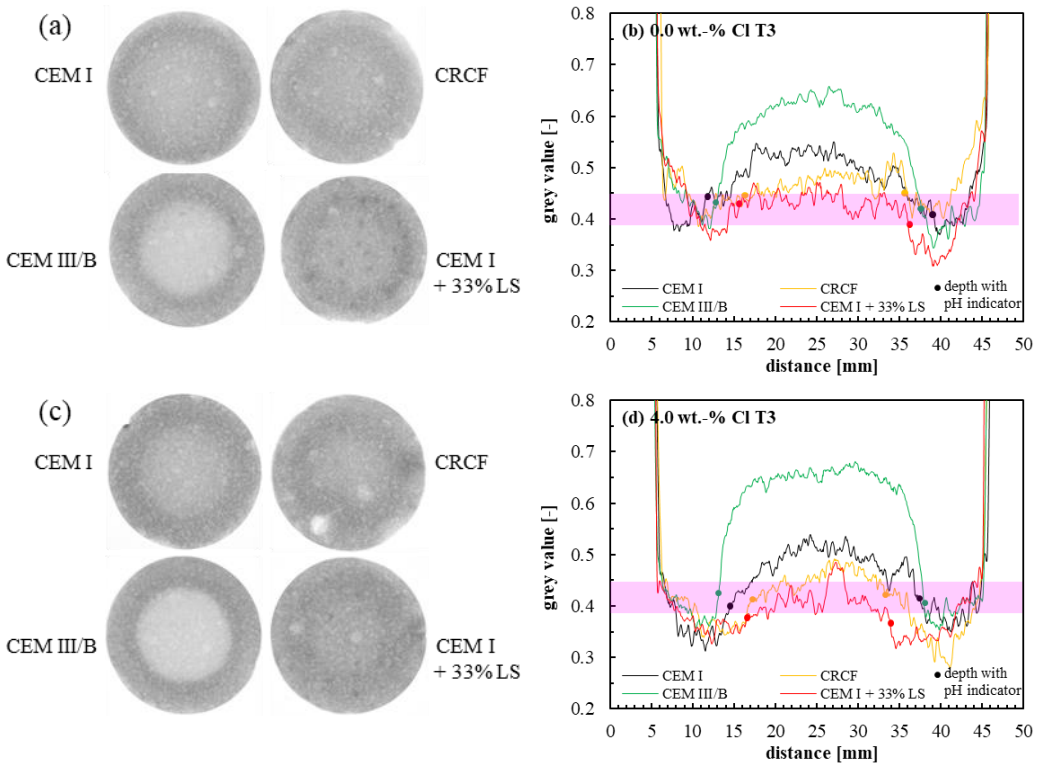

Fig. 116 *Neutron imaging and grey value profiles of mortars with 4.0 wt.-% Cl/binder at exposure time T3: (a) neutron radiographs of CEM I, CRCF, CEM III/B and CEM I + 33% LS; (b) corresponding grey value profiles across the specimen diameter. Symbols indicate phenolphthalein color change depth; the pink band marks the grey value range associated with neutralization.*

The grey value in the unaffected central region decreases in the sequence: CEM III/B → CEM I → CRCF → CEM I + 33% LS i.e. the central zone becomes progressively darker. Since neutron attenuation is strongly influenced by hydrogen and phase composition, this trend correlates with differences in calcite content and bound water distribution. Higher calcite contents (notably in CEM I + 33% LS and CRCF) reduce grey values in the core region.

For chloride-containing samples, the grey value increase in the central region is more pronounced where larger amounts of Friedel's salt are formed, indicating additional chloride binding and associated phase changes. In contrast, the slightly lower grey values in the decalcified outer zone of chloride-containing samples suggest increased porosity and enhanced water exchange compared to chloride-free specimens.

The investigations confirm that neutron imaging clearly distinguishes:

- the decalcified outer zone (water exchange region),
- the unaffected core,
- and binder-dependent differences in phase assemblage and chloride binding.

5.2.4 Chemical mapping μXRF

Fig. 117 presents μ-XRF elemental maps of CEM I mortars without and with 1 wt.-% Cl/binder (added as NaCl) after leaching in 6M NH_4NO_3.

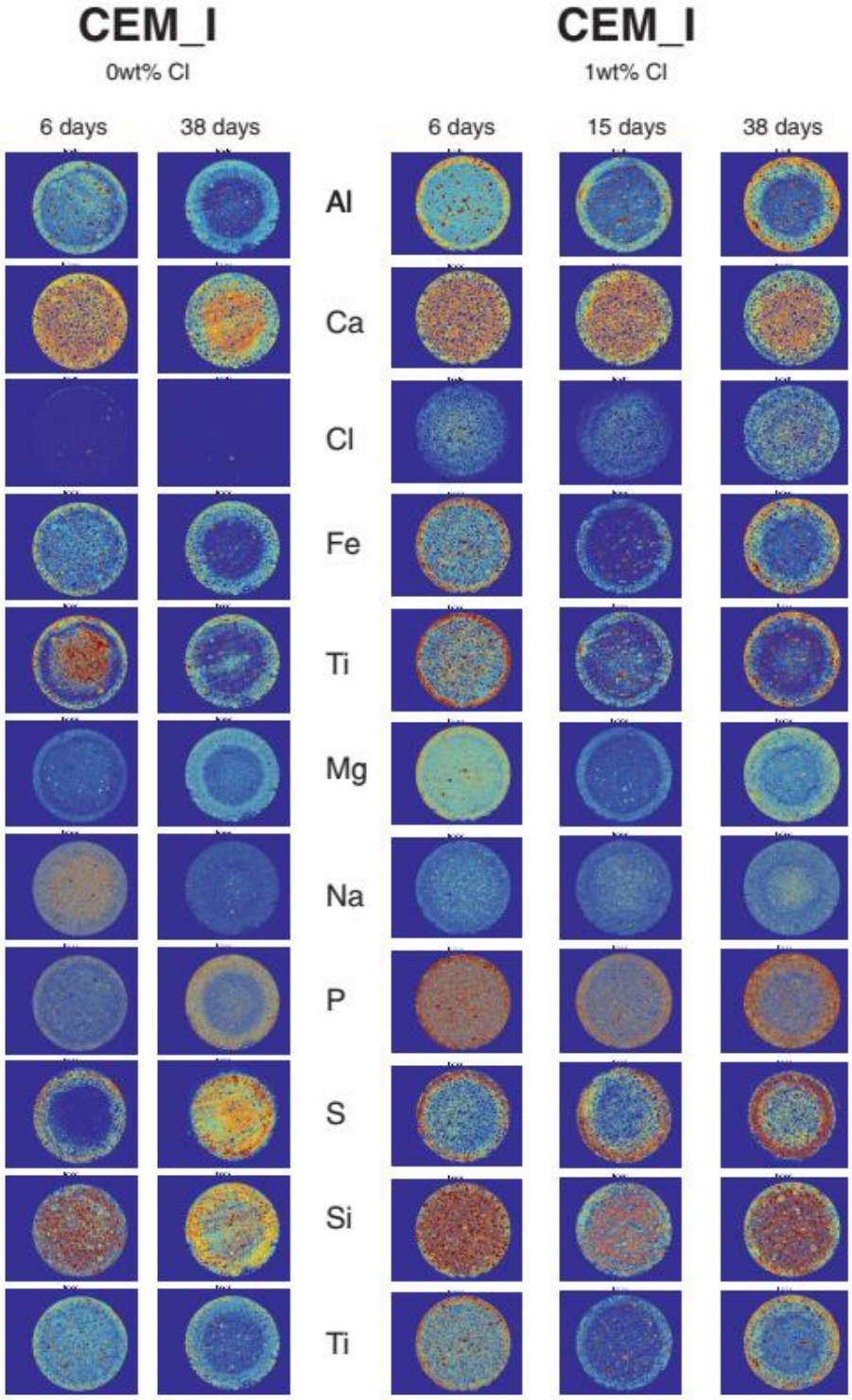

Fig. 117 *μ-XRF chemical imaging of CEM I mortar samples with 0 and 1 wt.-% Cl/binder after 6, 15 and 38 days of decalcification.*

For Fe, Ti, Mg, P and S, a consistent pattern is observed: depletion in the central region and relative enrichment in the outer zone. This spatial redistribution reflects progressive

dissolution and outward transport during decalcification. The deterioration mechanism appears similar for these elements, independent of chloride addition.

Calcium shows the clearest signature of decalcification. After 6 days, Ca depletion is more pronounced in chloride-containing samples, which is consistent with manual Ca measurements and neutron imaging results. At later exposure times, however, the difference between chloride-free and chloride-containing samples becomes negligible. The central Ca depletion becomes less pronounced with increasing time, in agreement with neutron imaging for CEM I (but not for CEM III/B).

This indicates that the slower carbonation process observed in chloride-containing concrete is primarily related to a higher degree of saturation rather than a direct chemical stabilization effect of chlorides.

In contrast to Ca depletion, Al and Si show relative enrichment in the decalcified zone. Their enrichment zones are narrower and follow Ca depletion, reflecting the stepwise dissolution sequence of Ca-bearing phases:

1. Portlandite
2. AFm phases
3. C-(A)-S-H

As Ca is removed, the remaining Al- and Si-rich skeleton becomes concentrated, producing the observed enrichment patterns.

No Cl signal is detected in chloride-free samples, confirming negligible initial chloride content in the cement. In chloride-containing specimens, Na and Cl signals are significantly elevated due to NaCl addition. A clear depletion of Cl is observed toward the outer zone. The spatial distribution suggests that chloride diffusion toward the solvent proceeds at a rate comparable to inward redistribution from the core.

5.2.5 Modelled phase change

The phase evolution during decalcification in 6 M NH_4NO_3 was modelled thermodynamically by progressively increasing the amount of leaching solution in contact with 100 g of cement paste (w/c = 0.5). Fig. 118 presents the calculated phase changes for (a) CEM I, (b) CRCF, (c) CEM III/B and (d) CEM I + 33% LS. For each binder, the reference system without added chlorides is shown on the left (1), and the system with 4 wt.-% Cl/cement (added as NaCl) on the right (2).

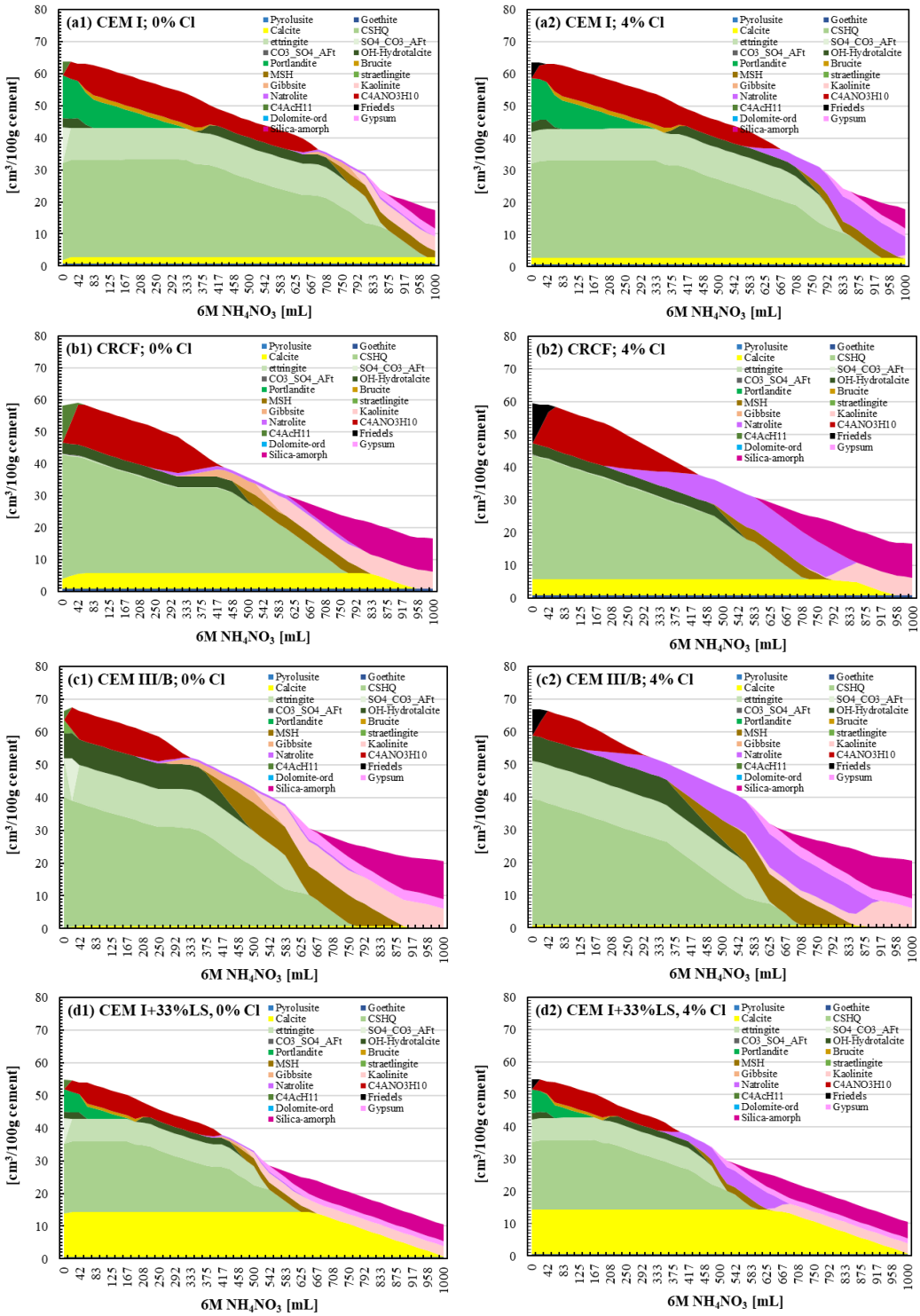

Fig. 118 *Thermodynamic modelling of phase evolution during decalcification in 6 M NH_4NO_3 for (a) CEM I, (b) CRCF, (c) CEM III/B and (d) CEM I + 33% LS. Left (1): without mixed-in chlorides. Right (2): with 4 wt.-% Cl/cement added as NaCl. Phase quantities are shown as mass (g) and corresponding solid volume (cm³).*

In chloride-containing systems (Fig. 118 (2)), Friedel's salt is the first phase to dissolve. Its presence becomes significant from ≥1 wt.-% Cl addition and it is almost completely consumed within the first ~10 mL of added solvent. Simultaneously, portlandite begins to dissolve, accompanied by partial dissolution of calcite and the destabilisation of ettringite and OH-hydrotalcite.

During the early stages of leaching, Friedel's salt and ettringite are transiently replaced by nitrate-bearing AFm-type phases and, in some systems, by thaumasite. Dissolution of OH-hydrotalcite is associated with temporary brucite formation. As decalcification progresses and portlandite is depleted, the C–S–H phase begins to dissolve, marking the transition from buffered to unbuffered leaching conditions.

Once C–S–H is substantially dissolved, the remaining primary and intermediate hydrates transform into secondary phases such as gypsum, gibbsite and silica gel. This stage corresponds to severe decalcification and structural breakdown of the hydrate assemblage. The formation of kaolinite was suppressed in the modelling, as its precipitation under the given experimental conditions is considered unlikely.

Compared to the chloride-free systems (Fig. 118 (1)), the presence of chlorides primarily affects the early dissolution sequence through the prior consumption of Friedel's salt. However, the overall decalcification pathway—portlandite dissolution followed by progressive C–S–H degradation—remains similar across all binders. Differences between binders are mainly governed by their initial hydrate assemblage and the relative amounts of portlandite, AFm phases, and C–(A)–S–H.

Fig. 119 compares the calculated phase evolution of all investigated cement types without mixed-in NaCl during progressive decalcification: (a) initial state, (b) decalcified to pH 12, (c) to pH 10 and (d) to pH 8.

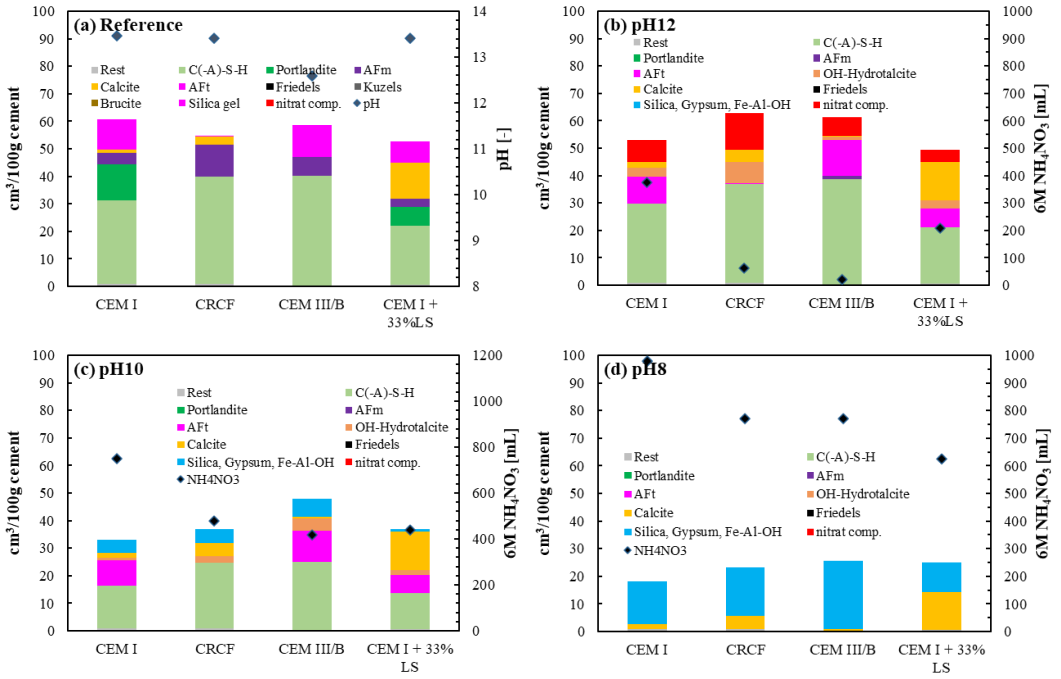

Fig. 119 *Calculated phase assemblage during decalcification in 6 M NH_4NO_3 without added NaCl: (a) initial state, (b) decalcified to pH 12, (c) to pH 10 and (d) to pH 8.*

At early stages of decalcification (pH ≈ 12), portlandite and AFm phases dissolve and are replaced by calcium nitrate. With further leaching, these calcium nitrates transform into Fe- and Al-hydroxides and amorphous silica. Subsequently, OH-hydrotalcite and AFt phases destabilize and also convert into Al-rich hydroxides and silica gel. Calcite neither forms nor dissolves significantly within the modelled conditions.

The amount of 6 M NH_4NO_3 required to reach full decalcification (pH ≈ 8) differs between binders. The lowest solvent demand is calculated for CEM I + 33% LS, whereas CEM I requires the highest amount. This indicates the fastest overall leaching progression for CEM I + 33% LS and the slowest for CEM I under the given thermodynamic assumptions.

However, differences are stage-dependent. To reach pH 12, CRCF and CEM III/B require the smallest amount of solvent. To reach pH 10, similar solvent amounts are calculated for CRCF, CEM III/B and CEM I + 33% LS. Although phase assemblage considerations would suggest faster leaching of CEM III/B compared to CEM I, the comparatively high volume of C-(A)-S-H in CEM III/B appears to buffer the system and delay the overall decalcification progress.

Fig. 120 compares the calculated phase assemblages of the investigated binders when (a) 1 wt.-% and (b) 4 wt.-% chloride (added as NaCl) are incorporated prior to decalcification. For each chloride level, the phase composition is shown for (1) the initial state, and after progressive decalcification to approximately (2) pH 12, (3) pH 10 and (4) pH 8 in 6M NH_4NO_3.

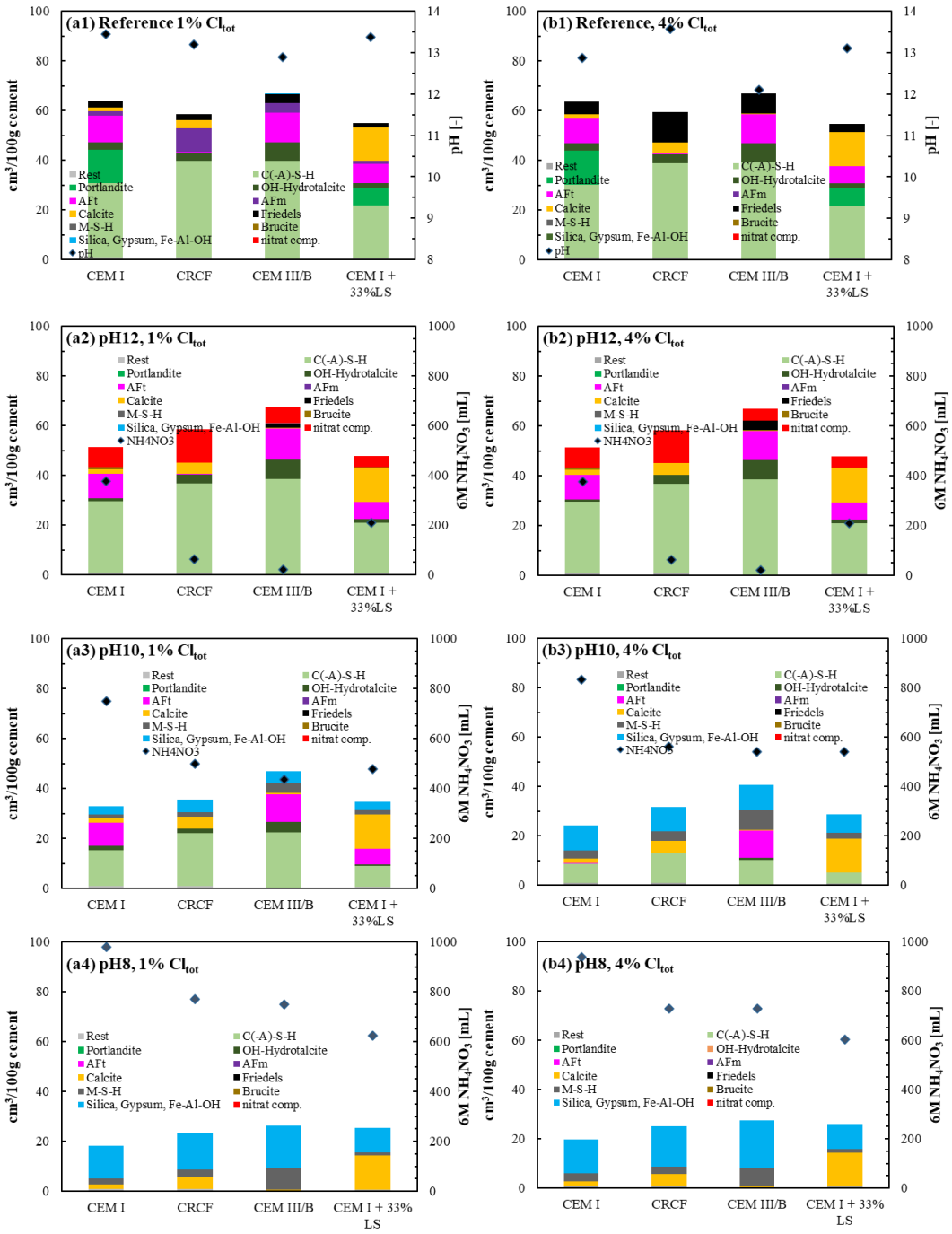

Fig. 120 *Calculated phase assemblage during decalcification in 6M NH_4NO_3 of binders containing (a) 1 wt.-% and (b) 4 wt.-% total chlorides (added as NaCl). For each binder, phase compositions are shown from top to bottom as: (1) initial state prior to leaching, (2) after decalcification to approximately pH 12, (3) to pH 10, and (4) to pH 8.*

Friedel's salt forms by chloride binding to AFm (monosulfoaluminate) via anion exchange. At 1 wt.-% Cl, AFm is only partially converted and residual AFm remains. At 4 wt.-% Cl, AFm is almost completely transformed into Friedel's salt in all binders.

In agreement with the results presented in Chapter 3.5, CRCF exhibits the highest chloride binding capacity at high total chloride contents (4 wt.-%/binder), whereas at lower chloride contents (≤ 1 wt.-%), CEM III/B shows the highest chemical chloride binding capacity.

Although CEM III/B paste has the lowest initial pH among the binders, it is the only system in which Friedel's salt remains stable at approximately pH 12 during decalcification. At this stage, ammonium nitrate phases form transiently. In CEM I and CEM I + 33% LS systems, brucite formation is additionally predicted.

Upon further decalcification to pH 10, C-(A)-S-H partially transforms to M-S-H, particularly in CEM III/B due to its Mg-bearing phase assemblage. At pH 8, the remaining phases are predominantly calcite (primary phase) and secondary phases including silica gel, gypsum, Fe- and Al-hydroxides, and M-S-H.

Consistent with the chloride-free reference systems, the amount of 6M NH_4NO_3 required to reach pH 8 is lowest for CEM I + 33% LS, indicating the lowest resistance against full decalcification. Similar solvent amounts are required to reach pH 10 for CRCF, CEM III/B and CEM I + 33% LS. The smallest amount of solvent to reach pH 12 is required for CRCF and CEM III/B.

5.3 Corrosion

5.3.1 Potential and macrocell corrosion measurement

Fig. 121 presents the evolution of the free corrosion potential (Ecorr vs. Ag/AgCl) and the corresponding macrocell corrosion rate for (a) CEM I, (b) CRCF, (c) CEM III/B and (d) CEM I + 33% LS mortar samples during exposure to 6 M NH_4NO_3 solution.

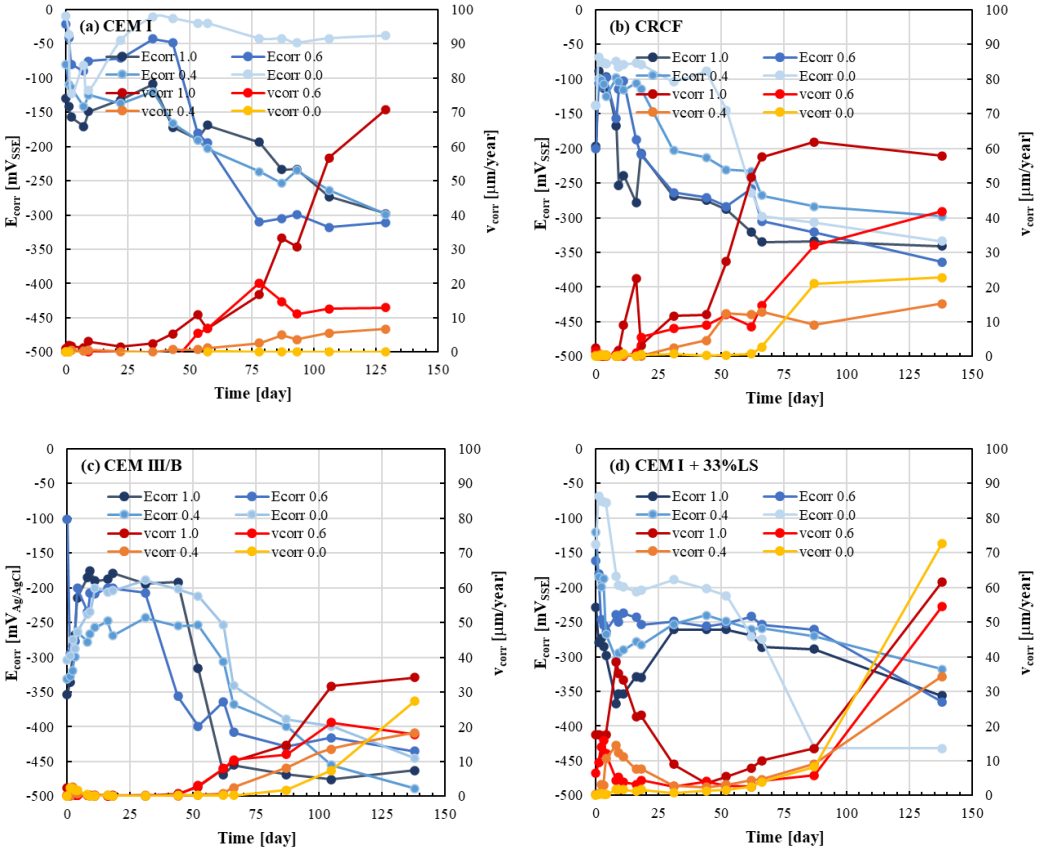

Fig. 121 *Free corrosion potential Ecorr vs. Ag/AgCl (SSE) reference electrode and macrocell corrosion rate for (a) CEM I, (b) CRCF, (c) CEM III/B and (d) CEM I + 33% LS mortars with different mixed-in chloride contents.*

For all binders, specimens containing 0.4 wt.-% Cl/binder remained passive or showed repassivation during the initial exposure period, despite the presence of chlorides. This behaviour is attributed to the inhibiting effect of nitrate ions from the NH_4NO_3 solution, which temporarily stabilise the passive film.

With increasing chloride content (≥ 0.6 wt.-%), a clear transition towards active corrosion is observed:

5.3.2 Chloride induced corrosion initiation

Tab. 25 summarizes the time to corrosion initiation (t_ini) for the different binders and chloride contents under leaching exposure.

***Tab. 25** Time at corrosion initiation in day*

mix	no chlorides	0.4 wt.-% Cl/binder	0.6 wt.-% Cl/binder	1.0 wt.-% Cl/binder
CEM I	-	-	60	50
CRCF	70	35	25	20
CEM III/B	85	65	50	50
CEM I +33%LS	70	15	10	10

For CEM I, no corrosion occurred at 0.4 wt.-% Cl, while higher chloride contents resulted in initiation after 50–60 days. In contrast, CRCF and CEM I + 33% LS exhibited significantly earlier corrosion, even at 0.4 wt.-% Cl. CEM III/B showed the longest resistance against chloride-induced corrosion, particularly at lower chloride contents.

To quantify the critical chloride content at corrosion initiation, the total chloride content (Cl_{tot}), the leached chloride amount at t_{ini}, and the remaining chloride content at initiation were calculated (Tab. 26).

***Tab. 26** total chloride content Cl^-_{tot}, leached chloride content at corrosion initiation Cl^- and remaining chloride content at corrosion initiation*

Sample	Cl^-_{tot} [mg]	Leached Cl^- at t_{ini} [mg]	Cl at initiation [wt.-%]
CEM I 0.6	159.4	134.6	0.27
CEM I 1.0	297.9	192.1	0.39
CRCF 0.4	87.5	106.5	0.22
CRCF 0.6	94.9	197.1	0.40
CRCF 1.0	132.2	353.8	0.73
CEM III/B 0.4	55.8	138.2	0.29
CEM III/B 0.6	106.6	184.4	0.38
CEM III/B 1.0	147.1	337.9	0.70
CEM I+33%LS 0.4	68.2	125.8	0.26
CEM I+33%LS 0.6	87.1	203.9	0.42
CEM I+33%LS 1.0	123.8	361.2	0.74

The lowest critical chloride contents C_{tot} have been found with 0.22 to 0.29 wt.-%/binder.

6 Summary

6.1 Effect of combined action on chloride ingress

Under cyclic wet–dry exposure (Wf-Cl), chloride ingress is significantly faster than under constant saturation (R-Cl). The ingress rates at 1 wt.-% Cl relative to cement increase typically by 30–40 %. This acceleration is governed by capillary transport, which is approximately 20–26 times faster than pure diffusion.

The influence of carbonation is strongly binder-dependent. For CEM I, carbonation slightly reduces chloride ingress (19.2 → 15.8 mm/√year, −18 %). For CEM III/B, carbonation significantly accelerates chloride ingress (9.9 → 17.5 mm/√year, +77 %). The mechanisms include:

- Release of chemically bound chlorides (Friedel's salt),
- Reduced chloride binding capacity,
- Pore structure modification during C-(A)-S-H carbonation.

Thus, carbonation does not act uniformly; its effect depends on binder chemistry and buffering capacity.

Under cyclic conditions, apparent diffusion coefficients increase by approximately 30 % compared to constant saturation. Under cyclic exposure, a chloride concentration maximum develops below the surface, typically within the convection zone (~6–7 mm).

With carbonation, the maximum shifts deeper and follows the carbonation front (e.g., ~15–17 mm for CEM III/B), while the peak concentration decreases. Carbonation therefore reduces local peak concentrations but redistributes chlorides deeper into the cover.

Chloride exposure slightly reduces total porosity (≈ 10 %). Carbonation reduces porosity more strongly but simultaneously alters pore structure. Under combined exposure free chloride concentration increases, Ca^{2+} concentration and pH decreases.

Already at pH ≈ 11, the $[Cl^-/OH^-]$ ratio increases significantly, even before full carbonation is detectable by phenolphthalein. Slag-containing binders (e.g., CEM III/B) exhibit stronger pH reduction and therefore higher sensitivity under combined exposure.

Chloride ingress correlates well with w/SiO_2 and $w/(SiO_2+Al_2O_3)$. Higher ratios result in higher chloride ingress rates. The combined oxide ratio provides a slightly stronger correlation, as it accounts for both C-(A)-S-H formation and AFm phase availability.

6.2 Effect of combined action on carbonation

Cyclic wetting and drying reduces natural carbonation rates by 40–70 % compared to sheltered exposure. For example, CEM I decreases from 3.5 to 1.0 mm/√year (−71 %) and CEM III/B from 7.0 to 3.7 mm/√year (−47 %). The reduced time exponent under cyclic conditions (b = 0.25–0.45) confirms that carbonation becomes moisture-controlled rather than purely diffusion-controlled.

Simultaneous chloride ingress reduces carbonation by an additional ~30 % on average, with stronger effects in dense systems. For CEM I, the rate decreases from 1.0 to 0.3 mm/√year (−70 %) under combined exposure. In slag-rich CEM III/B, the reduction is smaller (3.7 to 3.3 mm/√year, −11 %). The governing mechanism is the increase in degree of saturation caused by the hygroscopic nature of chlorides, which reduces the air-filled pore volume available for CO_2 transport.

Chloride contamination reduces total and hydration pore porosity to approximately 0.9 × reference values (≈10 % reduction). Carbonation caused an even stronger reduction due to $CaCO_3$ precipitation. However, durability behaviour is not governed by total porosity alone. Moisture retention and pore solution chemistry play a more decisive role under combined exposure.

Across the entire relative humidity range, chloride-contaminated specimens exhibit the highest degree of saturation, followed by carbonated and reference concretes.

This increased moisture content explains:

- Reduced carbonation rates
- Strongly reduced resistivity
- Binder-dependent changes in influential depth

Carbonation progress correlates well with $w/S\mathrm{CaO}$.

6.3 Risk for combined action

Systematic experimental investigations showed that chloride transport in carbonated concrete is similar or up to 1.2 times faster than in non-carbonated concrete. Carbonation in chloride-contaminated concrete is approximately 30 % slower than in chloride-free concrete. Combined exposure is therefore not a linear superposition of both mechanisms.

By converting carbonation and chloride ingress rates under combined action in carbonation and chloride ingress rates determined under standardized laboratory conditions (SIA 262/1) a diagram is delivered, from which the risk for combined action can be derived directly from standard test results.

Furthermore, the key compositional indicator derived in the project to assess the risk of combined action from material composition was $SiO2/CaO$.

Under XD3 & XC4 (Severe Deicing Conditions) the risk for combined action was high when:

- $SiO_2/CaO \approx 0.7 - 0.9$

However, under most XD3 scenarios, chloride ingress remains the governing process.

Under XD1 & XC4 (Moderate Combined Exposure) the risk for combined action was high when:

- $SiO_2/CaO \approx 0.5 - 0.7$

For the investigated materials CEM III/B concretes showed low diffusion coefficients, high chloride binding and strong pH reduction under carbonation and are therefore sensitive for combined action, CRCF and CEM II/B-M(S-T) show nearly equal carbonation and chloride rates under isolated exposure and favor from the reduction in carbonation rate and increase in chloride ingress rate under combined action, reducing their risk for combined action. CEM I + limestone tends to favor chloride dominance.

6.4 Effect of combined action on corrosion initiation

Under non-carbonated conditions (pH ≈ 12.5-13.5), the critical total chloride content at corrosion initiation (C_{Crit}) ranged between approximately 0.6 and >1.5 wt.-% per binder, depending strongly on binder composition. Slag-rich binders (e.g. CEM III/B, CEM II/B-M(S-T)) exhibited the highest C_{Ccrit} values due to increased chloride-binding capacity via Friedel's salt formation and higher volumes of Al-bearing hydrates and C-(A)-S-H phases. A positive correlation between Al_2O_3 content and C_{Crit} confirms the compositional control of chloride threshold in highly alkaline systems.

In contrast, when carbonation progressed to within approximately 6 mm of the reinforcement ($\Delta d_c \leq 6$ mm), a pronounced and binder-independent reduction of C_{Crit} was observed. At measured pH values of approximately 10–11, C_{Crit} decreased to 0.3–0.4 wt.-% per binder. In solution tests under full saturation and reduced binding conditions, values as low as ~0.2 wt.-% per binder were determined

The reduction of C_{Crit} was independent of the initial chloride threshold of the non-carbonated concrete. Once alkalinity fell below approximately pH 11, the chloride-binding capacity became secondary, and corrosion initiation was governed primarily by the reduced stability of the passive film.

Thermodynamic modelling confirmed that carbonation progressively reduces pore solution pH from initial values around 13.5 towards 8 - 9, governed by dissolution of portlandite and decalcification of hydrates. Depassivation in chloride-free systems corresponded to pH ≈ 9.7–10 when expressed via the $[CO_3^{2-}]/[HCO_3^-]$ criterion. The presence of chlorides shifted depassivation to lower pH values (≈ 9.0), consistent with experimental observations

Comparison of depassivation criteria showed that the $[Cl^-]/[OH^-]$ ratio predicts earlier corrosion initiation than carbonate-based criteria, whereas the $[SO_4^{2-}]/[OH^-]$ threshold appears overly conservative.

6.5 Effect of combined action on corrosion progress

Under carbonation-only exposure (Wf-CO_2) depassivation was driven by pH reduction, while the corrosion rate remained strongly controlled by moisture state. Corrosion propagation was governed by more uniform microcell corrosion (macrocell to microcell ratio ≈ 2:1). Measured macro- and microcell corrosion rates in this project (≈ XC4 conditions) were approximately 7 and 4 μm/year. Polarisation resistances generally remained above 1 kΩ·cm² in carbonated concrete with active corrosion, and free corrosion potentials were moderately negative. Corrosion activity decreased markedly during drying phases, indicating strong dependence on electrolyte continuity. Concrete resistivity ranged between 300–20000 Ω·m.

In contrast, chloride-induced corrosion was more dominated by localised macrocell processes (microcell:microcell ratio ≈ 3:1). Measured macro- and microcell corrosion rates in this project (≈ XC4 conditions) were approximately 10 and 4 μm/year. Depassivation is triggered by chloride accumulation at the steel surface, while corrosion propagation is driven by potential differences along the reinforcement. Polarisation resistances generally remained above 0.5 kΩ·cm² in chloride loaded concrete with active corrosion, and free corrosion potentials were mostly more negative. Typical resistivity ranged between 20–2000 Ω·m.

Under combined action macrocell corrosion rates were approximately twice as high as under chloride-only exposure with measured macro- and microcell corrosion rates in this project (≈ XC4 conditions) were approximately 16 and 5 μm/year. In total the corrosion rates where approximately ≈ 2.4 times higher than solely carbonation-induced corrosion and ≈ 1.7 times higher than solely chloride-induced corrosion. Polarisation resistances generally remained above 0.3 kΩ·cm² in chloride loaded concrete with active corrosion, and free corrosion potentials were mostly more negative. Typical resistivity ranged between 20–500 Ω·m.

The intensified corrosion under combined exposure can be explained by several interacting mechanisms identified in the literature and confirmed experimentally

- Influence on corrosion progress
- Release of bound chlorides during carbonation
- Reduction of pore solution alkalinity
- Shift to more negative free corrosion potentials
- Decrease in electrical resistivity
- Increased macrocell contribution

Consequently, carbonation weakens chemical passivity, while chlorides enhance electrochemical kinetics. Their combination therefore accelerates both depassivation and propagation.

7 Conclusions for standards

7.1 SIA 269/2

According to the concrete investigation the total critical chloride content C_{crit} in wt.-%/binder without carbonation effect was found between 0.6 up to > 1.5 wt.-%/binder or app. 0.075 up to > 0.188 wt.-%/concrete. Upon carbonation corrosion is initiated at a similar level of critical chloride content between 0.3 and 0.4 wt.-%/binder or from thermodynamic calculations 0.2 to 0.4 wt.-%/binder. The investigations reveal that some of the chlorides may remain physically bound in the not yet fully decalcified C(-A)-S-H.

7.2 Risk for simultaneous action in SN EN 206

Using the correlation between the carbonation coefficient expressed as KW and the chloride diffusion coefficient expressed as CW (as defined in SN EN 206 and SIA 262/1), as well as the material parameter SiO_2/CaO, it is possible to identify concrete compositions that are susceptible to combined action under XD3&XC4 and XD1&XC4 exposure conditions. Fig. 8 illustrates these relationships. Areas with dominant chloride ingress are shown in dark grey, areas with dominant carbonation in light grey, and intermediate zones indicate simultaneous progression. The performance ranges of tested NPK-A to NPK-F concretes are added.

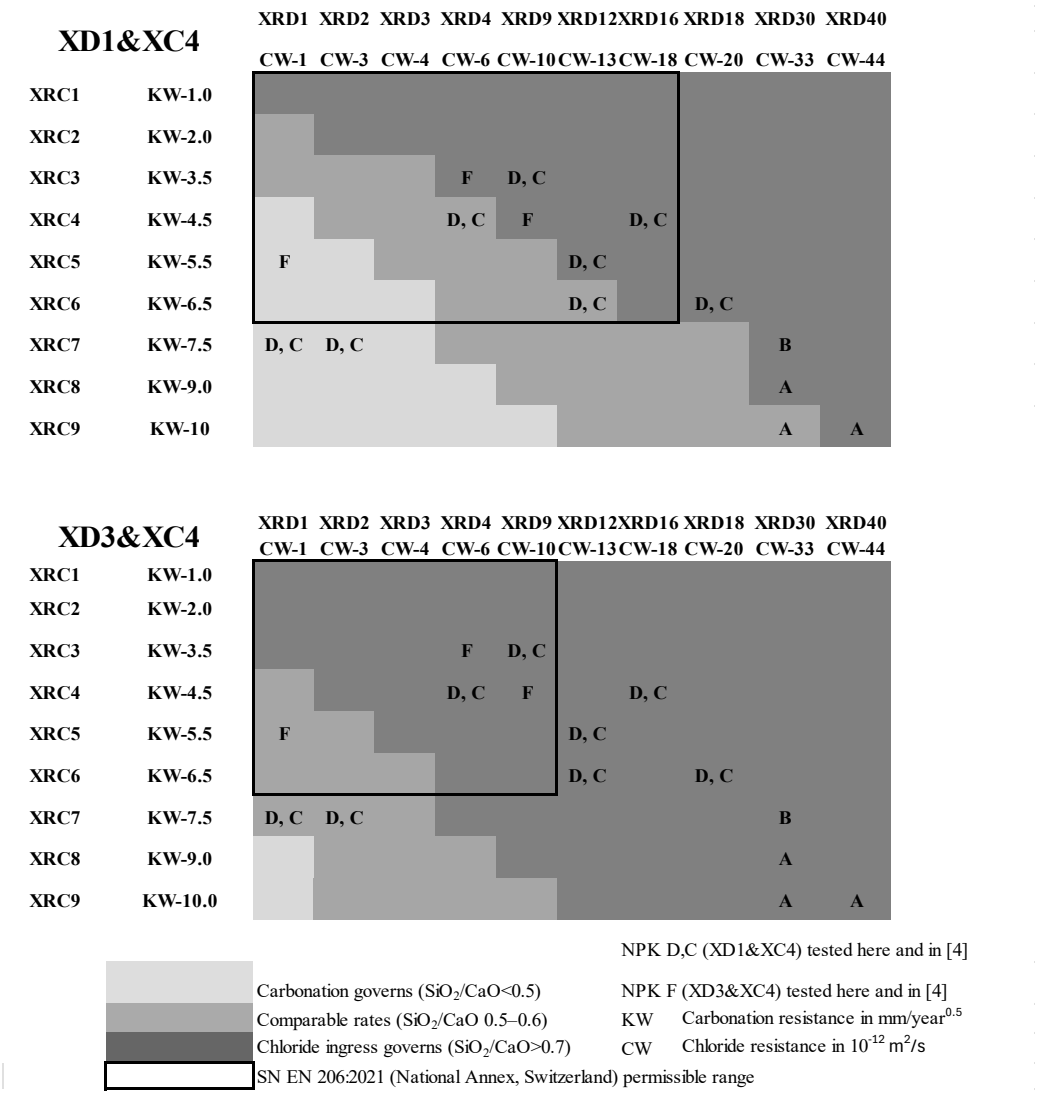

Fig. 1 *Estimation of class combinations leading to combined action for (top) XD1&XC4 and (bottom) XD3&XC4 exposure classes.*

(a) Assessment of the risk for combined action in SN EN 206 (black square range Fig. 8)

For **XD1**&XC4 exposure, SN EN 206 specifies a carbonation resistance requirement of KW-6.5, while no explicit limit is defined for chloride resistance. Based on the investigated NPK-D concretes, a corresponding chloride diffusion coefficient of approximately CW-18 can be derived. The required concrete cover is identical for XC4 and XD1.

Under XD1&XC4 exposure, chloride ingress is faster if the required material performance is exactly met, despite identical cover requirements. The reason for this is the slowing of carbonation progress in chloride contaminated concrete.

Critical conditions for combined actions occur for concretes with carbonation resistance close to the limit value KW-6.5 and moderate chloride resistance (CW between 6–10). In this case, corrosion is induced earlier than expected from chloride ingress solely and the corrosion progress is accelerated.

For **XD3**&XC4 exposure, SN EN 206 requires KW-6.5 and CW-10. In this case, the required concrete cover is higher for XD3 than for XC4 solely.

Where the limiting values for KW and CW are exactly met, chloride ingress determines the corrosion initiation. But at lower chloride resistance, combined effects are possible. Because the concrete cover is higher than required for carbonation solely, combined action seems not critical for corrosion initiation before the end of design service life.

7.3 Risk for simultaneous action in SN EN 1992-1-1

The Exposure Resistance Class (ERC) concept introduced in EN 1992-1-1:2023 allows a balance between material resistance and concrete cover. Higher resistance can compensate for reduced cover and vice versa. This approach facilitates the use of more sustainable concrete mixes that may not comply with the fixed KW limits of SN EN 206. A single concrete composition may also be applied to several exposure classes if the cover is adjusted accordingly.

Because cover and resistance are defined separately for each exposure class, combinations of XRC and XRDS classes requiring identical cover were identified. These combinations may lead to combined action. To avoid corrosion risk due to combined action, the middle grey combinations in fig. 8 should be avoided.

List of abbreviations

Abkürzung	Bedeutung
K_N	Carbonation resistance determined according to SIA 262/1 Anhang I
KW	Limiting value for the carbonation resistance according to SN EN 206
k_{NA}	Natural carbonation rate or coefficient in [mm/year$^{0.5}$] [mm/day$^{0.5}$]
k_{AC}	Accelerated carbonation rate or coefficient [mm/year$^{0.5}$] [mm/day$^{0.5}$]
b	Time exponent [-]
D_{nss}	Non-steady-steate Diffusion coefficient determined through regression to a chloride profile [10^{-12} m^2/s]
$D_{app}(t)$	Non-steady-steate Diffusion coefficient determined through regression to a chloride profile [10^{-12} m^2/s] at time t according to EN 12390-11
$D_{app}(t_0)$	Apparent Diffusion coefficient determined through log-log regression to at least three D_{nss} over time [10^{-12} m^2/s] with t_0 = 1 year
D_{Cl}	Chloride migration coefficient according to SIA 262/1 Annex B [10^{-12} m^2/s]
M_{Cl}	Chloride migration coefficient according to standards different from SIA 262/1 Annex B [10^{-12} m^2/s]
$v_{Clx\%}$	Ingress rate of a chloride content x calculated through the complementary error function solution to Fick`s second law of diffusion or determined through at least three measured chloride profiles [mm/year$^{0.5}$]
CW	Limiting value for the chloride resistance according to SN EN 206
α	Age exponent [-]
Δx	Depth with deviation from Fick`s second law of diffusion profile
$C_{s,\Delta x}$	Chloride maximum concentration either at the concrete surface ($\Delta X = 0$) or in depth Δx [wt.-%/binder or wt.-%/concrete]
x_{corr}	maximum corrosion depth as a reduction of diameter [mm]
x_{crit}	Depth with a critical corrosion inducing chloride content [mm]
E_{corr}	Free corrosion potential [mV]
SSE	Saturated silver silver chloride electrode
v_{corr}	Corrosion rate in [μm/year]
Rp	Polarization resistance in [kΩcm^2]
i_{corr}	Current density [μA/cm^2]
CW	Chloride resistance according to SN EN 206 [10^{-12} m^2/s]
KW	Carbonation resistance according to SN EN 206 [mm/year$^{0.5}$]
XRC	Exposure resistance class carbonation [mm/year$^{0.5}$]
XRD	Exposure resistance class chloride (deicing salt) [10^{-13} m^2/s]
ERC	Exposure resistance class according to EN 1992-1-1
XC	Exposure class carbonation induced corrosion
XD	Exposure class chloride induced corrosion
ToW	Time of Wetness [rainy days / year]

Bibliography

[1] FprEN 1992-1-1:2023-04, Eurocode 2 - Design of concrete structures - Part 1-1: General rules and rules for buildings, bridges and civil engineering structures

[2] CEN-TC250-SC2-N2087: March 2023 Background document to FprEN 1992-1-1:2023-04 (Formal-Vote-Draft): Eurocode 2 - Design of concrete structures - Part 1-1: General rules and rules for buildings, bridges and civil engineering structures-Durability ERC (Hallgren M, Andrade C, Toutlemond F, Nieson C, Greve-Dierfeld Sv) Chapter 2.1 and 3.1 (Greve-Dierfeld S.v.)

[3] SIA 269/2 (2011), «Erhaltung von Tragwerken – Betonbau»

[4] Greve-Dierfeld Sv, Paglia C (2025) Klassifizierung von nachhaltigen Betonen in ERC Klassen nach EN 1992-1-1. Cemsuisse Forschungsbericht 01/2025

[5] Hunkeler F, Greve-Dierfeld Sv (2019) Karbonatisierung von Beton und Korrosionsgeschwindigkeit der Bewehrung im karbonatisierten Beton. Bericht zum Forschungsprojekt AGB 2013/005 auf Antrag der Arbeitsgruppe Brückenforschung (AGB)

[6] Leemann A, Moro F (2016) Carbonation of concrete: the role of CO_2 concentration, relative humidity and CO2 buffer capacity. Materials and Structures 50(1):30. DOI: 10.1617/s11527-016-0917-2

[7] SN EN 206 (2021), „Beton – Herstellung, Eigenschaften und Konformität“, *Norm SIA 262/1:2019*.

[8] SN EN 262 (2021), „Betonbau“, *Norm SIA 262/1:2019*.

[9] prSN EN 206 (2024) Arbeitsdokument zur NA SN EN 206:2024

[10] SIA MB 2069 (2024) Kritischer Chloridgehalt im Stahlbeton – Prüfmethode zur Bestimmung an Bauwerksproben

[11] Steffen (2000) Modellierung von Karbonatisierung und Chloridbindung zur numerischen Analyse der Korrosionsgefährdung der Betonbewehrung. Dissertation Institut für Statik Technische Universität Braunschweig. Bericht Nr. 2000-90

[12] Bakker R (1993) Model to calculate the rate of carbonation in concrete under different climatic conditions, Technical report, CMIJ bv Laboratorium, Imuiden, The Netherlands, 1993

[13] *fib* Model Code for service life design (2006) International Federation for Structural Concrete (*fib*).

[14] Hunkeler F, Lammer (2012) Anfoerderungen an den Karbonatisierungswiderstand von Beton. Forschungsbericht ASTRA AGB 2008 /012

[15] ISO 16204:2012 Durability — Service life design of concrete structures

[16] Stanczak D, Kuziak J, Woyciechowski P, Czarnecki L (2020) Experimental verification of carbonation models used for estimation of reinforced concrete structures durability, Technical Sciences Warsaw 68(5):159-1166. DOI:10.24425/bpasts.2020.134652

[17] Woyciechowski P, Wolinski P, Adamczewski G (2019) Prediction of Carbonation Progress in ConcreteContaining Calcareous Fly Ash Co-Binder. Materials 12(17):2665

[18] Bary B, Sellier A (2004) Coupled moisture-carbon dioxidecalcium transfer model for carbonation of concrete. Cement and Concrete Research 34:1859–1872

[19] Georget F, Wilson W, Matschei T (2023) Long-term extrapolation of chloride ingress: An illustration of the feasibility and pitfalls of the square root law. Cement and Concrete Research 170:107187.

[20] Fjendbo S, Sørensen HE, De Weerdt K, Geiker MR (2021) The square root method for chloride ingress prediction - Applicability and limitations. Materials and Structures 54:61. https://doi.org/10.1617/s11527-021-01643-8 (0123456789().,-volV) (01234567 89().,-volV)

[21] Wilson W, Georget F, Scrivener KL (2023) xCr/√t as an indicator of the resistance against bulk chloride diffusion. International RILEM Conference on syngergising expertise towards sustainability and robustness of cement-based materials and concrete structures.

[22] Poulsen SL, Sørensen HE, Jönsson U (2018) Chloride ingress in concrete blocks at the Rødbyhavn marine exposure site—status after 5 years. 4th international conference on service life design for infrastructures (SLD4), Delft, The Netherlands

[23] Sun C, Sun M, Tao T, Qu F, Wang G, Zhang P Li Y, Duan J (2021) Chloride binding capacity and its effect on the microstructure of mortar made with marine sand. Sustainability 13:4169. https://doi.org/10.3390/su13084169

[24] Yoon IS (2015) Analysis on Adsorption Rate & Mechanism on Chloride Adsorption Behavior with Cement Hydrates. Journal of the Korea Concrete Institute 27(1):85-92

[25] Guo Y, Zhang T, Tian W, Wei J, You Q (2019) Physically and chemically bound chlorides in hydrated cement past: a comparison study of the effects of silica fume and metakaolin. Journal of Materials Science 54:2152-2169.

[26] Justnes H (1997) A Review of Chloride Binding in Cementitious Systems.

[27] Delagrave A, Marchand J, Ollivier JP, Julien S, Hazrati K (1997) Chlolride binding capacity of various hydrated cement paste systems. Advanced Cement bbased Materials 6(1):28-35.

[28] Wilson W, Gonthier JN, Georget F, Scrivener KL (2022) Insights on chemical and physical chloride binding in blended cement pastes. Cement and Concrete Research 156:106747.

[29] Ahmed DA, Mohammed MR (2011) Influence of chloride ion on the hydration reaction of C3A in presence of gypsum and lime. Advances in Cement Research 23(6):309-316

[30] Homayoonmehr R, Ramezanianpour AA, Moodi F, Ramezanianpour AM, Geaudan JP (2022) A review on the effect of metakaolin on the chloride binding of concrete, mortar and paste specimens. Sustainability 14:15022. https://doi.org/10.3390/su142215022

[31] Wang Y, Shui Z, Gao X, Huan Y, Yu R, Ling G (2019b) Chloride binding behaviors of metakaolin-lime hydrated blends: Influence of gypsum and atmospheric carbonation. Construction and Building Materials 201:380–390.

[32] Elakneswaran Y, Nawa T, K. Kurumisawa, Influence of surface charge on ingress of chloride ion in hardened pastes, Mater. Struct. 42 (2009b) 83–93, https://doi.org/10.1617/s11527-008-9368-8.

[33] Elakneswaran Y, Nawa T, Kurumisawa K. (2009a) Electrokinetic potential of hydrated cement in relation to adsorption of chlorides, Cement and Concrete Research 39(4): 340–344, https://doi.org/10.1016/j.cemconres.2009.01.006.

[34] Hirao H, Yamada K, Takahashi H, Zibara H (2005) Chloride binding of cement estimated by binding isotherms of hydrates. Journal of Advanced Concrete Technology 3(1):77-84.

[35] Guo B, Qiao G, Han P, Li Zhenming, Fu Q (2022) Effect of natural carbonation on chloride binding behaviours in OPC paste investigated by a thermodynamic model. Journal of Building Engineering 49:104021.

[36] Dousti A, Beaudoin JJ, Sheckarchi M (2017) Chloride binding in hydrated MK, SF and nautral zeolite-lime mixtures. Construction and Building Materials 154:1035-1047

[37] Zibara H, Hooton RD, Thomas MDA, Stanish K (2008) Influence of the C/S and C/A ratios of hydration products on the chloride ion binding capacity of lime-SF and lime-MK mixtures, Cement and Concrete Research 38:422–426

[38] Jones M.R., et al. (2003) Studies using 27Al MAS NMR of AFm and AFt phases and the formation of Friedel's salt. Cement and Concrete Research 33:177–182.

[39] Jun Y, Yoon S, Oh JE (2017) A comparison study for chloride-binding capacity between alkali-activated fly ash and slag in the use of seawater. Applied Sciences 7:971

[40] Machner A, Zajac M, Ben Haha M, Kjellsen K, Geiker M, De Weerdt K (2018b) Chloride-binding capacity of hydrotalcite in cement pastes containing dolomite and metakaolin. Cement and Concrete Research 107:163-181.

[41] Lee Y, Lim S, Lee H (2020) Chloride Resistance of Portland Cement-Based Mortar Incorporating High Aluminate Cement and Calcium Carbonate. Materials 13:359. doi:10.3390/ma13020359

[42] Tran Van Mien, Nguyen Van Chanh (2008) Contributions of C-S-H and AFm hydrates to chloride binding isotherms of various cements. The 3rd aCF International Concerence – ACF/CVA 2008

[43] Panesar DK, Chidiac SE (2011) Effect of cold temperature on the chloride-binding capacity of cement. Journal of Cold Regions Engineering 12:133-144.

[44] Dousti A, Shekarchi M (2015) Effect of exposure temperature on chloride-binding capacity of cementing materials. Magazine of Concrete Research 67:821–832.

[45] Wowra O, Setzer M, Setzer M, Auberg R. (1997) Sorption of chlorides on hydrated cements and C3S pastes. In Frost Resistance of Concrete; CRC Press: Boca Raton, FL, USA, 1997; pp. 147–153

[46] Yuan Q, Denk D, Shi C, De Schutter G (2013) Chloride binding isotherm from migration and diffusion test. Journal of Wuhan University of Technology – Materials Science Edition 28:548-556

[47] Nguyen T, Lorente S, Carcasses M (2009) Effect of the environment temperature on the chloride diffusion through CEM-I and CEM-V mortars: An experimental study. Construction and Building Materials 23:795–803

[48] Fraj AB, Bonnet S, Khelidj A (2012) New approach for coupled chloride/moisture transport in non-saturated concrete with and without slag. Constr Build Mater 35:761–771

[49] De Vera G, Climent MA, Viqueeira E, Anton C, Andrade C (2007) A test method for measuring chloride diffusion coefficients through partially saturated concrete. Part II: The instantaneous plane source diffusion case with chloride binding consideration. Cement and Concrete Research 37:714-724.

[50] Georget F, Benier C, Wilson W, Scrivener K (2022) Chloride sorption by C-S-H quantified by SEM-EDX image analysis. Cement and Concrete Research 152:106656

[51] Hemstad P, Machner A, De Weerdt K (2020) The effect of artificial leaching with HCl on chloride binding in ordinary Portland cement paste. Cement and Concrete Research 130:105976. https://doi.org/10.1016/j.cemconres.2020.105976

[52] De Weerdt K., Colombo A, Coppola L, Justnes H, Geiker M.R. (2015) Impact of the associated cation on chloride binding of Portland cement paste. Cement and Concrete Research 68: 196-202. https://doi.org/10.1016/j.cemconres.2014.01.027

[53] De Weerdt K (2021) Chloride binding in concrete: recent investigations and recognized knowledge gaps: RILEM Robert L`Hermite Medal Paper 2021. Materials and Structures 54:214. https://doi.org/10.1617/s11527-021-01793-9

[54] Dhir RK, El-Mohr MAK, Dyer TD (1996) Chloride binding in GGBS concrete. Cement and Concrete Research 26(12):1767-1773

[55] Luo R, Cai Y, Wang C, Huang X (2003) Study of chloride binding and diffusion in GGBS concrete. Cement and Concrete Research 33(1):1-7.

[56] Tang L, Nilsson LO (1993) Chloride binding capacity and binding isotherms of OPC pastes and mortars, Cement and Concrete Research 23(2):247–253.

[57] Wang Y, Shui Z, Gao X, Yu R, Huang Y, Cheng S (2019a) Understanding the chloride binding and diffusion behaviors of marine concrete based on Portland limestone cement-alumina enriched pozzolans. Construction and Building Materials 198:207-217.

[58] Jasielec J, Stec J, Szyszkiewicz-Warzecha JS, Lagosz A, Deja J, Lewenstam A, Filipek R (2020) Effective and Apparent Diffusion Coefficients of Chloride Ions and Chloride Binding Kinetics Parameters in Mortars: Non-Stationary Diffusion–Reaction Model and the Inverse Problem. Materials 13:5522. doi:10.3390/ma13235522

[59] Lee Y, Lim S, Lee H (2020) Chloride resistance of Portland cement based mortar incorporating high aluminate cement and calcium carbonate. Materials 13:359. doi:10.3390/ma13020359

[60] Yang Z, Sui S, Wang L, Feng T, Gao Y, Mu S, Tang L, Jiang J (2020) Improving the chloride binding capacity of cement paste by adding nano-Al2O3: The cases of blended cement pastes. Construction and Building Materials 232:117219

[61] Sui S, Wilson W, Georget F, Maraghechi H, Kazemi-Kamyab H, Sun W, Scrivener K (2019b) Quantification of methods for chloride binding in Portland cement and limestone systems. Cement and Concrete Research 125:105864

[62] Zheng Y, Russell M, Davis G et al. (2021) Influence of carbonation on the bound chloride concentration in different cementitious systems. Construction and Building Materials 302:124171. https://doi.org/10.1016/j.conbuildmat.2021.124171

[63] Fu C, Ling Y, Ye H, Jin X (2019) Chloride resistance and binding capacity of cementitious materials containing high volumes of fly ash and slag. Magazine of Concrete Research. https://doi.org/10.1680/jmacr.19.00163

[64] Saillio M, Baroghel-Bouny V, Barberon F (2014) Chloride binding in sound and carbonated cementitious materials with various types of binder, Consruction and Building Materials 68:82–91.

[65] Ukpata JO, Basheer PAM and Black L (2019) Slag hydration and chloride binding in slag cements exposed to a combined chloride-sulphate solution. Construction and Building Materials, 195. pp. 238-248. https://doi.org/10.1016/j.conbuildmat.2018.11.055

[66] Kopecskó K and Balázs GL (2017) Concrete with Improved Chloride Binding and Chloride Resistivity by Blended Cements. Advances in Materials Science and Engineering Volume 2017, Article ID 7940247, 13 pages https://doi.org/10.1155/2017/7940247

[67] Loser R, Lothenbach B, Leemann A, Tuchschmid M (2010) Chloride resistance of concrte and ist binding vapacity – comprison between experimental results and thermodynamic modeling. Cement and Concrete Composites 32:34-42

[68] Sui S, Georget F, Maraghechi H, Sun W, Scrivener K (2019a) Towards a generic approach to durability: Factors affecting chloride transport in binary and ternary cementitious materials. Cement and Concrete Research 124:105783

[69] Babaahmadi A, Machner A, Kunther W, Figueira J, Hemstad P, De Weerdt K (2022) Chloride binding in Portland composite cements containing metakaolin and silica fume. Cement and Concrete Research 161 (2022) 106924. https://doi.org/10.1016/j. cemconres. 2022.106924

[70] Dousti A, Shekarchi M, Alizadeh R, Taheri-Motlagh A (2011) Binding of externally supplied chlorides in micro silica concrete under field exposure conditions. Cement and Concrete Composites 33:1071-1079.

[71] Ipavex A, Vuk T, Gabrovsek R, Kaucic V (2013) Chloride binding into hydrated clended cements: The influence of limestone and alkalinity. Cement and Concrete Research 48:74-85.

[72] Thomas MDA, Hooton RD, Scott A, Zibara H (2012) The effect of supplementary cementitious materials on chloride binding in hardened cement paste. Cement and concrete research 42:1-7

[73] Ma Z, Liu X, Hu R, Ba G, Wang C (2023) Using recycled aggregate and powder from high-strength mortar waste for durable cement-based materials: Microstructure and chloride transport. Journal of Cleander Production 417:137998

[74] Shi Z (2016) Durability of portland cement – calcined clay – limstone blends. PhD thesis Interdisciplinary Nanoscience Centre (iNANO) Department of Chemistry Aarhus University Denmark January 2016

[75] Sun R, Hu X, Ling Y, Zuo Z, Zhuang P, Wang F (2020) Chloride diffusion behavior of engineered cementitious composite under dry-wet cycles. Construction and Building Materials 260 (11): 119943. https://doi.org/10.1016/j.conbuildmat.2020.119943

[76] Yue Y, Wang JJ, Basheer PAM, Bai Y (2018) Raman spectroscopic investigation of Friedel's salt. Cement and Concrete Composites 86 (2): 306–314. https://doi.org/10.1016/j.cemconcomp.2017.11.023

[77] Shi Z, Geiker MR, De Weerdt K, Ösnor TA, Lothenbach B, Winnefeld F, Skibsted J (2017) Role of calcium on chloride binding in hydrated Portland cement–metakaolin–limestone blends. Cement and Concrete Research 95:205-216.

[78] Shi C, Hu X, Wang X, Wu Z, de Schutter G (2017) Effects of chloride ion binding on microstructure of cement pastes. Journal of Materials in Civil Engineering 29(1):04016183.

[79] Greve-Dierfeld Sv, Lothenbach B (…) De Belie N; et al. (2020) Understanding the carbonation of concrete with supplementary cementitious materials: a critical review by RILEM TC 281-CCC. Matériaux et Construction 53, H. 6.https://doi.org/10.1617/s11527-020-01558-w

[80] Zhang Y, Yang Z, Ye G (2020) Dependence of unsaturated chloride diffusion on the pore structure in cementitious materials. Cement and Concrete Research 127:105919.

[81] Malheiro R, Camoes A, Meira G, Reis R, Nobrega A (2024) Impact of combined action of chloride and carbonation on cement-based materials with fly ash. Science 13(6):https://doi.org/10.3390/sci6010013

[82] Xu L, Zhan Y, Zhan S, Fan S, Chang H (2022) Effect of carbonation on chloride maximum phenomena of concrete subjected to cyclic wetiting-drying conditions: A numerical and experimental study. Materials 1:2874. https://doi.org/10.3390/ma15082874

[83] Luna FJ, Fernandez A, Alonso MC (2018) The influence of curing and aging on chloride transport through ternary blended cement concrete. Materials de Constuccion 68(332): https://doi.org/10.3989/mc.2018.11917

[84] Chang H, Zuo Z, Qu M, Wang F, Ge Z, Liu J (2019) Influence of Pore Structure on Chloride Penetration in Cement Pastes Subject to Wetting-Drying Cycles. Advances in Materials Science and Engineering. https://doi.org/10.1155/2019/3909348

[85] Nielsen EP, Geiker MR (2003) Chloride diffusion in partially saturated cementitious material. Cement and Concrete Research 33:133-138

[86] Olsson N, Baroghel-Bouny V, Nilsson L.-O, Thiery M (2013) Non-saturated ion diffusion in concrete–A new approach to evaluate conductivity measurements. Cement and Concrete Composites 40:40-47.

[87] Olsson N (2019) Experimental studies of ion transport in cementitious materials under partially saturated conditions. Doctoral Dissertation Faculty of Engineering, Lund University, Sweden, and Université Paris-Est, France.

[88] Mercado-Mendoza H, Lorente S, Bourbon X (2014) Ionic aqueous diffusion through unsaturated cementitious materials - A comparative study. Construction and Building Materials 51:1-8.

[89] Zhou C, Chen W, Wang W, Skoczylas F (2015) Unified determination of relative molecular diffusivity and fluid permeability for partially saturated cement-based materials. Cement and Concrete Research 67:300-309.

[90] Zhang Q,Wang F, Ling Y, Chen H, Li Z (2021) Investigation on numerical simulation of chloride transport in unsaturated concrete. Advances in Materials Science and Engineering https://doi.org/10.1155/2021/7548071

[91] Liu C, Zhang M (2023) Microstructure-based modelling of chloride diffusivity in non-saturated cement paste accounting for capillary and gel pores. Cement and Concrete Research 168:107153

[92] Helsing E (2021) Redistribution of chlorides in concrete specimens occurring during storage. Materials and Structures 54:105. https://doi.org/10.1617/s11527-021-01704-y

[93] Dousti A, Rashetnia R, Ahmadi B, Shekarchi M (2013) Influence of exposure temperature on chloride diffusion in concretes incorporating silica fume or natural zeolite. Construction and Building Materials 49:393-399

[94] Touil B, Ghomari F, Bezzar A, Khelidj A, Bonnet S (2017) Effect of Temperature on Chloride Diffusion in Saturated Concrete. Materials. Materials Journal, American Concrete Institute 114(5): 10.14359/51688929

[95] An B, Cho P, Shittu R, Kim TY, Rostron P, AlFantazi A, Yi Y (2022) Effect of Temperature Gradient on Chloride Ion Diffusion in Nuclear Reactor Containment. Energies 15:5581.

[96] Boumaaza M (2021) Experimental investigation of gas diffusivity and CO2-binding capacity of cementitious materials. Materials. PhD Thesis Université de La Rochelle & Technische Universität (Munich, Allemagne)

[97] Ye H, Jin Y, Chen W, Fu C, Jin N (2016) Prediction of chloride binding isotherms for blended cements. Computers and Concrete 17(5):635-672.

[98] Hemkemeier T, Almeida F, Sales A, Klemm A (2022) Carbonation and chloride penetration of repair mortars with water treatment plant sludge and sugercane bagasse ash sand. International Conference on Concrete Relair, Rehabilitation and Retrofitting 2022.
https://doi.org/10.1051/matecconf/202236404011

[99] Chen C, Wang L, Liu R, Yu J, Liu H, Wu J (2023) Chloride Penetration of Recycled Fine Aggregate Concrete under Drying–Wetting Cycles. Materials 16:1306

[100] Fenaux M (2013) Modelling of chloride transport in Non-saturated concrete from Microscale to macroscale. PhD thesis Unviesity Poltecnica de Madrid

[101] Shah V, Bishnoi S (2021) Understanding the Process of Carbonation in Concrete using Numerical Modeling. Journal of Advanced Concrete Technology 19:1148-1161.

[102] Fjendbo S, Sörensen HE, De weerdt K, Jakobsen UH, Geiker MR (2022) Correlating the development of chloride profiles and microstructural changes in marine concrete up to ten years. Cement and Concrete Composites 131:104590.

[103] Zhu A, Zhang X, Yang R, Wang C (2023) The deterioration mechanisms of hardened cement paste exposed to combinde action of cyclic wetting-drying, salt attack and carbonation. Construction and Building Materials 36:130148

[104] Zhu X, Zi G, Cao Z, Cheng X (2016) Combined effect of carbonation and chloride ingress in concrete. Construction and Building Materials 110:369-380.

[105] Gao Y, Zhang J, Zhu Y, Zi G, Gao Z, Cheng X (2014) Shrinkage stress in concrete under dry–wet cycles: an example with concrete column. Mech Time-Depend Mater 18:229–252 DOI 10.1007/s11043-013-9225-1

[106] Vanoutrive H, Minne P, Cizer Ö, Gruyaert E (2023) The impact of chloride binding on the resistance to carbonation: from single cycle degradation towards the comlexity of multi cycle degradation. Synercrete 2023

[107] Malheiro R, Camoes A, Meira G, Amorim MT, Castro-Comes J (2020) Interaction of carbonation and chloride ions ingress in concrete. RILEM Technical Letters 5:56-62.

[108] Delnavaz A, Ramezanianpour AA (2012) The assessment of carbonation effect on chloride diffusion in concrete based on artificial neural network model. Magazine of Concrete Research 64(10):877-884

[109] Al-Ameeri AS, Rafiq IM, Tsioulou O (2021) Combined impact of carbonation and crack Width on the chloride penetration and corrosion resistance of concrete structures. Cement and Concrete Composites 115:103819. https://doi.org/10.1016/j.cemconcomp.2020.103819

[110] Wang Y, Nankuttan S, Bai Y, Basheer PAM (2017) Influence of combined carbonation and chlolride ingress regimes on rate of ingress and redistribution of chlorides in concrete. Construction and Building Materials 140:173-183.

[111] Liu J, Ou G, Qiu Q, Chen Y, Hong J, Xing F (2017a) Chloride transport and microstructure of concrete with/without fly ash under atmospheric chloride condition. Construction and Building materials 146:493-501.

[112] Li K, Zhang Y, Wang S, Zeng J (2018) Impact of carbonation on the chloride diffusivity in concrete: experiment, analysis and application. Materials and Structures 51:164. https://doi.org/10.1617/s11527-018-1295-8

[113] Holthuizen P, Çopuroğlu O, Polder R (2017) Chloride ingress of carbonated blast furnace slag cement mortars. *fib* Symposium 2017 (HIGH TECH CONCRETE: Where technology and engineering meet!), At Maastrich, the Netherlands

[114] Liu J, Ou G, Qiu Q, Chen Y, Xing F, han N, He Y, Ma Y (2017b) Understanding the interacted mechanism between carbonation and chloride aerosol attack in ordinary Portland cement concrete. Cement and Concrete Research 95:217-225.

[115] Malheiro R, Camoes A, Meira G, Amorim MT, Castro-Gomes J, Ferreira RM (2018) Behaviour of cementitious matrices subjected to the combined action of chloride ions and carbonation. Revista Materia 23(03): 10.1590/S1517-707620180003.0496

[116] Xie M, Dangla P, Li K (2021) Reactive transport modelling of concurrent chloride ingress and carbonation in concrete. Materials and Structures 54:177. https://doi.org/10.1617/s11527-021-01769-9

[117] Angst U, Elsener B, Larsen CK, Vennesland O (2009) critical chloride content in reinforced concrete – A review. Cement and Concrete Research 39(12):1122-1138

[118] Angst U, Geiker M, Alonso MC, Polder R, Isgor B, Elsener B, Wong H, Michel A, Hornbostel K, Gehlen C, Francois R, Sanchez M, Ciado M, Sörensen H, Hansson C, Pillai R, Mundra S, Gulikers J, Raupach M, Pacheco J, Sagües A (2019) The effect of the steel-concrete interface on chlolride-induced corrosion initiation in concrete: a critical review by RILEM TC 262-SCI. Materials and Structures 52:88. https://doi.org/10.1617/s11527-019-1387-0

[119] Lollini F, Redaelli E, Bertolini L (2016) Investigation on the effect of suppementary cementitious materials on the critical chloride threshold of steel in concrete. Materials and Structures 49:4147-4165. DOI 10.1617/s11527-015-0778-0

[120] Greve-Dierfeld Sv, Bisschop J, Schiegg Y (2017) Nichtrostende Bewehrungsstähle zur Verlängerung der korrosionsfreien Lebensdauer von Stahlbetonbauwerken. Beton- und Stahlbetonbau 112(9):601-610.

[121] Andrade C, Izquierdo D (2022) Statistical Treatments of Chloride Threshold and Corrosion Propagation Rate. Corrosion and Materials Degradation 3:598-611.

[122] Wong HS, Angst UM, Geiker MR, Isgor OB, Elsener B, Michel A, Alonso MC, Correia MJ, Pacheco J, Gulikers J, Zhao Y, Ciado M, Raupach M, Sörensen H, Francois R, Mundra S, Rasol M, Polder R (2022): Methods for characterising the steel-concrete interface to enhance understanding of reinforcment corrosion: a critical review by RILEM TC 262-SCI. Materials and Structures 55:124. https://doi.org/10.1617/s11527-022-01961-5

[123] Poulsen SL, Sörensen HE (2012) Chloride thresold values – state of the art. Danish expert centre for infrastructure constructions. Final Report of Texnologisk instuture.

[124] Angst U, Vennesland Ö (2007) Critical chloride content. COIN P4 Operational service life design SP4.2 Critical chloride content. Finale technical Report SINTEF Building and Infrastucutrue

[125] Zanotto F, Sirico A, Balbo A, Bernardi P, Meerchiori S, Grassi V, Belletti B, Malcesvschi A, Monticelli C (2024) Study of the corrosion behaviour of reinforcing bars in biochar-added concrete under wet and dry exposure to calcium chloride solutions. Construction and Building Materials 420:135509.

[126] Chalhoub C (2022) Study of the initiation and propagation phases of chloride induced corrosion in reinforced concrete structures. Material chemistry. Université Paul Sabatier - Toulouse III, 2020. English. ffNNT : 2020TOU30311ff. fftel-03561562ff

[127] Hausmann D (1967) Steel corrosion in concrete – how does it occur? Materials Protection 6(11):19-23.

[128] Gauda VK (1970) Corrosion and corrosion inhibition of reinforcing steel. British Corrosion Journal 5:198-203

[129] Tuutti K (1982) Corrosion of steel in concrete. Doctoral Thesis, Division of Building Materials, Swedish Cement and Concrete Research Institute, Stockholm

[130] Achenbach R, Raupach M (2023) Comparative investigation on the influence of metakaolin, metaillite and steel slag as SCMs in mortar on the corrosion behavior of embedded steel. Corrosion and Material Protection Journal 67:21-32.

[131] Bui HAT, Maekawa K, Tan KH (2024) Electrochemical corrosion kindetics of steel bars in pseudo-transparent concrete under different alkaline properties and chloride contamination levels. Construction and Building Materials 421:135636. https://doi.org/10.1016/j.conbuildmat.2024.135636

[132] Femenias YS, Angst U, Moro F, Elsener B (2018) Development of a novel methodology to assess the corrosion threshold in concrete based on simultaneous monitoring of pH and free chloride concentration. Sensors 18:3101. doi:10.3390/s18093101.

[133] Alonso C, Castellote M, Andrade C (2002) Chloride threshold dependence of pitting potential of reinforcements, Electrochimica Acta, 47 (2002) 3469-3481.

[134] Trejo D, Pillai RG (2003) Accelerated chloride threshold testing: Part I – ASTM A 615 and A 706 reinforcement. ACI Materials Journal 100 519-527

[135] Wang Y, Zuhua X, Tangwei M, Yu J, Xing F, Li W (2023) Corrosion mechanism of reinforcement in LC3 cement pastes under coupled carbonation and chloride attack. Cement and Concrete Composites 140:105080.

[136] Schiegg Y, Hunkeler F, Keller D, Ungricht H (2017) Massnahmen zur Erhöhung der Dauerhaftigkeit – Fortsetzung des Feldversuchs Naxberg. Astra Forschungsprojekt AFB 2005/016_OBF

[137] Mi T, Li Y, Liu W, Dong Z, Gong Q, Min C, Xing F, Wang YC, Chu SH (2022) The effect of carbonation on chloride redistribution and corrosion of steel reinforcement. Construction and Building Materials 363. DOI: 10.1016/j.conbuildmat.2022.129641

[138] Lizarazo-Marriaga J, Salazar-Mayoraga LF, Pena-Cruz LE (2023) Carbonation or chloride ingress? Which one is the durability key factor in low reactivity clay and limstone blended concrete. International RILEM Conference on Synergizing Expertise towards Sustainability and Robustness of cemet-based materials and concrete structures Volume 2, pp.899-910.

[139] Parrott LJ (1990) Damage caused by carbonation of reinforced concrete. Materials and Structures 23(3):230-234

[140] Huet B, L'Hostis V, Tricheux L, Idrissi H (2010) Influence of alkali, silicate, and sulfate content of carbonated concrete pore solution on mild steel corrosion behavior. Materials and Corrosion 61(2):111–124.

[141] Schiessl P, Osterminski K, Isecke B, Beck M, Burkert A, Lehmann J, Faulhaber A, Raupach M, Harnisch J, Warkus J, Tian W, Gehlen C (2012) Dauerhaftigkeitsbemesseung von Stahlbetonbauteilen auf Bewehrungskorrosion Teil 1: Systemparameter der Bewehrungskorrosion, DAfStb Heft 601.

[142] Müller HS, Bohner E, Fischer C, Ozbold C, Gehlen C, Osterminski K, Siessl P, von Greve-Dierfeld S (2012) Dauerhaftigkeitsbemessung von Stahlbetonbauteilen auf Bewehrungskorrosion Teil 2: Dauerhaftigkeitsbemessung , DAfStb Heft 602.

[143] Beck M (2016) Zur Entwicklung der Eigenkorrosion von Stahl in Beton. Dissertation der RWTH Aachen und BAM.

[144] Jasniok T, Jasniok M (2015) Influence of rapid changes of moisture content in concrete and temperature on corrosion rate of reinforcing steel. Procedia Engineering 108:316-323.

[145] Ahmed S, Hou Y, Lepkova K, Pojtanabuntoeng (2023) Investigation of the effect of chloride ions on carbon steel in closed environments at different temperatures. Corrosion and Materials Degradation 4:364-381

[146] Rodrigues R, Caboreau S, Gance J, Ignatiadis I, Betelu S (2021) Reinforced concrete structures: a review of corrosion mechanisms and advances in electrical methods for corrosion monitoring. Construction and Building Materials 121240. 10.1016/j.conbuildmat.2020

[147] Angst U, Moro F, Geiker M, Kessler S, Beushausen H, Andrade C, Lahdensivu J, Arto K, Imamoto K, Greve-Dierfeld Sv, Serdar M (2020) Corrosion of steel in carbonated concrete: mechanisms, practical experience and research priorities – a critical review by RILEM TC 281-CCC. RILEM Technical Letters 5, https://doi.org/10.21809/rilemtechlett.2020.127

[148] Stefanoni M (2018) The corrosion of steel in near-neutral porous media – Corrosion rate in carbonated concrete. Doctoral Thesis at ETHZ BAUG.

[149] Ramirez DEA, Meira GR, Quattrone M, John VM (2023) A review on reinforcement corrosion propagation in carbonated concrete – Influence of material and environmental characteristics. Cement and Concrete Composites 140:105085.

[150] Cheng L, Maruyama I (2023) A Prediction Method for the Corrosion Rate of Steel Rebar in Carbonated Mortar under Variable Environmental Conditions. Journal of Advanced Concrete Technology 21:611-630

[151] Schmid T, Zhang Z, Angst U (2023) Ensuring the durability of reinforced concrete structures during carbonation and alternating wet/dry exposure. Cemsuisse report 2023.

[152] Hornbostel K, Elsener B, Anst U, Larsen CK, Geiker MR (2016) Limitations of the use of concrete resistivity as an indicator for the rate of chloride-induced macro-cell corrosion. *fib* Structural Concrete 18(2):326-333. https://doi.org/10.1002/suco.201500141

[153] Fagerlund, G. (Ed.), & et al. (2001). CONTECVET : A validated Users Manual for assessing the residual service life of concrete structures. (Report TVBM (Intern 7000-rapport); Vol. 7161). Division of Building Materials, LTH, Lund University.

[154] Mansoori, H, Young D, Brown B, Nesic S, Singer M (2019) Effect of CaCO3-saturated solution on CO2 corrosion of mild steel explored in a system with controlled water chemistry and well-defined mass transfer conditions. Corrosion Science 158:108078.

[155] De Weerdt K, Pluquellec G, Belda Revert A, Geiker MR, Lothenbach B (2019) Effect of carbonation on the pore solution of mortar. Cement and Concrete Research 118:38-56.

[156] Fraundorfer A, Dauberschmidt C, Gehlen C (2022) Approach to consider self-corrosion in corrosion monitoring of reinforced concrete structures exposed to chlorides. Materials and Corrosion 75(4) DOI: 10.1002/maco.202314115

[157] Bui HAT, Maekawa K, Kang HT (2023) Microcell and macrocell corrosion of steel bars in reinforced concrete slabs under different corrosive environments and cathode/anode configurations. Cement and Concrete Composites 138:104989.

[158] Albert C, Mundra S, Isgor OB, Angst U (2023) Corrosion kinetics of steel in carbonated pore solutions containing chlorides and sulphates. Proceedings of International RILEM conference SynerCrete 2023. DOI https://doi.org/10.1007/978-3-031-33187-9_97

[159] Liu G, Zhang Y, Ni Z, Huang R (2016) Corrosion behavior of steel submitted to chloride and sulphate ions in simulated concrete pore solution. Construction and Building Materials 115 (Supplement C):1–5.

[160] Ramazanianpour A, Rezaei H, Savoy H (2015) Influence of silica fume on chloride diffusion and corrosion resistance – A review. Asian Journal of Civil Engineering 16(3):301-321

[161] Eawg – Aquatic Research (2012) EAWG Jahresbericht 2011. https://doi.org/10.3929/ethz-b-000299039

[162] Österreichisches Bundesministerium für Verkehr, Innovation und Technology – Leitfaden from 2019

[163] Tuinukuafe A, Chopperla K, Weiss W, Ideker J, Isgor B (2022) Estimation Na+ and K+ concentrations of the pore solution based on ex-situ leaching tests and thermodynamic modeling. RILEM Technical letters 7:88-97.

[164] Reichling K (2014) Bestimmung und Bewertung des elektrischen Widerstands von Beton mit geophysikalischen Verfahren = Determination and evaluation of the electrical concrete resistivity using geophysical methods, Dissertation RWTH Aachen 2014

[165] Baroghel-Bouny V, Belin P, Maultzsch M, Hency D (2007) AgNO3 spray tests : avantages, weaknesses, and various applications to quantify chloride ingress into concrete. Part 1 : Non-steady-state diffusion tests and exposure to natural conditions. Materials and Structures 40 :759-781.

[166] Meck E, Sirivivatnanon V (2003) Field indicator of chloride penetration depth. Cement and Concrete Research 33(8):1113-1117. https://doi.org/10.1016/S0008-8846(03)00012-7

[167] Lothenbach B, Kulik DA, Matschei T, Balonis M, Baquerizo L, Dilnesa B, Myers RJ (2019) Cemdata18: a chemical thermodynamic database for hydrated Portland cements and alkaliactivated materials. Cement and Concrete Research 115:472-506. https://doi.org/10.1016/j.cemconres.2018.04.018.

[168] Thermodynamic database, provided by EMPA, available at: https://www.empa.ch/web/s308/thermodynamic-data.

[169] Kulik D, Wagner T, Dmytrieva S, Kosakowski G, Hingerl F, Chudnenko K, Berner U (2013) GEM-selektor geochemical modeling package: revised algorithm and GEMS3K numerical kernel for coupled simulation codes. Comput. Geosci. 17:1–24.

[170] Wagner T, Kulik D, Hingerl F, Dmytrieva SV (2012), « GEM-Selektor geochemical modeling package: TSolMod library and data interface for multicomponent phase models », The Canadian Mineralogist, 50:1173–119505.

[171] Kulik D (2011) Improving the structural consistency of C-S-H solid solution thermodynamic Models. Cement Concrete Research 41:477–495.

[172] Greve-Dierfeld S.v. (2015) Bemessungsregeln zur Sicherstellung der Dauerhaftigkeit XC-exponierter Bauteile. Disssertation TU München und DAfStb Heft 622 (2016)

[173] Bishop J, Schiegg Y, Hunkeler F (2016) Modelling the corrosion intiation of reinforced concrete exposed to deicing salts. Final Report ASTRA 676

[174] Greve-Dierfeld Sv, Schiegg Y (2016) TFB report on investigations performed over the last 30 years at a bridge over a kantonal road in Schwiez

[175] Greve-Dierfeld Sv (2022) Korrosionsrisiko in der XC2-Exposition (Corrosion due to Ca-leaching). cemuisse – Projekt 201903.

[176] *fib* Bulletin 76 (2015), Benchmarking of deemed-to-satisfy provisions in standards. State-of-the-art report. Prepared by Gehlen C, Greve-Dierfeld Sv, Gulikers J, Helland S, Rahimi R (2015)

[177] Gorlatschow O, Özdogan S, Jenny S (2022) Elektrochemische Erfassung von Korrosionsprozessen bei zyklischen Feuchtebedingungen. Abschlussbericht CAS SIB 2022/2023

[178] *fib* Model Code 2020 (2024), Model Code for Concrete Structures

Project conclusion

Schweizerische Eidgenossenschaft
Confédération suisse
Confederazione Svizzera
Confederaziun svizra

Eidgenössisches Departement für
Umwelt, Verkehr, Energie und Kommunikation UVEK
Bundesamt für Strassen ASTRA

FORSCHUNG IM STRASSENWESEN DES UVEK

Version vom 09.10.2013

Formular Nr. 3: Projektabschluss

erstellt / geändert am: 17.6.2025

Grunddaten

Projekt-Nr.:	BGT_20_03A_01
Projekttitel:	Carbonation - passivation behaviour and corrosion kinetic under the combined effect of wet-dry cycles in presence of chlorides
Enddatum:	18.02.2026

Texte

Zusammenfassung der Projektresultate:

Das Projekt untersuchte systematisch die kombinierte Einwirkung von Karbonatisierung (XC4) und Chlorideintrag (XD1/XD3) auf Transportprozesse, Korrosionsinitiierung und Korrosionsfortschritt unter Schweizer Klimabedingungen.

Die wichtigsten Ergebnisse sind:
In chloridbelastetem Beton führt erhöhte Sättigung zu verlangsamter Karbonatisierung.
In karbonatisiertem Beton werden zuvor gebundene Chloride freigesetzt, was den Chlorideintrag geringfügig beschleunigen kann.
Der kritische Chloridgehalt ohne Karbonatisierung lag zwischen ca. 0.6 und >1.5 M.-%/Binder; nach Karbonatisierung reduzierte sich Ccrit auf ca. 0.2 – 0.4 M.-%/Binder
Unter kombinierter Einwirkung waren die Korrosionsraten signifikant erhöht:
- ca. 2.4-fach höher als bei rein karbonatisierungsinduzierter Korrosion
- ca. 1.7-fach höher als bei rein chloridinduzierter Korrosion
Die kombinierte Einwirkung beschleunigt sowohl Depassivierung als auch Korrosionsfortschritt infolge:
- Freisetzung gebundener Chloride
- Absenkung des pH-Wertes
- Reduktion der elektrischen Widerstände
- verstärkter Makroelementbildung
Mit Hilfe der Kenngrössen KW (Karbonatisierung), CW (Chlorid) sowie des SiO/CaO-Verhältnisses können betonzusammensetzungsabhängige Risiken für kombinierte Einwirkung identifiziert werden
Die Untersuchungen zeigen, dass die Annahme "Karbonatisierung ist massgebend in XD1&XC4" und "Chlorid ist massgebend in XD3&XC4" Exposition nicht allgemein gültig ist.

Schweizerische Eidgenossenschaft
Confédération suisse
Confederazione Svizzera
Confederaziun svizra

Eidgenössisches Departement für
Umwelt, Verkehr, Energie und Kommunikation UVEK
Bundesamt für Strassen ASTRA

Zielerreichung:

Die Projektziele wurden erreicht.

Es wurde:
- experimentell untersucht, wie sich simultane Einwirkung auf Transport, Phasenbestand und Korrosion auswirkt,
- geklärt, unter welchen Randbedingungen kombinierte Einwirkung maßgebend wird,
- eine quantitative Einordnung des reduzierten kritischen Chloridgehalts in karbonatisiertem Beton vorgenommen,
- eine Bewertungsmethodik zur Identifikation kritischer Kombinationen von XRC- und XRDS-Klassen entwickelt

Folgerungen und Empfehlungen:

1. Bei karbonatisiertem Beton ist mit einer signifikanten Reduktion des kritischen Chloridgehalts zu rechnen (0.2 - 0.4 M.-%/Binder)
2. Unter kombinierter Einwirkung treten deutlich erhöhte Korrosionsraten auf (bis Faktor 2.4)
3. Bei der Kombination von XRC- und XRDS-Klassen sind kritische Kombinationen zu vermeiden (vgl. Fig. 8 im Bericht)
4. Die alleinige Überprüfung der Karbonatisierungsanforderungen in XD1&XC4 ist nicht in allen Fällen ausreichend.
5. Für nachhaltige neue Betone mit erhöhtem SiO/AlO-Gehalt ist eine differenzierte Betrachtung erforderlich.

Publikationen:

Der Schlussbericht wurde als ASTRA-Forschungsbericht veröffentlicht.

Der Projektleiter/die Projektleiterin:

Name: v. Greve-Dierfeld Vorname: Stefanie

Amt, Firma, Institut: TFB AG

Unterschrift des Projektleiters/der Projektleiterin:

Sv Greve - Dierfeld

Forschung im Strassenwesen des UVEK: Formular 3 Seite 2 / 3

FORSCHUNG IM STRASSENWESEN DES UVEK

Formular Nr. 3: Projektabschluss

Beurteilung der Begleitkommission:

Beurteilung:

Das Projekt liefert eine systematische quantitative Bewertung der kombinierten Einwirkung von Karbonatisierung und Chloriden unter Schweizer Expositionsbedingungen und leistet einen Betrag, eine relevante Wissenslücke zu schliessen.

Umsetzung:

Die Ergebnisse können:

in SIA 269/2 bei der Bewertung des kritischen Chloridgehalts berücksichtigt werden,

in SN EN 206 / SIA 262 bei der Bewertung kombinierter XD/XC-Exposition einfliessen,

in die Umsetzung des ERC-Konzepts nach EN 1992-1-1 integriert werden

weitergehender Forschungsbedarf:

Quantifizierung der Reduktion von Ccrit in Abhängigkeit vom Carbonatisierungsgrad

Langzeituntersuchungen unter natürlichen Expositionsbedingungen

Erweiterung der Datenbasis für nachhaltige Bindemittelsysteme

Einfluss auf Normenwerk:

SIA 269/2

SN EN 206 / SIA 262

EN 1992-1-1 (ERC-Konzept

Der Präsident/die Präsidentin der Begleitkommission:

Name: Angst Vorname: Ueli

Amt, Firma, Institut: ETH Zürich, Institut für Baustoffe

Unterschrift des Präsidenten/der Präsidentin der Begleitkommission:

Forschung im Strassenwesen des UVEK: Formular 3 **Seite 3 / 3**